Low frequency radar imaging from ramp responses in arbitrary directions

Yanhua Wen

Thèse de Doctorat

Yanhua WEN

Mémoire présenté en vue de l'obtention
du grade de Docteur de l'Université de Nantes
Sous le label de l'Université Nantes Angers Le Mans

Discipline : Electronique
Spécialité : Propagation Localisation
Laboratoire : IETR UMR 6164

Soutenance le 25 octobre 2013

École doctorale Sciences et Technologies de l'Information et Mathématiques (STIM), France
Thèse N° ED503-204

Imagerie radar basse fréquence à partir de réponses en rampe dans des directions arbitraires

JURY

Président :	**M. Christian PICHOT du MEZERAY**, Directeur de Recherche CNRS, LEAT, Université Nice Sophia Antipolis
Rapporteurs :	**Mme Amélie LITMAN**, Maître de Conférences/HDR, Université Aix-Marseille, Institut Fresnel, Marseille
	M. Lionel PICHON, Directeur de Recherche CNRS, LGEP-SUPELEC, Gif sur Yvette
Examinateurs :	**M. Jérôme IDIER**, Directeur de Recherche CNRS, IRCCyN, Nantes
	M. Bernard UGUEN, Professeur, IETR, Université de Rennes 1
Directeur de Thèse :	**M. Philippe POULIGUEN**, Ingénieur DGA/HDR, DGA/MRIS, Bagneux
Co-encadrants :	**Mme Nicole de BEAUCOUDREY**, Chargé de Recherche CNRS, IETR, Nantes
	M. Janic CHAUVEAU, Ingénieur DGA/Docteur, DGA/MI, Bruz

Remerciements

First and foremost, I would like to express my sincere gratitude to my supervisor, Mr. Philippe Pouliguen, for his endless patience, sagacious guidance and immense knowledge, which helped me all the time of the research during the three years of my Ph.D study.

Meanwhile, I would like to give my deepest gratitude to my advisors, Madame Nicole de Beaucoudrey and Mr. Janic Chauveau, for their patience, encouragement, enthusiasm and continuous support on my research, also for kindly treating me as their friend and for helping a great number of personal difficulties in my life. I could not have imagined having a better advisor.

Then, I would like to thank Mr. Christian Pichot, Mr. Bernard Uguen and Mr. Jérome Idier for accepting to be examiners of this thesis. I also thank Madame Amélie Litman and Mr. Lionel Pichon for being the reviewers of my thesis. Especial thank goes to Madame Amélie Litman for providing us helpful advices to solve the principle problems of my thesis.

I would like to thank Mr. Joseph Saillard and Mr. Yide Wang, for offering me the opportunity to study in France and also for providing me the generous support during my research and life here.

My sincere thanks also go to Madame Sandrine Charlier for providing gentle help, patience and advices for administrative issues.

Late, I offer my best regards and blessings to all friends and colleagues in the lab IETR for their endless support and encouragement. I especially want to thank Hongkun Li, my friend, for helping me deal with technical problems and sharing ideas, which permit me to have progress on certain difficulties of my thesis.

Last but not the least, I would like to thank my family, my parents Shuaibin Wen and Lingzhi Wen, for giving birth to me at the first place and supporting me spiritually throughout my life. My deepest gratitude goes to my husband Xiao Hu for his unflagging love and support throughout my life.

Contents

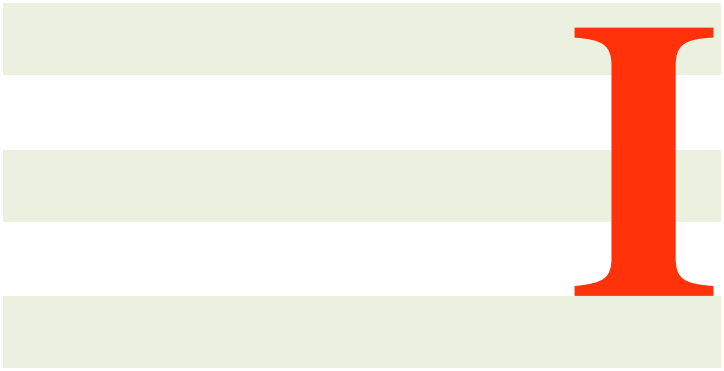

Part I: Text in English

Introduction

When a progressing disturbance in the form of a wave encounters an obstacle in a medium, it deviates from the original direction of propagation. This phenomenon is called wave diffraction or scattering. The direct scattering problem refers to the calculation of the scattered field from a known object, while the inverse scattering problem refers to the determination of the characteristic information of an unknown object from its direct scattered data [1]. In electromagnetic domain, an important problem is the characterization and identification of radar targets. Radar (Radio Detection and Ranging) is an object detection system which measures the range and exploits characteristic information of objects by transmitting electromagnetic waves and receiving the response from the objects [2]. It is mainly applied to the military detection. During the World War II, British Air Ministry was the first to fully exploit the ability of Radar as a defense of aircraft attack and succeeded in detecting approaching German aircrafts in 1940. With the rapid development of radar technology, the objectives of radar are not only detection but also characterization and identification.

Among radar targets identification problems, the scattering characterization of stealthy targets is a relevant topic. The stealthiness is intended to produce a very weak radar return and this can be obtained by shaping the target and using composite materials, which absorb electromagnetic waves in usual radar frequency bands. But, this can be countered by using lower frequencies. Moreover, the use of low frequency bands is very important in the case of Ground Penetrating Radar (GPR) applications for characterization of buried targets, since the wave attenuation in most soil increases with the frequency. These lower frequency bands correspond to the Rayleigh region and the resonance region for object dimensions respectively small and of the same order, compared to electromagnetic wavelengths. Contrary to high frequency imaging, low frequency methods cannot provide high resolution but they still bring useful information on the overall dimension and approximate shape of the target.

The use of transient scattered response resulting from a wave in the form of a ramp function in low frequency was first applied to radar targets identification by Kennaugh and Moffatt in 1965 [3]. Such a ramp response was found to be approximately proportional to the profile function of a radar target, which is defined as its

transverse cross-sectional area versus distance along the line-of-sight parallel to the incident wave direction. This property was applied by Young [4, 5] to reconstruct the shape of radar targets. He implemented the reconstruction of the target from a finite number of projections based on the relationship given by Kennaugh and Moffatt. His method, well known as the ramp response technique, uses the profile functions from 3 mutually orthogonal viewing angles and encloses the unknown target with approximate limiting surface to generate likely contours, then iteratively adjusts some geometrical parameters to obtain optimal images.

Considerable efforts have been made to improve the ramp response technique which has been applied to identification of dielectric targets [6, 7] as well as to acoustic imaging of underwater objects [8, 9]. However, former research on image reconstruction from ramp response technique uses the 'approximate limiting surface' method, proposed by Young and therefore limited to single convex objects [5]. The method of reconstruction from projections requires a considerable number of viewing angles and plane-symmetrical objects [10, 11, 12]. Chauveau's algorithm [13] permits to generate good estimates for both single and separated objects from only 3 mutually orthogonal directions. Therefore, it conquers the limitation of Young's method. While in non-orthogonal cases, the 3 methods produce distorted images. However, in practice, the radar equipment often have a limited viewing angle for remote sensing or for large targets. Therefore, it is necessary to optimize the reconstruction in arbitrary directions.

Therefore, My Ph.D. thesis is devoted to develop an algorithm with improved performances for arbitrary directions. It is necessary to use an optimization process to obtain promising estimates of the target from the observed data. The optimization process includes two sub-problems:

- A direct problem which aims to calculate the profile functions from known objects without any limitation on shapes or directions.

- An inverse problem which attempts to minimize the errors between the profile functions calculated from the estimate and the profile functions of the original object. We choose to use an iteration process to resolve this problem.

This thesis is organized as follows:

In chapter 1, the purpose is to give some background knowledge related to the context of this thesis, that is to recall some basic notions and methods to characterize the electromagnetic response of a radar stealthy target. For this, firstly, the radar cross-section (RCS), radar frequency bands and the transfer function as well as the impulse response are recalled. Then, some main stealth and counter-stealth technologies are presented and the choice of low frequency radar explained. Next, to efficiently exploit target characteristic information from the return radar signals, existing inverse scattering methods are reviewed. In conclusion of this first chapter,

we explain why we choose the method of radar imaging from ramp responses.

In chapter 2, Radar imaging from ramp responses is presented. After giving the definitions of the ramp response, the profile function and the required frequency band, the state of the art of algorithms for radar image reconstruction from profile functions is presented. Examples of various objects are reconstructed with Chauveau's method [13], for mutually orthogonal and non-orthogonal directions.

In chapter 3, we present our contribution on the optimization of image reconstruction with profile functions from arbitrary directions.

In section 3.1, the objective is to solve the direct problem. For this, we develop an algorithm calculating the geometrical profile function of a 3-dimensional (3D) object of arbitrary shape. Then, we apply it to quantitatively evaluate the quality of image reconstructions and to identify radar targets with a database of possible models.

In section 3.2, the objective is to solve the inverse problem. Firstly, we explain why the least-square method (LSQR) [14], a classical inverse method for linear problems, fails to extract a correct binary shape. Therefore, we review the existing methods for shape representation and deformation. Then, we focus on the level set method, which is adapted to our problem: we detail the principle of this method as well as the different types of evolution velocity. We present the level set method in our case of image reconstruction from profile functions in arbitrary directions, with the example of a sphere to illustrate the iterative process. Finally, we present an efficient method to reduce the computational cost, the 'narrow-band' level set method.

In section 3.3, 3D reconstructed results using 'narrow-band' level set method are presented for various objects: firstly, with geometrical profile functions in 3 mutually orthogonal directions; secondly, with geometrical profile functions in non-orthogonal directions; thirdly, with physical profile functions. Then, the effect of some parameters for the reconstruction is studied.

Finally, in chapter 4, general conclusions are given to sum up the work dealt within this thesis and some perspectives for the future work are proposed.

1

Characterization and identification of radar targets

Radar system uses electromagnetic waves illuminating targets to get scattered signals back from them. Using these signals, one can exploit characteristics information (size, shape and orientation) of target and then identify them, which is, indeed, a typical inverse scattering method. Among radar targets identification problems, the scattering characterization of stealthy targets is a relevant topic. The stealth technology aims to attenuate the radar cross-section (RCS), which is a measure of how detectable an object is by radar. To detect and identify stealthy targets, two challenging problems that should be concerned are:

- the choice of technology which involves in acquiring more RCS of the target to counter the stealthiness.

- the choice of inverse scattering method which efficiently exploits characteristic information from the return signal, considering the chosen counter-stealth technology as well. In this thesis, we are concerned by this problem.

Therefore, in this chapter, firstly, we recall , in section 1.1, some basic notions, such as the radar cross-section (RCS), the radar frequency bands, transfer function and radar impulse response. In section 1.2, a brief introduction of stealth and counter-stealth technology is given. In section 1.3, previous work related to inverse scattering methods are reviewed. Finally, conclusion is given for characterization and identification of stealthy targets in section 1.4.

1.1 Basic notions of radar signatures

In this section, we introduce the basic notions utilized for the response of the target to an excitation electromagnetic wave from a radar.

1.1.1 Radar cross-section or RCS

Radar uses electromagnetic waves to illuminate targets such that it can detect and identify them from the return waves. In fact, when an object is illuminated by an electromagnetic wave, it will be excited and produce a current on the surface until the electrostatic equilibrium is achieved again. Meanwhile, the object becomes a luminous body or a heat source. Therefore, it will re-radiate electromagnetic energy in all directions so that it can be seen by the radar receiver. This ability to reflect radar energy to the radar receiver can be measured by a term: Radar cross-section or RCS. It is noted as σ, and has a unit of m^2. The RCS of an target is the cross-sectional area of a perfectly reflecting sphere that would produce the same strength reflection as would the target. It measures the ratio between the received power after reflection and the incident power.

If we consider a bistatic radar, where the transmitter and the receiver are located in different places, as show in Fig. 1.1 (a), the amount of effective reflected power received by the radar is defined by the following equation [15]:

$$P_r = P_t \frac{G_t G_r \sigma \lambda^2}{(4\pi)^3 R_1^2 R_2^2} \tag{1.1}$$

where:

- G_t is the gain of the transmitter (dimensionless);
- G_r is the gain of the receiver (dimensionless);
- R_1 is the distance between the transmitter and the target (meter, m);
- R_2 is the distance between the receiver and the target (meter, m);
- P_t is the transmitting power (watt, W);
- σ is the RCS of the target (square meter, m^2);
- λ is the wavelength (meter, m).

For a monostatic radar, the transmitter and the receiver are located in the same position ($R_1 = R_2 = R$), as shown in Fig. 1.1 (b).

Assuming that the target is located in the far-field of the radar, the RCS is given by the following equation [16]:

$$\sigma = \lim_{R\to\infty} 4\pi R^2 \frac{|\vec{E}_r|^2}{|\vec{E}_i|^2} = \lim_{R\to\infty} 4\pi R^2 \frac{|\vec{H}_r|^2}{|\vec{H}_i|^2} \tag{1.2}$$

where:

- $\vec{E}_r$ is the reflected or scattered electric field received by the receiver, (volt per meter, V/m);

- $\vec{H}_r$ is the reflected or scattered magnetic field received by the receiver, (ampere per meter, A/m);

- $\vec{E}_i$ is the incident electric field (volt per meter, V/m);

- $\vec{H}_i$ is the incident magnetic field (ampere per meter, A/m).

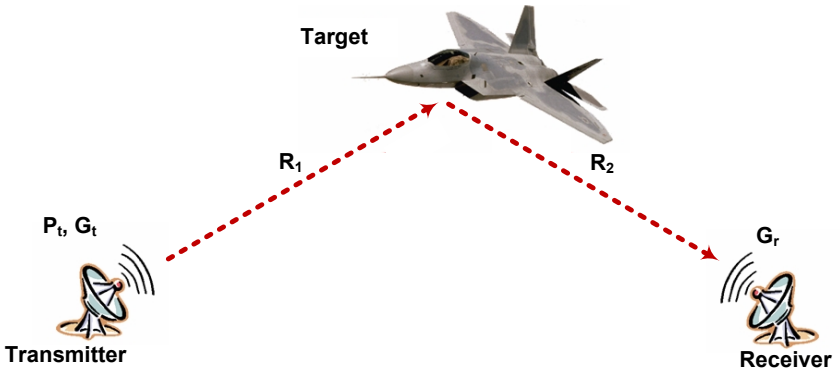

(a)

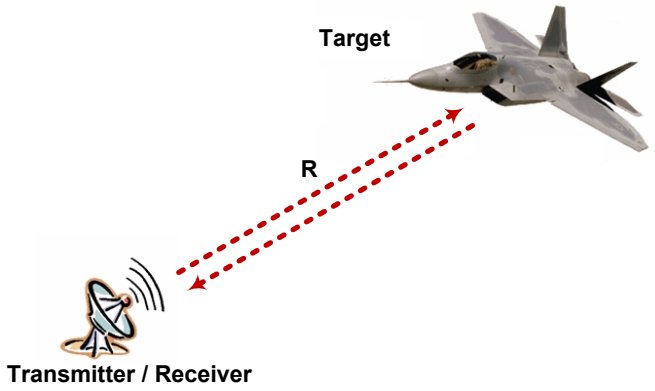

(b)

Figure 1.1: Configuration of radars: (a) bistatic radar; (a) monostatic radar.

In fact, the above equations hold with the assumption that the reflected or scattered radar energy by a radar target is isotropic. However, it is impossible in practice. It is a characteristic information for different objects, which can be used to identify them. The RCS of an object depends on several factors:

- the ratio between the object size and the wavelength (frequency) of the excitation;

- the reflectivity of the object surface (surface roughness and material composition);

- the directivity of the radar reflection (target shape and aspect angle related with the incident wave);

- the polarization of the radar.

To sum up, the RCS is an intrinsic information depending on the target characteristics (shape, size and materials), the excitation and the observation (direction and polarization). This information is particularly important for military applications.

1.1.2 Wavelength and frequency band

To demonstrate the effect of the ratio between target size and radar wavelength (frequency) to the RCS, we first present in Table 1.1, the radar frequencies f and corresponding wavelengths $\lambda = c/f$, with c being the speed of light in the freespace.

Table 1.1: Radar frequency and corresponding wavelength.

Frequency f	Wavelength λ
1 MHz	300 m
10 MHz	30 m
100 MHz	3 m
1 GHz	30 cm
10 GHz	3 cm
100 GHz	3 mm

If a perfectly electric conducting (PEC) sphere of radius r is illuminated by electromagnetic waves at sufficiently high frequencies ($\lambda \ll r$), its monostatic RCS is given by:

$$\sigma = \pi r^2 \tag{1.3}$$

When the wavelength is not less than the radius, the calculation of the RCS becomes more complicated. Fig. 1.2 gives the RCS of the PEC sphere for 3 regions classified by the relations between the wavelength λ and the characteristic dimension D of the target [1][17].

The three regions are defined by:

Rayleigh region ($D \ll \lambda$) This region corresponds to low frequencies of the wave excitation. In this region, the object characteristic dimension is less than the wavelength. The RCS varies as the fourth power of the frequency and provides information on the volume of the illuminated object.

Resonance region ($D/2 < \lambda < 10D$) It is named as Mie region for the case of the sphere. It corresponds to a region where the RCS is oscillating. As can be seen in Fig.1.3, this oscillating behavior, as a function of the frequency, is due to

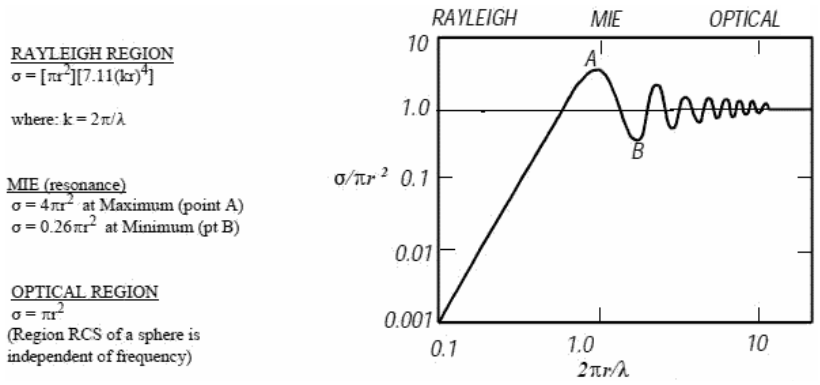

Figure 1.2: RCS for a perfectly electric conducting sphere of characteristic dimension $D = 2r$, as a function of r/λ

the interference between the different forms of the signals reflected by the object: direct scattering from the illuminated surface or body, the creeping waves from the "shadow" region, etc. Therefore, the resonance region gives information on the details of the object.

Optical region ($D \gg \lambda$) This region corresponds to high frequencies of wave excitation and it occurs when the wavelength is greatly below the object characteristic dimension. The optical region produces more details of the object comparing to the two other regions.

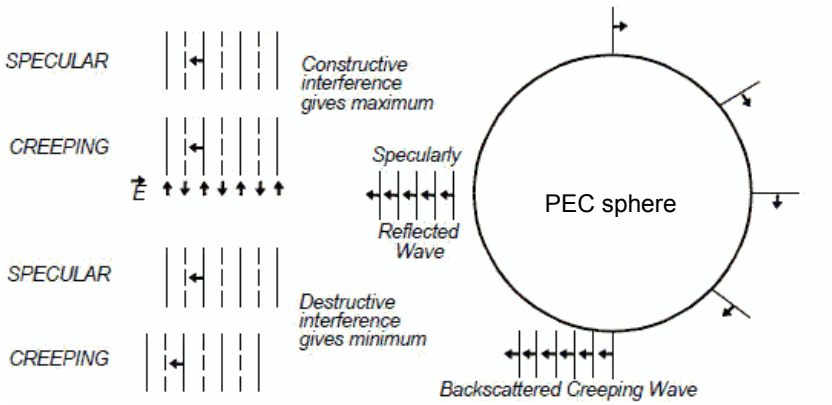

Figure 1.3: The specular (mirror) reflected waves and creeping waves.

1.1.3 Transfer function and impulse response

To detect and identify a radar target, one can analyze the radar response either in temporal domain or in frequency domain. The choice of the domain for the study mainly depends on the method for getting the radar response. It is necessary to use a large frequency band to get a very significant response from the target. Indeed,

larger the frequency band of excitation is, more scattered signal is returned from the target. The impulse response of a target, namely the temporal response of a wave in the form of Dirac function, corresponding to an infinite frequency band, is a key information for the target characterization.

Fig. 1.4 illustrates the temporal impulse response of a radar target: an incident plane wave, corresponding to an electromagnetic impulse of amplitude $\vec{E}_i(t)$, propagates along the direction y towards a target centered in the origin O and located at the distance r to the radar.

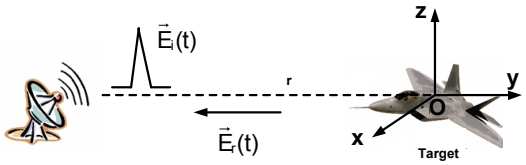

Figure 1.4: Illustration of the temporal impulse response of a radar target.

The wave scattered from the target $\vec{E}_r(t)$ can be represented by the analogy with the theory of linear filters, as shown in Fig. 1.5, where $H_{rec}(j\omega)$ is the complex gain of signal received by the radar at infinity, and $h_{rec}(t)$ is its Inverse Fourier Transform (IFT):

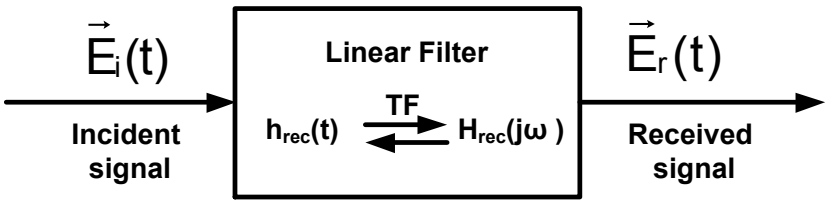

Figure 1.5: Analogy with the theory of linear filters.

This complex gain $H_{rec}(j\omega)$ can be obtained by normalizing the transfer function of the target $H(j\omega)$ [18]:

$$H_{rec}(j\omega) = \frac{|\vec{E_r}|^2}{|\vec{E_i}|^2} = \frac{c}{2r}H(j\omega) \tag{1.4}$$

where the constant c is the speed of the light propagating in the freespace.

Then, the temporal impulse response of the target, namely the IFT of its transfer function, is given by:

$$h(t) = \frac{2r}{c}h_{rec}(t) = \int_0^{+\infty} H(j\omega)e^{j\omega t}d\omega \tag{1.5}$$

For an arbitrary excitation, the signal received by the radar is expressed by the following convolution:

$$E_r(t') = \int_0^{+\infty} h_{rec}(\tau) E_i(t' - \tau) d\tau \tag{1.6}$$

For the particular case where the incident signal is a Dirac impulse, $E_i(t) = \delta(t)$, the received signal is equal to:

$$E_r(t') = \int_0^{+\infty} h_{rec}(\tau)\delta(t' - \tau)d\tau = h_{rec}(t') = h_{rec}(t - r/c) \tag{1.7}$$

We can see that the impulse response of a Dirac function corresponds to the Inverse Fourier Transform of the complex gain of the received signal. From the Eq. (1.5), the impulse response $h(t)$ reflected from the target is obtained by normalization with a time shift r/c and a amplitude factor $2r/c$.

The considered target always has a finite size, we note that the impulse response decreases for t' of high value. This exponential decrease is due to the decrease of the current on the target surface (and in the interior of the non-perfectly conducting objects). In fact, the current on the surface decreases eventually until the electrostatic equilibrium is achieved by energy transformation and re-radiation to the space. This decrease is then described mathematically by a set of damping exponentials, whose time constants are completely and extremely low in all practical cases.

If the incident signal is of the form $E_i(t) = e^{j\omega t}$, the received signal is expressed by:

$$E_r(t') = e^{j\omega t'} \int_0^{+\infty} h_{rec}(\tau) e^{-j\omega\tau} d\tau = H_{rec}(j\omega) e^{j\omega t'} \tag{1.8}$$

By normalizing the Eq. (1.4), we can obtain:

$$\frac{2r}{c} E_r(t') = 2rcH_{rec}(j\omega)e^{j\omega t'} = H(j\omega)e^{j\omega t'} \tag{1.9}$$

Applying the definition of the RCS Eq. (1.2), we obtain the relation between the RCS and the transfer function of the target:

$$\sigma = \pi c^2 |H(j\omega)^2| \tag{1.10}$$

1.2 Stealth and counter-stealth

As mentioned before, the RCS is a specific information of an arbitrary object permitting to quantify its ability to be detected and identified by a radar. It plays a significant role in military applications. Low RCS is always desired during the combat or other military missions, for the sake of attacking the adversaries secretly and

moreover increasing combat effectiveness and survivability. Therefore, the stealth technology aims to reduce the RCS. On contrary, the counter-stealth technology aims to increase the RCS to defend the enemy.

1.2.1 Stealth technology

Stealth technology, also named LO (low observable technology), involves a combination of various methods to make an object less detectable from radar, infrared or other detection methods. Recently, stealth technologies are one of the main electronic countermeasures used to make aircrafts, ships, helicopters, UAVs (Unmanned aerial vehicle), missiles and other military vehicles less detectable from the radar. According to the factors that have influences on the RCS, here, we introduce two main techniques of RCS reduction:

Shaping The principle of shaping is to radiate away from the radar so that the received power density can be minimized at possible intercept receiver locations. Generally, an ordinary aircraft has a very complex shape and has a lot of components, i.e, air inlets, compressor blades, vertical stabilizers, all discontinuities and corners, which can reflect energy back to the source or the receivers. For example, the tailplane of a conventional aircraft directly reflects a great part of the signal back to the radar. This is due to a corner reflector formed by the orthogonal metal plates of the tailplanes. Therefore, $F-117$ Nighthawk (Fig. 1.6), formerly operated by the United States Air Force (USAF), changes the direction of the tailplanes to avoid forming a corner reflector. Another example of the stealth aircraft operated currently by USAF, the $B2$ spirit (Fig. 1.7), completely reduces the tailplanes. It has compact, smoothly blended external shape without vertical plane, which permits to produce less reflection in order to receive less radar signals [19].

Radar Absorbent Material (RAM) Radar absorbent material is used to help converting electromagnetic energies to heat rather than reflect them back. This is often realized by coating or painting the edges of metal surface with special materials, such as carbon products of poor conductivity and epoxy resin against the radiating currents [21]. The limit of RAM is that it can not be used as the main technique for the low observability, because its ability of wave absorption is very limited and it never decrease the RCS of an aircraft to a large extent. Moreover, RAM is effective only in some frequencies and angles.

To achieve an extremely low RCS levels for stealth aircrafts, only a single technique is not enough. The two main techniques should be combined together with other stealth techniques, such as passive and active cancellation of RCS, to make them nearly invisible to the adverse radars [22].

Figure 1.6: Photo of $F-117$ Nighthawk [20].

Figure 1.7: Photo of $B2$ spirit [19].

1.2.2 Counter-stealth technology

During the combat, one side tries to be lower detectable and to give less detectable signals by stealth technology. On the contrary, the other side attempts to get more signals and to exploit them more efficiently to identify the threat. This is so-called counter-stealth or anti-stealth technology. The two main techniques for the counter-stealth are presented as following:

Bistatic and multistatic radar Since the stealth technology is designed to focus on defeating ordinary monostatic radar, it reduces the RCS by reflecting radar signals to other directions, rather than reflecting back to the source. Therefore, if we receive the signals in a direction different from the direction of the source, better RCS will be achieved and the stealthiness is less effective. This is realized

by bistatic and multistatic radars where the transmitter and receiver are located in different positions [23].

Low frequency radar In optical region, the wavelength is much smaller than the physical size of the target, therefore, the shaping technique is effective by changing the directions of the reflection, but this can be countered by using low frequency bands. These radars operating in HF (High Frequency, 1 MHz − 30 MHz) and VHF (Very High Frequency, 30 MHz − 300 MHz) as well as UHF (Ultra High Frequency, 300 MHz − 3 GHz) correspond to the Rayleigh region and the resonance region for object dimensions respectively small and of the same order, compared to electromagnetic wavelengths [24, 25, 26].

Moreover, in low frequency bands, RAM become very heavy and expensive to get desired the reduction of RCS.

The limit of the low frequency radar is that contrary to the high frequency corresponding to the optical region, only approximate and rough information on the target geometrical characteristic can be obtained. But still, it can give useful information on the target size, volume, which can be used to generate images for the target's global shape.

Therefore, we are interested in low frequency radar. With available signals obtained by such technique, our objective is the characterization and identification of targets. Therefore an adapted inverse scattering method, operating in low frequency and generating accurate enough images of targets, is required.

1.3 Inverse scattering methods

When a progressing disturbance in the form of a wave encounters an obstacle in a medium, it deviates from the original direction of propagation. This phenomenon is called wave diffraction or scattering. The direct scattering problem is to determine the electromagnetic field (magnitude and phase) resulting from the interaction between the wave emitted by the source and the object. The input data are the source, defined by the field it creates and its electromagnetic properties (emission frequency or pulse width, radiation pattern,...), and the object characterized by its geometry, its position relative to the source and its electromagnetic properties. On the contrary, the inverse scattering problem is to determine, from the electromagnetic field reflected or scattered by an object, some characteristic information on it, such as its geometry (identification problem) and/or electromagnetic properties (diagnosis problems), etc. In this case, the input data are the source and the resulting interaction of the incident wave field with the object. This scattered or diffracted field is known either for any point in the studied domain or for a small region in the studied domain.

The methods for solving inverse scattering problems are numerous and various. They can be divided into two categories: fast but approximate method, based on algorithms using linear approximations, and slower but more accurate method, using non-linear algorithms. We present below three linear methods which are based on the approximation of physical optics (Born or Rytov) diffraction tomography [27, 28, 29, 30], the method of Bojarski [31] and the inverse Born approximation [32, 33]. The approximation of physical optics makes it possible to use a linear relationship between the field diffracted by an object and its geometrical characteristics. In general, these geometrical characteristics are obtained by the spatial Fourier transform of the response from the object and are used to develop algorithms for simple and fast reconstruction. The technique of the ramp response [5] is a linear method, but its originality is that it uses a particular form of incident wave. Unlike linear algorithms, non-linear algorithms [34, 35, 36, 37] generally require significant calculations for the inverse problem, usually by iteration (Newton method). An intermediate method that lies between linear and non-linear methods, named the "Linear Sampling Method" (LSM), was developed by David Colton and Andreas Kirsch [38]. This method has received much attention in the mathematics domain and the electromagnetic domain, because it permits the characterization of aircraft in the resonance region [39]. Other alternatives to identify a target intend to extract characteristic parameters of the target instead of reconstructing an image of it. These parameters characterize the target geometry and can be used in an identification process.

1.3.1 Diffraction tomography

Mathematical models for the diffracted wave tomography were developed by Wolf [40] and Devaney [30] for ultrasound and Bojarski [41] and Richmond [42] for the microwave. This technique has grown rapidly in the domain of medical and industrial imaging. The generalization of the Radon theorem, used in X-ray tomography, to the wave diffraction tomography helps to understand how to map the Fourier space of the diffracting object to field measurements that it diffracts. However, the wave propagation is expressed by differential equations and, in general, we can not get explicit solutions which link the diffracted field to the object. Hence, a first step intends to make a limited development (currently most often in the first order) of the solution by introducing additional assumptions about the problem (low diffracting object, low index variations, etc..). This step has the effect of introducing an explicit relationship between the measured data in different directions (diffracted field or "projections") and the object to be reconstructed. However, due to the necessarily limited number of projections, the obtained information of the object is incomplete. The second step is to develop a method of extrapolation

and interpolation permitting to obtain a unique and stable (if possible) solution for the reconstruction problem. This can only be done by introducing, explicitly or implicitly, a priori information on the object to be reconstructed.

To sum up, this method is a mono-frequency method which operates at high frequency and requires a large number of angles.

1.3.2 Bojarski's Method

The method proposed by Bojarski [31] in 1967 is a method which permits to link the complex backscattered electromagnetic field (amplitude and phase) to the geometrical characteristics of the object by using the Fourier transform. This method, based on the Kirchhoff's formula, is valid for objects whose dimensions are large compared to the wavelength, namely the optical region. Under these conditions, assuming a perfectly conducting object, Bojarski shows that the measurement of the diffracted field at infinity permitting to determine a function, $\rho(\vec{p})$, where $\vec{p}$ is a vector whose direction corresponds to the direction in which the target is observed and whose modulus is $|\vec{p}| = 2\omega c$, where ω is the angular frequency and c is the speed of electromagnetic waves. It then shows that the function, $\Gamma(\vec{p}) = 2\sqrt[2]{\pi}\frac{\rho(\vec{p})+\rho^*(-\vec{p})}{\vec{p}^2}$, and the characteristic function of the target, $\gamma(x)$, form a pair of Fourier transform. $\gamma(x)$ is defined to be equal to 1, if the point x is inside the target, and equal to 0 if the point is outside the target. A measure of the backscattered field in all space of $\vec{p}$, which is to say in all aspects and all frequencies, can give an accurate reconstruction of the target.

In 1969, R. Lewis examines, from a theoretical point of view, the relationship established by Bojarski and it can provide accurate information on an obstacle [31].

In 1971, two studies were conducted in parallel but independently. The first by W. Tabbara [43, 44] is based on a numerical simulation of the conditions of the Bojarski's method to evaluate its applicability. The second study is an experimental study conducted by J. Young [5]. It is based on a relationship established by Kennaugh and Cosgriff in 1958 [45] then reiterated by Kennaugh and Moffatt in 1965 [3] and it is a special case of the fundamental relationship of Bojarski.

Since then, various authors have examined this method from both the theoretical and numerical points of view. N. Bleistein [46] generalized it to the temporal domain and applied to the underwater acoustic problems (seabed profile). W. Perry examined theoretically the stability of this method [47]. S. Rosenbaum-Raz [48] extended this method to the multistatic case without numerical study. W. Boerner [49] showed that in some cases this approach could be linked to methods based on the use of the Radon transform [50], which allows to reconstruct an object from its projections on well-chosen plans.

To conclude, this method is a multi-frequency method which operates in high frequencies and requires a large number of observing directions.

1.3.3 Inverse Born Approximation

The Inverse Born Approximation (IBA) is used to determine the size, shape and orientation of a weakly diffracting object. This method is often used in the domain of biomedical ultrasound, in the case of structures with low contrast. The IBA is very similar to the Bojarski's method and also consists in solving a pair of Fourier transforms. This improved approximation method has been developed to extend the range of applications, for example in the case of objects with higher index of refraction. The reverse Born approximation requires a very large number of incidence angles ($360°$ around the object) and the backscattered response from the target for a low frequency band corresponding to the resonance and the upper Rayleigh zones of the target.

The IBA method is a multi-frequency method which operates in low frequencies and requires a large number of observing directions.

1.3.4 Radar imaging from ramp responses

This method of radar imaging is based on ramp responses of targets, highlighted by the work of Kennaugh and Moffatt [3, 45] and Young [4, 5]. We can consider that this method is a special case of the fundamental relationship of Bojarski. Indeed, Bojarski has shown that, with the physical optics approximation, the field diffracted by an object is equal to the spatial Fourier transform of a function characterizing the profile of the object. Kennaugh and Moffatt then showed that this characteristic function of the object profile is also equal to the double integral of the impulse response of the target. In the frequency domain, this profile function is obtained by inverse Fourier transform of the transfer function divided by the factor $j\omega^2$ (ω being the angular frequency). Thus, low frequencies are preferred for this factor.

Young then turned his attention to the implementation process of reconstruction of the target from a finite number of directions of the object by using the relationship of Kennaugh and Moffatt. From 10 frequency measures of the backscattered field by a target in low-frequency, Young calculates the ramp response which is proportional to the function of the target profile. Then, from three profile functions of the target, obtained for three mutually orthogonal viewing angles, he reconstructs a "correct" image of the target with the method of "approximate limiting surfaces". If the profile functions are calculated for maximum viewing angles around the object ($360°$), Young's approach provides an unique image of the target. In general, the greater the number of angle is, better quality of reconstructed images can be achieved.

However, in practice, it is very difficult or impossible to get the scattered field of a target in the full range. Therefore, this radar imaging method seems to be most appropriate to provide a reasonably accurate image of a target in such a situation.

The first advantage of using the ramp response radar imaging is that it is a low frequency technique. Indeed, working at low frequencies is a necessity in order to counter stealth military equipment. Secondly, unlike other radar imaging techniques, where a large number of observations is required to obtain a correct image of an object, the ramp response technique does not require more than three observations to generate a suitable image. It even seems possible, with a priori information on the target to be reconstructed, to generate a 3D image of the target from one or two observations [7, 51]. Another important advantage is the robustness of this imaging technique to noise. Indeed, a ramp response of good quality can be obtained from noisy data [52]. Finally, the major advantage of this technique for the user is the simplicity of the calculations for a ramp response. A simple inverse Fourier transform is enough to calculate the profile and to determine the characteristic dimension of an object in a certain observing configuration.

However, this technique has some limitations. Its biggest drawback is correlated with its most important advantage: the low frequency band. Indeed, it is essential that the minimum frequency of the analysis frequency band is in the Rayleigh region of the studied object in order to generate a valid ramp response. Therefore, the lower the minimum frequency is required and consequently the greater the size of the antenna. The second drawback is the difficulty to obtain the profile of an object in its shadow region. Some solutions [9, 52, 53] should be studied to solve this problem.

To sum up, this method is a multi-frequency method (number of frequencies around 10) which operates at low frequency and requires a very small number of angles (no more than 3). That's why we choose to study this method and use it for the 3D image reconstruction of radar targets in chapter 2.

1.3.5 Linear Sampling Method

The "Linear Sampling Method" was introduced by Colton and Kirsch in 1996 [54, 38, 50] for the identification of an object in resonance zone from its far-field measure at a given frequency, the diffracting object being illuminated by plane waves from any direction. The specificity of this method, compared to conventional methods, is that it does not use simplifying assumptions on the solution of the direct problem (the Born approximation). At the same time, it avoids to use the resolution of the direct problem, which can be detrimental in the case of large scale problems (this is typically the case if a 3D problem is treated). Furthermore, this method does not require, in principle, a prior knowledge of the nature of the

object (reflecting, absorbing penetrable ...). Its only limitation is that it provides the information only on the support of the diffracting object (not its characteristics, for example). But in many problems (radar, medical imaging,...), this support is the only useful information.

To sum up, this method is a mono-frequency method which operates in resonance zone and requires a large number of angles.

1.3.6 Parameter extraction method

There are still many options to get the information on the size, shape, or the composition of a target from its response to an electromagnetic wave. The methods presented in this section are not imaging methods but parameter extraction methods that characterize the geometry of the target.

An example is the Singularity Expansion Method (SEM), developed by Baum in 1976 [55]. This method makes it possible to obtain information on the shape and size of a target from the singularities of its response to a wide band electromagnetic wave in the resonance region of the target. These singularities, named resonance poles, are intrinsic to each target and can therefore be used in a process of identification such as E-pulse method [56]. However, the extraction of these resonance poles is very sensitive to noise, and therefore, this method has problems in the case of experimental data.

Another interesting solution [57, 58] is based on the ESPRIT algorithm which, in the same way as the SEM method, extracts characteristic parameters of an object so that one can use the resonant frequencies, the damping factors, parameters that are functions of the object dimensions to identify the target.

1.4 Conclusion

In this chapter, characterization and identification of radar targets is studied. Especially, the stealthy radar targets are concerned. The stealth technologies, which aims to attenuate the radar cross-section (RCS) of the radar target, can be mainly realized by using adapted shaping and radar-absorbent materials (RAM). However, this is less effective for radars operating in low frequency bands which correspond to the Rayleigh region and the resonance region for object dimensions respectively small and of the same order, compared to electromagnetic wavelengths. Therefore, the low frequency radars are chosen to counter the stealthiness. Among the inverse scattering methods, radar imaging from the ramp response is adapted to the low frequency band and permits to reconstruct 3D images of the target to be identified. Therefore, in this thesis, this method is chosen for the the radar characterization and identification and will be presented in the following chapter.

2

Radar imaging from ramp responses

The use of transient back-scattered response resulting from a ramp wave was first applied to radar targets identification by Kennaugh and Moffatt in 1965 [3, 54]. Such a ramp response was found to be approximately proportional to the profile function, which is defined as the transverse cross-sectional area versus the distance along the line-of-sight parallel to the incident wave direction. Radar imaging from ramp responses consists in reconstructing a 3D image of the radar target with profile functions, obtained from the backscattered temporal ramp response in several viewing angles. Therein, the 3D image reconstruction algorithm plays an important role for generating an accurate image.

The purpose of this chapter is to present the principle of radar imaging from ramp responses. In section 2.1, the concept of the ramp response is presented. In section 2.2, the profile function of an object as well as its relationship with the ramp response are illustrated. In section 2.3, the required frequency band, which validates the relationship between the ramp response and the profile function, is introduced. The temporal and spatial resolution limits are illustrated. In section 2.4, an example of PEC object is used to demonstrate the process for calculating profile functions from ramp responses. In section 2.5, existing 3D image reconstruction algorithms from profile functions are reviewed. In section 2.6, various single and separated objects are reconstructed in arbitrary directions. In section 2.7, limitations of existing reconstruction algorithms are given.

2.1 Ramp response of radar targets

Electromagnetic scattering refers to the physical phenomenon: when an electromagnetic wave encounters an obstacle in a homogeneous, isotropic medium, the wave deviates from its original propagation direction. Back-scattered response is the waveform scattered in a direction opposite to the direction of incidence.

As given in section 1.1.3, the impulse response, $h_i(t)$, is the response of the target illuminated by a plane electromagnetic wave in the form of $E_0(t) = E_0\delta(t)$ (where $\delta(t)$ is a Dirac, see Fig. 2.1). This response is normalized (without dimension) resulting from the receiving field divided by the transmitting field. It is related to the transfer function, $H(j\omega)$, by the pair of Fourier Transforms:

$$H(j\omega) = \int_{-\infty}^{+\infty} h_i(t)e^{-j\omega t}dt; \qquad h_i(t) = \int_{-\infty}^{+\infty} H(j\omega)e^{j\omega t}d\omega \tag{2.1}$$

where $\omega = 2\pi f$ is the angular frequency.

The ramp response of a radar target, $h_r(t)$, is defined as the far-field back-scattered wave resulting from illumination by a plane electromagnetic wave with a temporal ramp waveform (Fig. 2.1).

- In time domain, the ramp response is the second integral of its impulse response, $h_i(t)$:

$$h_r(t) = \int_{-\infty}^{t}\int_{-\infty}^{t} h_i(t')dt'dt \tag{2.2}$$

- In frequency domain, the ramp response can be expressed as the Inverse Fourier Transform of the weighted transfer function, $H_r(j\omega) = H(j\omega)/(j\omega)^2$, from the Eq. (1.5):

$$h_r(t) = IFT[H_r(j\omega)] = IFT[\frac{H(j\omega)}{(j\omega)^2}] \tag{2.3}$$

Generally (during simulation and experiment), instead of using directly the temporal ramp, its equivalent in frequency domain $H_r(j\omega)$ is preferred. With an electromagnetic plane wave illuminating the target in the far field, the backscattered field and then the transfer function $H(j\omega)$ can be obtained. Finally, $h_r(t)$ is calculated by Eq. (2.3).

2.2 Profile function

2.2.1 Geometrical profile function

Before introducing the profile functions, an incident direction to the target is defined by an unit vector determined by its inclination angle θ and its azimuthal angle ϕ in a spherical coordinate system (Fig 2.2). Therefore, an incident direction

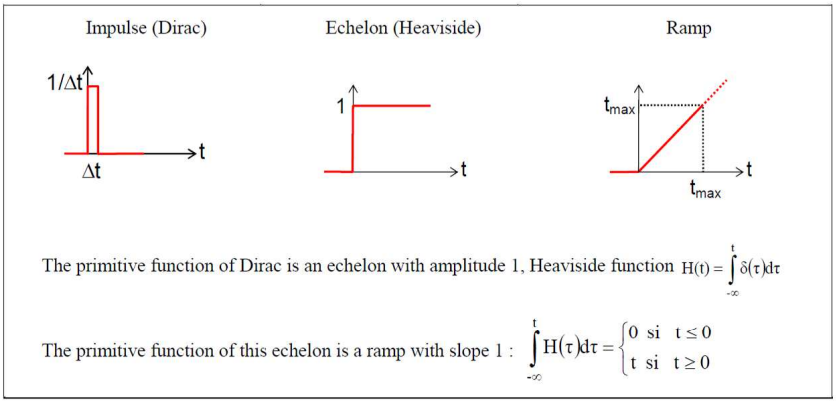

Figure 2.1: Definitions of waveforms : impulse, echelon and ramp functions in time domain

is noted as $u(\theta, \phi)$. For example, the direction vector of axis x is represented by $x(90°, 0°)$.

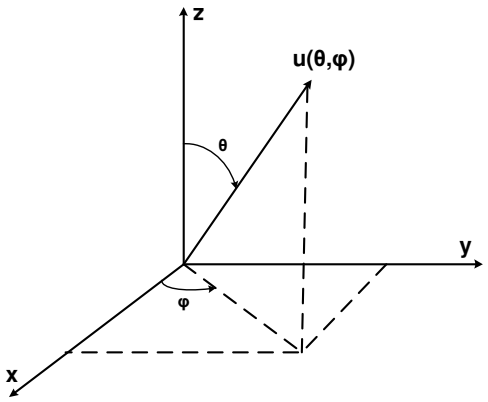

Figure 2.2: Definition of an unitary direction $u(\theta, \phi)$ in spherical coordinate system.

We define the "geometrical" profile function of an object, in direction u, as its transverse cross sectional area, $A_g(u)$, along u. Fig. 2.3 presents an example of geometrical profile function, $A_g(x)$, which is the area of transverse slices of the target at successive positions along the direction x.

$$A_g(u) = \int_{-\infty}^{+\infty} \int_{-\infty}^{+\infty} O(x, y, z) dy dz \tag{2.4}$$

with

$$O(x, y, z) = \begin{cases} 1 \text{ if } (x, y, z) \text{ inside object} \\ 0 \text{ if } (x, y, z) \text{ outside object} \end{cases}$$

where $O(x, y, z)$ is a binary object function.

In monostatic configuration, Kennaugh et Moffatt have shown that the geometrical profile function, $A_g(u)$, is approximately proportional to the transient ramp response of the target, $h_r(t)$, [3, 54]:

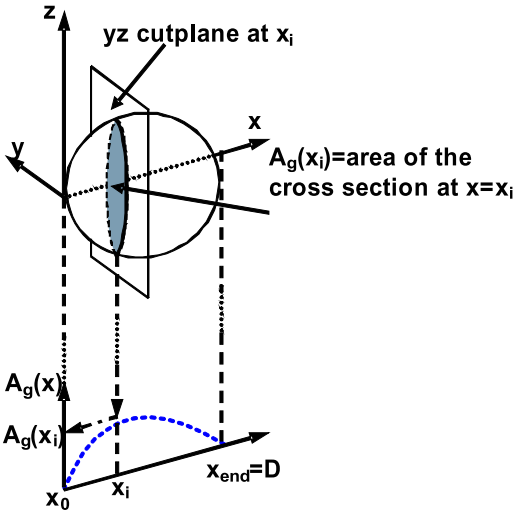

Figure 2.3: Illustration of the geometrical profile function of an object along x direction, $A_g(x)$. D is the characteristic dimension of the object in x direction.

$$h_r(t) \approx -\frac{1}{\pi c^2} A_g(u) \quad \text{with} \quad u = \frac{ct}{2} \tag{2.5}$$

where c is the speed of light in freespace, t the time variable, and u the space variable. Indeed, the time variable is the sum of the incidence time and the back-scatter time.

Because the demonstration of Kennaugh and Moffatt is based on the physical optics approximation in high frequency, it is valid only in the part of the object directly illuminated by the incident wave. At low frequencies, Eq. (2.5) has not been demonstrated, but it is verified empirically [59]. Furthermore, it has been also proved to be approximatively valid in the shadow region of the object by Young [5].

2.2.2 Physical profile function

Using the relationship between the ramp response and the geometrical profile function in Eq. (2.5), we define the "physical" profile function, $A_p(u)$, as exactly proportional to the transient ramp response.

$$h_r(t) = -\frac{1}{\pi c^2} A_p(u) \tag{2.6}$$

Note that, through the whole thesis, the subscript "g" stands for the geometrical case and "p" for the physical case.

2.3 Frequency band and resolution limit

2.3.1 Required frequency band

To make sure that the physical profile function $A_p(u)$ calculated by Eq. (2.6) is a good estimate of the geometrical profile function $A_g(u)$ of a radar target, it is necessary to choose an appropriate frequency range comparing to the scale of the target. According to the literature [3, 4, 5, 54], the wavelengths ranging from D/2 up to 200D, where D is the characteristic dimension of the target in the direction of incidence, are sufficient to obtain an accurate profile function. This corresponds to areas of Rayleigh and resonance (object dimensions are respectively small and of the same order comparing to electromagnetic wavelengths). The corresponding frequency band is given by:

$$f = [f_{min}; f_{max}] = \left[\frac{c}{200D}; \frac{2c}{D}\right] \tag{2.7}$$

A priori knowledge of the target dimension is necessary to define the frequency bands. If the target is not known in advance, the frequency spectrum must be scanned until a suitable profile function is obtained.

Indeed, the frequency band, Δf, required by the literature is not really suitable for the identification of large targets. In the case of an object with a characteristic dimension $D = 10m$, the frequency band of investigation, given by Eq. (2.7), extends from $150KHz$ to $60MHz$. It is very difficult and expensive to work at such low frequencies. Accordingly, some extrapolation methods can be applied to increase the lower frequency limit f_{min} [60, 61]. Accordingly, the lower limit of the frequency band, f_{min}, can be increased up to $10f_{min}$ which are more suitable for antennas in applications.

2.3.2 Resolution limit

The temporal resolution of the ramp response, δt, is determined by the frequency bandwidth Δf. As $f_{max} >> f_{min}$, the frequency bandwidth can be expressed as:

$$\Delta f = f_{max} - f_{min} \approx f_{max} \tag{2.8}$$

Hence, the temporal resolution limitation is calculated by:

$$\delta t = \frac{1}{2\Delta f} \approx \frac{1}{2f_{max}} \tag{2.9}$$

The spatial resolution of the physical profile function of the target is given by:

$$\delta u = \frac{c\delta t}{2} = \frac{c}{4\Delta f} \approx \frac{c}{4f_{max}} \tag{2.10}$$

From Eq. (2.7), with the maximum frequency $f_{max} = \frac{c}{2D}$, the spatial resolution limitation is:

$$\delta u = \frac{D}{8} \tag{2.11}$$

Accordingly, to characterize complex shape objects, it is often necessary to increase f_{max} in order to obtain a better spatial resolution δu on the corresponding profile function.

2.4 Example of a PEC sphere

To illustrate the process of getting the ramp profile function from the backscattered field, we present now the example of a perfectly electric conducting (PEC) sphere of diameter $D = 10$ cm in freespace (Fig. 2.4). For such value of D, the frequency band of investigation given by Eq. (2.7) is [15 MHz ; 6 GHz]. An electromagnetic simulation software based on the Method of Moments [62] is used to calculate the transfer function $H(f)$ of this object in monostatic configuration and for an incident direction x. Fig. 2.5 shows the modulus of this transfer function, $H(f)$, and the modulus of the weighted transfer function, $H_r(f) = H(f)/(j2\pi f)^2$. The main contribution is located in low frequencies on account of the weighting in $1/(j2\pi f)^2$. Next, the ramp response, $h_r(t)$, is calculated by IFT of $H_r(f)$ using Eq. (2.3), and the physical profile function, $A_p(x)$, is finally obtained from Eq. (2.6). Fig. 2.6 presents the ramp response, $h_r(t)$, (upper) and the corresponding physical profile function, $A_p(x)$, (lower) of the PEC sphere. Because of the symmetry of the sphere, the transfer function, the ramp response and the profile function are independent of the observing direction.

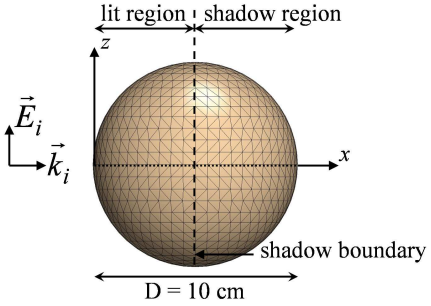

Figure 2.4: Configuration of study for a PEC sphere of diameter $D = 10$ cm.

After selecting the useful part of $A_p(x)$, we compare, in Fig. 2.7, this physical profile function (solid line) with the geometrical profile function (dash line), cal-

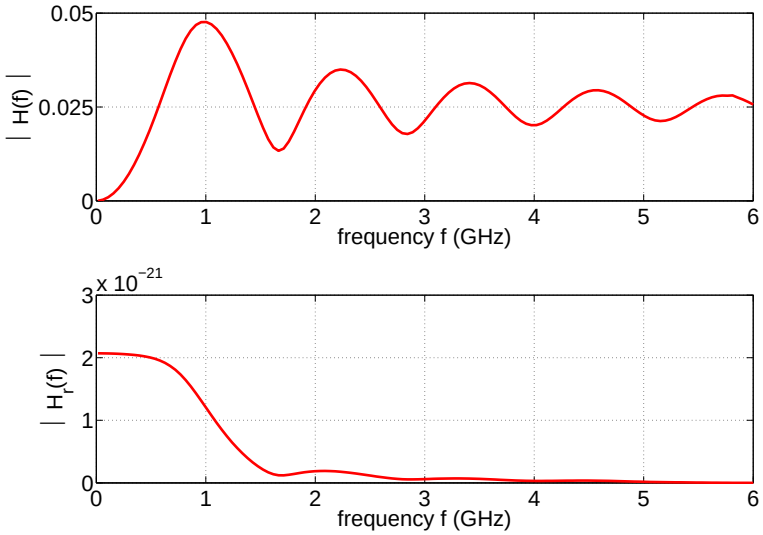

Figure 2.5: Modulus of the transfer function $H(f)$ (upper) and the weighted transfer function $H_r(f)$ (lower) for a PEC sphere of diameter $D = 10$ cm, in the frequency band f = [15 MHz ; 6 GHz] in monostatic configuration.

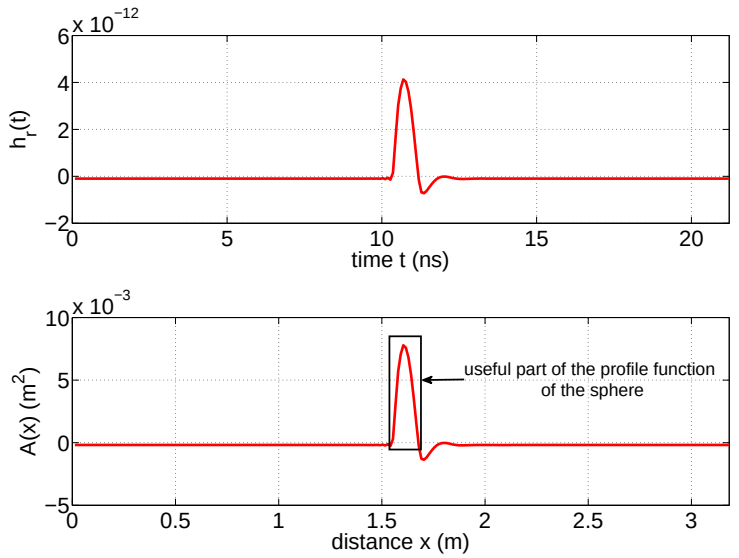

Figure 2.6: Ramp response $h_r(t)$ (upper) and physical profile function $A_p(x)$ (lower) of the PEC sphere.

culated analytically with Eq. (2.4): For the sphere, we get $A_g(x) = \pi x(D-x)$ for $0 \leq x \leq D$ and $A_g(x) = 0$ outside. The curves are very similar in the lit region ($x \leq D/2 = 5$ cm). However, in the shadow region of the target ($x > D/2$), physical and geometrical profile functions differ. Indeed, in the lit region, the main contribution to the backscattered response at a given time t comes from the direct reflection of the incident wave on the surface of the PEC sphere at distance $x = ct/2$. On the contrary, in the shadow region, the contribution to the backscattered response comes from creeping waves traveling on the surface of the target, with a resulting additional delay in the response. This additional delay involves a spread of the physical profile function in the shadow region. Note that, we name here this phenomenon as the "shadow effect". In the case of the canonical PEC sphere, this spread, δ_A, is approximately equal to the path difference between the travel on the surface of the sphere ($1/4$ perimeter of the sphere) and the direct path (radius of the sphere): $\delta_A \approx \frac{D}{2}\left(\frac{\pi}{2}-1\right) = 2.85$ cm. This difference might give inaccurate information on the target shape and must be compensated. One possible solution is to get the response in the opposite direction.

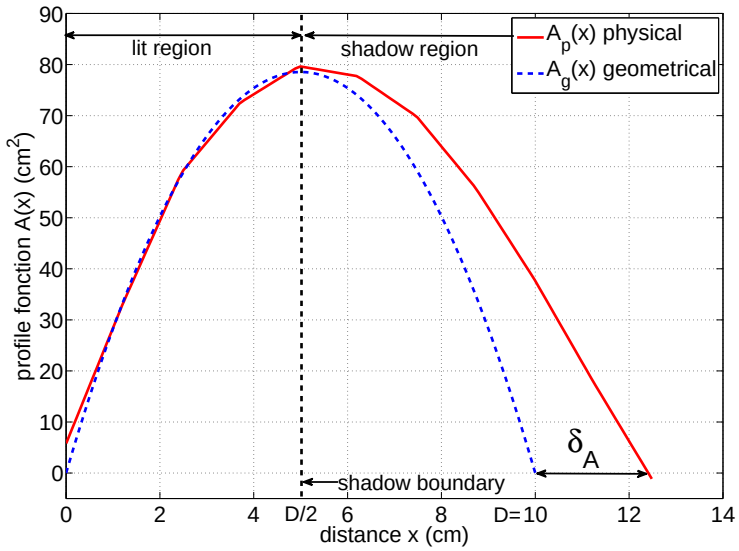

Figure 2.7: Comparison between physical $A_p(x)$ and geometrical $A_g(x)$ profile functions of the PEC sphere of diameter $D = 10$ cm.

2.5 Image reconstruction from profile functions

As mentioned earlier, radar target imaging from ramp response refers to 3D image reconstruction with the target profile functions calculated from its ramp responses at a finite number of viewing angles. Due to the low frequency, the objective of the image reconstruction algorithm is to generate an approximate rough

image of the target contour, rather than a high resolution image as in the case of high frequency. The initial reconstruction method using profile functions was proposed by Young [5]. His method, using "Approximate limiting surface" , has been applied to electromagnetic scattering [6, 7, 51, 52, 53, 63, 64] as well as acoustic imaging of underwater objects [8, 9]. However, Young's method is limited to single convex objects while a more recent algorithm proposed by Chauveau overcomes this limitation [13]. Another class of methods consists in applying algorithms of reconstruction from projections, but they require a considerable number of viewing angles and plane-symmetrical objects [10, 11, 12]. In this section, these 3 methods are reviewed.

2.5.1 Young's method

Young's method requires 3 profile functions, obtained from arbitrary angles, orthogonal or not. It is based on the use of hyperbolic surfaces limiting the contour of the object for each of the 3 angles. An iterative adjustment of geometrical parameters of these bounding surfaces yields an estimate of the final image by selecting the common volume inside the boundaries of the three surfaces.

The principle of Young's method is given in following steps:

- Firstly, the equation used to generate hyperbolic surfaces limiting the contour of the object, in the yz plane at x_i, is given by:

$$K|yz| = A(x_i) \tag{2.12}$$

where the constant K can have values between 4 and 2π. The value $K = 4$ corresponds to any rectangle (Fig. 2.8 (a)) of area $A(x_i)$, inscribed in the hyperbolic contour. The value K = 2π is any ellipse (Fig. 2.8 (b)) with area $A(x_i)$, inscribed in the hyperbolic contour.

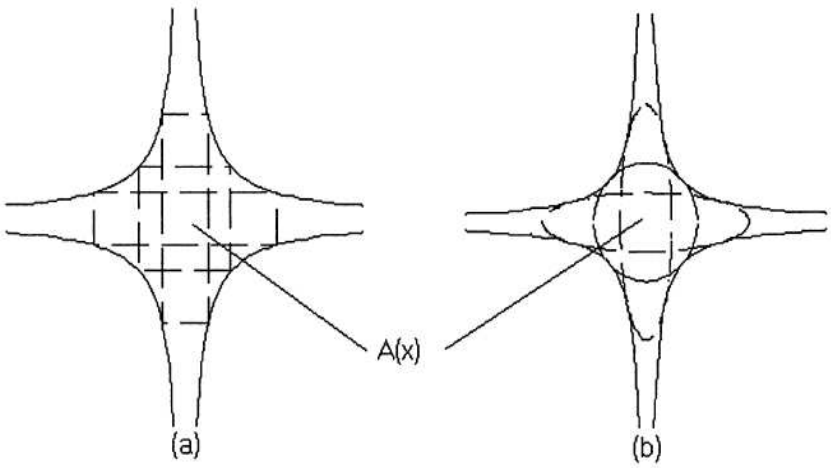

Figure 2.8: hyperbolic contour: (a) $K = 4$; (b) K = 2π [5]

- Secondly, to improve the reconstructed image, bounding surfaces are fitted by such as limiting the branches of the hyperbola, the axes of rotation of the bounding surface for each angle. After determining the optimal hyperbolic surface corresponding to each angle, the final 3D image is given by the intersection of the volumes included within these 3 hyperbolic surfaces. These changes are made iteratively by a procedure fitting the parameters of each limiting hyperbola, to minimize the difference between the initial profile function and the profile function calculated from the reconstructed image at each iteration.

Young's method takes advantage of the ramp response technique and 3 viewing angles are sufficient to generate a likely 3D image. Its main limitation is the type of object that can be reconstructed. Indeed, the reconstructed objects tend to approximate to an elliptical or rectangular shape, convex and without holes. In the case where the targets are complex shapes, this method can not be applied [5].

2.5.2 Chauveau's method

To conquer the limitation of Young's method, Chauveau proposed a new method which permits to reconstruct non-convex and separated objects [13, 65]. He also uses profile functions from only 3 observing directions. The main advancement of this method is to introduce a weighting function to select the points which belong to the object. Because it exploits more effectively the information from the input data (namely the profile functions), it avoids the bias generated by the limiting surfaces and therefore improves the accuracy of images.

To present Chauveau's method, for simplification, 3 mutually orthogonal observing directions (x, y, z) and the corresponding profile functions, $A_x(x)$, $A_y(y)$ and $A_z(z)$, are used. This method consists in the following steps:

1° Calculation of the weighting function. For each point p of coordinates (x_i, y_j, z_k), the weighting function is calculated by the product of these 3 profile functions, $A_{3D}(p)$. This 3D weighting function represents the probability that the point p belongs to the object.

$$A_{3D}(p)(x_i, y_j, z_k) = A_x(x_i) \times A_y(y_j) \times A_z(z_k) \tag{2.13}$$

2° Construction of the slices. To get successive slices of the unknown target, a scan direction x, y or z is chosen. This choice is somewhat arbitrary, while the direction with the most varying profile function gives more information on the shape characteristics, therefore more accurate images can be obtained along this direction. The slices are a set of surfaces (squares) perpendicular to the chosen scan direction, for example z, enclosing the unknown object.

3° Selection of "real" points. Herein, the "real" points are these points which are belong to the unknown object. For each slice, at position $z = z_k$, the points

which have the highest values of $A_{3D}(p)$ are selected, and moreover their resulting area should be equal to the profile function at z_k, $A_z(z_k)$.

$$\sum_i \sum_j p(x_i, y_j, z_k) = A_z(z_k) \tag{2.14}$$

4° Binarization of the object. After the previous step, at each slice, the "real" points which are selected as belonging to the object are assigned to be "1" and others to be "0". Consequently, a binary object is reconstructed.

Chauveau's method needs only 3 viewing angles and it can reconstruct non-convex and separated objects [13]. However, it has bad performance with non-orthogonal observing directions [66].

2.5.3 Reconstruction from projections

Another class of methods consists in applying algorithms of reconstruction from projections [10, 11, 12], by using a method based on the Radon transform [27, 67]. In two-dimensional Euclidean space, the Radon transform (RT) of a function $f(x, y)$ are line integrals along a set of parallel paths $\vec{\xi} \cdot (x, y) = \rho$, where $\vec{\xi} = \{\xi_1, \xi_2, \cdots, \xi_n\}$ is an unit vector representing the direction and ρ is the shortest distance from the line to the origin of the coordinates system.

$$R(\vec{\xi}, \rho) = \int \int f(x, y)\delta[\rho - (\vec{\xi} \cdot (x, y))]dxdy \tag{2.15}$$

Actually, the Radon transform maps the spatial domain (x, y) to the projection domain (φ, ρ), with φ being the incidence angle of these lines and each line in the R^2 space can be parameterized as $x \cos\varphi + y \sin\varphi = \rho$. Therefore, the Radon transform of $f(x, y)$ can also be represented as follows:

$$R(\varphi, \rho) = \int \int f(x, y)\delta[\rho - (x \cos\varphi + y \sin\varphi)]dxdy \tag{2.16}$$

In practice, the inverse Radon transform, which determines the function $f(x, y)$ for all values of (φ, ρ), is of the particular interest [67, 68].

Fig. 2.9 shows the geometric interpretation of the Radon transform. Let $\gamma(x, y)$ be a characteristic function of the bounded region V:

$$\gamma(x, y) = \begin{cases} 1 & \text{if } (x, y) \in V \\ 0 & \text{if } (x, y) \notin V \end{cases} \tag{2.17}$$

Then the Radon transform from $\gamma(x, y)$ is the area formed by the intersection of the bounded region V and the line $\vec{\xi} \cdot (x, y) = \rho$. The Radon transform of the characteristic function $\gamma(r, \theta, \varphi)$ is indeed the cross-sectional area of V along the incidence direction. Therefore, the geometrical profile functions and the characteristic

function can be considered as a pair of Radon transform. Accordingly, the image reconstruction of a 3D object can be solved by using the inverse Radon transform of the profile functions.

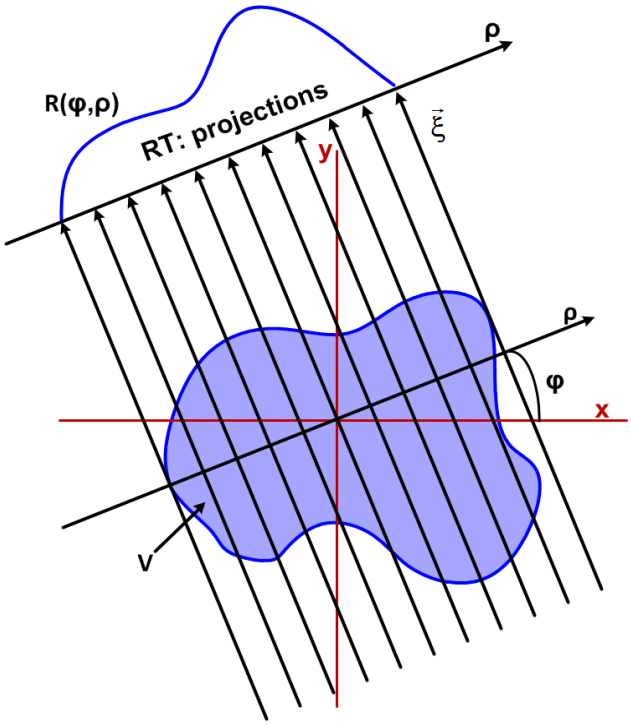

Figure 2.9: Geometric interpretation of the Radon transform.

As shown in Fig. 2.10 (a), for a three-dimensional space R^3, the characteristic function γ is expressed as a function of the profile functions, here denoted as $A(\eta, \psi, \rho)$ of the object V:

$$\gamma(x_1, x_2, x_3) = \gamma(r, \theta, \varphi) = \frac{1}{8\pi^2} \int_0^{2\pi} \int_0^{\frac{\pi}{2}} [\frac{\partial^2 A(\eta, \psi, \rho)}{8\pi^2} \partial\rho^2] d\eta d\psi \tag{2.18}$$

with

$$\{x_1, x_2, x_3\} = r\{\cos\theta\cos\varphi, \cos\theta\sin\varphi, \sin\theta\}$$

$$\vec{\xi} = \{\xi_1, \xi_2, \xi_3\} = \{\cos\eta\cos\psi, \cos\eta\sin\psi, \sin\eta\}$$

$$\gamma(x_1, x_2, x_3) = \gamma(r, \theta, \varphi) = \begin{cases} 1 & \text{if } (x_1, x_2, x_3) \in V \\ 0 & \text{if } (x_1, x_2, x_3) \notin V \end{cases}$$

$$\rho = r[\cos\theta\cos\eta\cos(\varphi - \psi) + \sin\theta\sin\eta]$$

To get a solution for the characteristic function, it can be seen in Eq. (2.18) that one needs profile functions from all possible directions. Hence, a method was used to transform the three-dimensional problem to the two-dimensional case [11]. This method considers only the aspects ψ varying on the (x_1, x_2) plane with $\eta = 0$. The width of the object, $W(x_1, x_2)$, in the x_3 direction at point (x_1, x_2), is determined by the inverse Radon transform of the profile functions $A(\psi, \rho)$:

$$W(x_1, x_2) = W(r_0, \psi) = \frac{-1}{2\pi} \int_0^{\pi} \int_{-\infty}^{\infty} \frac{\partial A(\psi, \rho)}{\partial \rho} \frac{d\rho d\psi}{\rho - r_0 \cos(\varphi - \psi)} \tag{2.19}$$

where r_0 is the radius on the (x_1, x_2) plane.

As shown in Fig. 2.10 (b), when the object is symmetric relatively to the (x_1, x_2) plane, the 3D shape can be obtained by:

$$S_1(x_1, x_2) = -S_2(x_1, x_2) = \frac{W(x_1, x_2)}{2} \tag{2.20}$$

In conclusion, this method requires far more than 3 observing angles and plane-symmetric objects.

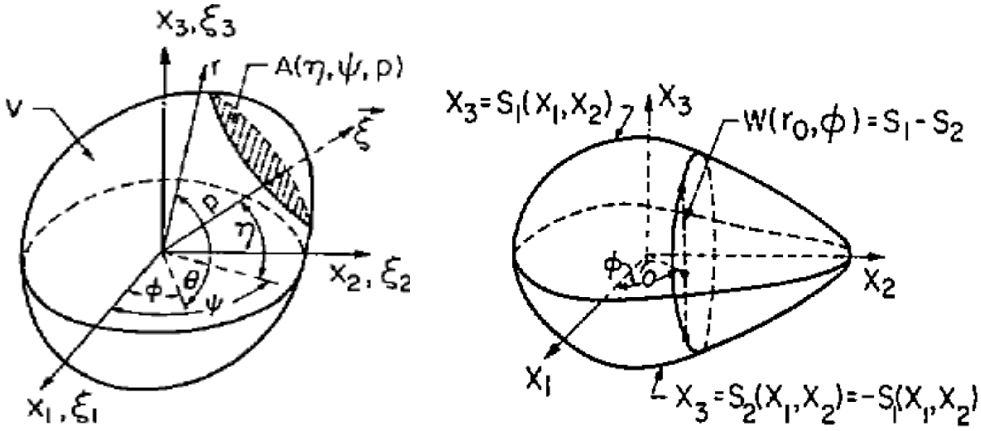

(a) (b)

Figure 2.10: Reconstruction from projections: (a) using three-dimensional Radon transform; (a) using two-dimensional Radon transform [12].

2.6 Reconstructed results with Chauveau's method

The purpose of this section is to demonstrate the performance of existing methods of reconstruction from profile functions. As discussed in the previous section, among the 3 existing methods, Chauveau's method requires no more than 3 observing angles and overcomes the limitation of Young's method. Therefore, we choose

it to reconstruct various single and/or separated objects from arbitrary directions (orthogonal and non-orthogonal case).

2.6.1 Reconstruction in orthogonal case

Firstly, we consider the reconstruction in orthogonal case, namely 3 mutually orthogonal directions, $[u_1 = x, u_2 = y, u_3 = z]$. Applying Chaveau's method (section 2.5.2), configurations of study will be presented for several canonical objects: a sphere (Fig. 2.11), an asymmetric object (Fig. 2.12), an union of three cylinders of different diameters (Fig. 2.13, noted as "step-cylinder"), a non-convex object (Fig. 2.14)), and two separated objects (a sphere and a cone, Fig. 2.15).

As shown in these figures, we reconstruct each object both from geometrical and physical profile functions in the 3 mutually orthogonal directions, (x, y, z). For each object, the geometrical profile functions (the cross-sections), A_g, are analytically calculated using the known equation, and the physical profile functions, A_p, are calculated by Eq. (2.6) from the ramp response. According to Chauveau's method, we chose the direction of the most varying profile function to scan the object. Note that we center the profile functions and reconstructed images in the origin of the coordinates system.

Sphere For a PEC sphere of diameter $D = 10$ cm in Fig. 2.4, the frequency band required by Eq. (2.7) is equal to [15 MHz ; 6 GHz]. Because of its geometrical symmetry, its profile function is the same for any direction. In Fig. 2.11 (b), the physical profile function, $A_p(x)$, and the geometrical profile function, $A_g(x)$, along x direction, are compared. Difference between them are mainly due to the shadow region effect (section 2.4). From the outcome obtained with the two sets of profile functions with the same scan direction, x, the image reconstructed from geometrical profile functions in Fig. 2.11 (c) is visually in agreement with the initial sphere, while, due to the bias introduced by the shadow region effect, the image reconstructed from physical profile functions in Fig. 2.11 (d) is slightly distorted.

For the following objects, of largest dimension $D = 30$ cm, the frequency band required by Eq. (2.7) should be [5 MHz ; 2 GHz], but we increase the upper limit to 8 GHz in order to improve the spatial resolution.

Asymmetric object For a PEC asymmetric object in Fig. 2.12 (a), Fig. 2.12 (b) compares the geometrical and physical profile functions along the directions x, y, z, respectively. Once again, in the shadow region, the physical profile functions are spreading. We choose direction x as the scanning direction for the reconstruction. As shown in Fig. 2.12 (c), from 3 geometrical profile functions, the object is ac-

curately reconstructed. On contrary, as shown in Fig. 2.12 (d), 3 physical profile functions result in a strongly distorted image.

Step-cylinder For a PEC step-cylinder in Fig. 2.13 (a), we compare in Fig. 2.13 (b) the geometrical and physical profile functions along the directions x, y, z. With the scanning direction z, we obtain a well-reconstructed image in Fig. 2.13 (c) from 3 geometrical profile functions, but a distorted one in Fig. 2.13 (d) for the physical case.

As said before, Young's method is limited to convex and individual objects. However, Chauveau's method overcomes this limitation. Therefore, we now consider the non-convex object and two separated objects.

Non-convex object The continuous and non-convex object in Fig. 2.14 (a) is formed by 3 cylinders with circular sections of two different diameters (5 and 10 cm) and its total length is $D = 30$ cm. Fig. 2.14 (b) compares its geometrical and physical profile functions obtained in the 3 orthogonal directions (x, y, z). We choose the direction x as the scanning direction for the reconstruction. For the geometrical case, shown in Fig. 2.14 (c), the object is correctly reconstructed. For the physical case, shown in Fig. 2.14 (d), the reconstructed image is easily identifiable, even though it still has a deformation in the shadow region.

Separated objects For two separated objects, a sphere and a cone, the geometric configuration is shown in Fig. 2.15 (a). Fig. 2.15 (b) compares its geometrical and physical profile functions obtained in the 3 orthogonal directions (x, y, z). Once again, the two objects are correctly reconstructed and easily identifiable for the geometrical case Fig. 2.15 (c). While in the physical case Fig. 2.15 (d), the reconstructed images are slightly distorted.

These results confirm that, in the orthogonal case, Chauveau's method guarantees the consistency between the input and output data. Moreover, from Eq. (2.11), the physical profile functions have poor spatial resolution due to the low frequency and therefore result in a low resolution for the reconstructed image. Nevertheless, these images are still more than enough to meet the needs of target identification.

2.6.2 Reconstruction in non-orthogonal case

Now, using the example of the previous step-cylinder (Fig. 2.13 (a)), we consider 3 non-orthogonal directions (u_1, u_2, u_3): the first direction $u_1(90, \phi)$ varies in xoy plane, respectively with $\phi = 30°, 50°, 135°$, and the two other directions are $u_2 = y$ and $u_3 = z$ axis. Because the object is symmetric relatively to the direction Z, profile functions for any direction in xoy plane are the same. That is to say,

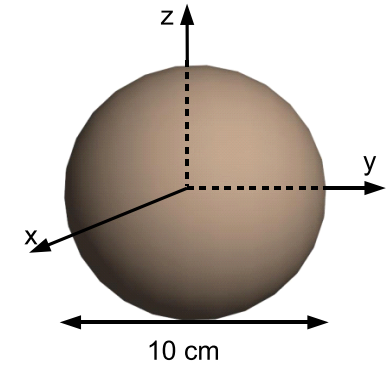

(a)

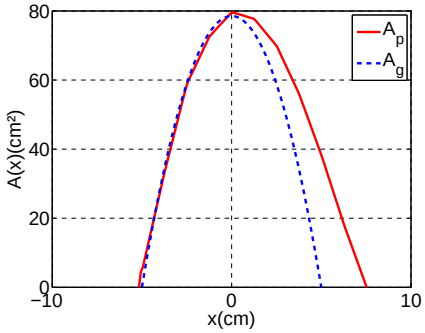

(b)

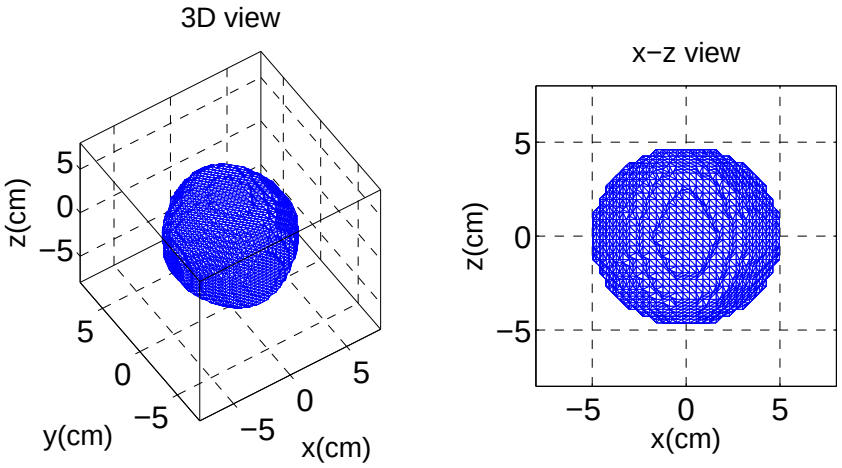

(c)

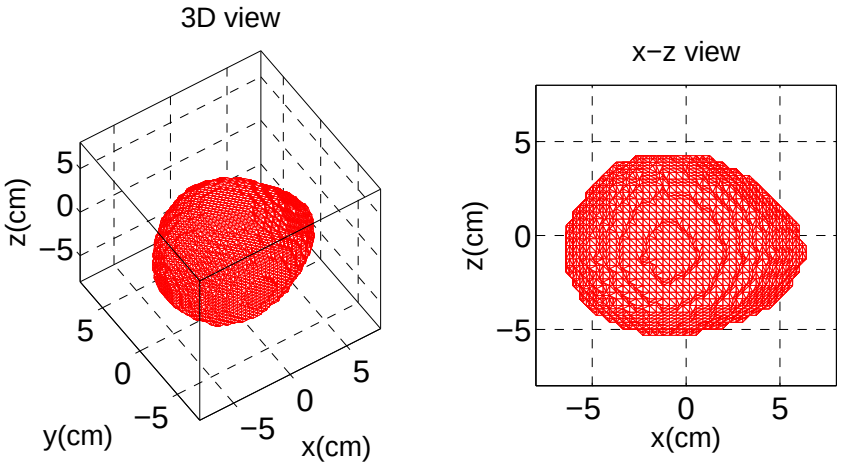

(d)

Figure 2.11: Configuration of study for a PEC sphere: (a) object shape ($D = 10$ cm); (b) comparison between physical (solid curve) and geometrical profile functions (dash curve) along direction x (frequency band [15 MHz ; 6 GHz]); reconstructed images from (c) geometrical and (d) physical profile functions, with scan direction x.

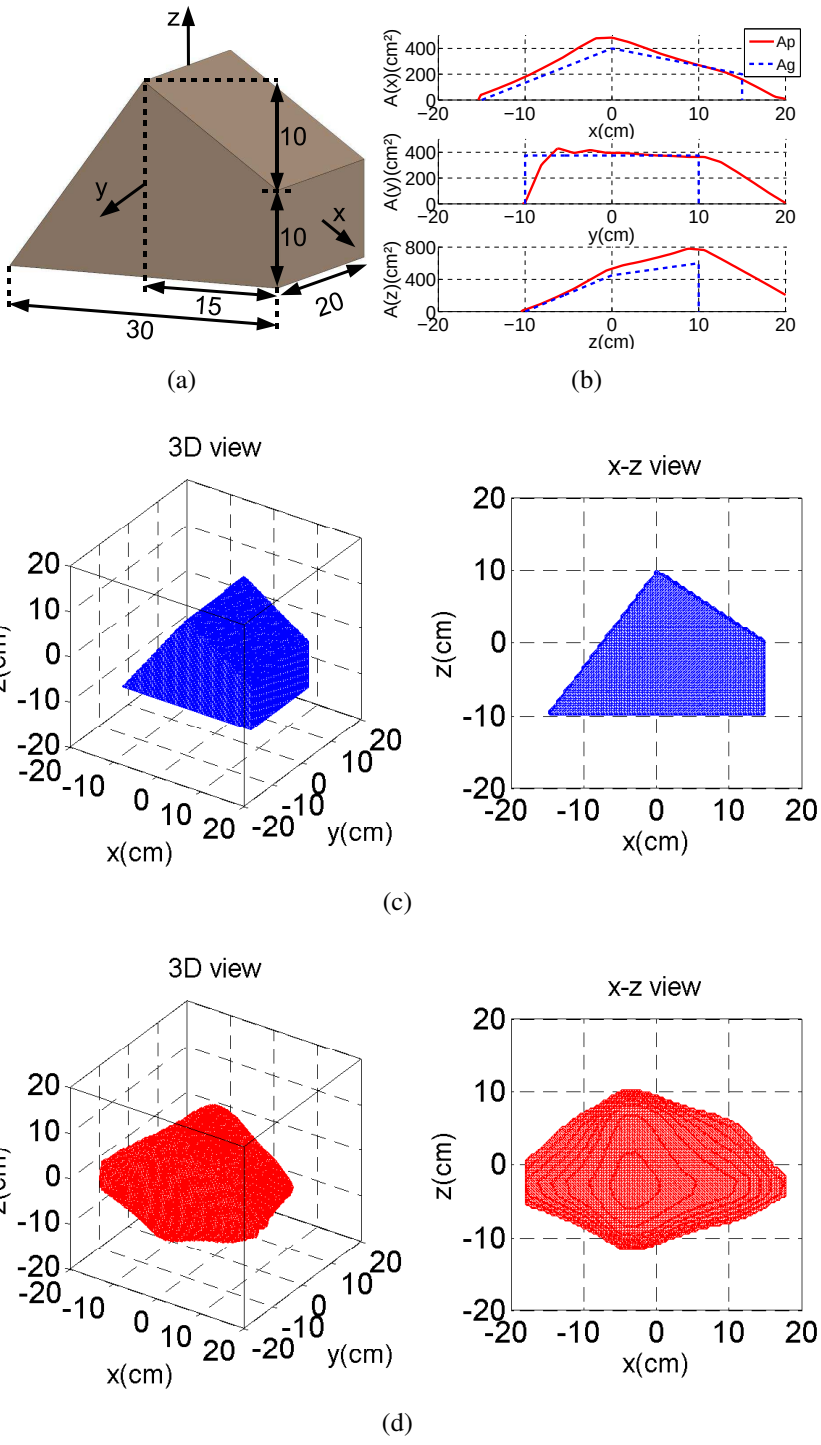

Figure 2.12: Configuration of study for a PEC Asymmetric object: (a) object shape ($D = 30$ cm); (b) comparison between physical (solid curves) and geometrical profile functions (dash curves) along direction x, y z, respectively, (frequency band [5 MHz ; 8 GHz]); reconstructed images from (c) geometrical and (d) physical profile functions, with scan direction x.

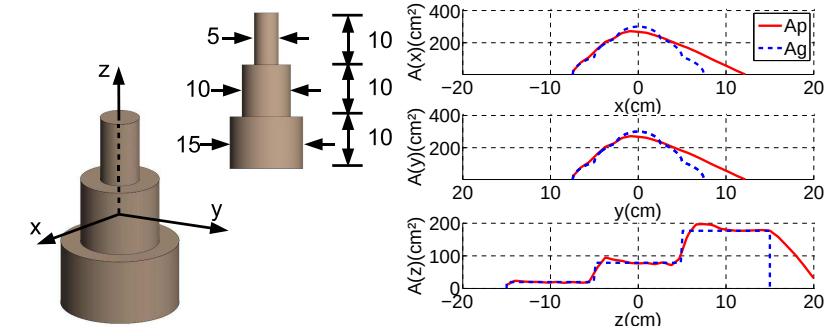

(a) (b)

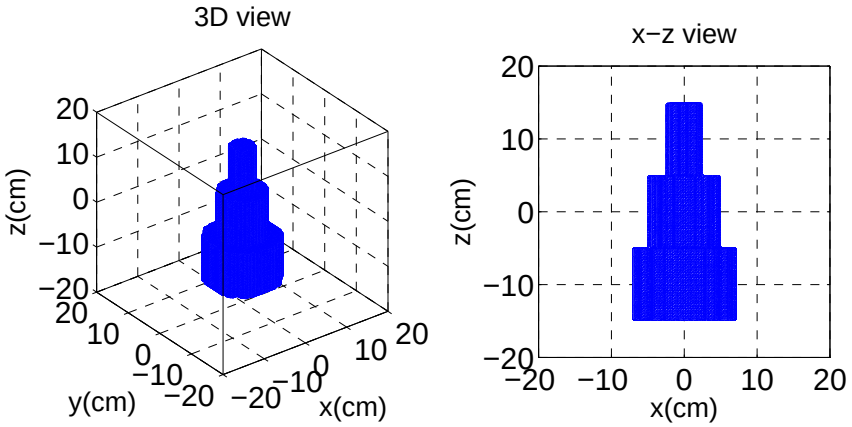

(c)

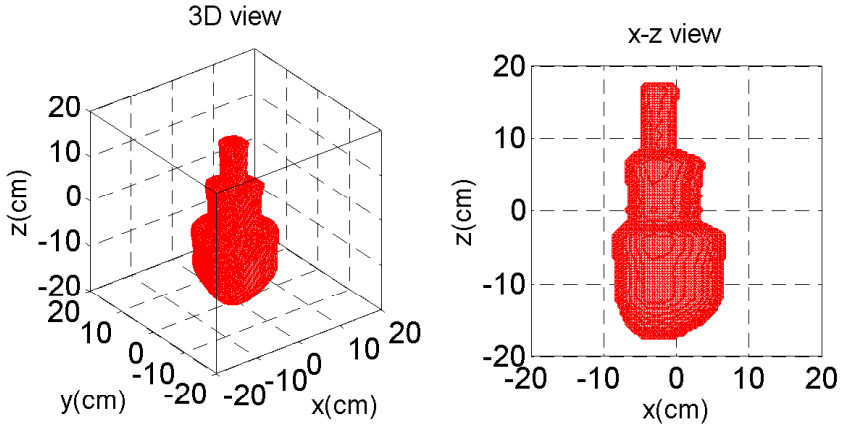

(d)

Figure 2.13: Configuration of study for a PEC step-cylinder: (a) object shape ($D = 30$ cm); (b) comparison between physical (solid curves) and geometrical profile functions (dash curves) along direction x, y z, respectively, (frequency band [5 MHz ; 8 GHz]); reconstructed images from (c) geometrical and (d) physical profile functions, with scan direction z.

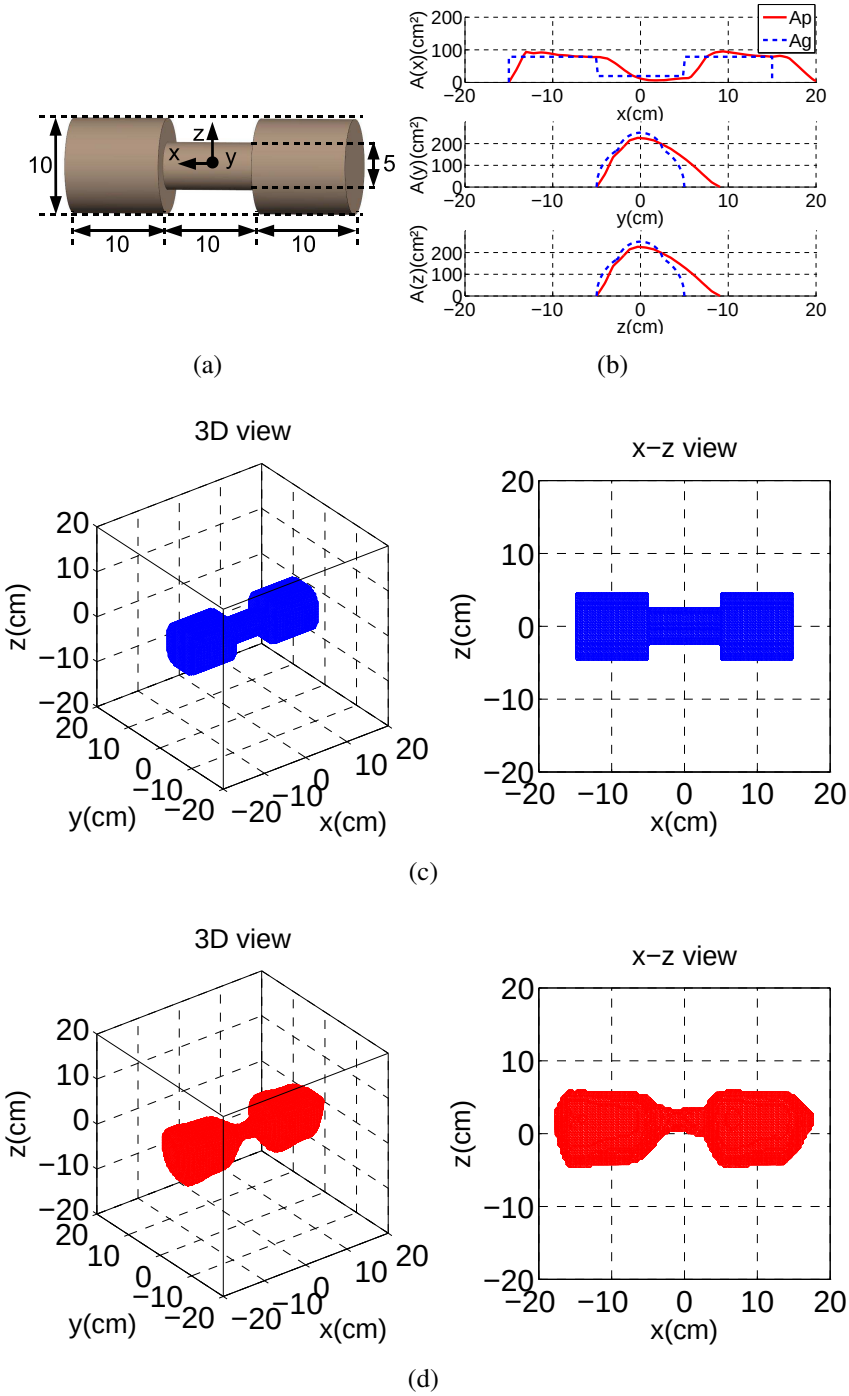

Figure 2.14: Configuration of study for a non-convex PEC object: (a) object shape ($D = 30$ cm); (b) comparison between physical (solid curves) and geometrical profile functions (dash curves) along direction x, y z, respectively, (frequency band [5 MHz ; 8 GHz]); reconstructed images from (c) geometrical and (d) physical profile functions, with scan direction x.

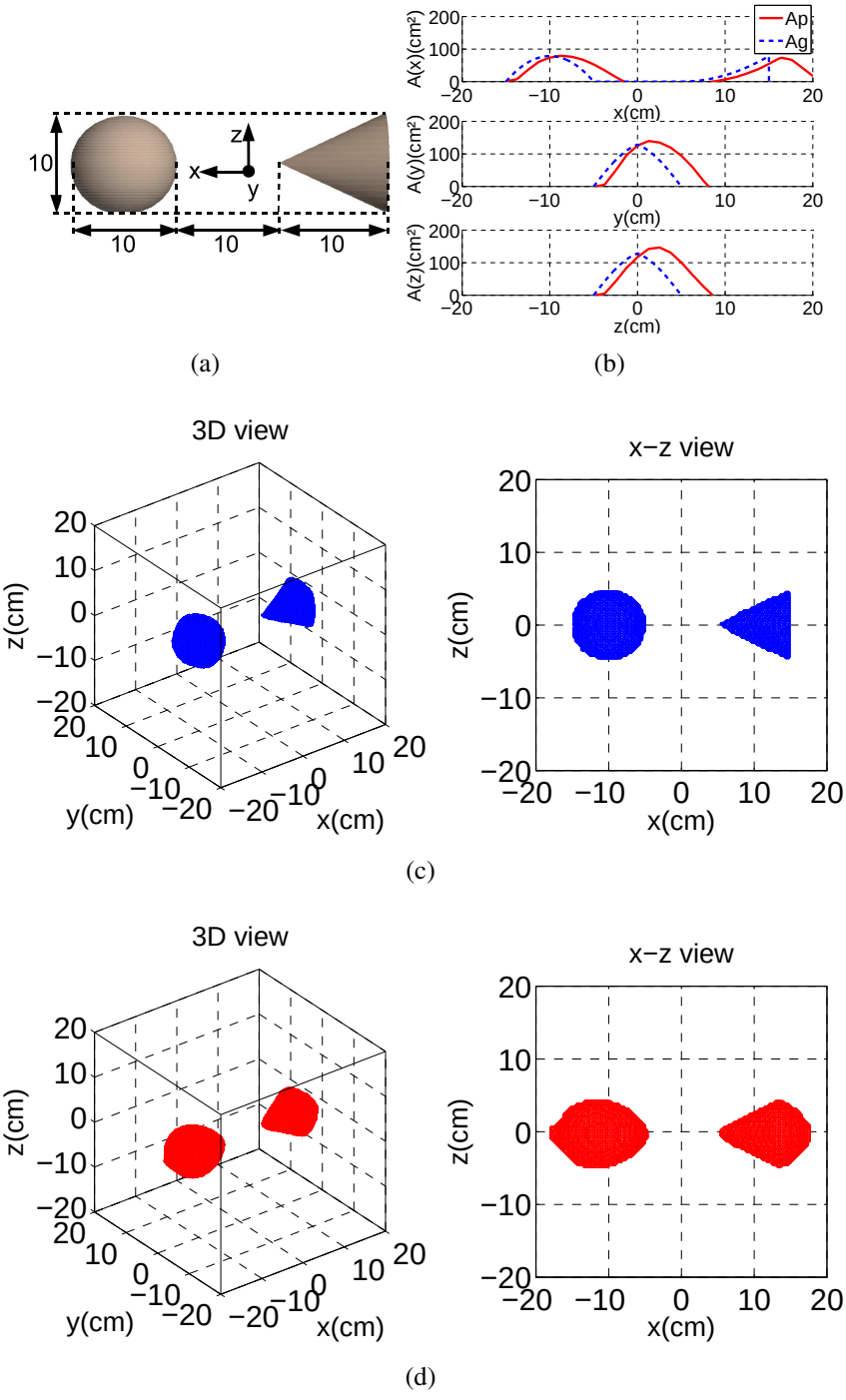

(a) (b)

(c)

(d)

Figure 2.15: Configuration of study for two separated PEC objects: (a) object shape ($D = 30$ cm); (b) comparison between physical (solid curves) and geometrical profile functions (dash curves) along direction x, y z, respectively, (frequency band [5 MHz ; 8 GHz]); reconstructed images from (c) geometrical and (d) physical profile functions, with scan direction x.

the resulting profile functions for the direction $u_1(90, \phi)$ are the same as that along direction x. Therefore, for the 3 non-orthogonal cases with $\phi = 30°, 50°, 135°$, the geometrical and physical profile functions can be shown as Fig. 2.13 (b). For comparison, we present again the 3D images reconstructed with 3 orthogonal directions (Fig. 2.13 (c) and (d) for the geometrical and physical case, respectively.), as well as the $x - y$ view where the first direction $u_1(90, \phi)$ varies.

Firstly, with geometrical profile functions, 3D images reconstructed by Chauveau's method from the 3 arbitrary directions are shown in Fig. 2.16. We can see that the reconstructed result for each non-orthogonal case is elongated along the direction perpendicular to the bisector of the 2 non-orthogonal directions (u_1 and u_2). Similarly, with physical profile functions, 3D images reconstructed by Chauveau's method from the 3 arbitrary directions are shown in Fig. 2.17. Once again, the results are strongly distorted.

2.7 Conclusion

In this chapter, radar imaging from ramp response is presented. With low frequency radar corresponding to the Rayleigh and resonance scattering, far field backscattered ramp response of the target is approximately proportional to its transverse cross-sectional area along the incidence direction, namely the profile function. This property can be used to generate 3D likely contours. Taking advantage of the ramp response technique, there are three reconstructions algorithms: Young's method [5], Chauveau's method [13] and reconstruction from projections [11, 12]. The method of reconstruction from projections requires a huge number of observing directions and plane-symmetric objects, while Young's method and Chauveau's method permit to obtain approximate contours with no more than 3 observing directions. Chauveau's method exploits more effectively the information from profile functions, hence it can reconstruct non-convex and separated objects, which overcomes Young's limitation. Examples indicate that, with 3 mutually orthogonal profile functions, Chauveau's method generates promising reconstructions. On contrary, it produces distorted estimates for non-orthogonal directions. However, in practice, due to the limited viewing angles of radar equipment for remote sensing or large-scale targets in far distance, it is very difficult, almost impossible, to illuminate the target from 3 mutually orthogonal directions. Therefore, it is necessary to optimize the reconstruction from arbitrary directions. In the following chapter, the optimization of reconstruction from arbitrary direction, which is the main contribution of this thesis, will be presented.

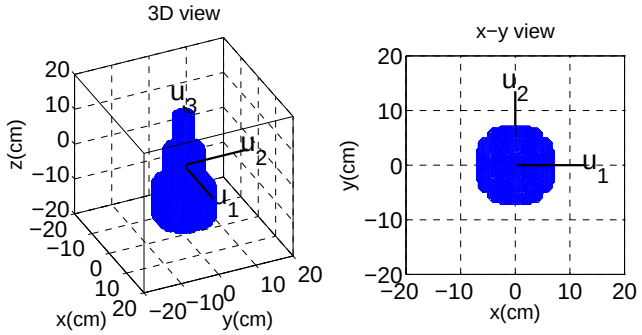

(a)

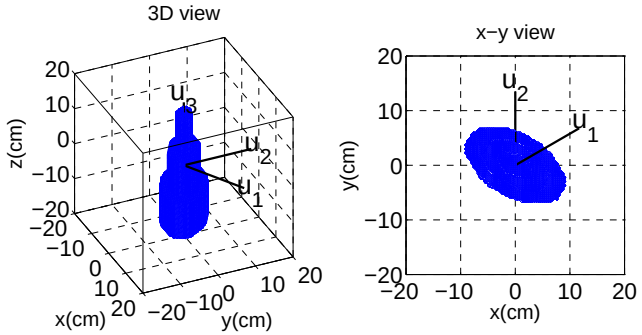

(b)

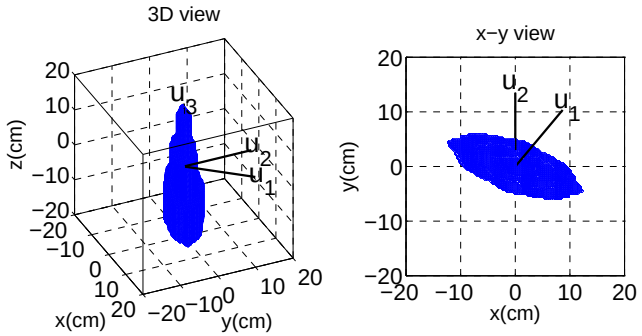

(c)

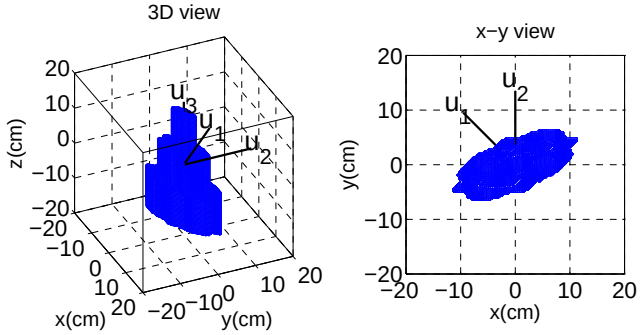

(d)

Figure 2.16: 3D reconstructed images of the step-cylinder (Fig. 2.13) with Chauveau's method from geometrical profile functions in 3 arbitrary directions: (a) $[u_1 = x, u_2 = y, u_3 = z]$; (b) $[u_1(90°, 30°), u_2 = y, u_3 = z]$; (c) $[u_1(90°, 50°), u_2 = y, u_3 = z]$; (d) $[u_1(90°, 135°), u_2 = y, u_3 = z]$, with scan direction z.

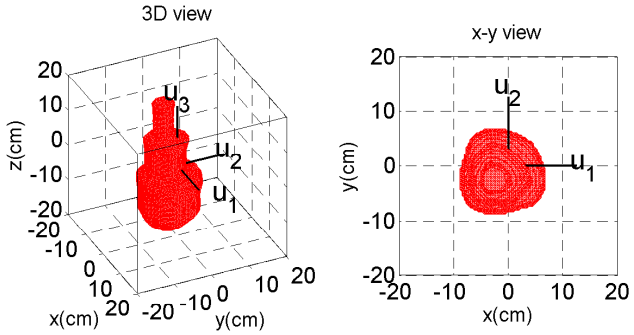

(a)

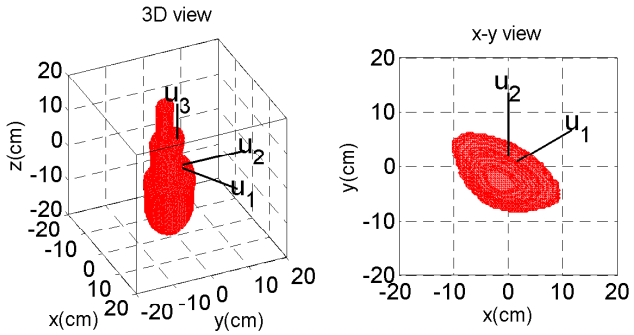

(b)

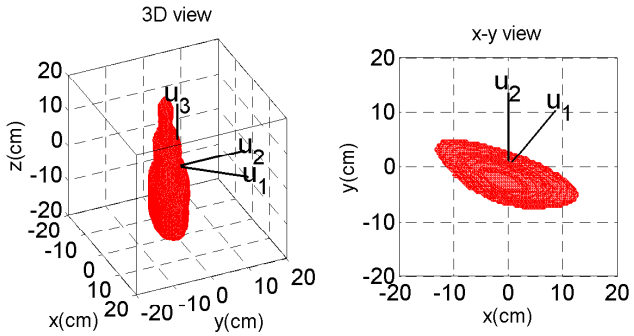

(c)

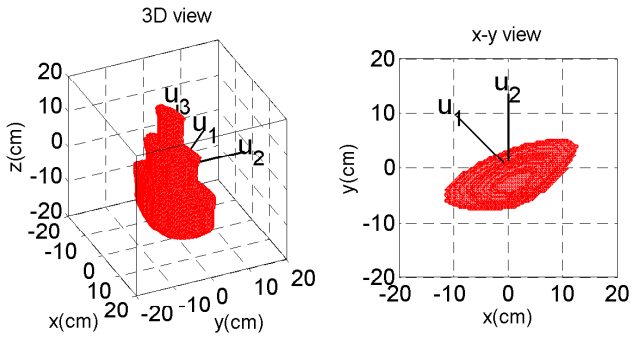

(d)

Figure 2.17: 3D reconstructed images of the step-cylinder (Fig. 2.13) with Chauveau's method from physical profile functions in 3 arbitrary directions: (a) $[u_1 = x, u_2 = y, u_3 = z]$; (b) $[u_1(90°, 30°), u_2 = y, u_3 = z]$; (c) $[u_1(90°, 50°), u_2 = y, u_3 = z]$; (d) $[u_1(90°, 135°), u_2 = y, u_3 = z]$, with scan direction z.

3

Optimization of image reconstruction from arbitrary directions

As presented in chapter 2, the profile function of an object gives its overall dimension for the incidence direction and provides information for its transversal surface perpendicular to this incidence direction. On the other way, if the observing directions are mutually orthogonal, more geometry information can be obtained so that the reconstructed image might be more correct. While for the non-orthogonal case, less shape information results in distorted image. Due to the limited observed data, 3D image reconstruction from arbitrary directions is itself an ill-posed problem. To optimize the distorted reconstructions, an iterative process is applied to obtain a correct estimate of the target shape by minimizing the error between the observed data (profile functions observed from the initial object) and the profile functions of the estimated object. This problem can be formalized by the following equation for each observing direction:

$$G^u O = A^u \tag{3.1}$$

where $A^u(M, 1)$ is the observed data, namely the profile function along the observing direction u in the form of one dimension vector of size M (M is the number of points of the profile function), $O(N^3, 1)$ is the unknown 3D object in the form of a vector in one dimension (N is the number of points of the object space along one dimension). $G^u(M, N^3)$ is the forward observing matrix between the observed profile function, A^u, and the unknown object, O.

It is important to note that the observed profile functions can be either geometrical profile functions, A_g, for the ideal case or physical profile functions, A_p, for the practical case. In order to focus on improving the performance for reconstructions in arbitrary directions, in this thesis, the forward observing matrix G is only considered as describing the relationship between the geometrical profile function obtained from the initial object and that from the estimated object.

The optimization process includes two problems:

- A direct (or forward) problem which aims to obtain the geometrical profile functions of a 3D object in arbitrary directions. This can be used to get geometrical profile functions from the estimated object during the iterative process as well as their errors with the profile function observed from the initial object. This is required at each iteration for the inverse problem.

- An inverse problem which attempts to find the unknown object using an appropriate iterative method to minimize the error between the profile functions of estimated object and the observed data. An optimal estimate is obtained when an user-defined error tolerance is reached.

The purpose of this chapter is to iteratively optimize the reconstruction of a target from profile functions at a finite number (generally ≤ 3) of arbitrary viewing angles. In section 3.1, to find the forward matrix G between the unknown object and observed data, an algorithm for calculating geometrical profile functions for a 3D arbitrary object was developed [69] and is presented as well. The validity of this algorithm is verified and it is applied for quantitatively evaluating the quality of image reconstructions and for further identifying reconstructed images with a database of possible models. In section 3.2, possible iterative methods are reviewed and are experimented for the problem of image reconstruction from profile functions. An adapted method, the level-set method, is then selected and applied to our specific case. A 'Narrow band' version of this level set method is used to reduce the computational cost. In section 3.3, the performance of the narrow band level set method is studied and reconstructed results are presented for various objects with orthogonal as well as arbitrary directions. In section 3.4, conclusions are given for both the direct and inverse problems of image reconstruction from arbitrary directions.

3.1 Direct problem: Algorithm for calculating geometrical profile functions [69]

The geometrical profile function of a 3D object is defined as the area of its transverse slices perpendicular to a chosen direction. The known basic formulas to get areas are generally limited to some basic geometries (e.g. circle, square, etc.) and orthogonal directions. However, an estimated object often has an irregular shape.

Moreover, profile functions in arbitrary directions are required for the image reconstruction. Therefore, a numerical method to get the geometrical profile function is necessary.

3.1.1 Algorithm description

Given a binary 3D object $O(x, y, z)$ enclosed in a computational domain C_D, the algorithm for calculating geometrical profile function is described with the following steps:

- Firstly, as shown in Fig. 3.1(a), the computational domain is cut in successive slices perpendicular to the observing direction $u(\theta, \phi)$ with a thickness δu, where δu is the discrete step in the direction $u(\theta, \phi)$. Hence, the slice S_i at position $u = u_i$ (middle plane of S_i) is the region enclosed by the plane at $u_{il} = u_i - \delta u/2$, the plane at $u_{ih} = u_i + \delta u/2$ and the edges of the computational domain C_D. The numerical profile function $A_c(u_i)$ at position $u = u_i$ can be calculated by:

$$A_c(u_i) = V_{S_i}/\delta u \tag{3.2}$$

where V_{S_i} is the volume of the slice S_i.

- Secondly, the computational domain C_D is distributed into N^3 elementary cubic pixels $P(x, y, z)$, each with a volume δu^3, where N is the number of discrete samples in each direction. The computational domain is represented by 2 different kinds of pixels: pixels inside the object (solid points) and pixels outside the object (hollow points). For simplification, it is represented in Fig. 3.1(b)-(c) in a two-dimensional view.

$$O(x, y, z) = \begin{cases} 1 \text{ if } P(x, y, z) \text{ inside object} \\ 0 \text{ if } P(x, y, z) \text{ outside object} \end{cases} \tag{3.3}$$

- Thirdly, a weight function W is applied to calculate the proportion that each pixel gives to the slice S_i. Taking into account that points closer to the middle plane u_i give higher contribution, this weight function W is defined as:

$$W = \begin{cases} 1 - |d/\delta u|; & d \in [-\delta u, \delta u] \\ 0; & \text{otherwise} \end{cases} \tag{3.4}$$

where $d = u_P - u_i$ is the signed distance from the center of pixel P, with coordinate u_P along the direction vector u, to the plane at u_i.

According to the distance d, there are 5 different types of pixels $P1$, $P2$, $P3$, $P4$ and $P5$, shown in Fig. 3.1(c).

$P1 : -\delta u \leq d < 0$; it gives W to S_i and $1 - W$ to S_{i-1}.

$P2 : d = 0, W = 1$; it entirely belongs to S_i .

$P3 : 0 < d \leq \delta u$; it gives W to S_i and $1 - W$ to S_{i+1}.

$P4 : d \geq \delta u$; its contribution for S_i is null.

$P5 : d \leq -\delta u$; its contribution for S_i is null.

- Fourthly, the volume of the slice S_i is obtained by summing up individual contributions from each pixel.

$$V_{S_i} = \sum_x \sum_y \sum_z W \times \delta u^3 \times O(x, y, z) \tag{3.5}$$

- Finally, combining Eq. (3.2) and (3.5), the numerical profile function $A_c(u_i)$ at position u_i is calculated by:

$$A_c(u_i) = \sum_x \sum_y \sum_z W \times \delta u^2 \times O(x, y, z) \tag{3.6}$$

3.1.2 Algorithm verification

In order to quantitatively measure the difference between a reference profile function $A_{ref}(u)$ and a profile function $A_c(u)$ computed by this algorithm, along direction u, two types of error are considered.

- The absolute error, which is a function of position along the direction u, is defined as

$$E(u) = |A_{ref}(u) - A_c(u)| \tag{3.7}$$

- The relative global error for the given direction u is defined as

$$E_r^{(u)} = \frac{\int E(u)du}{\int A_{ref}(u)du} \times 100\% \tag{3.8}$$

To validate this algorithm, two spheres of diameter $D = 10$ cm and $D = 30$ cm are considered. A cubic computational domain of dimension $d_c = 45$ cm, which is divided into $N^3 = 128^3$ pixels, with $\delta u = d_c/N = 0.35$ cm, is chosen to completely enclose the studied objects.

For each sphere, two types of profile functions are compared:

-A_g^O, the known geometrical profile function of the sphere, taken as the reference profile function for verification. For example, the area of each cross section along x for a sphere is equal to $\pi r^2(x)$, $r(x)$ being the radius of each cross section (a circle).

-A_c^O, the geometrical profile function computed by this algorithm from the object.

Because of the symmetry of the sphere, one direction $u(0°, 0°)$ is chosen for studying the performance of this algorithm. Comparison between $A_g^O(u)$ and $A_c^O(u)$ for the two different spheres are shown in Fig.3.2 (a) and (b) respectively, as well as

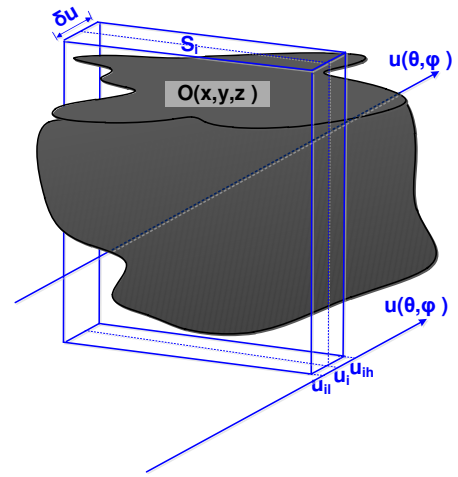

(a)

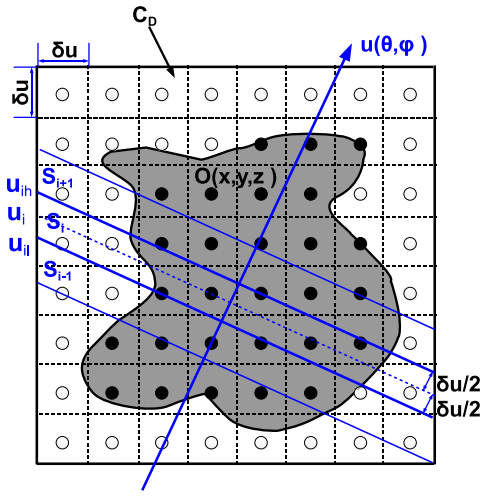

(b)

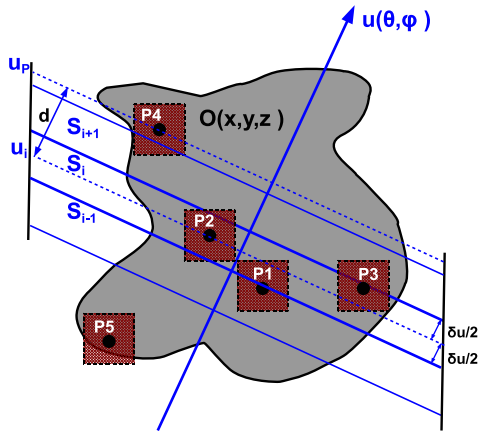

(c)

Figure 3.1: (a) Slices S_i in a three-dimensional view, (b) Slices S_i in a two-dimensional view, (c) Contribution of different types of pixels to the slice S_i.

their corresponding absolute errors for each slice. Due to the discretization, the errors mainly lie in the starting and ending positions of the profile functions. Relative global errors calculated by Eq. (3.8) are 3% and 1% for the two spheres respectively. Fig.3.3 shows the effect of the discretization, with relative global errors $E_r^{(u)}$ decreasing when the number of samples N increases. The larger sphere ($D = 30$ cm) gives a lower relative global error since it is related to the object volume (Eq. (3.8)).

3.1.3 Application for quality evaluation for 3D image reconstruction

In this section, the algorithm for calculating geometrical profile functions is applied to quantitatively evaluate the quality of 3D image reconstruction from profile functions, presented in section 2.6.

The flow chart in Fig. 3.4 describes the process of quality evaluation for 3D image reconstruction from profile functions.

The notations related to this process are given as following:

- A_g^O, the geometrical profile function of the initial object analytically calculated by known formulas for regular geometries.

- A_p^O, the physical profile function calculated by Eq. (2.6) from the far-field back-scattered ramp response obtained by FEKO [62].

- Rg, the 3D object reconstructed from analytical geometrical profile functions A_g^O, for example, the reconstructed sphere of Fig. 2.11 (c).

- Rp, the 3D object reconstructed from physical profile functions A_p^O, for example, the reconstructed sphere of Fig. 2.11 (d).

Accordingly, the geometrical profile functions are calculated by the algorithm presented in section 3.1.1:

- A_c^{Rg}, from the 3D reconstructed object Rg.

- A_c^{Rp}, from the 3D reconstructed object Rp.

The quality evaluation for the reconstructed image (Rg or Rp) consists in quantitatively calculating the errors between A_g^O and A_c^{Rg} or A_p^O and A_c^{Rp}, respectively.

To demonstrate the performance of this image evaluation process, we consider the 3D images reconstructed by Chauveau's method for the orthogonal and non-orthogonal cases, which are respectively presented in section 2.6.1 and in section 2.6.2.

Firstly we consider the images reconstructed in orthogonal case: the sphere (Fig. 2.11), the asymmetric object (Fig. 2.12), the step-cylinder (Fig. 2.13), the non-convex object (Fig. 2.14)), and the separated objects, Fig. 2.15). For each object, reconstructed objects Rg and Rp are obtained from geometrical and physical profile functions, respectively. The relative global errors are calculated by Eq. (3.8), taking

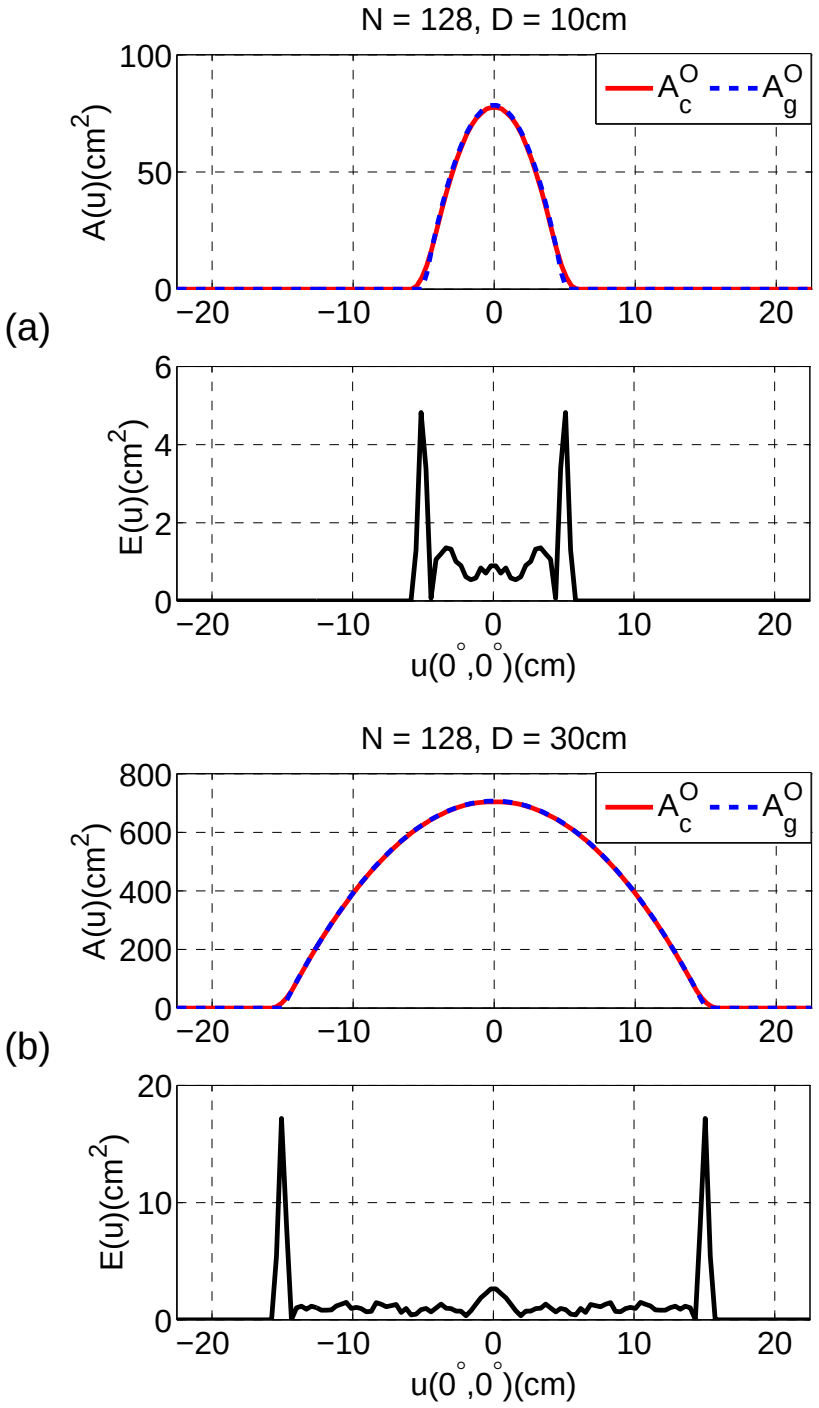

Figure 3.2: Comparison between the analytical geometrical profile function, $A_g^O(u)$, and the computed profile function, $A_c^O(u)$, at direction $u(0°, 0°)$ for the sphere with diameter (a) $D = 10$ cm; (b) $D = 30$ cm.

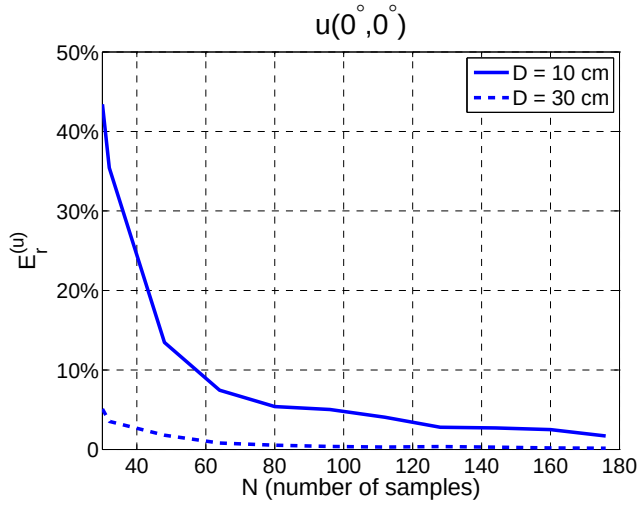

(a)

Figure 3.3: Effect of the number of samples on the relative global error, $E_r^{(u)}$, along the direction, $u(0°, 0°)$, for the two spheres.

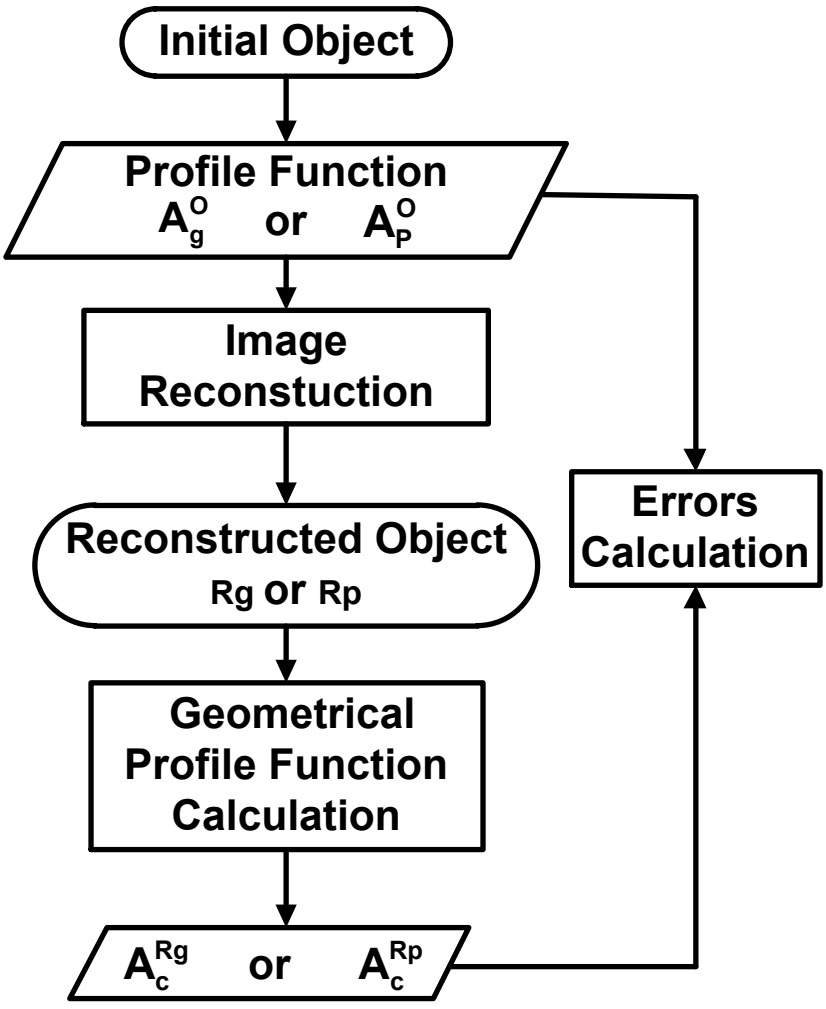

(a)

Figure 3.4: A flow chart describing the process of quality evaluation for 3D image reconstruction from profile functions.

the profile functions of the original object as the reference profile functions A_{ref} for each case.

Sphere For the reconstructed sphere Rg, the analytical geometrical profile function A_g^O from the initial sphere is taken as the reference profile function. Comparison between A_g^O and A_c^{Rg} is shown in Fig. 3.5 (a). It shows quite small differences with relative errors 4%, 5%, 5% in directions x, y, z respectively. This confirms a very good agreement of the 3D reconstructed image with the initial sphere. For the distorted reconstructed sphere Rp, the physical profile function A_p^O from the initial sphere is taken as the reference profile function. Comparison between A_p^O and A_c^{Rp} is shown in Fig. 3.5 (b). The difference is more significant with relative errors equal to 1%, 21%, 21% in directions x, y, z respectively. The errors are higher for y and z, while it remains limited in x direction, because it is the scan direction of the reconstruction.

Asymmetric object For the reconstructed asymmetric objects (Fig. 2.12), comparison between initial profile functions (A_g^O or A_p^O) and the corresponding computed ones from the reconstruction (A_c^{Rg} or A_c^{Rp}) are presented in Fig. 3.6 (a) and (b) respectively. Once again, in the scanning direction x, the relative error for the accurate reconstructed object Rg and the distorted reconstructed object Rp are almost the same, (2% and 3%, respectively). However, the relative errors for Rg, (6% and 6%), are much smaller comparing to the errors, (21%, 37%), for Rp in directions y, z, respectively.

Step-cylinder For the reconstructed step-cylinder (Fig. 2.13), as can be seen in Fig. 3.7 (a), the correct image Rg gives a small difference between the profile functions A_g^O and A_c^{Rg}, with relative errors $(6\%, 6\%, 7\%)$ in directions (x, y, z) respectively. On the contrary, in Fig. 3.7 (b), for the distorted image Rp reconstructed from physical profile functions, this difference becomes very significant, with relative errors $(29\%, 29\%, 2\%)$ in directions (x, y, z) respectively. Once again, the errors in the scan direction z are smaller.

Non-convex object For the reconstructed non-convex objects (Fig. 2.14), comparisons between the initial profile functions (A_g^O or A_p^O) and the computed ones (A_c^{Rg} or A_c^{Rp}) from reconstructed objects are respectively presented in Fig. 3.8 (a) and (b). Similarly, comparing to the distorted reconstructed object Rp, the accurate image Rg shows much more agreement between the initial profile functions and the computed ones. It gives lower relative global errors $(7\%, 7\%, 7\%)$ than the errors $(2\%, 25\%, 25\%)$ of the distorted one, for directions (x, y, z) respectively.

Separated object Finally, for the two separated objects (Fig. 2.15), we get similar results. Fig. 3.9 (a) and (b) compare the initial profile functions (A_g^O or A_p^O) and the computed ones (A_c^{Rg} or A_c^{Rp}) respectively for the reconstructed objects Rg and Rp. For the good result Rg, the two sets of curves (A_g^O and A_c^{Rg}) almost coincide with each other, with small global errors $(7\%, 4\%, 4\%)$ for directions (x, y, z) respectively. However, for the distorted result Rp, the difference between the two sets of profile functions are much more significant, with higher relative gloabl errors $(14\%, 18\%, 18\%)$ for directions (x, y, z) respectively.

Non-orthogonal case Now we apply the algorithm for calculating profile functions in the non-orthogonal case. The reconstructed step-cylinders obtained from geometrical profile functions in orthogonal directions (Fig. 2.13 (c)), $[u_1 = x, u_2 = y, u_3 = z]$, and in non-orthogonal direction (Fig. 2.16 (c)), $[u_1 = 50°, u_2 = y, u_3 = z]$, are compared. Because of the geometrical symmetry of this object, its geometrical profile functions are identical for any direction in xoy plane. Therefore, for both reconstructed step-cylinders, the 3 initial geometrical profile functions, A_g^O, are shown in Fig. 3.10 (blue dash curve) and are taken as the reference profile functions. In the orthogonal case, the relative global errors between the initial profile function, A_g^O, and the computed profile function from the well reconstructed object, A_c^{Rg} ("ortho"), are pretty small (6%, 6% , 7% in x, y, z, respectively). On the contrary, in the non-orthogonal case, the differences between the initial profile function, A_g^O, and the computed profile function, A_c^{Rg} ("non ortho"), are much more significant (13%, 13%, 7% along the 3 observing directions, respectively), which indicates that the image is distorted.

Table 3.1 sorts out the relative global error $E_r^{(u)}$ along the 3 observing directions $[u_1, u_2, u_3]$ for the images reconstructed using Chauveau's method (section 2.6.1). The outcome allows us to confirm that our algorithm for calculating profile functions can be considered as an effective tool to quantitatively assess the quality of image reconstructions:

- In the orthogonal case, with geometrical profile functions, Chauveau's method generates accurate reconstructed images for single and/or separated objects. It guarantees the agreement between the profile functions A_g^O of the original object and the profile functions A_c^{Rg} calculated from the reconstructed object for each of the 3 orthogonal directions. The relative global errors for these cases are always very small, $E_r^{(u)} \leq 7\%$. However, with physical profile functions, the reconstructed images are distorted, but still they can meet the need of identification. Since his method chooses a scanning direction to reconstruct the studied object, it still gives, in this direction, a small difference between the profile functions A_p^O and A_c^{Rp}. However, it produces more significant differences, with much higher relative global errors $(18\% \leq E_r^{(u)} \leq 37\%)$ for the other two directions.

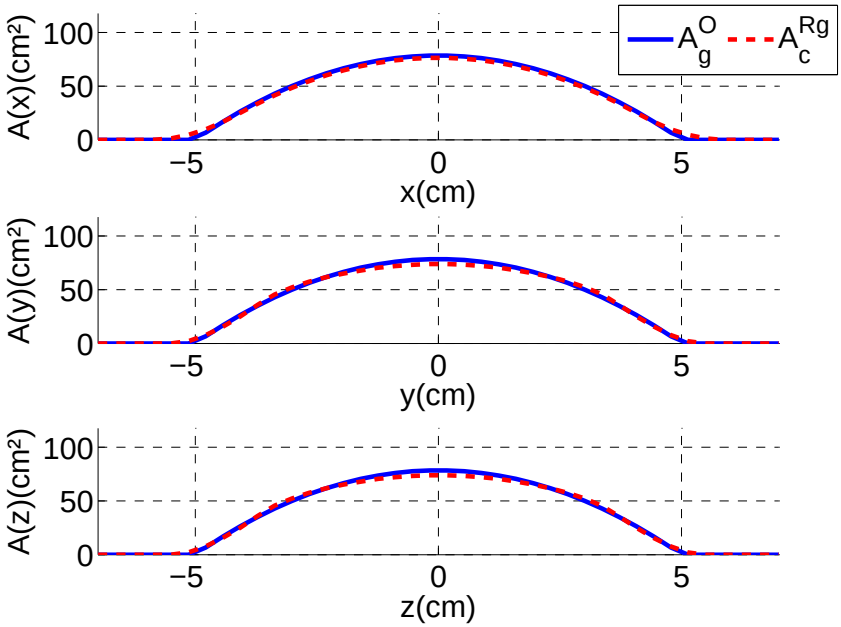

(a)

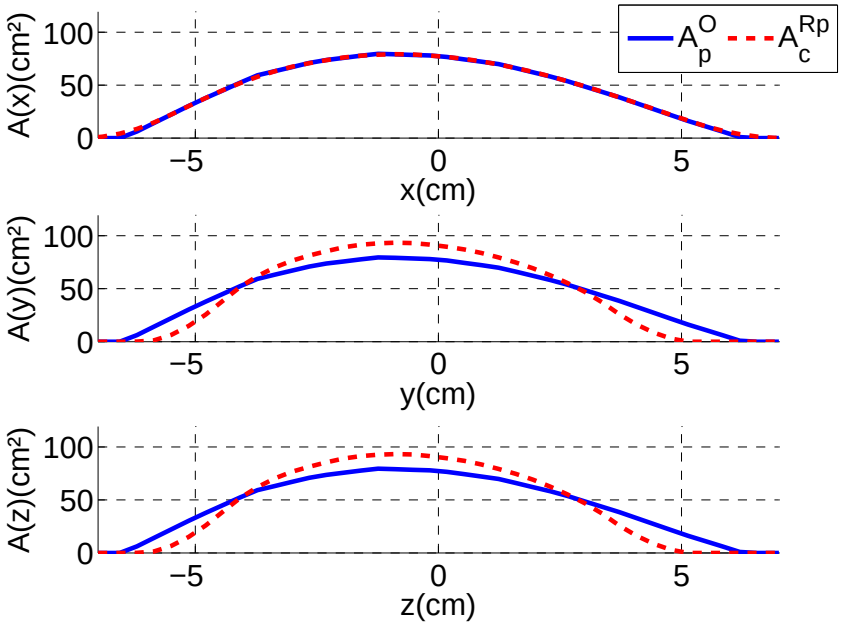

(b)

Figure 3.5: Quality evaluation of image reconstruction in Fig. 2.11: (a) Comparison between the analytical geometrical profile functions A_g^O of the initial sphere and the profile functions A_c^{Rg} computed from its reconstructed object Rg; (b) Comparison between the physical profile functions A_p^O of the initial sphere and the profile functions A_c^{Rp} computed from its reconstructed object Rp, in direction x, y, z, respectively.

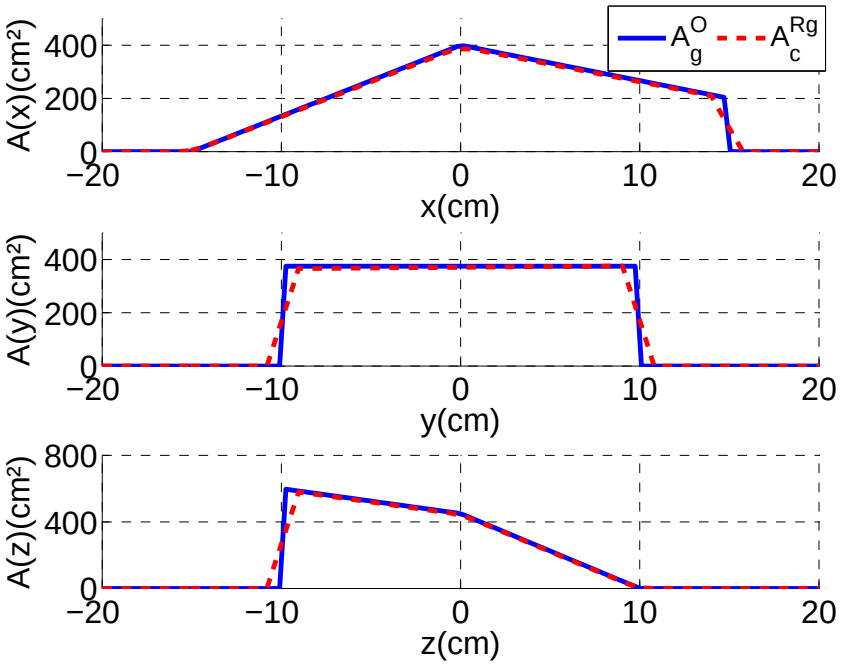

(a)

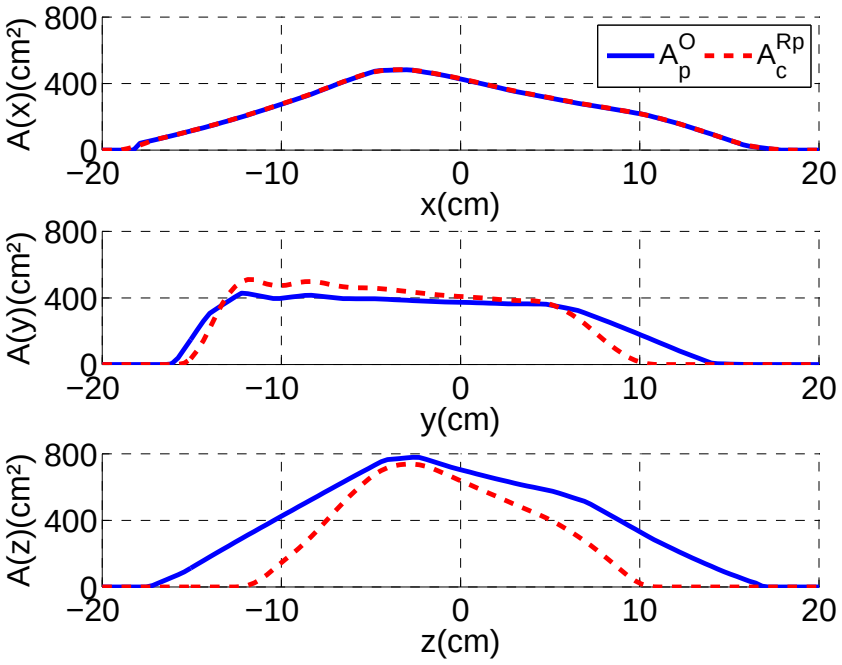

(b)

Figure 3.6: Quality evaluation of 3D image reconstruction in Fig. 2.12: (a) Comparison between the analytical geometrical profile functions A_g^O of the initial object and the profile functions A_c^{Rg} computed from its reconstructed object Rg; (b) Comparison between the physical profile functions A_p^O of the initial object and the profile functions A_c^{Rp} computed from its reconstructed object Rp, in direction x, y, z, respectively.

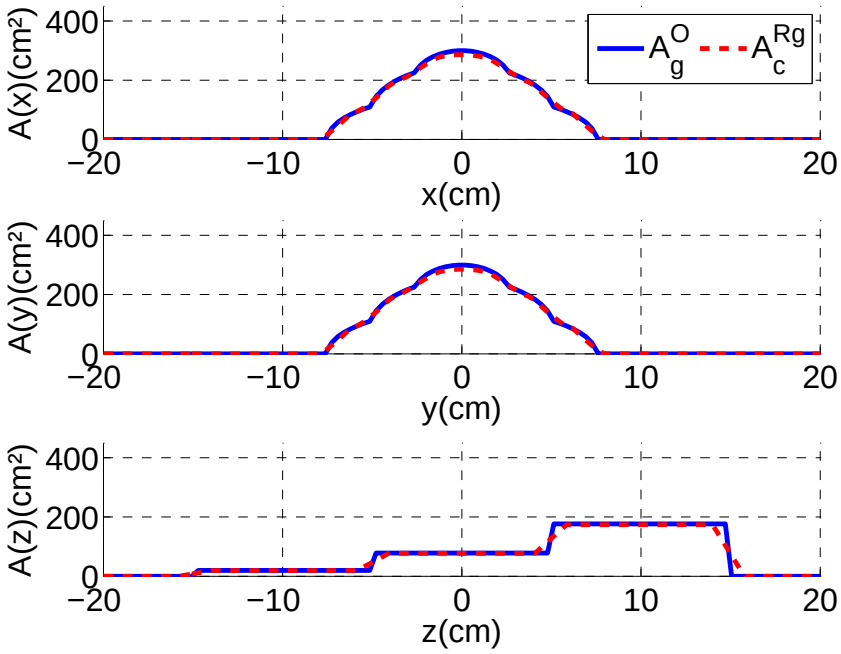

(a)

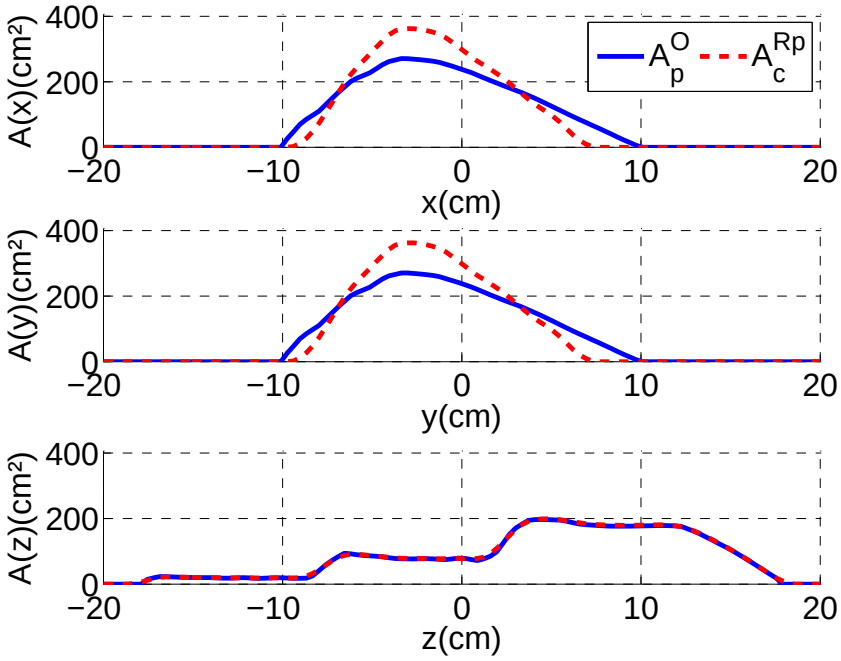

(b)

Figure 3.7: Quality evaluation of 3D image reconstruction in Fig. 2.13: (a) Comparison between the analytical geometrical profile functions A_g^O of the initial object and the profile functions A_c^{Rg} computed from its reconstructed object Rg; (b) Comparison between the physical profile functions A_p^O of the initial object and the profile functions A_c^{Rp} computed from its reconstructed object Rp, in direction x, y, z, respectively.

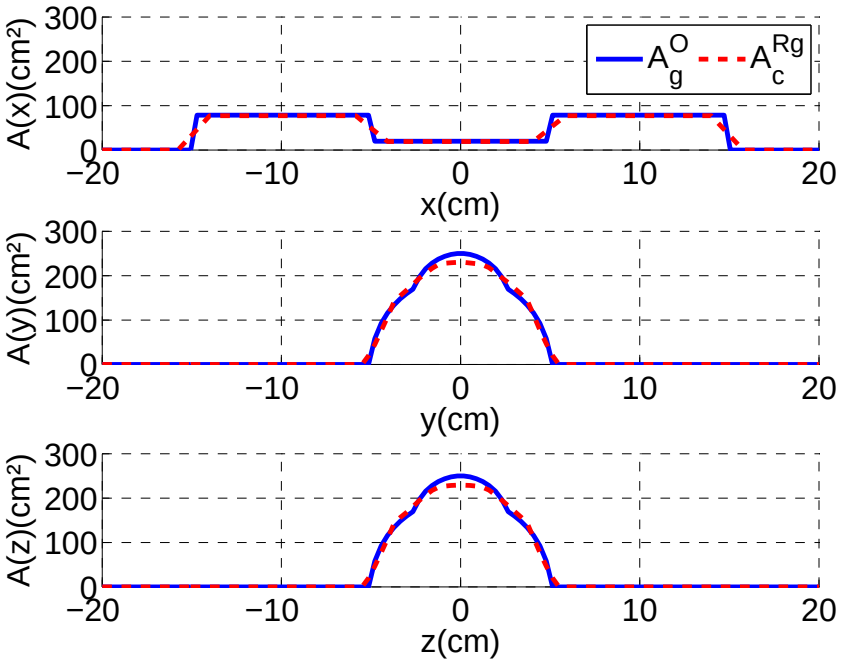

(a)

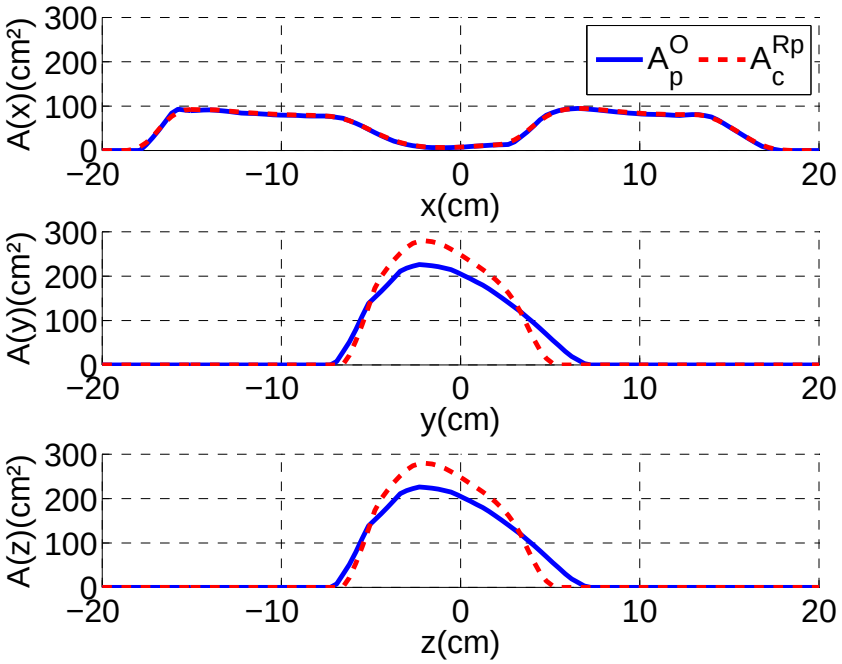

(b)

Figure 3.8: Quality evaluation of 3D image reconstruction in Fig. 2.14: (a) Comparison between the analytical geometrical profile functions A_g^O of the initial object and the profile functions A_c^{Rg} computed from its reconstructed object Rg; (b) Comparison between the physical profile functions A_p^O of the initial object and the profile functions A_c^{Rp} computed from its reconstructed object Rp, in direction x, y, z, respectively.

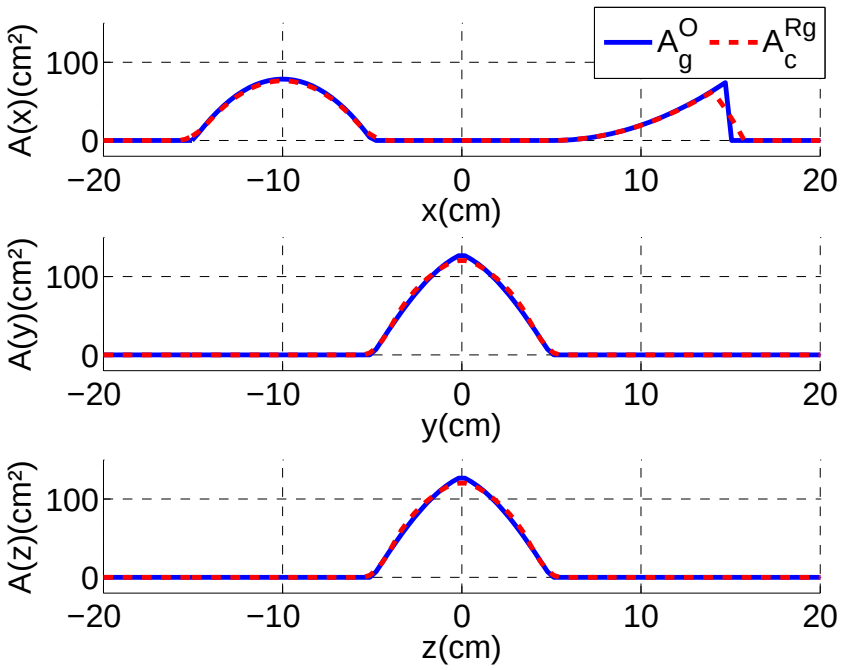

(a)

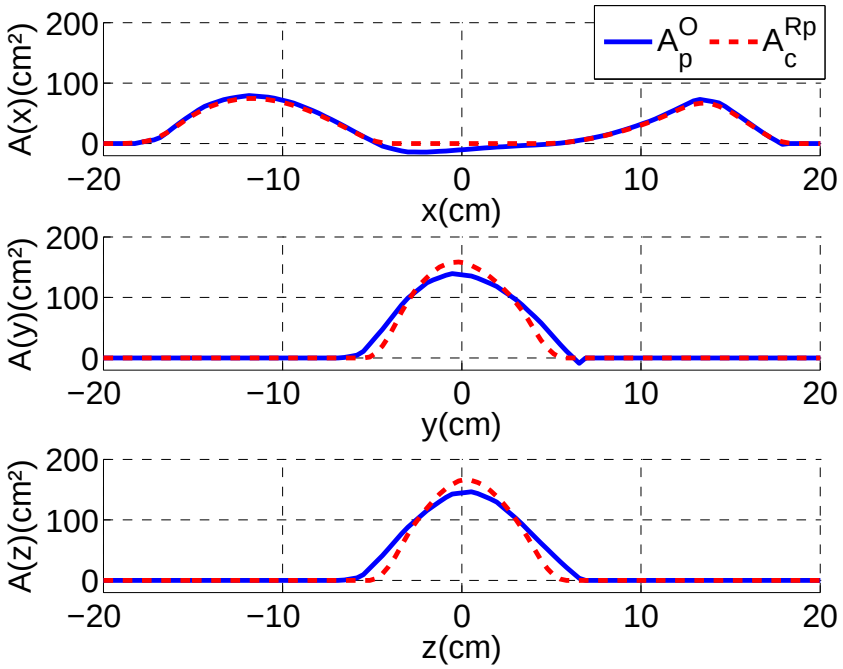

(b)

Figure 3.9: Quality evaluation of 3D image reconstruction in Fig. 2.15: (a) Comparison between the analytical geometrical profile functions A_g^O of the initial object and the profile functions A_c^{Rg} computed from its reconstructed object Rg; (b) Comparison between the physical profile functions A_p^O of the initial object and the profile functions A_c^{Rp} computed from its reconstructed object Rp, in direction x, y, z, respectively.

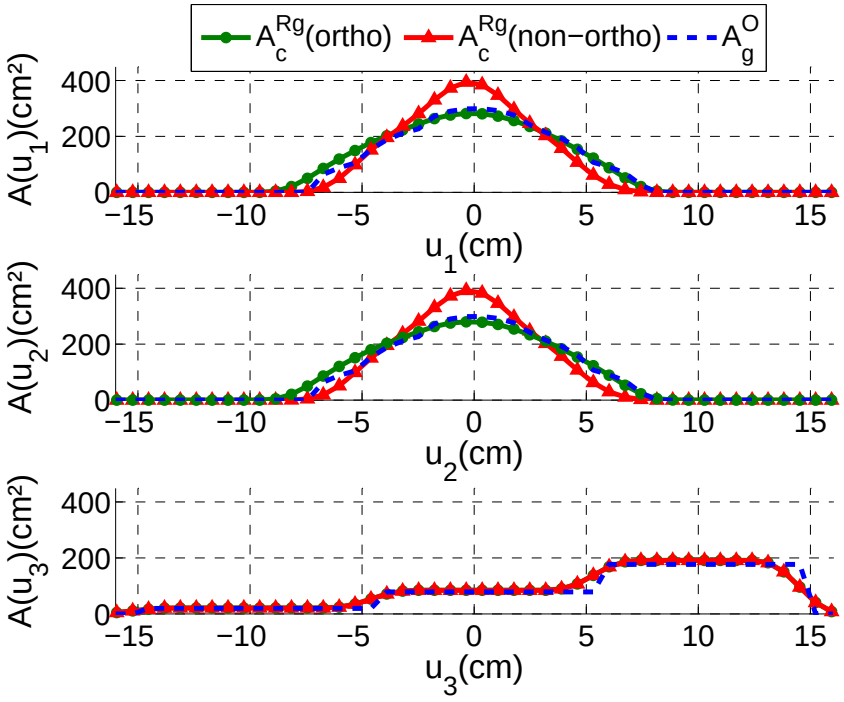

Figure 3.10: Comparison between input geometrical profile functions, A_g^O, and calculated profile functions from the reconstructed step-cylinder in orthogonal case, A_c^{Rg} ("ortho"), $[u_1 = x, u_2 = y, u_3 = z]$, and in non-orthogonal case, A_c^{Rg} ("non ortho"), $[u_1 = 50°, u_2 = y, u_3 = z]$.

- In the non-orthogonal case, even with geometrical profile functions, the reconstructed images are distorted and elongated along the direction perpendicular to the bisector of the 2 non-orthogonal directions. Correspondingly, it gives higher errors between the profile functions of the initial object and that computed from the distorted reconstructed object, which confirms again that this error can behave as a quantitative indicator of the quality of the reconstructed image.

3.1.4 Application for identification of radar targets

To identify a radar target, a common way consists in directly comparing its image to models in a database, for example the contour of the radar image and that of the models [10]. Here, an alternative feature for the identification is proposed: the profile function along chosen directions, which can be calculated by the algorithm presented in section 3.1.1. Before the identification process itself, we create a database containing K models of 3D objects. The method is given by following steps:

- Firstly, using the object's physical profile functions A_p^O in 3 directions, we obtain a 3D reconstructed object Rp by using Chauveau's method.

- Then, we choose L arbitrary directions. Each direction $u^{(l)}(l = 1, 2 \cdots, L)$ is noted as u in the following for simplification. By the algorithm for calculating pro-

Table 3.1: Relative global error $E_r^{(u)}$ along the 3 observing directions for the images reconstructed using Chauveau's method (section 2.6.1).

Direction	Object	Profile function	$E_r^{(u_1)}$	$E_r^{(u_2)}$	$E_r^{(u_3)}$
Orthogonal	Sphere	A_g	4%	5%	5%
		A_p	1%	21%	21%
	Asymmetric object	A_g	2%	6%	6%
		A_p	3%	21%	37%
	Step-cylinder	A_g	6%	6%	7%
		A_p	29%	29%	2%
	Non-convex object	A_g	7%	7%	7%
		A_p	2%	25%	25%
	Separated objects	A_g	7%	4%	4%
		A_p	14%	18%	18%
Non-orthogonal	Step-cylinder	A_g	13%	13%	7%

file functions presented in section 3.1.1, we calculate the geometrical profile functions $A_c^{Rp}(u)$ from the reconstructed object Rp and the geometrical profile functions profile functions $A_c^M(u)$ from each model.

- Next, for each direction u, using Eq. (3.7), we measure the absolute error $E(u_i)$ in each slice S_i at position u_i, between $A_c^{Rp}(u)$ and $A_c^M(u)$:

$$E(u_i) = |A_c^{Rp}(u_i) - A_c^M(u_i)| \tag{3.9}$$

From this error, $E(u_i)$, we define a function, $Sim(u_i)$, to calculate the similarity of slice S_i between the reconstructed object and each model:

$$Sim(u_i) = \begin{cases} 1 & E(u_i) \leq E_{min} \\ \frac{E_{max} - E(u_i)}{E_{max} - E_{min}} & E_{min} < E(u_i) < E_{max} \\ 0 & E(u_i) \geq E_{max} \end{cases} \tag{3.10}$$

where E_{min} and E_{max} are the minimum tolerance and maximum tolerance of error respectively.

For each slice, if the error $E(u_i)$ is quite small, less than the minimum tolerance of error, the slice at this position can be considered to be totally matched. On the contrary, if this error is greater than the maximum tolerance of error, they are considered to be unmatched.

Furthermore, we calculate the global similarity $Sim_g^{(u)}$ of all slices along u as the similarity for this direction by:

$$Sim_g^{(u)} = \frac{\sum_{i=1}^{N} Sim(u_i)}{N} \tag{3.11}$$

where N is the number of slices along the direction u.

Finally, in this manner, the similarities of the L chosen directions give an overview similarity between the object and each model. Models with higher similarities are selected as the most possible shapes for the studied object.

To present the principle and performance of this model match process, the step-cylinder presented in Fig. 2.13 (a) is taken as the studied target. For the database of models, only models which have same level of volume and similar shape as the studied object are considered, because models of much larger or smaller dimension are not comparable. Hence, $K = 6$ models of the same dimension are shown in Fig. 3.11: 4 step-cylinders, Model 1, 2, 3, 4, each with 3 sub-cylinders (circle, square or triangle cylinder), a cone (Model 5) and a circle cylinder (Model 6). For Model 1, 2, 3, 4, each slice in the same position along z axis has equal area, for example, at position z_i along z axis, the slice (a circle) of Model 1 and the slice (a square) of Model 3 have same area. Each corresponding sub-cylinder of the 4 step-cylinders has equal height. Model 5 (the cone) and Model 6 (the circle cylinder) have same diameter of the base and same height as the studied object, namely the Model 1. Detailed dimensions (in cm) of these models are presented in Table 3.2.

Table 3.2: Dimensions of the 6 models (in cm).

Model	Sub-cylinder	Diameter or side	Height
Step-cylinder	Cylinder 1	5	10
	Cylinder 2	10	10
	Cylinder 3	15	10
Cone		15	30
circle cylinder		15	30

We use a cubic computational domain of dimension 45 cm with $N^3 = 128^3$ pixels for all the objects (or models). We take the reconstructed step-cylinder Rp presented in Fig. 2.13 (d) as the image for automatic identification process. It is reconstructed by Chauveau's method from physical profile functions in 3 mutually orthogonal directions of observation. Geometrical profile functions both for the reconstructed object and for each model, namely A_c^{Rp} and A_c^M are calculated for arbitrary directions by the algorithm presented in section 3.1.1. For each model,

the similarity of each slice and the global similarity for each direction are given by Eq. (3.10) and (3.11) respectively.

The choice of the minimum and maximum tolerances of error is somewhat arbitrary: it is related to the expected accuracy. With S_{C_D} the area of each slice of the computational domain, E/S_{C_D} is the ratio between the number of false pixels and the total number of pixels in each slice. Here, $E_{min}/S_{C_D} = 0.2\%$ and $E_{max}/S_{C_D} = 6\%$ are used as an experimental value.

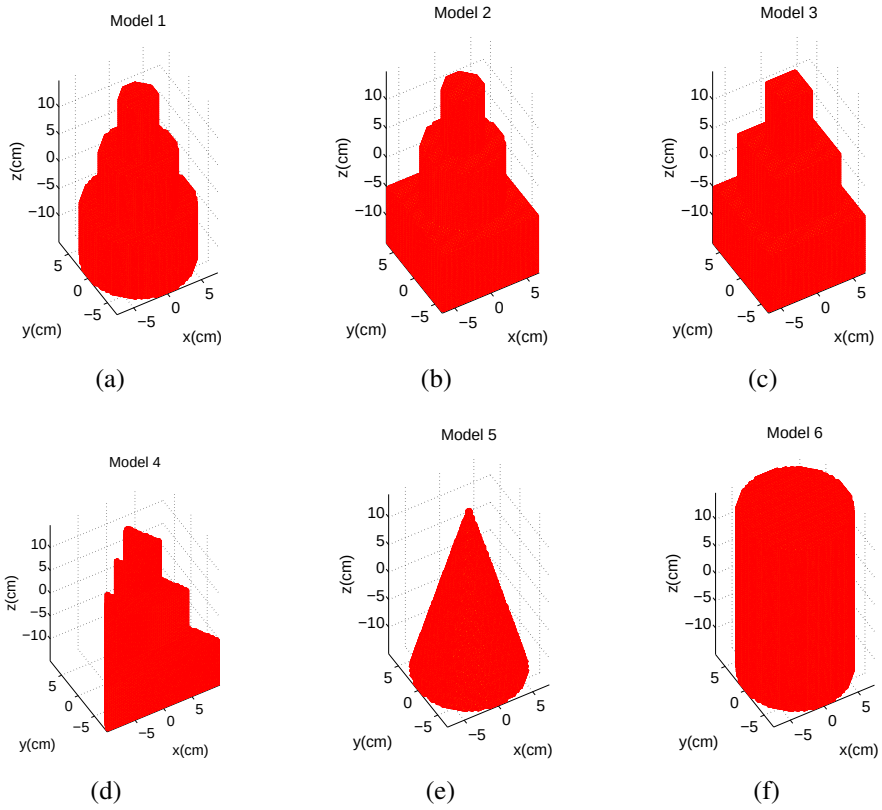

Figure 3.11: Configuration of 6 Models: (a) Model 1; (b) Model 2; (c) Model 3; (d) Model 4; (e) Model 5; (f) Model 6.

To show the performance of this method, we compare the global similarities for the 6 models in some chosen directions. Firstly, we consider the directions in xoz and yoz plane, namely directions with fixed azimuthal angle $\phi = 0°$ or $90°$ and inclination angle θ varying in $[0°, 180°]$ with a step $\delta\theta = 15°$. The global similarities between the object and the 6 models for the case $\phi = 0°$ and the case $\phi = 90°$ are presented in Fig. 3.12 (a) and (b) respectively. For each direction, the global similarities of Model 1, 2, 3 are very close, with slight differences among them. For $\phi = 0°$, Model 4, namely the triangle step-cylinder, has same level of global similarities as Model 1, 2, 3, while for $\phi = 90°$, it has much lower similarities so that we can separate it from the 3 other step-cylinders. Comparing to the 3 step-cylinders, Model 5 and 6 has lower similarities for most of the chosen directions. Secondly, we consider directions with fixed inclination angle, $\theta = 45°$ or $90°$, and

azimuthal angle ϕ varying in $[0°, 180°]$ with a step $\delta\phi = 15°$. In the case of $\theta = 45°$, shown in Fig. 3.12 (c), we can classify the similarities of the 6 models into 3 levels: Model 1, 2, 3 have the highest similarities for all chosen directions, Model 4 has lower levels and Model 5 and 6 have the lowest levels for most of the directions. While in the case of $\theta = 90°$ shown in Fig.3.12 (d), the difference between models is not significant, especially in the directions $\phi = [0°, 90°]$, but still, Model 1, 2, 3 have the highest similarities for most of the chosen directions.

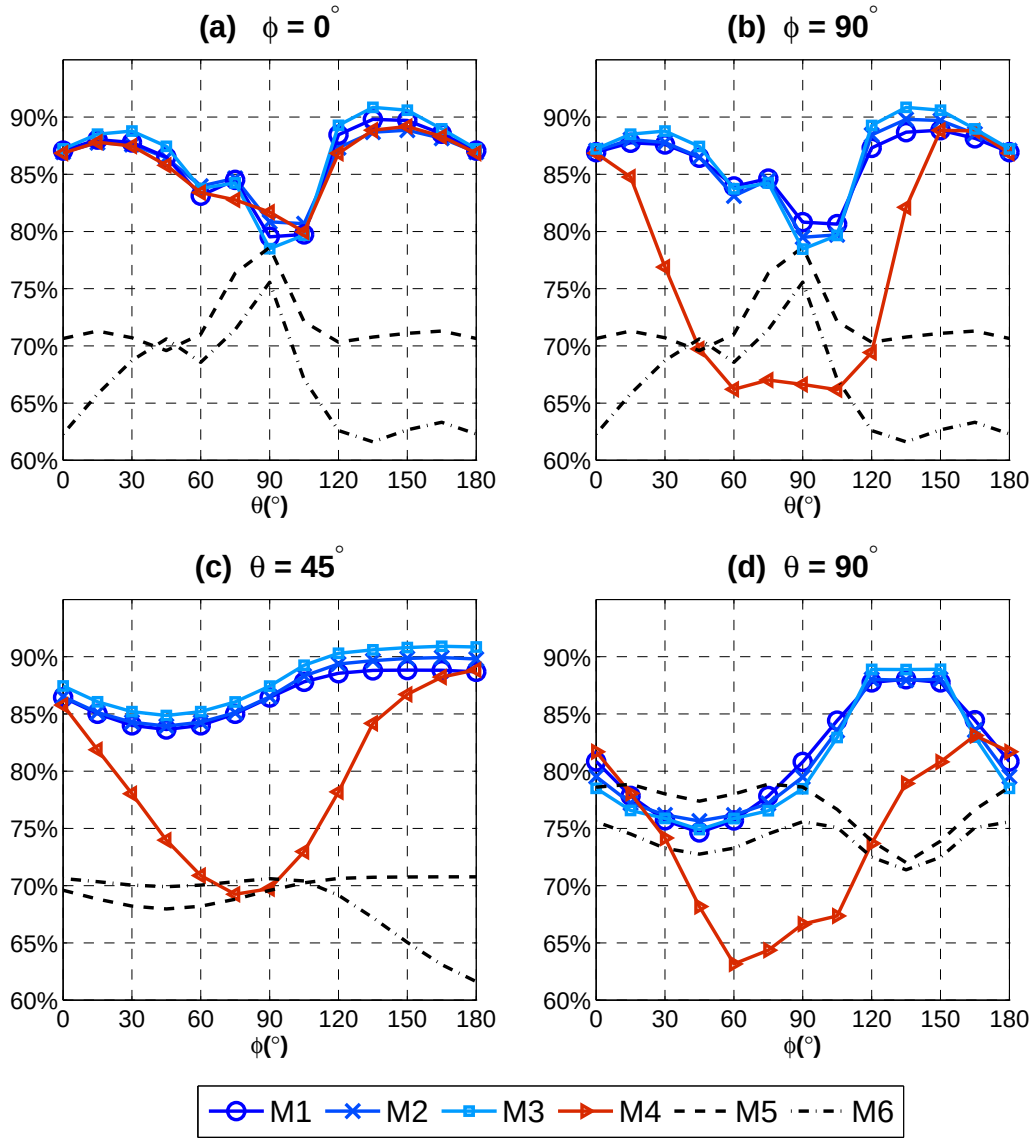

Figure 3.12: Global similarities $Sim_g(u)$ between the object and each model for chosen directions: (a) $\phi = 0°$, $\theta = [0°, 180°]$; (b) $\phi = 90°$, $\theta = [0°, 180°]$; (c) $\theta = 45°$, $\phi = [0°, 180°]$; (d) $\theta = 90°$, $\phi = [0°, 180°]$

.

To select optimal models, we consider now the mean of the global similarities $\overline{Sim_g}$ for the full range of possible directions, namely directions $u(\theta, \phi)$ with θ and

ϕ both varying in $[0°, 180°]$ with a step $\delta\theta = \delta\phi = 15°$. The global similarity $\overline{Sim_g}$ is calculated by:

$$\overline{Sim_g} = \sum_{\theta} \sum_{\phi} Sim_g^{(u)}(\theta, \phi)/N_u \tag{3.12}$$

where N_u is the total number of directions.

Table 3.3 gives the mean of the global similarities $\overline{Sim_g}$ for the whole set of directions for each model. From the outcome, the 3 'step-cylinders' (Model 1, 2, 3) have the highest mean similarity (around 86%) and cannot be distinguished. In fact, contrary to high frequency radar imaging, low frequency methods cannot give high resolution, i.e. details on the target, but they provide information only on the approximate shape of the target. Therefore, models 1, 2 and 3 should be considered as the same and can be selected as the optimal models of the studied object.

Table 3.3: Mean of global similarities.

Model	Model 1	Model 2	Model 3	Model 4	Model 5	Model 6
$\overline{Sim_g}$	86%	86%	87%	82%	72%	66%

3.1.5 Conclusion

In this section, an algorithm for numerical calculating geometrical profile functions from a 3D object is developed. It has no limitation for any geometries (even irregular shapes) and arbitrary directions. It is verified to be effective with only a few discretization errors, which can be reduced by increasing the number of samples.

- Firstly, it can be applied to quantitatively evaluate the quality of reconstructions by calculating errors between profile functions from the initial object and profile functions from its reconstructed image.

- Secondly, with a database containing possible models, it also can be applied to automatically identify a radar target using its reconstructed object obtained from physical profile functions in only 3 directions. The method permits to compare the reconstructed object and models in a full range of directions so as to avoid that different shapes might have same profile functions in some directions. Taking into account the poor condition of limited resolution encountered in low frequency radar imaging, the identification process succeeds in finding the best possible models for the studied object.

- Finally, in the following section, the developed algorithm can be used to calculate profile functions of the evolving object in the inverse problem so as to get satisfactory reconstructions in the non-orthogonal case.

3.2 Inverse problem: image reconstruction with level set method

As can be seen in Eq.(3.1), our problem is formalized as a linear problem. Because it has a much higher number of unknowns, N^3, than the number of data, $3 \times M$ (with 3 profile functions), the system is under-determined. The flow chart in Fig. 3.13 illustrates the process of iterative optimization. An iterative method is considered to find a solution that minimizes the cost function, F_k, a function of the profile function observed from the studied object A and the profile function calculated from the estimate. An initial estimate, obtained by the Chauveau's reconstruction algorithm, is used to generate successive approximations to an optimal solution.

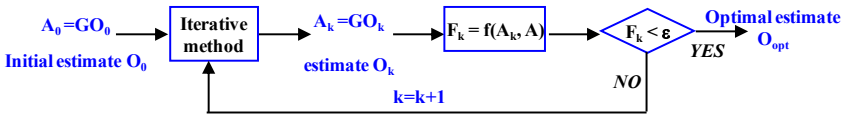

Figure 3.13: The process of iterative optimization

An iterative method is a mathematical procedure that generates a sequence of improving approximate solutions for a class of problems. A specific implementation of an iterative method, including the termination criteria, is an algorithm of the iterative method. An iterative method is called convergent if the corresponding sequence converges for given initial approximations. A mathematically rigorous convergence analysis of an iterative method is usually performed.

In the case of a system of linear equations, there are two main classes of iterative methods: stationary iterative methods, and more general Krylov subspace methods [70]. Stationary iterative methods solve a linear system with an operator approximating the original one. Based on a measurement of the error in the result (the residual), they form a correction equation for which this process is repeated. While these methods are simple to derive, implement, and analyze, convergence is only guaranteed for a limited class of matrices. Examples of stationary iterative methods are the Jacobi method, Gauss-Seidel method and the Successive over-relaxation method [70]. Krylov subspace methods work by forming an orthogonal basis of the sequence of successive matrix powers times the initial residual (the Krylov sequence). The approximations to the solution are then formed by minimizing the

residual over the subspace formed. The original method in this class is the conjugate gradient method (CG). Other methods are the generalized minimal residual method (GMRES) and the bi-conjugate gradient method (BiCG). More details about those methods are presented in [70].

In our case, we need an iterative method adapted to a large and sparse ill-conditioned system. Numerical test comparing LSQR (least square method) with several other conjugate-gradient algorithms indicates that LSQR is the most reliable algorithm when G is ill-conditioned [71]. Therefore, we firstly use the least square method (LSQR) to get an idea of how challenging our problem is. In the following section, we present the principle and numerical results of this method.

3.2.1 Least square method

The term least squares describes a frequently used approach to solve under-determined or inexactly specified systems of equations in an approximate sense. Instead of solving the equations exactly, we seek only to minimize the sum of the squares of the residuals. The most important application is in data fitting. The best fit in the least-squares sense minimizes the sum of squared residuals, a residual being the difference between an observed value and the fitted value provided by a model. Least squares problems fall into two categories: linear or ordinary least squares and non-linear least squares, depending on whether or not the residuals are linear in all unknowns. The linear least-squares problem occurs in statistical regression analysis; it has a closed-form solution. The non-linear problem has no closed-form solution and is usually solved by iterative refinement; at each iteration the system is approximated by a linear one, thus the core calculation is similar in both cases. The least-squares method was first described by Carl Friedrich Gauss around 1794 [14]. Least squares corresponds to the maximum likelihood criterion if the experimental errors have a normal distribution and can also be derived as a method of moments estimator.

The objective consists in adjusting the parameters of a model function to best fit a data set. A simple data set consists of n points (data pairs) $(x_i, y_i), i = 1, ..., n$, where x_i is an independent variable and y_i is a dependent variable whose value is found by observation. The model function has the form $f(x, \beta)$, where the m adjustable parameters are held in the vector β. The goal is to find the parameter values for the model which “best" fit the data. The least squares method finds its optimum when the sum, S, of squared residuals is a minimum.

$$S = \sum_{i=1}^{n} r_i^2 \tag{3.13}$$

A residual is defined as the difference between the value predicted by the model and the actual value of the dependent variable.

$$r_i^2 = |y_i - f(x_i, \beta)|^2 \tag{3.14}$$

An example of a model is that of the straight line.Its equation is given by:

$$f(x, \beta) = \beta_0 + \beta_1 x \tag{3.15}$$

The minimum of the sum of squares is found by setting the gradient to zero. Since the model contains m parameters there are m gradient equations.

$$\frac{\partial S}{\partial \beta_j} = 2 \sum_i r_i \frac{\partial r_i}{\partial \beta_j} = 0, j = 1, ..., m \tag{3.16}$$

and since $r_i = y_i - f(x_i, \beta)$ the gradient equations become:

$$-2 \sum_i \frac{\partial f(x_i, \beta)}{\partial \beta_j} r_i = 0, j = 1, ..., m \tag{3.17}$$

The gradient equations apply to all least squares problems. Each particular problem requires particular expressions for the model and its partial derivatives.

A regression model is a linear one when the model comprises a linear combination of the parameters, i.e.

$$f(x_i, \beta) = \sum_{j=1}^{m} \beta_j \phi_j(x_i) \tag{3.18}$$

when the coefficients, $\phi_j(x_j)$, are functions of x_i.

Letting

$$X_{ij} = \frac{\partial f(x_i, \beta)}{\partial \beta_j} = \phi_j(x_i) \tag{3.19}$$

we can then see that in that case the least square estimate, β, is given by

$$\hat{\beta} = (X^T X)^{-1} X^T y \tag{3.20}$$

To solve our optimization problem, we used the LSQR in Matlab and also programmed a modified least square method, named RRLSQR, proposed in [71]. This method is based on the bidiagonalization procedure of Golub and Kahan. It is analytically equivalent to the standard method of conjugate gradients, but the process has more favorable numerical properties.

To study the performance of RRLSQR, we firstly applied the iterative process to the sphere Fig. 2.11 (a). We use two different initial estimates: a small cube totally

inside the studied sphere and a rectangular that has some part outside the studied sphere. We consider both 3 orthogonal ($[u_1 = x, u_2 = y, u_3 = z]$) and 3 non-orthogonal directions ($[u_1(90°, 30°, u_2 = y, u_3 = z]$). All experiments are carried with a maximum tolerance $\epsilon = 10^{-6}$ to stop the iteration. Note that, because the mapping matrix we developed, so far, considers only the geometrical case, herein geometrical profile functions are used as the observed data. As shown in Fig. 3.14, with a small cube, with 3 orthogonal directions, we obtained a correct estimate comparing with the original sphere, but a distorted one for the non-orthogonal case.

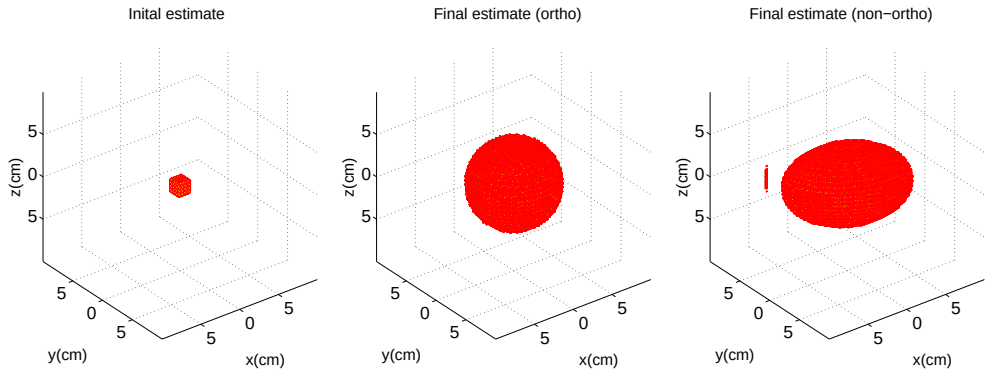

(a) (b) (c)

Figure 3.14: Iteration of a sphere (Fig. 2.11 (a)) starting from a small cube: (a) the initial estimate (b) final estimate in orthogonal case (c) final estimate in non-orthogonal case

In the case of a rectangular, the result seems similar (Fig. 3.15), except that the iterative process can not remove the extra part. This extra part is due to the fact that the matrix G is singular and is not invertible. That is to say there exist some rows of A which are all zero, corresponding to the part which does not belong to the object. Therefore, during the iterative process, the extra parts are fitted by any value rather than 0. To avoid this problem, we add a constraint to the iterative process:

$$A(x_j) = 0 \Longleftrightarrow O(x_j) = 0 \tag{3.21}$$

where $A(x_j)$ is the observed profile function value in point x_j, and $O(x_j)$ is the characteristic function of the object.

With this constraint, the extra parts are well eliminated both in the orthogonal (Fig. 3.16 (a)) and non-orthogonal cases (Fig. 3.16 (b)).

The estimate obtained by the LSQR iteration is not binary any more but is fitted by arbitrary values. The pixels, which belong to the original object, should have equal probabilities and contributions to be fitted, while the iterative process gives more attention to the intersection projected by all the 3 directions. We attempted to apply a binarization process, however the convergence of the iteration process can not be reached.

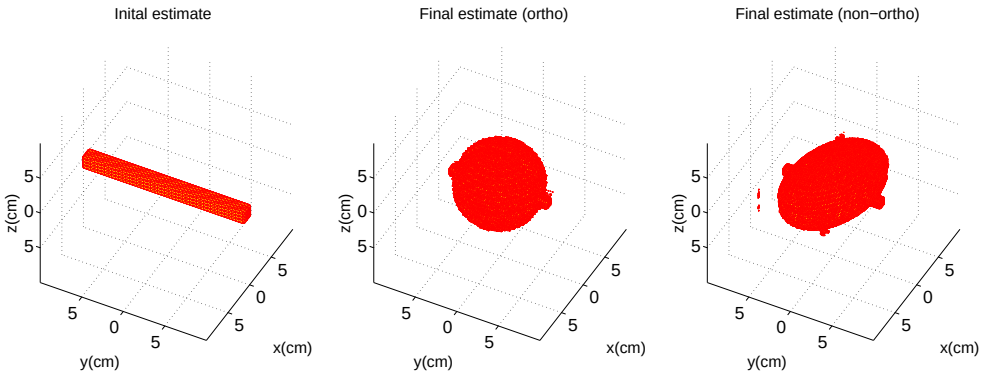

(a) (b) (c)

Figure 3.15: Iteration of a sphere (Fig. 2.11 (a)) starting from a long rectangular: (a) the initial estimate (b) final estimate in orthogonal case (c) final estimate in non-orthogonal case

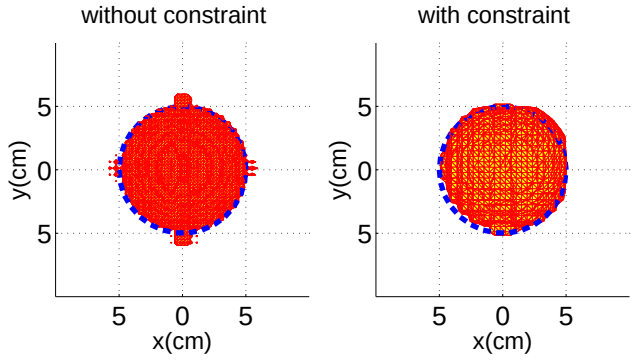

(a)

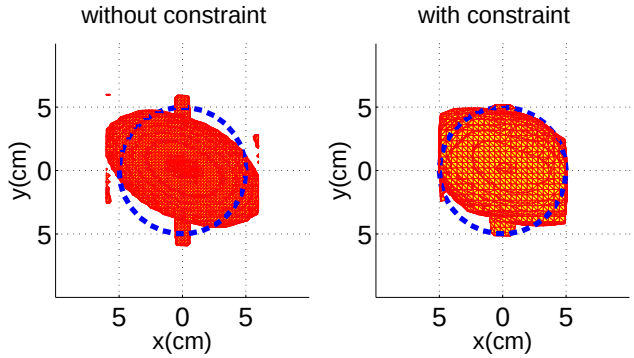

(b)

Figure 3.16: Final estimate by the iteration starting from the long rectangular Fig. 3.15 (a) without or with constraint in : (a) orthogonal case (b) non-orthogonal case (dash curve : contour of the original sphere)

LSQR, as most inverse methods, can succeed in minimizing the cost function. However, it updates directly the unknown object by fitting arbitrary values, therefore it is difficult to represent a shape. Therefore, an iterative method, which can fit the unknown vector with binary values or an appropriate way to represent the three-dimensional(3D) object with arbitrary values is required.

3.2.2 Shape representation

In n-dimensional space R^n, an object is always bounded by its boundary of $n-1$ dimension. For a one-dimensional line, the boundary is composed by two border points of zero-dimension. For a two-dimensional object, the boundary is a curve. For a three-dimensional object, the boundary is a surface. Once the boundary is determined, the object is obtained. Therefore, to represent the shape of an object is somewhat equivalent to the representation of its boundary. An explicit representation of boundary is to directly express the points that belong to the boundary. While, an implicit representation is to define the points belonging to the boundary as the solution of some function. For iterative shape optimization problems, it is very convenient to use an analytical expression or function to represent the boundary in an explicit way. However, this can be hardly achieved for general objects, especially for these objects of irregular shapes. Consequently, we introduce, in the following, numerical approaches for boundary representation. They can be divided into two classes:

- Lagrangian approach. This method is an approximation of explicit boundary representation. Instead of specifying all points on the boundary, it discretizes the boundary in a relatively dense and uniform manner to consider enough points, $p_1 < \cdots < p_{i-1} < p_i < p_{i+1} < \cdots < p_{end}$. Their corresponding n-dimensional positions are recorded by a vector function $\vec{x}_p$. Moreover, it is required to store the connectivities of these selected boundary points so that a sufficiently accurate outline of the shape can be obtained. It is very easy and convenient to determine the connectivity for the two-dimensional case, because it is based on the straightforward ordering. For example, the point p_i is connected to p_{i-1} and p_{i+1}. However, for 3D space, the boundary points are sampled on a 2D surface, their connectivity can be various and more difficult to be determined. It will be even more complicated when topology change occurs, for example, merging or splinting. The algorithm to determine the connectivity has to be carefully designed, otherwise incorrect shape can be obtained. Another disadvantage of this kind of approach is that, to restore the shape from the boundary, it needs to decide whether a point is inside or outside the boundary. A general way for this is to cast a ray from the point in question to some far-off place that is known to be outside the boundary. Then if the ray has an even

number of intersections, the point is outside, and vice versa. This determination process is complicated and requires a huge amount of computation.

- Eulerian approach. This method is a type of implicit representation. It defines a one-higher dimension ($n+1$ dimension) function on a rectangular box around the shape. The boundary is represented as the zero isocontour of this function. One can then evolve this function instead of the boundary itself, therefore, there is no need to determine the connectivity. The topology change can be easily handled during the evolution. Moreover, this method defines that the value of this function is negative for the points inside the boundary and positive for the points outside. This greatly reduces the complexity and the amount of computation for the process to restore the whole shape, comparing to the Lagrangian approach. The level set method is the pioneer method to use this kind of shape representation for inverse problems involving object shapes.

3.2.3 Level set method

The level set method, which was originally introduced by Osher and Sethian [72], has been well applied in the domain of fluid dynamics [73, 74, 75, 76, 77], image processing and computer vision [78, 79, 80, 81, 82, 83], and inverse problem involving object shapes [84, 85, 86, 87]. Researches show that the level set representation of contour only requires rather weak topological constraints and it is not restricted to 2D obstacles. Because of its implicit shape representation, it can handle topological change occurring during the shape deformation in a completely automatic and implicit way. As an Eulerian method, the level set method simply represents a boundary C as the zero-level isocontour of a one-higher dimension function, named as the level set function ϕ. This level set function is a smooth (at least Lipschitz continuous) function with negative values inside the boundary and positive values outside the boundary. During the iterative shape optimization, the level set function, noted as $\phi(\vec{x}, t)$, is a function of the spatial variable $\vec{x}$ and the time variable t. $\phi(\vec{x}, t)$ is defined by:

$$\begin{cases} \phi(\vec{x}, t) > 0 & \text{if } \vec{x} \notin \Omega; \\ \phi(\vec{x}, t) = 0 & \text{if } \vec{x} \in C; \\ \phi(\vec{x}, t) < 0 & \text{if } \vec{x} \in \Omega; \end{cases} \tag{3.22}$$

where Ω is the region or object bounded by the boundary C. Note that the parameter t can be omitted for simplification since it is an artificial time parameter. Fig. 3.17 (a) gives the shape representation using the level set function ϕ for an object Ω in the computational domain C_D.

Let $O(\vec{x})$ being the characteristic function of the object of interest Ω:

$$O(\vec{x}) = \begin{cases} O_{int} & \text{if } \vec{x} \in \Omega \\ O_{ext} & \text{if } \vec{x} \notin \Omega \end{cases} \tag{3.23}$$

The characteristic function can be linked to the level set function $\phi(\vec{x})$ with the following expression:

$$O(\vec{x}) = \begin{cases} O_{int} & \text{if } \phi(\vec{x}) \leq 0 \\ O_{ext} & \text{if } \phi(\vec{x}) > 0 \end{cases} \tag{3.24}$$

Fig. 3.17 (b) shows an example for shape deformation by the level set method, we can see that the shape changes its topology by splitting in two. It would be quite hard to describe this transformation numerically by parameterizing the contour of the shape and following its evolution. One would need an algorithm able to detect when the shape splits in two parts, and then construct parameterizations for the two newly obtained curves. This proves that it can be much easier to work with a shape through its level set function than with the shape directly, because using the shape directly would need to consider and handle all the possible deformations the shape might undergo.

Therefore, instead of evolving the boundary of the studied object directly, one can compute and analyze the update of its level set function and let the shape deformation update in a completely automatic and implicit way.

To characterize the evolution of the level set function ϕ, a velocity $\vec{V}(\vec{x})$ field is defined for the points on the boundary:

$$\vec{V}(\vec{x}) = \frac{\partial \vec{x}}{\partial t}|_{\vec{x} \in C} \tag{3.25}$$

The velocity can be derived from the relevant external physical fields, local geometrical parameters such as the unit outwards normal directional vector $\vec{N}$ and the curvature K. The two parameters can be expressed in the term of the level set function ϕ:

$$\vec{N} = \frac{\bigtriangledown \phi}{|\bigtriangledown \phi|} \qquad K = div\vec{N} = \bigtriangledown \cdot (\frac{\bigtriangledown \phi}{|\bigtriangledown \phi|}) \tag{3.26}$$

where $\bigtriangledown \phi$ is the spatial gradient of the level set function ϕ and div the divergence operator.

In fact, only the normal component of the deformation velocity V_N in the normal direction to the boundary can change the object shape. Therefore, the evolution of the level set function is linked with the normal velocity V_N by a Hamilton-Jacobi-type equation and it is known as the level set equation [88]:

$$\frac{\partial \phi}{\partial t} + \frac{\partial \vec{x}}{\partial t} \cdot \bigtriangledown \phi = \frac{\partial \phi}{\partial t} + V_N |\bigtriangledown \phi| = 0 \tag{3.27}$$

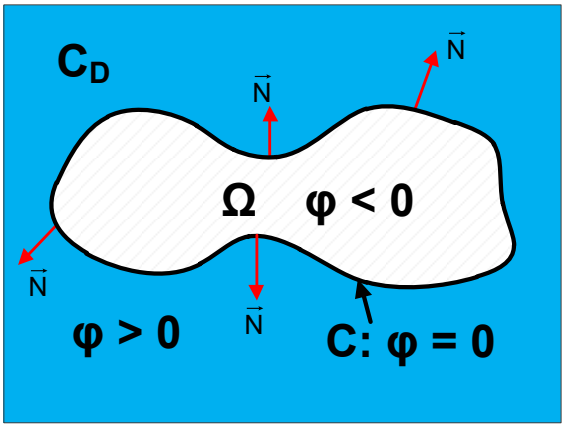

(a)

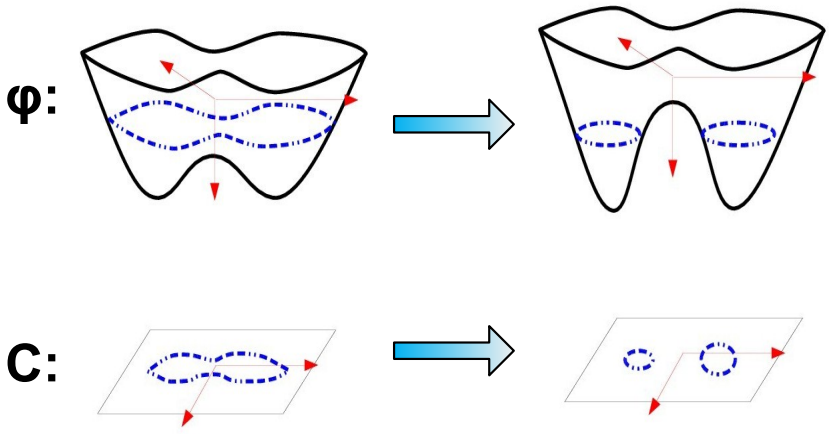

(b)

Figure 3.17: Illustration of the principle of level set: (a) shape representation; (b) shape deformation

For this partial differential equation, one can apply finite difference approximation to evolve the level set function ϕ on a Cartesian grid. A simple first order forward Euler method for the time discretization is applied:

$$\phi^{m+1} = \phi^m - \triangle t V_N | \bigtriangledown \phi | \tag{3.28}$$

where $\phi^m = \phi^{t^m}$ and $\phi^{m+1} = \phi^{t^{m+1}}$ represent the level set function at time t^m and t^{m+1}, respectively, and $\triangle t = t^{m+1} - t^m$ is the time step.

Because the numerical approximations produce errors proportional to the size of the Cartesian grid, i.e. $\triangle x$ or $(\triangle x)^n$, it is necessary to make the level set function as smooth as possible to obtain accurate estimates. Moreover, as can be seen in Eq. (3.26) the definition of normal vector $\vec{N}$ and curvature K, either too steep or flat gradient $\bigtriangledown \phi$ should be avoided, which requires again a smooth ϕ. A signed distance function is widely chosen to represent the level set function:

$$\phi(\vec{x}) = \begin{cases} -min(|\vec{x} - \vec{x_C}|) & \text{if } \vec{x} \in \Omega \\ 0 & \text{if } \vec{x} \in C \\ min(|\vec{x} - \vec{x_C}|) & \text{if } \vec{x} \notin \Omega \end{cases} \tag{3.29}$$

where $\vec{x_C}$ includes all points on the boundary C. This function satisfy that $\phi(\vec{x})$ is zero on the boundary, negative inside and positive outside. In addition, it is smooth enough because $min(|\vec{x} - \vec{x_C}|)$ is in fact Euclidean distance with gradient $|\bigtriangledown \phi| = 1$.

In general, only a viscosity solution can be founded for Eq. (3.28). This will result in jumps or singularities in spatial derivatives. Therefore, sophisticated numerical techniques should be considered for different situations depending on the order of the partial difference. If the velocity is given from the curvature K, Eq. (3.28) becomes a second-order partial differential equation. Therefore, the choice of the numerical schemes for the spatial derivatives $\bigtriangledown \phi$ depends on the type of the evolution velocity. Besides, the time step $\triangle t$ plays an important role for reaching a stable solution and the choice of time step is related to the form of the velocity as well. Therefore, in the next section, we will present different types of evolution velocity and corresponding choices for the time step as well as the numerical techniques for the spatial derivatives.

3.2.4 Evolution velocity

Generally, depending on the application, there are 3 different types of velocity function:

- External velocity An external evolution velocity is given from the external physical principles, such as the advection for computational fluid dynamics problems [73, 74, 75, 77]. As introduced by Sussman [73], using the level set method,

the zero-level isocontour of ϕ represents the boundary between two immiscible and incompressible fluids, such as water and air. The velocity is calculated by using the two-phase Navier-Stoker equation:

$$\begin{aligned} \rho_l \tfrac{\partial V_l}{\partial t} &= - \bigtriangledown p_l + 2\mu_l \bigtriangledown \cdot \varrho_l + \rho_l a, \qquad \bigtriangledown \cdot V_l = 0, \quad \vec{x} \in liquid \\ \rho_g \tfrac{\partial V_g}{\partial t} &= - \bigtriangledown p_g + 2\mu_g \bigtriangledown \cdot \varrho_g + \rho_g a, \qquad \bigtriangledown \cdot V_g = 0, \quad \vec{x} \in gas \end{aligned} \tag{3.30}$$

where ρ is the density, V the velocity, p the pressure, μ the viscosity of the fluid, ϱ the rate of deformation tensor, and a the gravity acceleration. The subscripts l and g denote the liquid and the gas phase, respectively.

The boundary C between the two phases satisfies the following condition:

$$(2\mu_l \varrho_l - 2\mu_g \varrho_g) \cdot \vec{N} = (\rho_l \rho_g + \sigma K) \cdot \vec{N} \qquad and \qquad V_l = V_g, \quad \vec{x} \in C \tag{3.31}$$

where $\vec{N}$ is the unit outwards normal direction vector and K the curvature defined in Eq. (3.26), and σ is the coefficient of surface tension.

Combining Eq. (3.30) and Eq. (3.31), we express the equation on the whole domain D including both the liquid and the gas fluid:

$$\rho \frac{\partial V}{\partial t} = - \bigtriangledown p + \bigtriangledown \cdot (2\mu\varrho) - \sigma K \delta(d) \vec{N} + \rho a, \quad \bigtriangledown \cdot V = 0, \qquad \vec{x} \in D \tag{3.32}$$

where δ is the Dirac function and d a signed distance function that has similar definition as Eq. (3.29). Then the evolution velocity V for the whole domain can be obtained by solving this equation.

With the external velocity, the level set equation Eq. (3.28) involves only the first order derivatives of ϕ and it is hyperbolic and linear. Hence the simple upwind differencing (or upwinding) schemes for the spatial derivatives are used:

$$\begin{aligned} \phi_{ijk}^{m+1} \quad = \quad & \phi_{ijk}^{m} - \triangle t [max(u_{ijk}^{m}, 0) D_{ijk}^{-x} + min(u_{ijk}^{m}, 0) D_{ijk}^{+x} + \\ & max(v_{ijk}^{m}, 0) D_{ijk}^{-y} + min(v_{ijk}^{m}, 0) D_{ijk}^{+y} + \\ & max(w_{ijk}^{m}, 0) D_{ijk}^{-z} + min(w_{ijk}^{m}, 0) D_{ijk}^{+z}] \end{aligned} \tag{3.33}$$

where $(u_{ijk}^{m}, v_{ijk}^{m}, w_{ijk}^{m})$ is the external velocity at time t^m and at point (i, j, k). The operator D^+ and D^- denote the first-order forward and backward differences, respectively.

The first-order forward difference of ϕ with respect to x is given by:

$$D_{ijk}^{+x} \approx \frac{\phi_{i+1,j,k} - \phi_{i,j,k}}{\triangle x} \tag{3.34}$$

where $\triangle x$ is the discrete spatial step along the dimension x.

The first-order backward difference of ϕ with respect to x is given by:

$$D_{ijk}^{-x} \approx \frac{\phi_{i,j,k} - \phi_{i-1,j,k}}{\triangle x} \tag{3.35}$$

The forward and backward differences with respect to y and z are analog to the case of x.

As demonstrated by the upwind differencing Eq. (3.33): if $u_i < 0$, the value of ϕ moves from left to right, therefore the value at the right point $i+1$ should be considered, then D^+ is used to approximate the derivative ϕ_x; if $u_i > 0$, the value of ϕ moves from right to left, therefore the value at the left point $i-1$ should be considered, then D^- is used to approximate the derivative ϕ_x. This scheme produces errors of $O(\triangle x)$.

For the convergence and the stability while numerically solving the hyperbolic partial differential equations, the choice of the time step $\triangle t$ should satisfy the Courant-Friedrichs-Lewy condition (CFL condition) [89]:

$$\triangle t < \frac{\triangle x}{max|u|} \tag{3.36}$$

This implies that the numerical velocity of $\triangle x / \triangle t$ must be at least as fast as the physical velocity $|u|$.

A three-dimensional CFL condition can be expressed by:

$$\triangle t max(\frac{|u|}{\triangle x} + \frac{|v|}{\triangle y} + \frac{|w|}{\triangle z}) = \alpha \tag{3.37}$$

where $\triangle x, \triangle y$ and $\triangle z$ denote the discrete spatial step for x, y and z, respectively and $0 < \alpha < 1$.

An alternative is widely used:

$$\triangle t(\frac{max|\vec{V}|}{min\{\triangle x, \triangle y, \triangle z\}}) = \alpha \tag{3.38}$$

- Gradient-type velocity This kind of velocity uses the idea of steepest descent method. Its principle is to construct a normal velocity as a function of the negative shape gradient (or derivative) such that an objective (or cost) functional can be minimized with a sufficiently small time step. The velocity is linked to a closed-form derivative of the cost functional with respect to a perturbation of the geometry. It was firstly introduced by Santosa [84] to solve a deconvolution problem and a diffraction screen reconstruction problem. Then, it has been applied by Litman et al. [85, 90] and applied later by Ramananjaona et al. [91, 92, 93] to inverse electro-

magnetic scattering problems, and applied by Dorn et al. [87, 94] and by Ferraye et al. [95] to electromagnetic tomography.

Generally, to iteratively solve an inverse problem involving the object $\Omega \in D$, a least-square cost functional is chosen as:

$$F(\xi) = \frac{1}{2} \parallel A\xi(\Omega) - Z \parallel^2 \tag{3.39}$$

where A denotes a certain linear operator, such as the direct scattering operator, ξ a characteristic function of the object Ω and Z the given data.

The characteristic function of the object is generally piece-wise:

$$\xi(x) = \begin{cases} \xi_{int} & \text{if } x \in \Omega \\ \xi_{ext} & \text{if } x \notin \Omega \end{cases} \tag{3.40}$$

To establish the relationship between the velocity and the shape derivatives, we firstly calculate the variation of the characteristic function due to the shape deformation governed by the evolution velocity. Following Santosa's method [84], as demonstrated in Fig. 3.18, when the object moves with an infinitesimal distance δx, the point x on the boundary C (blue solid curve) will move to the new location $x' = x + \delta x$ on the new boundary C' (red dash curve). The variation of ξ occurs at the points locating in the region between x and x'. Since the boundary moves outward, the variation is $\delta\xi = \xi_{int} - \xi_{ext}$.

The inner product of $\delta\xi$ with a test function F is defined as:

$$< \delta\xi, F >= \int_{\Omega} \delta\xi(x)\overline{F(x)}dx \tag{3.41}$$

where $\overline{(\bullet)}$ is the complex conjugate operator.

Since δx is infinitesimal, the area integral can be simplified to a line integral:

$$< \delta\xi, F >= \int_{C} \overline{F(x)}(\xi_{int} - \xi_{ext})\delta x \cdot \vec{N} ds(x) \tag{3.42}$$

where $\vec{N}$ is the unit outward normal direction and $ds(x)$ the incremental arc length along the boundary C.

Combining Eq. (3.41) and Eq. (3.42), we obtain:

$$\delta\xi(x) = (\xi_{int} - \xi_{ext})\delta x \cdot \vec{N}, \qquad x \in C \tag{3.43}$$

Therefore, the derivative of ξ with respect to the time t is expressed as:

$$\xi'_t(x) = (\xi_{int} - \xi_{ext})\frac{\partial x}{\partial t} \cdot \vec{N}, \qquad x \in C \tag{3.44}$$

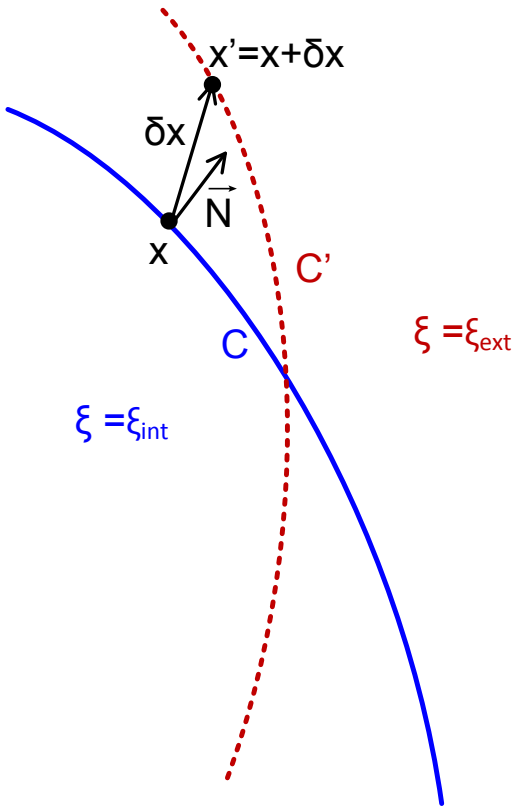

Figure 3.18: Variation of ξ due to the shape deformation.

From the expression of the evolution velocity Eq. (3.25) and the normal direction $\vec{N}$ Eq. (3.26), the variation of ξ is expressed by a term of normal velocity:

$$\xi_t'(x) = (\xi_{int} - \xi_{ext})V_N, \qquad x \in C \tag{3.45}$$

Next, the shape derivative of the function F in the direction of a perturbation $\delta\xi$ is defined by:

$$F_\xi' = ((A\xi(\Omega) - Z)^J)^*(A\xi(\Omega) - Z) \tag{3.46}$$

where the symbol $(\bullet)^*$ denotes the complex transpose operator and $(\bullet)^J$ is the Jacobian with respect to ξ.

Therefore, the shape derivative of the function F with respect to the time t is calculated by the following inner product:

$$F_t' =< [((A\xi(\Omega) - Z)^J)^*(A\xi(\Omega) - Z)], \xi_t' > \tag{3.47}$$

From Eq. (3.45), we can write the shape derivative as a function of the velocity by:

$$F_t' = \int_C ((A\xi(\Omega) - Z)^J)^*(A\xi(\Omega) - Z)\overline{\xi_{int} - \xi_{ext}}V_N ds(x) \tag{3.48}$$

where the complex conjugate operator $\overline{(\bullet)}$ can be omitted when the characteristic function has only real values, and it is always the case.

To make the cost function non-increasing, the shape derivate should be negative. Therefore, the velocity is chosen as the following form:

$$V_N(x) = -((A\xi(\Omega) - Z)^J)^*(A\xi(\Omega) - Z)(\xi_{int} - \xi_{ext}), \qquad x \in C \tag{3.49}$$

With the gradient-type velocity, the level set equation stays as a hyperbolic Hamilton equation. Following [85], the numerical approximation for the spatial gradient $\bigtriangledown\phi$ depends on the sign of the velocity.

If $V_{ijk} \geq 0$, the approximation of $|\bigtriangledown\phi|$ is given from:

$$\begin{aligned} |\bigtriangledown\phi_{ijk}|^2 &= max(D_{ijk}^{-x}, 0)^2 + min(D_{ijk}^{+x}, 0)^2 + max(D_{ijk}^{-y}, 0)^2 + \\ &\quad min(D_{ijk}^{+y}, 0)^2 + max(D_{ijk}^{-z}, 0)^2 + min(D_{ijk}^{+z}, 0)^2 \end{aligned} \tag{3.50}$$

If $V_{ijk} < 0$, the approximation of $|\bigtriangledown\phi|$ is given from:

$$\begin{aligned} |\bigtriangledown\phi_{ijk}|^2 &= min(D_{ijk}^{-x}, 0)^2 + max(D_{ijk}^{+x}, 0)^2 + min(D_{ijk}^{-y}, 0)^2 + \\ &\quad max(D_{ijk}^{+y}, 0)^2 + min(D_{ijk}^{-z}, 0)^2 + max(D_{ijk}^{+z}, 0)^2 \end{aligned} \tag{3.51}$$

where the operators D^+ and D^- denote the first-order forward and backward differences given by Eq. (3.34) and Eq. (3.35), respectively.

In the level set equation Eq. (3.28), the velocity V_N is defined in the whole computational domain. However, the gradient-type velocity which decreases the cost functional is defined only on the boundary. Therefore, it is necessary to expand the velocity to the whole domain. A natural choice of the velocity extension can be given as:

$$\tilde{V}_p = \begin{cases} V_p & \text{if } p \in C \\ V_q & \text{if } p \notin C \end{cases} \tag{3.52}$$

This implies that: for a point p belonging to the boundary C, its velocity stays the same as defined by Eq. (3.49); for a point p lying inside or outside the boundary C, its velocity is assigned as the same as the point q which is a boundary point and is the closest to p.

For this gradient-type velocity, the time step $\triangle t$ should also satisfy the CLF condition given Eq. (3.38).

- Mean curvature-dependence velocity This kind of velocity is used in active contour models (or snakes) for image segmentation and edge detection problems [96, 80, 78, 79]. The basic idea in active contour models (or snakes) is to evolve a

curve, subject to constraints from a given image I_0, in order to detect objects in that image. Starting with an initial curve around the object to be detected, the curve then moves normal to itself and stops at the boundary of the object. An edge detector depending on the gradient of the image I_0 is used to stop the curve at the boundary of the object in classical snake models [97].

A gray-scale image $I_0(x, y)$ maps the domain $x, y \in [0, 1]$ into R, with I_0 of discrete values between 0 and 255. A curve $L(I)$ is parameterized as a function of this image. To detect an object in this image, the snake model is to minimize

$$F_1(L) = \alpha \int_0^1 |L'(s)|^2 ds + \beta \int_0^1 |L"(s)| ds - \lambda \int_0^1 | \bigtriangledown I_0(L(s))|^2 ds \tag{3.53}$$

where α, β and λ are positive coefficients. The former two terms control the smoothness of the curve, while the third one evolves the contour toward the object in the image. The third term should arrive at a minimum value when the curve locates at the object boundary, where the gradient $| \bigtriangledown I_0|$ achieves a maximum value. This behaves as an edge indicator.

A typical choice of the edge indicator depending on the gradient of image $|\bigtriangledown I_0|$ is given as:

$$g(\bigtriangledown I_0) = \frac{1}{1 + |J * \bigtriangledown I_0|^p} \tag{3.54}$$

for $p \geq 1$, where J is a Gaussian of variance σ.

Following the work of Caselles et al. in [80], a simplified version of snake model is defined as an integral of the edge indicator function over the curve L:

$$F_2(L) = \int_0^1 g(\bigtriangledown I_0(s)) L'(s) ds \tag{3.55}$$

In order to minimize this snake model, gradient descent method is considered. Then the curve evolution equation is obtained by the following equation:

$$\frac{\partial L(t)}{\partial t} = -g(\bigtriangledown I_0) K \bar{N} - (\bigtriangledown g(\bigtriangledown I_0) \cdot \bar{N}) \bar{N} \tag{3.56}$$

where K is the curvature and $\bar{N}$ is the unit outward normal. The right hand side of the equation is given by the Euler-Lagrange of Eq. (3.55) as derived in [80].

L is the parameterized curve, therefore, using the shape representation in level set method, it can be represented as the zero-level of the level set function ϕ. Then, the snake curve evolution equation Eq. (3.56) can be naturally expressed in term of the level set function ϕ. This is firstly done by Caselles et al. in [96].

The level set equation for this snake model is given as:

$$\frac{\partial \phi(t)}{\partial t} = -[g(\bigtriangledown I_0) K | \bigtriangledown \phi| + (\bigtriangledown g(\bigtriangledown I_0) \cdot \bigtriangledown \phi] \tag{3.57}$$

Comparing to the level set equation defined in Eq. (3.27), we get the evolution velocity in the following form:

$$V = -[g(\bigtriangledown I_0)K + \bigtriangledown g(\bigtriangledown I_0) \cdot \bar{N}] \tag{3.58}$$

In the right hand part, the first term involves a normal velocity equal to the product of the edge indicator and the curvature and the second term involves a velocity equal to the normal component of the gradient of the edge detector which is a kind of external velocity.

For the external velocity, upwind schemes are chosen for the spatial derivatives, given as before by Eq. (3.33). Now, if we only consider the curvature-dependence velocity, when ϕ is a signed distance function with gradient $\mid \bigtriangledown \phi \mid = 1$, we can have:

$$\frac{\partial \phi(t)}{\partial t} = -g(\bigtriangledown I_0)K \mid \bigtriangledown \phi \mid = -g(\bigtriangledown I_0) \bigtriangleup \phi \tag{3.59}$$

Since there is a second order derivative of ϕ, the partial differential equation is parabolic. Therefore, the upwind difference breaks, and central differencing can be used to approximate the spatial difference by:

$$\bigtriangleup \phi_{ijk} = (D^{-x}D^{+x})_{ijk} + (D^{-y}D^{+y})_{ijk} + (D^{-z}D^{+z})_{ijk} \tag{3.60}$$

with

$$(D^{-x}D^{+x})_{ijk} = \frac{\phi_{i+1,j,k} - 2\phi_{i,j,k} + \phi_{i-1,j,k}}{\bigtriangleup x^2}$$

$$(D^{-y}D^{+y})_{ijk} = \frac{\phi_{i,j+1,k} - 2\phi_{i,j,k} + \phi_{i,j-1,k}}{\bigtriangleup y^2}$$

$$(D^{-z}D^{+z})_{ijk} = \frac{\phi_{i,j,k+1} - 2\phi_{i,j,k} + \phi_{i,j,k-1}}{\bigtriangleup z^2}$$

The time step restriction for the curvature-dependence velocity is given as:

$$\bigtriangleup t\{\frac{2g(\bigtriangledown I_0)}{\bigtriangleup x^2} + \frac{2g(\bigtriangledown I_0)}{\bigtriangleup y^2} + \frac{2g(\bigtriangledown I_0)}{\bigtriangleup z^2}\} < \alpha \tag{3.61}$$

with $0 < \alpha < 1$.

Combining with the CFL condition required for the external part of velocity, the time step for the velocity in Eq. (3.58) should satisfy:

$$\triangle t(\frac{u}{\triangle x}+\frac{v}{\triangle y}+\frac{w}{\triangle z}+\frac{2g(\bigtriangledown I_0)}{\triangle x^2}+\frac{2g(\bigtriangledown I_0)}{\triangle y^2}+\frac{2g(\bigtriangledown I_0)}{\triangle z^2})<1 \tag{3.62}$$

As demonstrated before, our problem, three-dimensional imaging from profile functions, is in fact an inverse scattering problem involving object shape. In the following section, we intend to use the level set method with the gradient-type velocity to solve our problem.

3.2.5 Level set method in our case

In our case, we attempt to represent the shape of a three-dimensional object in the space R^3. Explicit shape representation is difficult to construct and extremely complicated during the shape deformation for such a dimension. The Eulerian implicit shape representation in the level set method is much easier to achieve and it keeps the object binary, which is adapted to our problem. A powerful advantage of the level set method is that it is straightforward to go from a low dimension (R^1 or R^2) to a high dimension (more than R^3).

To calculate the gradient-type velocity and according to the formalized equation for our problem in Eq. (3.1), we define a least-square cost function F in the matrix way:

$$F=\frac{1}{2}\sum_u \parallel G^uO-A^u \parallel^2 \tag{3.63}$$

To make it easy to read, we give again the definition for each parameter involved:

- $A^u(M,1)$, the observed data, namely the profile function along the observing direction u in the form of one dimension vector of size M (M is the number of points of the profile function);

- $O(N^3,1)$, the characteristic function of the unknown 3D object in the form of a vector in one dimension (N is the number of points of the object space along one dimension);

- $G^u(M,N^3)$, the forward observing matrix between the observed profile function, A^u, and the unknown object, O;

- u the index of the direction.

Following the gradient-type velocity given by Eq. (3.49), where ξ is the characteristic function noted O in our case, and the cost function Eq. (3.63), we have, for

points belonging to the boundary:

$$V_N = -\sum_u ((G^u O - A^u)^J)^* (G^u O - A^u)(\xi_{int} - \xi_{ext}) \tag{3.64}$$

Since the object is desired to be binary, with value 1 for points inside the boundary and 0 for points outside, then $O_{int} - O_{ext}$ is equal to 1. The Jacobian term $[(G^u O - A^u)']^*$ with respect to O is $(G^u)^T$, because G^u includes only real values. Therefore, we obtain the evolution velocity, for points belonging to the boundary:

$$V_N = -\sum_u (G^u)^T (G^u O - A^u) \tag{3.65}$$

for $u = 1, 2, 3$ as we consider only 3 observing directions in this thesis.

Corresponding to this gradient-type velocity, to calculate the spatial gradient $|\bigtriangledown \phi|$, we use the Hamilton approximations defined in Eq. (3.50) and Eq. (3.51) for a negative and a positive velocity, respectively .

Then, we have the evolution equation iteratively updating the level set function ϕ:

$$\phi^{k+1} = \phi^k + \sum_u (G^u)^T (G^u O - A^u) \bigtriangleup t |\bigtriangledown \phi| \tag{3.66}$$

where k is the index of the iteration step.

For an iterative method, certain stop rules are required. A maximum number of iterations k_{max} or a minimum tolerance ε_{tol} of the cost function (or residual) are popular choices.

Starting with an initial level set function $\phi^k = \phi^0$, the iteration process for imaging with profile functions from 3 observing directions is given as follows:

while $k \leq k_{max}$ and $F \geq \varepsilon_{tol}$,

1° Calculating the evolution velocity by Eq. (3.65);

2° Calculating the spatial gradient $|\bigtriangledown \phi|$ by Eq. (3.50) and Eq. (3.51) according to the sign of the velocity obtained in 1°;

3° Updating the level set function ϕ^{k+1} by Eq. (3.66);

4° Determining the object by selecting the points with non-positive values of ϕ;

Now, we use the numerical results of the sphere of diameter $D = 10$ cm (Fig. 2.4) to illustrate this iterative process. To show the performance in arbitrary directions, we choose 2 sets of observing directions: 3 mutually orthogonal directions $[u_1(90°, 0°),\ u_2(90°, 90°),\ u_3(0°, 0°)]$ and 2 orthogonal directions plus

1 non-orthogonal direction $[u_1(90°, 30°),\ u_2(90°, 90°),\ u_3(0°, 0°)]$. The two sets of observing directions, noted as '3ortho' and '2ortho+1arb' are presented respectively in Fig. 3.19 (a) and (b). We choose the computational domain C_D around the object in order to reduce the computation cost. It is a three-dimensional cubic domain of dimension $d_{C_D} = 1.5 \times D$, equal to 1.5 times the object maximum dimension D, and we divide it into $N^3 = 32^3$ cells, with each cell of same discrete step $\triangle x = \triangle y = \triangle z = \triangle u = d_{C_D}/N$ along each of the 3 dimensions. Fig. 3.20 presents the numerical original sphere in the chosen computational domain with the discrete step $\triangle u$.

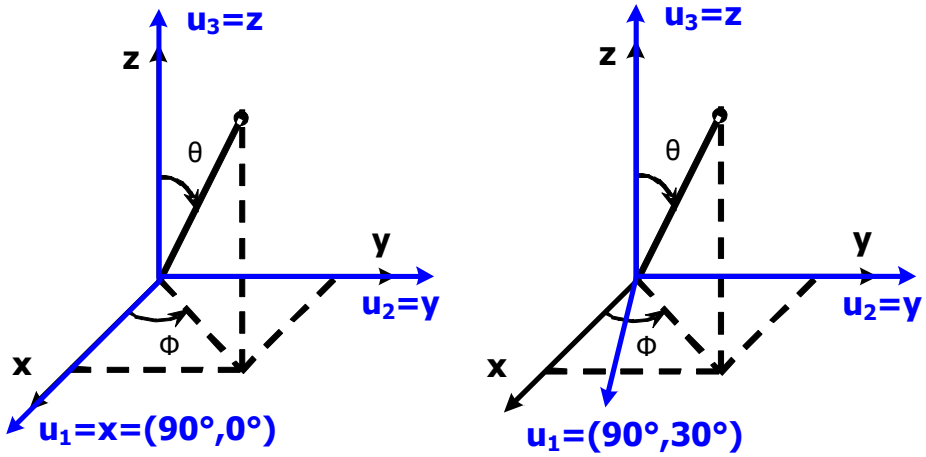

(a) (b)

Figure 3.19: Observing directions: (a) '3ortho' case with 3 mutually orthogonal directions $[u_1 = x = (90°, 0°),\ u_2 = y,\ u_3 = z]$; (b) '2ortho+1arb' case with 2 orthogonal directions plus 1 non-orthogonal direction $[u_1(90°, 30°),\ u_2 = y,\ u_3 = z]$.

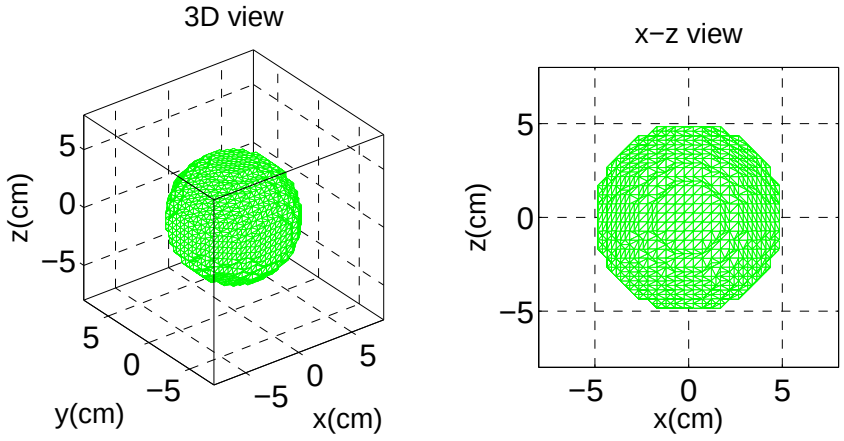

Figure 3.20: The sphere of diameter $D = 10$ cm in Fig. 2.4 in the chosen computational domain $d_{C_D} = 15$ cm with a number of points $N = 32$.

To start the iterative process, an initial estimate is required. It is somewhat arbitrary, only should be inside the computational domain. Here, we choose a small

cube of side $D = 1/4 \times d_{C_D} = 3.75$ cm centered in the computational domain, shown in Fig. 3.21. Once the initial contour is given, the initial level set function ϕ_0 is calculated by Eq. (3.29) as a signed distance between each point and the contour, negative inside and positive outside. Since the level set function ϕ of a 3D object is 4D, it is difficult to plot in the figure. Then, we choose to follow the evolution of a 2D slice, namely the middle slice of the computational domain, $S_m = S(z = 0)$, at position $z = 0$ perpendicular to z axis. Fig. 3.22 (a) and (b) show the middle slice S_m of the initial estimate and its level set function, respectively.

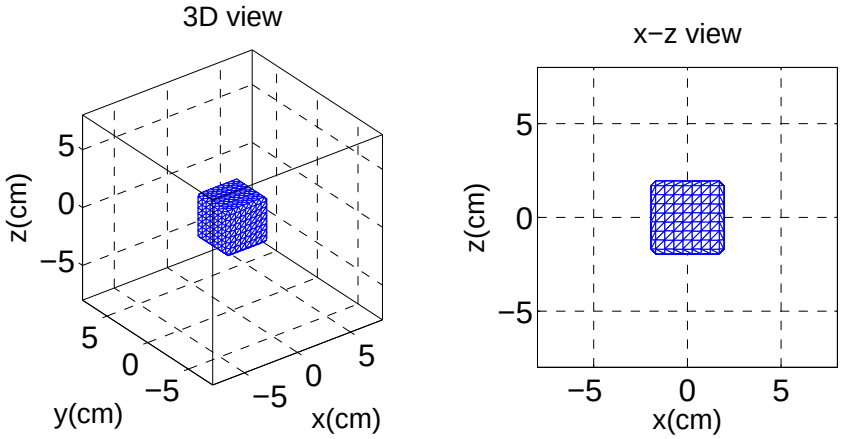

Figure 3.21: The initial estimate: a small cube of side $D = 3.75$ cm centered in the computational domain

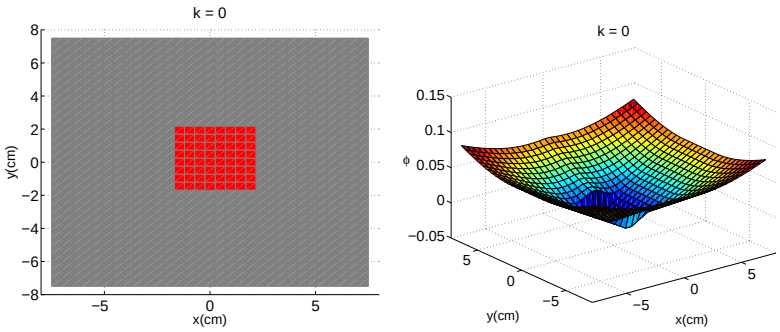

(a) (b)

Figure 3.22: (a) The middle slice of the initial estimate, $S_m = S(z = 0)$, at position $z = 0$ perpendicular to z axis; (b) the level set function ϕ for the initial middle slice S_m

Following the CFL condition given in Eq. (3.38), we choose $\alpha = 0.5$ to calculate the time step $\triangle t$ such that a relatively stable solution can be achieved.

To stop the iteration, we define a normalized residual r_k for each iteration k as follows:

$$r_k = \frac{1}{3}\sum_{u=1}^{3}\frac{\| A^u - G^u O_k \|_{L^2}}{\| A^u \|} \tag{3.67}$$

where $\| \bullet \|_{L^2}$ is the norm in Hilbert space.

We set a tolerance of the residual $\varepsilon_{tol} = 10^{-2}$ such that when $r_k \leq \varepsilon_{tol}$ is satisfied or a maximum number of iterations $k_{max} = 40$ is achieved, then the iteration stops.

Now, we consider the '3ortho' case given in Fig. 3.19 (a) with 3 mutually orthogonal directions. We track, in Fig. 3.23 (a) - (d), the evolution for the middle slice S_m of the evolving object at iteration steps $k = 5, 10, 15$ and $k_{final} = 19$, respectively. The initial curve (a small square) expands gradually into a circle located in the 'exact' position of the middle slice of the original sphere. To understand this evolution, Fig. 3.24 presents the evolution of the level set function $\phi(S_m)$ (left) and corresponding velocity (right) at steps $k = 5, 10, 15, 19$. It can be seen that the lower part of ϕ with non-positive values also gradually expands outwards, which leads to the shape deformation. This deformation behavior, expanding, is due to a positive normal velocity which decreases the shape derivatives. Similarly, a negative velocity will deform a shape by shrinking. Through the iterations, the amplitude of velocity decreases and approaches to be flat and near zero-level everywhere when the residual is less than the tolerance $\varepsilon_{tol} = 10^{-2}$ at $k_{final} = 19$. This can be considered as a sign of convergence. Fig. 3.25 presents the three-dimensional evolving (or reconstructed) object at steps $k = 5, 10, 15, 19$. Similar to the evolution of the middle slice, the object deforms gradually from a small cube to a sphere same as the original object.

Next, in the '2ortho+1arb' case given in Fig. 3.19 (b) with 2 mutually orthogonal directions plus 1 non-orthogonal direction, we track also the evolution of the object at steps $k = 5, 10, 15, 40$, since it stops at the step $k_{final} = k_{max} = 40$. The middle slice of the reconstructed object (Fig. 3.26) deforms towards the correct contour during the iterations. Fig. 3.27 presents the evolution of the level set function $\phi(S_m)$ (left) and corresponding velocity (right) at steps $k = 5, 10, 15, 40$. The non-positive part of the level set function ϕ expands gradually during the iterative process. Once again, this is due to the evolution velocity and it decreases to be a plateau after certain steps. Therefore, there is not much change between the results in iteration $k = 15$ and $k = 40$. As shown in Fig. 3.28, the three-dimensional evolving (or reconstructed) object quickly achieves a correct enough shape after iteration $k = 15$ and stays stable after.

To further evaluate the level set method, we introduce an error in pixels E_p between the reconstructed object and the original object. The example of Fig. 3.29, for a particular slice, shows that some pixels of the reconstructed object belong to the original object, the "true" pixels, P_t, while the other ones do not belong to the original object, the "false" pixels, P_f. $P_t + P_f$ is exactly the number of pixels of the reconstructed object. Next, the "missing" pixels, P_m, are pixels belonging to the initial object which are not selected in the reconstructed object. $P_t + P_m$ is exactly

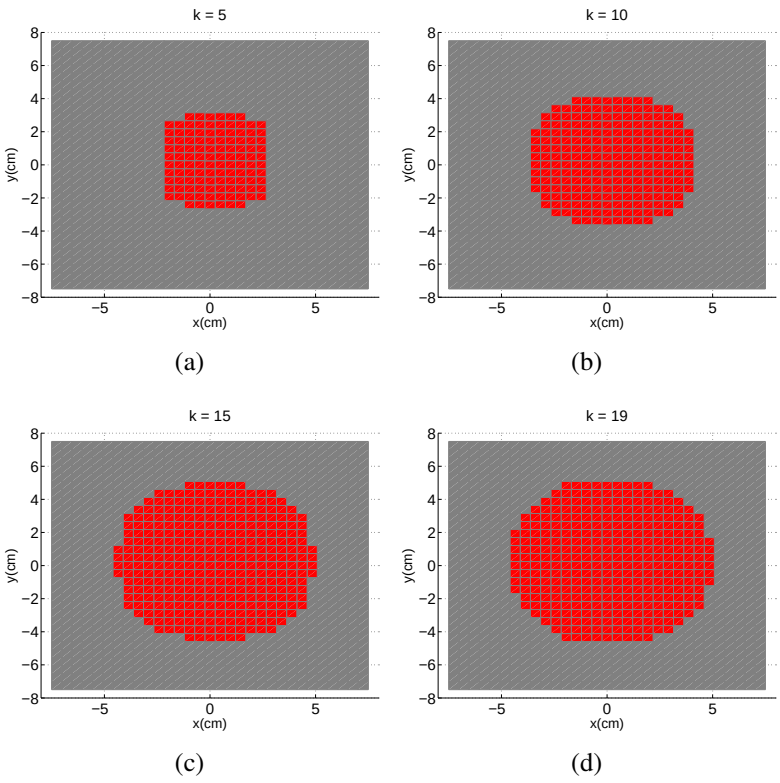

Figure 3.23: Evolution of the middle slice S_m in the '3ortho' case at iterations: (a) $k = 5$; (b) $k = 10$; (c) $k = 15$; (d) $k_{final} = 19$.

the number of pixels of the original object. Finally, the "outside" pixels, P_o, correspond to pixels which belong neither to the original object nor to the reconstructed object. The error in each slice S_j is the sum of false, $P_f(j)$, and missing, $P_m(j)$, pixels. The total error in pixels E_p is thus calculated as the sum of errors for each slice, normalized by the total number of pixels belonging to the initial object, P_{tot}.

$$E_P(\%) = 100 \times \frac{\sum_j (P_m(j) + P_f(j))}{P_{tot}} = \frac{\sum_j (P_m(j) + P_f(j))}{\sum_j (P_m(j) + P_t(j))} \tag{3.68}$$

Fig. 3.30 (a) compares the normalized residual r_k with respect to the iteration k between the '3ortho' and '2ortho+1arb' cases. The residual decreases very quickly during the first 15 iterations with almost the same speed in both cases. With 3 orthogonal directions, a residual lower than the tolerance is achieved at iteration $k = 19$, then the iteration stops. For the non-orthogonal case, the residual oscillates between $[0.01, 0.04]$, which can also be considered as convergence.

Next, we compare, in Fig. 3.30 (b), the error in pixels E_p between the '3ortho' and '2ortho+1arb' cases. It can be seen that this error decreases synchronously as the decreasing of the normalized residual. For the '3ortho' case, the error becomes negligible which shows that the object is nearly the same as the original object.

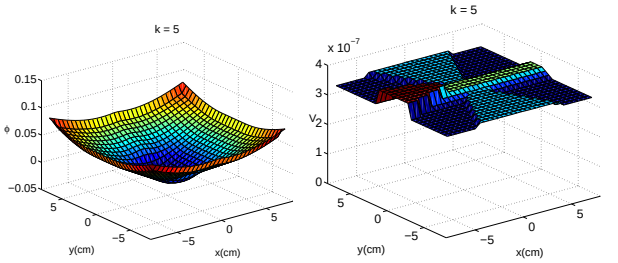

(a)

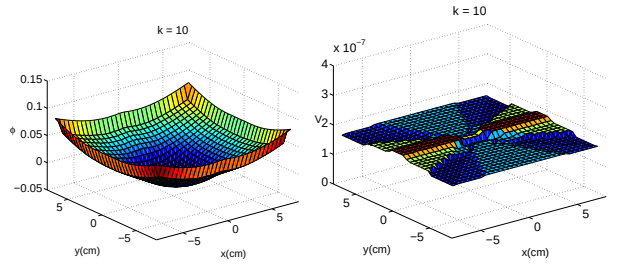

(b)

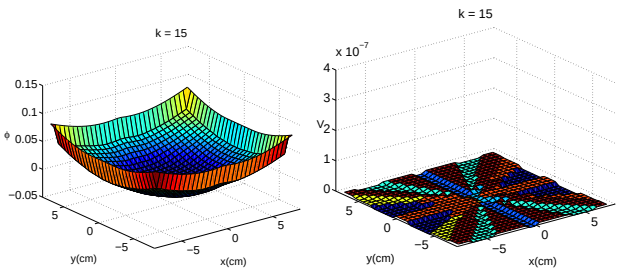

(c)

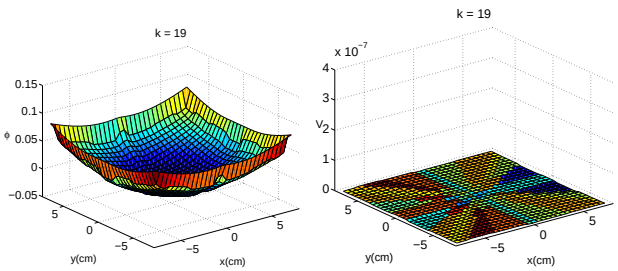

(d)

Figure 3.24: Evolution of the level set ϕ (left) and the velocity V (right), in the middle slice S_m at $z = 0$, with ordinary level set method in the '3ortho' case at iterations: (a) $k = 5$; (b) $k = 10$; (c) $k = 15$; (d) $k_{final} = 19$.

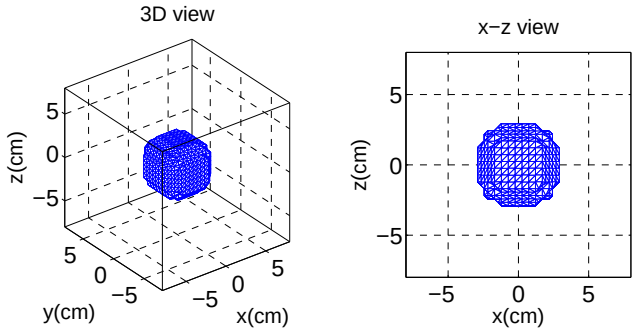

(a)

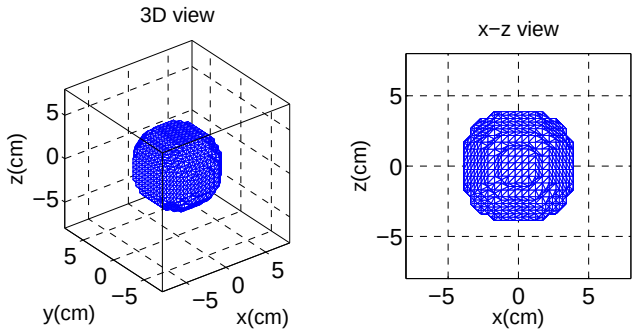

(b)

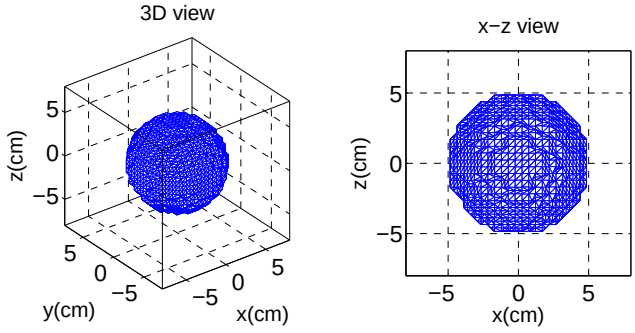

(c)

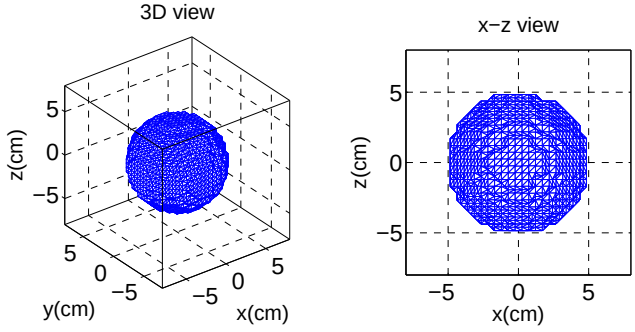

(d)

Figure 3.25: Evolution of the reconstructed 3D object in the '3ortho' case at iterations: (a) $k = 5$; (b) $k = 10$; (c) $k = 15$; (d) $k_{final} = 19$.

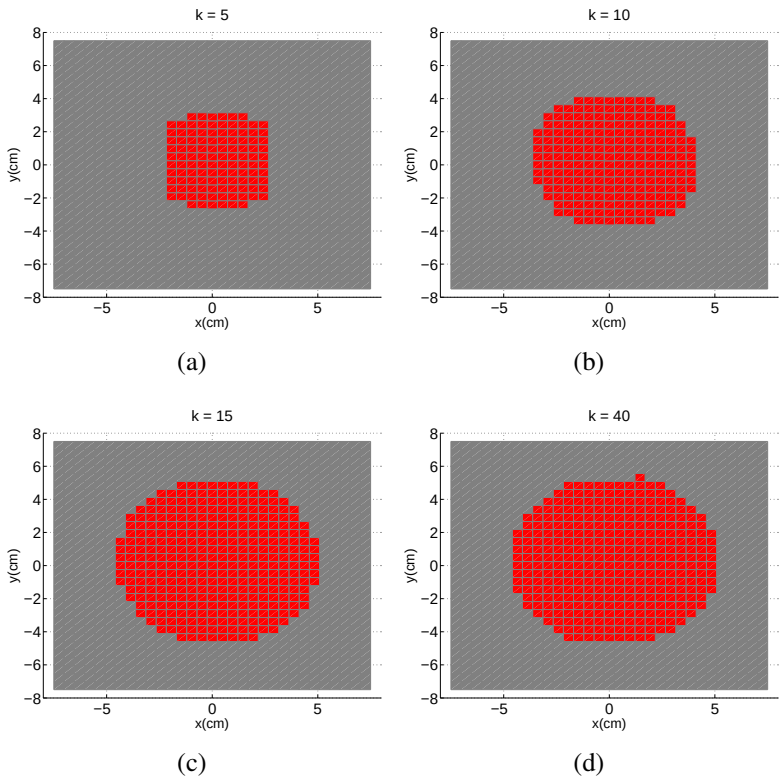

Figure 3.26: Evolution of the middle slice S_m in the '2ortho+1arb' case at iterations: (a) $k = 5$; (b) $k = 10$; (c) $k = 15$; (d) $k_{final} = 40$.

Although, for the '2ortho+1arb' case, the oscillation exists, the error is still very small and the object is accurately reconstructed as well.

All above numerical results illustrate that with profile functions from 3 observing directions, orthogonal or not, a three-dimensional sphere can be well reconstructed by using the level set method. While it also remains some difficulties during the implementation:

- Firstly, in order to have the velocity everywhere, the velocity has to be extended to the whole domain by Eq. (3.52). This is computationally expensive because, for each point, the boundary points with closest distance should be found during the iteration. This also causes numerical errors in the location of the zero level set, namely the boundary [83].

- Secondly, a complex and computationally expensive numerical finite difference scheme is required to approximate the spatial gradient of ϕ.

- Thirdly, the resolution of the reconstructed object greatly depends on the discretization parameter, i.e. N, but a large N will cause a huge amount of computational time. Because, when N increases, the above two problems become more complex.

In fact, as shown both in Fig. 3.24 and Fig. 3.27, at each iteration, the points close to the zero-level of ϕ update the most. It is wasteful to perform the calculation on the whole domain. Therefore, an efficient method is to perform the

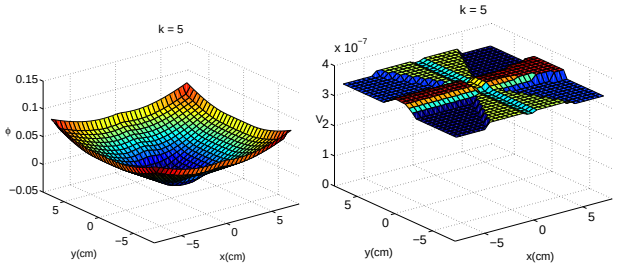

(a)

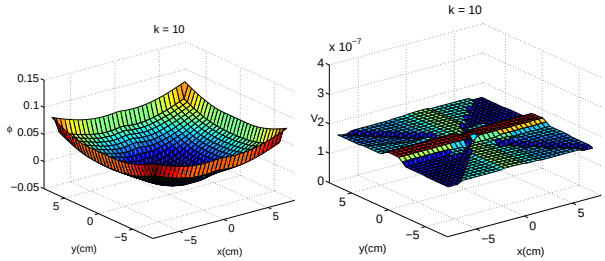

(b)

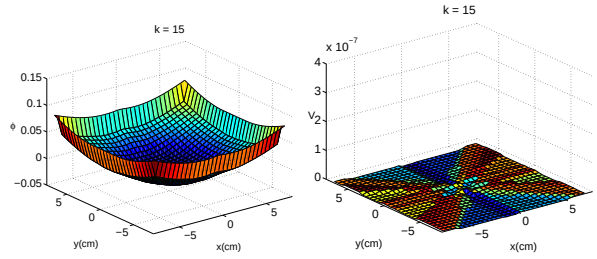

(c)

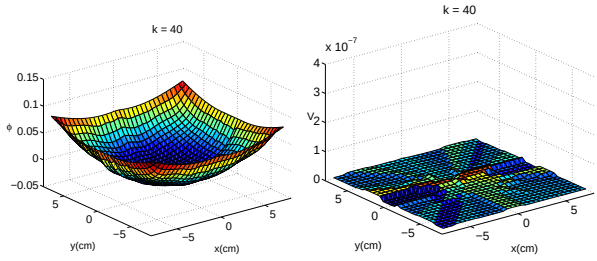

(d)

Figure 3.27: Evolution of the level set ϕ (left) and the velocity V (right), in the middle slice S_m at $z = 0$, with ordinary level set method in the '2ortho+1arb' case at iterations: (a) $k = 5$; (b) $k = 10$; (c) $k = 15$; (d) $k_{final} = 40$.

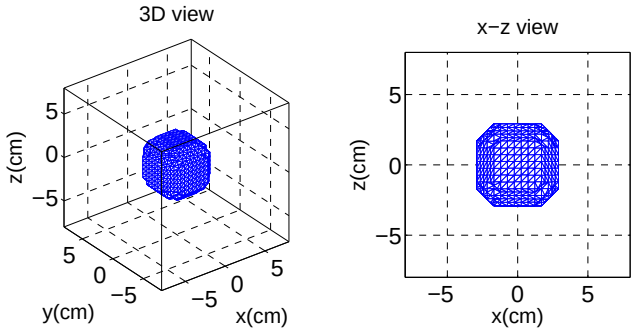

(a)

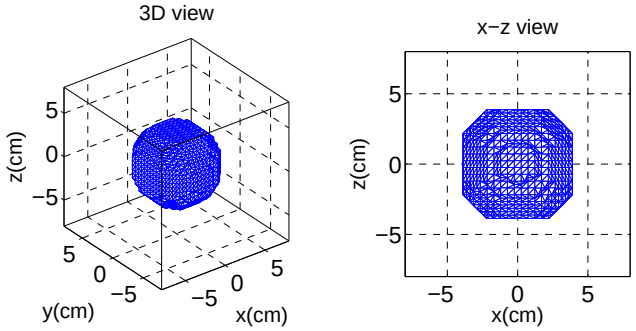

(b)

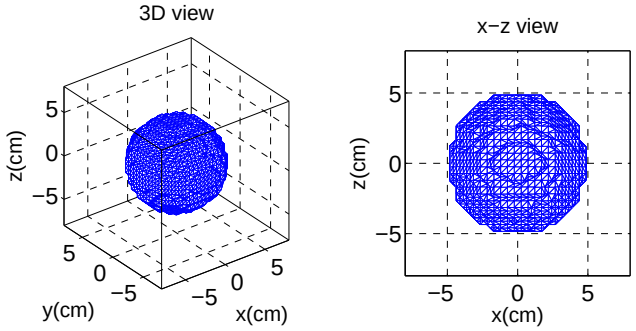

(c)

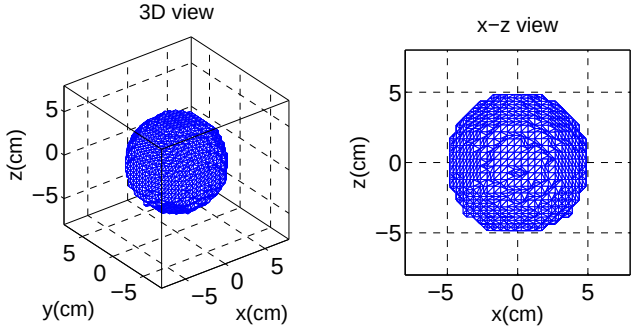

(d)

Figure 3.28: Evolution of the reconstructed 3D object in the '2ortho+1arb' case at iterations: (a) $k = 5$; (b) $k = 10$; (c) $k = 15$; (d) $k_{final} = 40$.

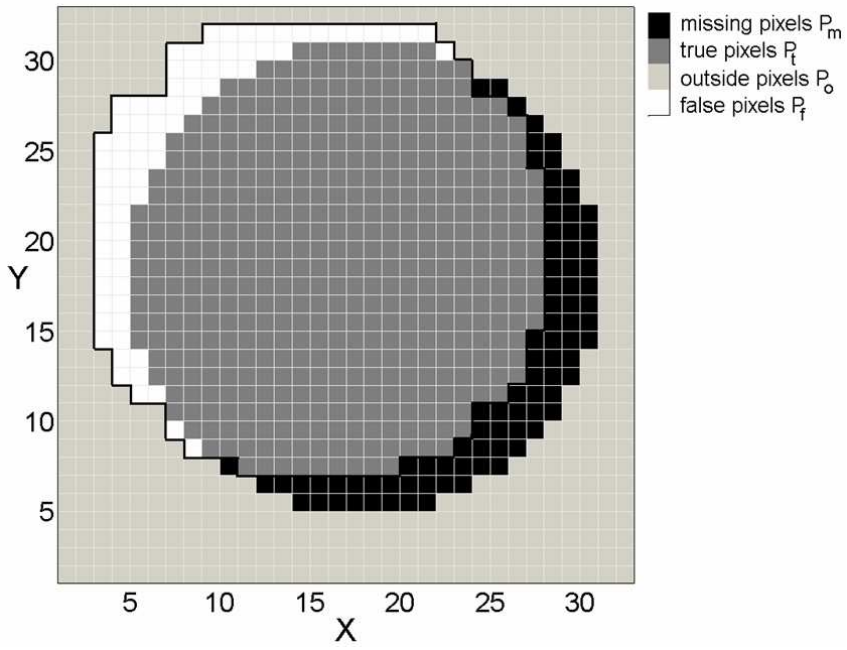

Figure 3.29: Example of the original and reconstructed objects in a slice.

evolution only on a set of neighbor points around the boundary, which is the so-called 'Narrow-band' level set method. In the following section, we introduce the principle of this method.

3.2.6 'Narrow-band' level set method

The idea to use a 'Narrow-band' was originally proposed by Chopp [98], it has been applied in shape recovering for images [78] and extensively developed by Adalsteinsson and Sethian [99]. The narrow band is constructed as an embedding of the boundary C by selecting a set of neighbor points within a finite distance to the zero-level curve or surface, then by assigning constant values to the level set function of the remaining points lying outside the narrow band. The level set evolution is performed only on this narrow band. During the evolution, the new zero-level contour of the surface (the boundary) is re-determined so that the narrow band can be updated depending on this new boundary in the same manner, then the evolution process is repeated on this new narrow band. This method is easy and operable, because the narrow band can be transformed or updated at any point in time and such an operation does not change the position of the level set so that the evolution will be unaffected by this change in the narrow band.

Fig. 3.31 gives the illustration of the construction of the narrow band. Let C be the zero-level set, namely the evolving boundary, its corresponding narrow band B_r is composed by the points lying in the region enclosed by the curves or the surfaces C^+ and C^-, where C^+ is obtained by expanding the boundary C to a curve located

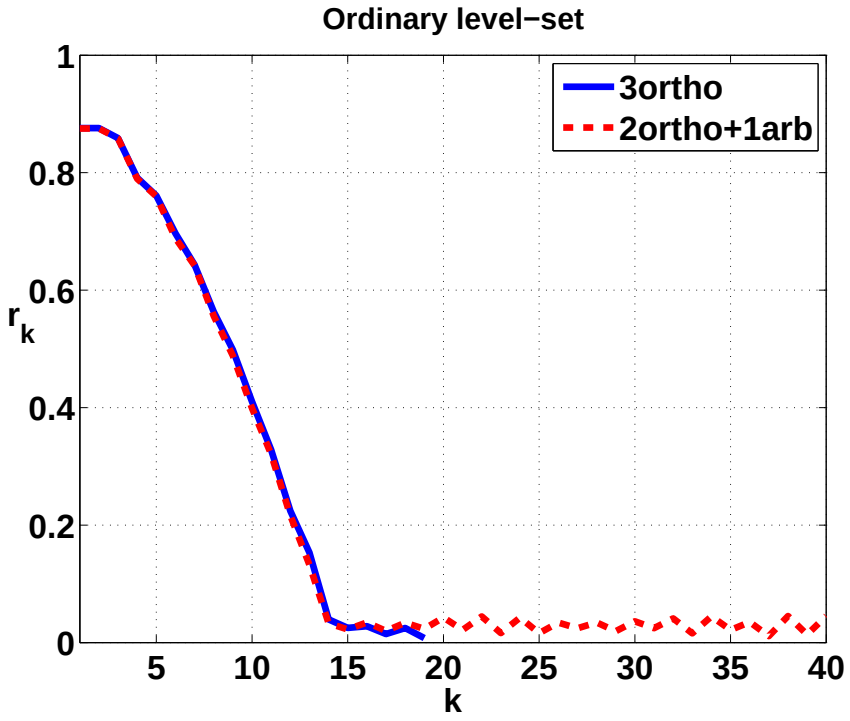

(a)

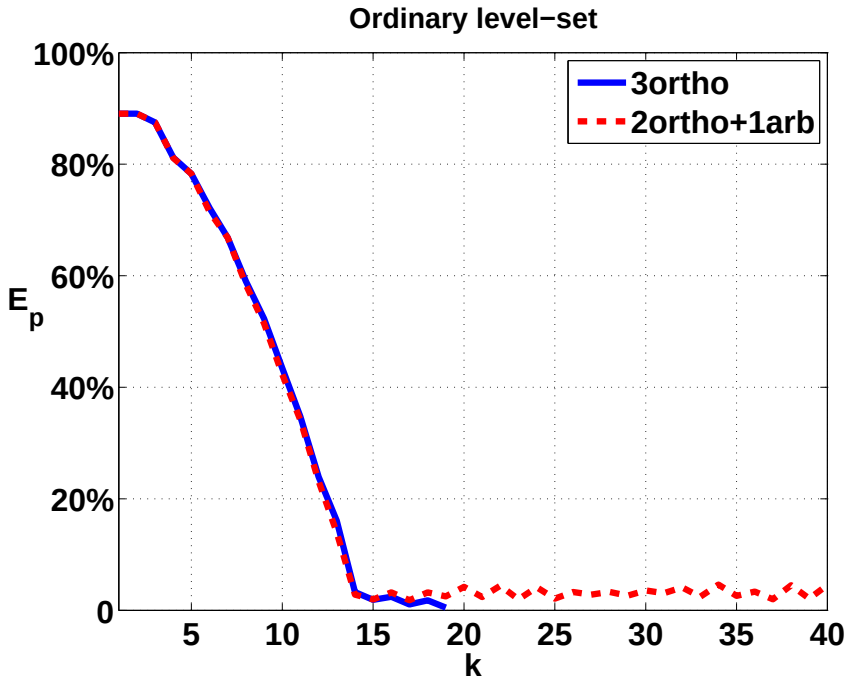

(b)

Figure 3.30: Comparison between the '3ortho' and '2ortho+1arb' cases for: (a) the normalized residual r_k with respect to the iteration k; (b) error in pixels E_p comparing to the original object

at a distance d_r and C^- is obtained by shrinking the boundary C to a curve located at a distance d_r.

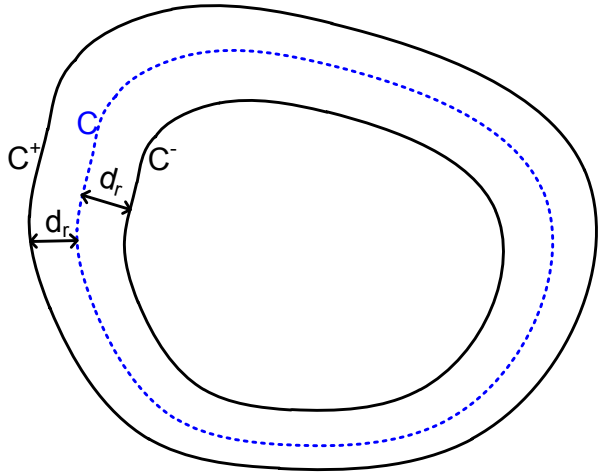

Figure 3.31: Illustration of the 'Narrow band'.

During implementation on Cartesian grids, we determine the grid points belonging to the boundary $p_C(i,j,k) \in C$ by treating them as zero-crossing points. This means that if the level set values ϕ of any pair of the points, [$p(i-1,j,k)$, $p(i+1,j,k)$], [$p(i,j-1,k)$, $p(i,j+1,k)$], [$p(i,j,k-1)$, $p(i,j,k+1)$], have opposite signs, the point $p(i,j,k)$ is considered as a boundary point. This works because the level set function is defined to be negative inside and positive outside the boundary. We construct the narrow band B_r as the union of the boundary points and their neighbor points. It can be expressed as:

$$B_r = \bigcup_{i,j,k} N^r_{i,j,k} \tag{3.69}$$

where $N^r_{i,j,k}$ is a $(2r+1)^3$ cubic block centered at the boundary points $p_C(i,j,k)$.

Starting with an initial narrow band B^0_r, the implementation of level set evolution consists the following steps:

while $k \leq k_{max}$ (where k denotes the number of the iteration) and $r_k \geq \varepsilon_{tol}$,

1° Calculating the evolution velocity by Eq. (3.65) only for points lying in the narrow band $p \in B^k_r$;

2° Calculating the spatial gradient $|\bigtriangledown \phi|$ by Eq. (3.50) and Eq. (3.51) according to the sign of the velocity, obtained in 1°, only for points lying in the narrow band $p \in B^k_r$;

3° Updating the level set function ϕ^{k+1} by Eq. (3.66) only for points lying in the narrow band $p \in B^k_r$;

4° Determining the new boundary C^{k+1} by selecting the zero-crossing points and the new narrow band B_r^{k+1} by Eq. (3.69);

5° Assigning values of ϕ for new points p_n which belong to the new boundary B_r^{k+1} but don't belong to B_r^k. The values are given by:

$$\phi_{p_n}^{k+1} = \begin{cases} +H & \text{if } \phi_{p_n}^k > 0 \\ -H & \text{if } \phi_{p_n}^k < 0 \end{cases} \tag{3.70}$$

where H is a positive constant, which can be set to $(r+1)\triangle u$, $\triangle u$ being the discrete step. This operation maintains the level set ϕ as a signed distance function.

Now, to compare with the results obtained using the ordinary level set method, we consider the same configuration: the sphere of diameter $D = 10$ cm in Fig. 2.4, the observing directions '3ortho' case and '2ortho+1arb' case presented respectively in Fig. 3.19 (a) and (b), the computational domain with $N^3 = 32^3$ cells and the initial estimate (a little cube) Fig. 3.21. Once again, to demonstrate the evolution, we choose to track the middle slice S_m at position $z = 0$ perpendicular to z axis. Fig. 3.32 (a) and (b) show the initial middle slice S_m (red pixels) and its boundary C^0 (yellow pixels), respectively. The narrow band is desired to be as narrow as possible to reduce the computational cost, however, if it is too narrow, few points evolve at each iteration and frequent re-construction of the narrow band is needed, which increases the computational cost. Fig. 3.32 (c) and (d) give the narrow band B_r^0 of the initial boundary with $r = 1$ and $r = 2$, respectively. It can be seen that the narrow band B_r is the union of the boundary (yellow pixels) and the neighbor points (green pixels) with a distance of r grids. For the following numerical results obtained using narrow band level set method, we choose $r = 2$, therefore the width of the narrow band is equal to $2r + 1 = 5$.

Firstly, for the image reconstruction in the '3ortho' case of Fig. 3.19 (a), the iteration stops at $k = 17$ when the normalized residual is zero. Therefore, we track, in Fig. 3.33 (a) - (d), the evolution of the middle slice S_m (left) and the corresponding narrow band B_2^k (right) at iterations $k = 5, 10, 15$ and $k_{final} = 17$, respectively. As the middle slice evolves towards the correct shape (a circle), the narrow band updates in the same manner. Accordingly, we present, in Fig. 3.34, the evolution of its level set function ϕ^k (left) and velocity V (right) at $k = 5, 10, 15, 17$. Unlike the ordinary level set method, ϕ updates only for the points lying in the narrow band and maintains a constant value for the remaining points outside the narrow band. This is due to the velocities for the remaining points which are equal to zero. During the evolution, the velocity of the narrow band decreases and it is zero everywhere at iteration $k_{final} = 17$, which indicates the convergence. Fig. 3.35 (a) - (d) respectively present the three-dimensional evolving (or reconstructed) object

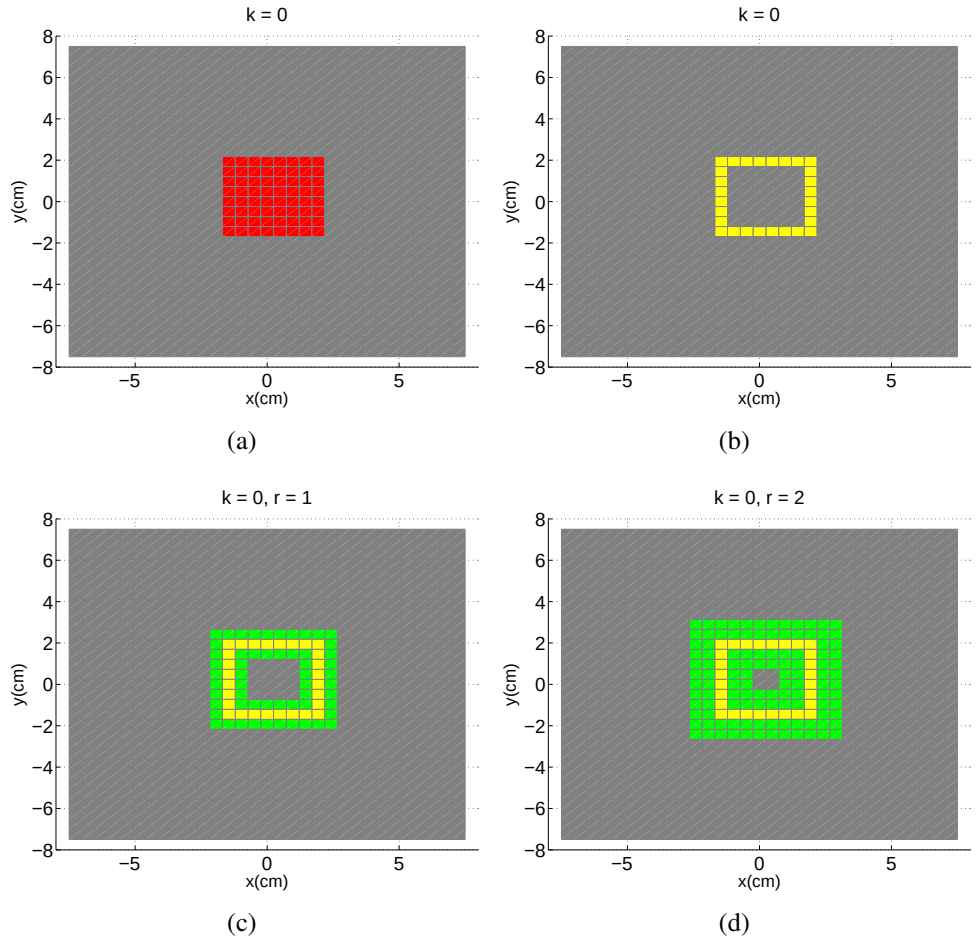

Figure 3.32: Example of narrow band for the middle slice S_m of an initial little cube in Fig. 3.22 : (a) the initial middle slice S_m (red pixels); (b) the initial boundary C^0 (yellow pixels); (c) the initial narrow band B_1^0, formed by the boundary (yellow pixels) and its neighbor points (green pixels) with $r = 1$; (d) the initial narrow band B_2^0, formed by the boundary (yellow pixels) and its neighbor points (green pixels) with $r = 2$.

at steps $k = 5, 10, 15, 17$. Similar to the evolution of the middle slice, the object deforms gradually toward a completely correct shape as the original sphere.

Next, for the image reconstruction in the '2ortho+1arb' case of Fig. 3.19 (b), the iteration stops at $k_{final} = k_{max} = 40$ with the residual $r_k = 0.01$. In the same way, we track, in Fig. 3.36 (a) - (d), the evolution of the middle slice S_m (left) and the corresponding narrow band B_2^k (right) at iterations $k = 5, 10, 15, 40$, respectively. The middle slice evolves correctly as well as its narrow band. Then, as respectively shown in Fig. 3.37 (a) - (d), the evolution of its level set function ϕ^k (left) and velocity V (right) at $k = 5, 10, 15, 40$ only deforms on the narrow band. Even if a residual lower than the tolerance is not obtained after $k = 40$ iterations, this method converges with a small velocity everywhere. The corresponding three-dimensional evolving (or reconstructed) objects are given in Fig. 3.38 (a) - (d) respectively. Although the three-dimensional images are not that smooth as the images obtained in '3ortho' case, the object is still accurately reconstructed.

Finally, we compare, respectively in Fig. 3.39 (a) and (b), the normalized residual r_k calculated by Eq. (3.67) and the error in pixels E_p defined by Eq. (3.68) between the '3ortho' and '2ortho+1arb' cases. In both cases, the residual decreases quickly and stays relatively stable when a certain small value is achieved. In the '3ortho' case, the error in pixels achieves zero at iteration $k = 17$ when the iteration stops. In the '2ortho+1arb' case, the minimum value $E_p = 1.6\%$ is obtained at iteration $k = 29$. Even if it is larger than that in the '3ortho' case, the image is accurate enough for identifying the object.

The above numerical results obtained by the narrow band level set methods imply that this method can reconstruct three-dimensional objects with geometrical profile functions from three directions (orghogonal or not).

To study the speed of the evolution, we define an average computing time T_a for each iteration by:

$$T_a = T_{tol}/k_{tol} \tag{3.71}$$

where k_{tol} and T_{tol} are the number of iterations and the total time cost (in seconds) when the evolution stops, respectively.

Table 3.4 compares, for the reconstruction of the sphere, the average computing time $T_a(s)$ in seconds (Operating environment: Hp Intel Core2 Duo CPU 3.16GHZ, win7 32bits 4G, Matlab) required by the ordinary level set method with that required by the 'Narrow band' method, both in '3ortho' and '2ortho+1arb' cases with different numbers of points ($N = 32$ or 64). When N is small, the difference of computational time is small for both the ordinary and the 'Narrow band' methods. However, when N increases, the 'Narrow band' is much faster (almost 10 times) than the ordinary level set method.

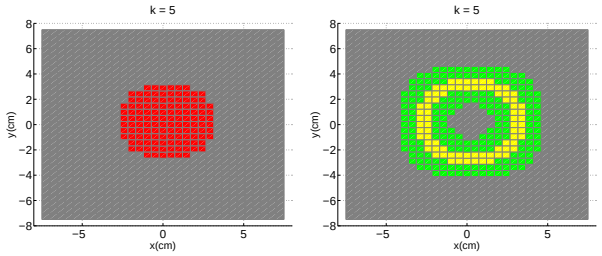

(a)

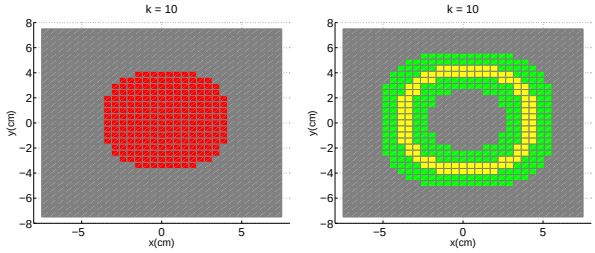

(b)

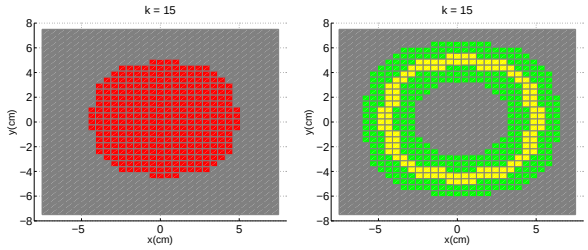

(c)

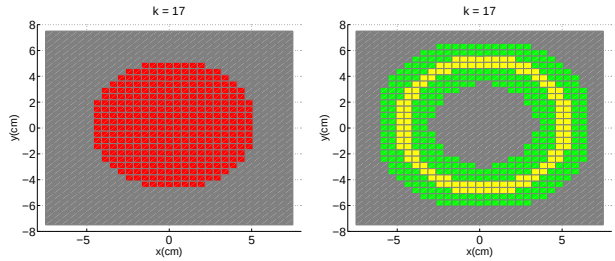

(d)

Figure 3.33: Evolution of the middle slice S_m (left) and the narrow band B_2^k (right) in the '3ortho' case at iterations: (a) $k = 5$; (b) $k = 10$; (c) $k = 15$; (d) $k_{final} = 17$.

Table 3.4: Comparison of the average computation time between the ordinary and 'Narrow band' level set methods (Operating environment: Hp Intel Core2 Duo CPU 3.16GHZ, win7 32bits 4G, Matlab).

Number of points N	Direction	$T_a(s)$ Ordinary	$T_a(s)$ Narrow band
$N = 32$	'3ortho'	8.7	6.6
	'2ortho+1arb'	8.9	6.8
$N = 64$	'3ortho'	222	23
	'2ortho+1arb'	225	23

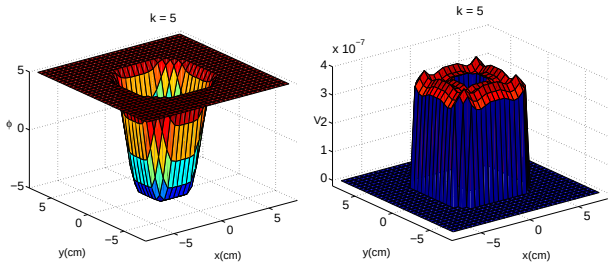

(a)

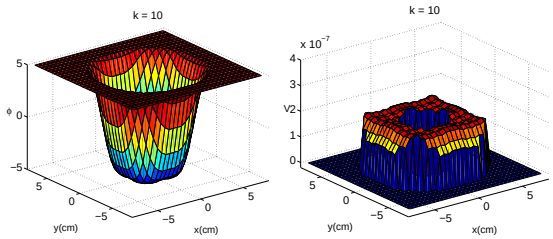

(b)

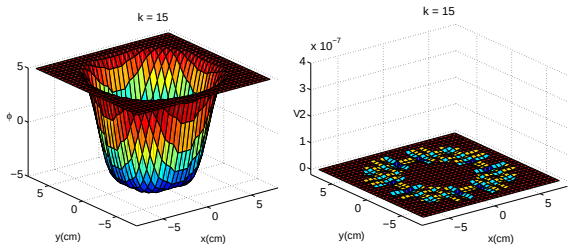

(c)

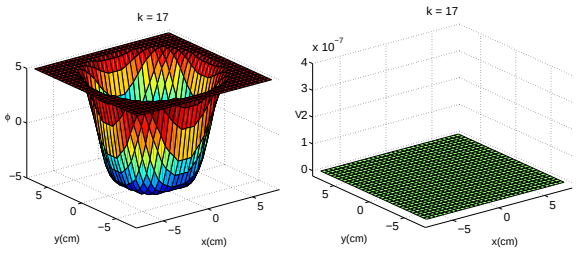

(d)

Figure 3.34: Evolution of the level set ϕ (left) and the velocity V (right), in the middle slice S_m at $z = 0$, with the 'Narrow band' method in the '3ortho' case at iterations: (a) $k = 5$; (b) $k = 10$; (c) $k = 15$; (d) $k_{final} = 17$.

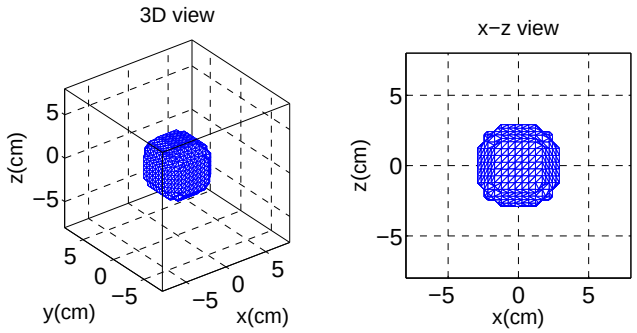

(a)

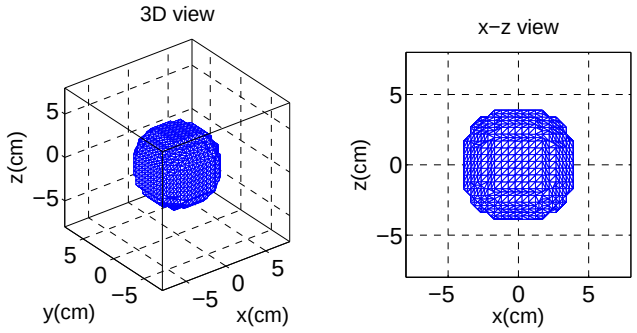

(b)

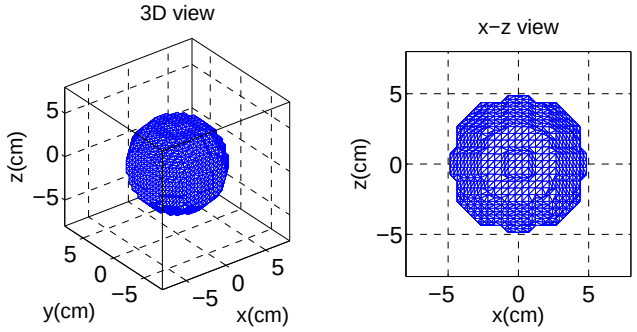

(c)

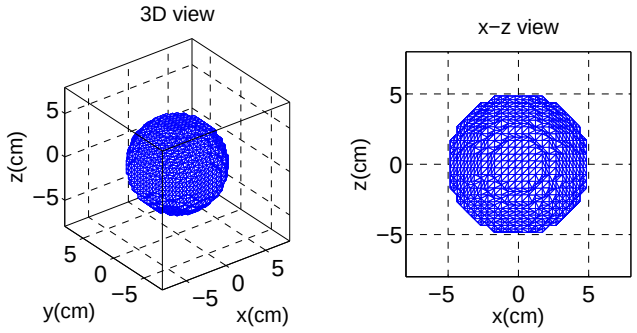

(d)

Figure 3.35: Evolution of the reconstructed 3D sphere with the 'Narrow band' method in the '3ortho' case at iterations: (a) $k = 5$; (b) $k = 10$; (c) $k = 15$; (d) $k_{final} = 17$.

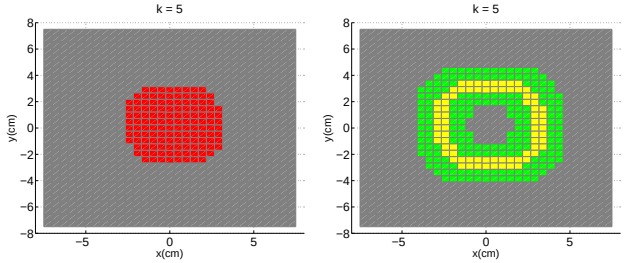

(a)

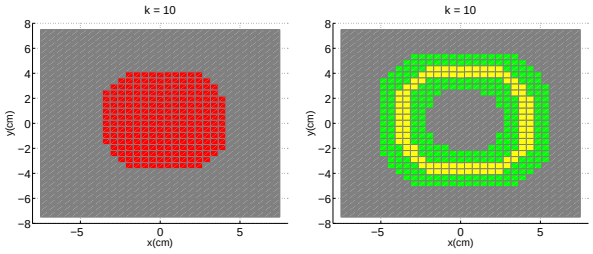

(b)

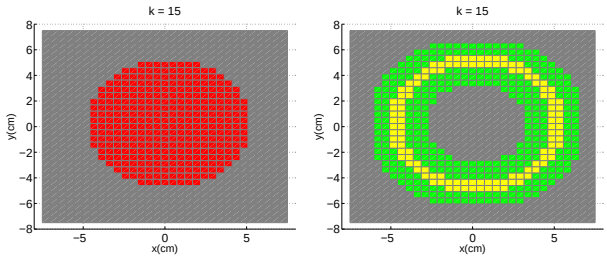

(c)

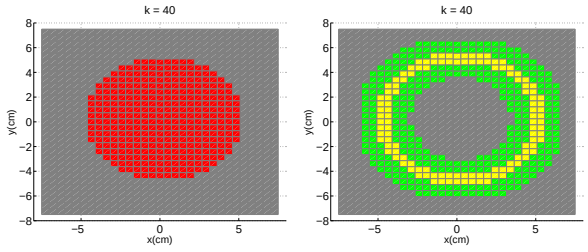

(d)

Figure 3.36: Evolution of the middle slice S_m (left) and the narrow band B_2^k (right) in the '2ortho+1arb' case at iterations: (a) $k = 5$; (b) $k = 10$; (c) $k = 15$; (d) $k_{final} = 40$.

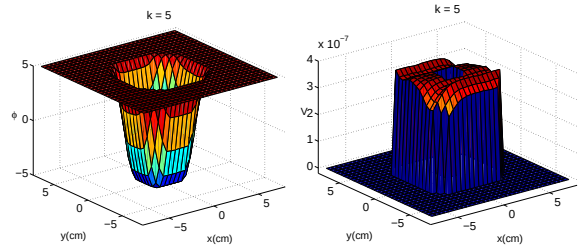

(a)

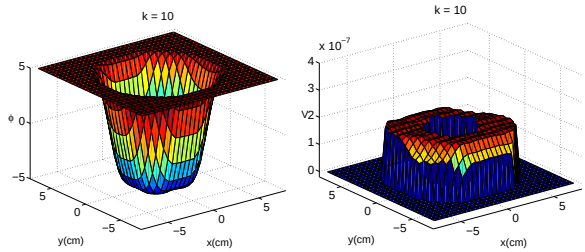

(b)

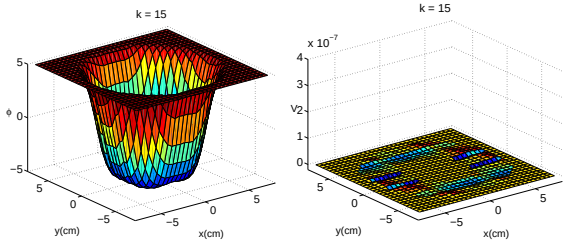

(c)

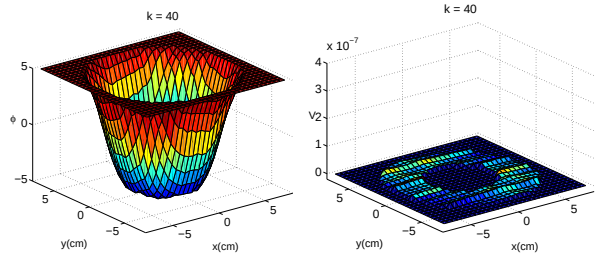

(d)

Figure 3.37: Evolution of the level set ϕ (left) and the velocity V (right), in the middle slice S_m at $z = 0$, with the 'Narrow band' method in the '2ortho+1arb' case at iterations: (a) $k = 5$; (b) $k = 10$; (c) $k = 15$; (d) $k_{final} = 40$.

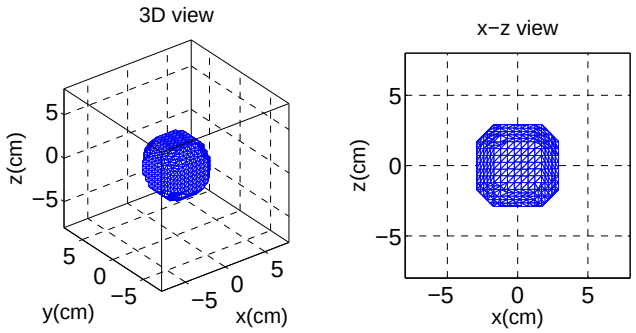

(a)

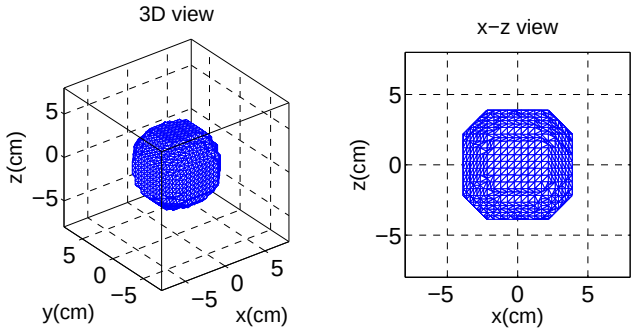

(b)

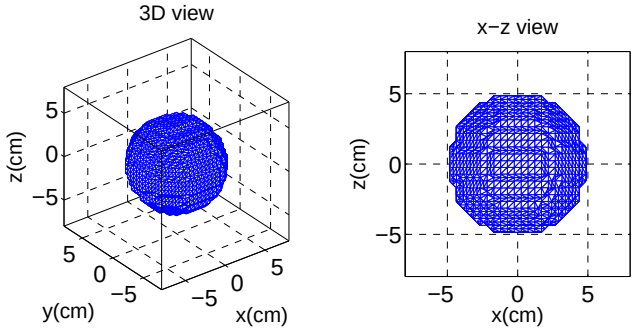

(c)

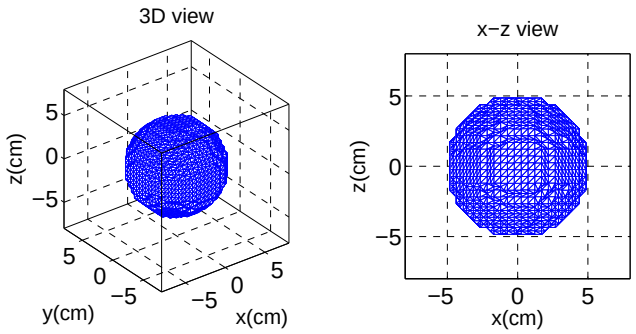

(d)

Figure 3.38: Evolution of the reconstructed 3D sphere with the 'Narrow band' method in the '2ortho+1arb' case at iterations: (a) $k = 5$; (b) $k = 10$; (c) $k = 15$; (d) $k_{final} = 40$.

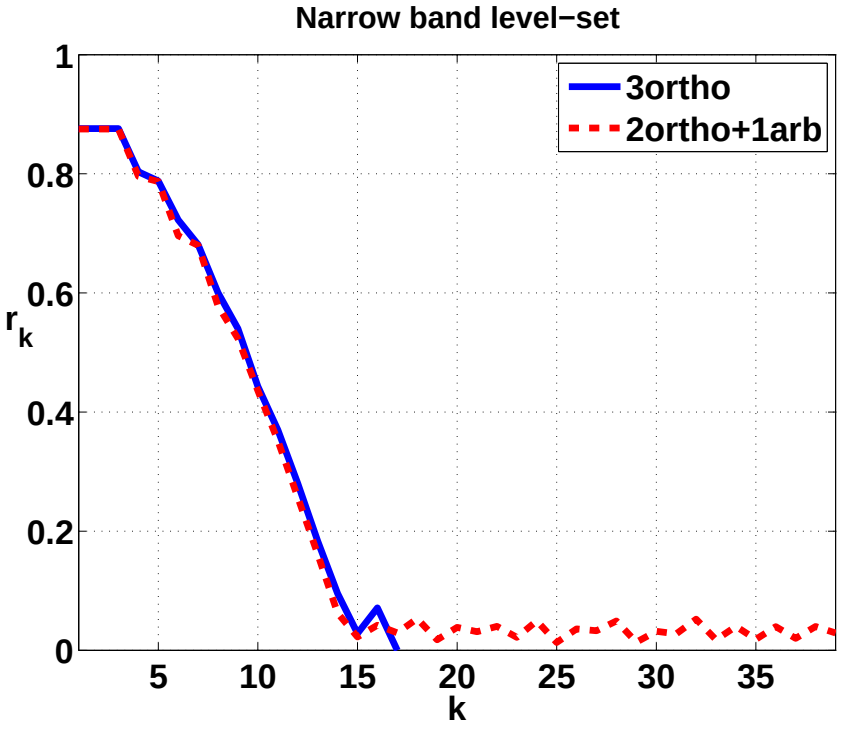

(a)

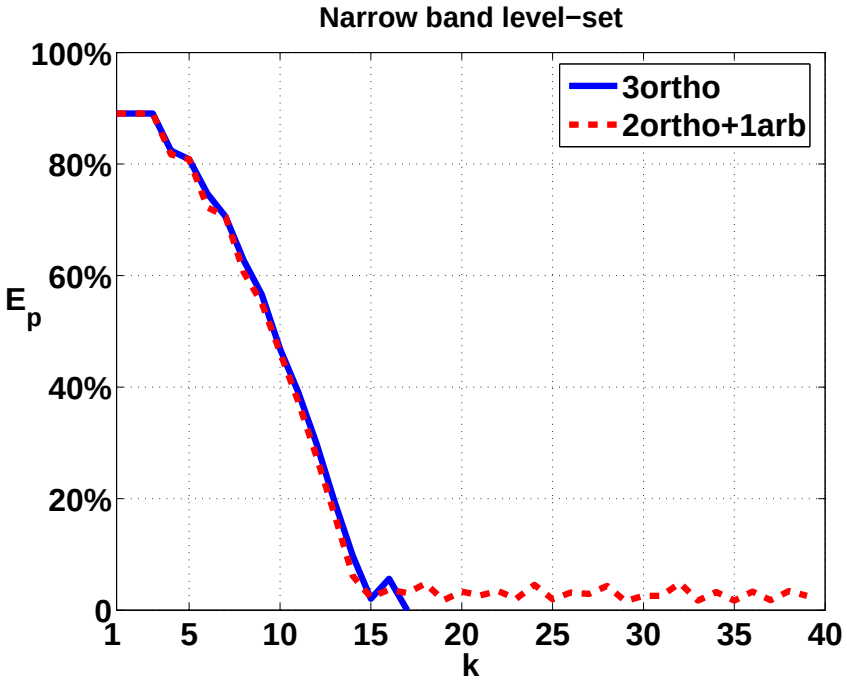

(b)

Figure 3.39: Comparison between the '3ortho' and '2ortho+1arb' cases for the sphere reconstruction with the 'Narrow band' method for: (a) the normalized residual r_k with respect to the iteration k; (b) error in pixels E_p comparing to the original object.

Therefore, to save the computational cost, in the following configurations, we choose the narrow band method for the image reconstruction from profile functions.

3.3 Reconstructed results with the 'Narrow band' level set method

In this section, we use the narrow band level set method to reconstruct the same objects than the results obtained with Chauveau's method (section 2.6): a sphere (Fig. 2.11), an asymmetric object (Fig. 2.12), an union of three cylinders of different diameters (Fig. 2.13, noted as "step-cylinder"), a non-convex object (Fig. 2.14), and two separated objects (a sphere and a cone, Fig. 2.15). For each object, we use a computational domain of dimension $d_{C_D} = 1.5 \times D$, where D is the characteristic dimension of the studied object. For the construction of the forward mapping matrix $G^u(M, N^3)$ in the direct problem and the iteration in the inverse problem, a huge amount of memory is required with a large N. Therefore, here, we choose $N^3 = 64^3$ to discretize the computational domain. To give a reference for each reconstructed object, we plot the 5 studied objects with $N^3 = 64^3$ respectively in Fig. 3.40 – Fig. 3.44. Note that, in order to put the object with the most varying characteristic information along the z axis, we clockwise rotate the non-convex object and the two separated objects with an angle of $90°$. To start the iterative process, we need an initial guess. It is somewhat arbitrary, it only has to be inside the computational domain. Therefore, we choose a small cube as the initial estimate (centered in the computational domain for a single object or a small cube for each sub-object for separated objects). To stop the iteration when an acceptable residual is achieved, we set the tolerance of the normalized residual $r_k \leq \varepsilon_{tol} = 0.01$ and a maximum number of iterations $k_{max} = 80$. To study the performance in arbitrary directions, we construct all the objects both with 3 directions orthogonal or not.

3.3.1 Reconstruction with geometrical profile functions in orthogonal case

Firstly, we consider the reconstruction in the '3ortho' case, namely 3 mutually orthogonal directions, $[u_1 = x, u_2 = y, u_3 = z]$ shown in Fig. 3.19 (a).

Sphere For the sphere (Fig. 3.40), its geometrical profile functions in the 3 mutually orthogonal directions are presented in Fig. 3.45 (a). With this observed data, as shown in Fig. 3.45 (b), the level set method reconstructs an object completely in agreement with the original sphere with a low error in pixels $E_p = 3.6\%$.

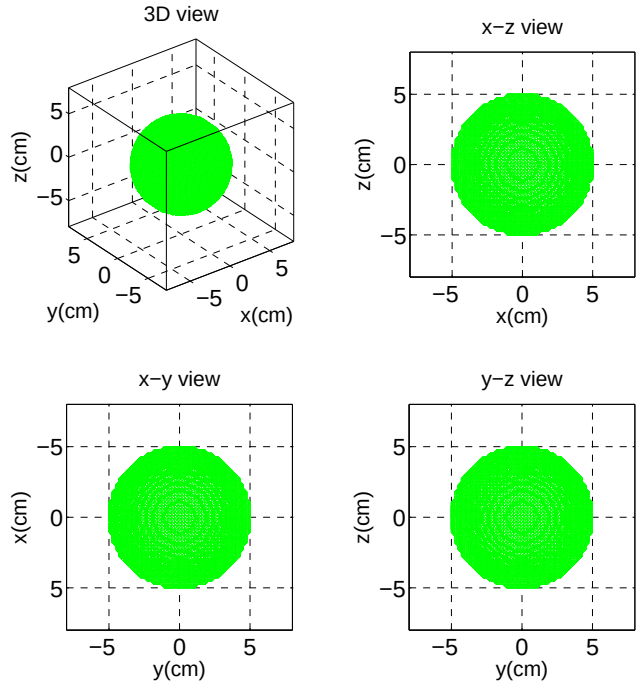

Figure 3.40: The original sphere (Fig. 2.11 (a)) with $N^3 = 64^3$.

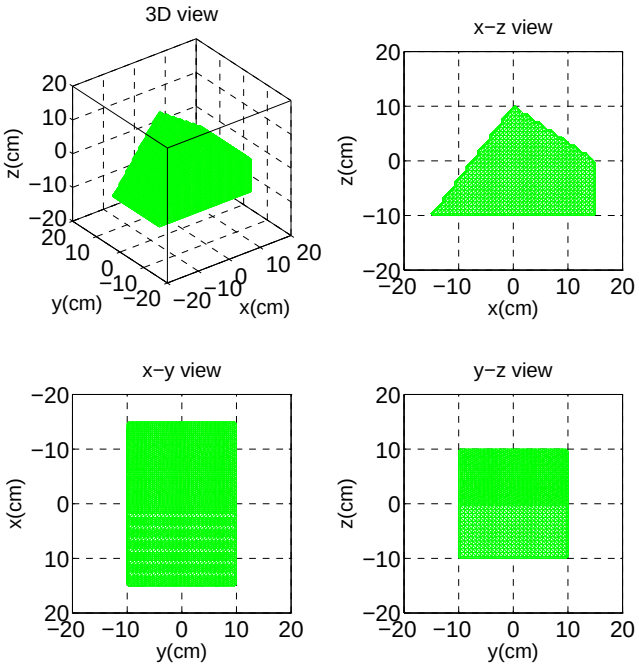

Figure 3.41: The original asymmetric object (Fig. 2.12 (a)) with $N^3 = 64^3$.

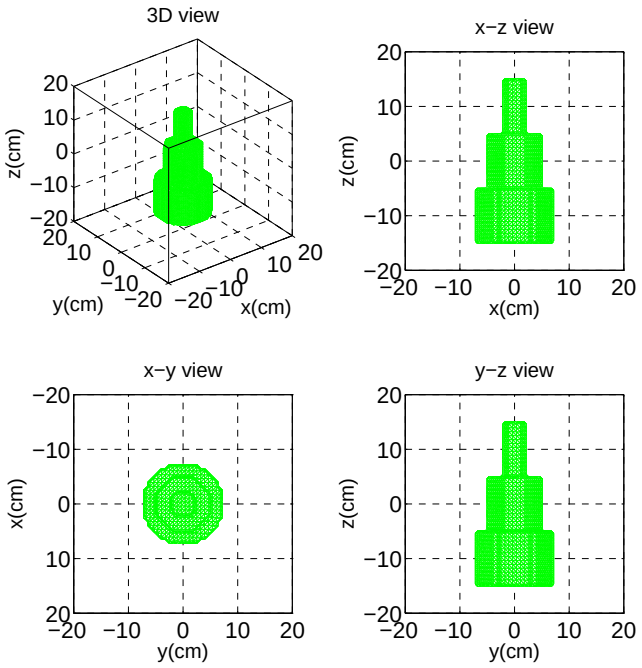

Figure 3.42: The original step-cylinder (Fig. 2.13 (a)) with $N^3 = 64^3$.

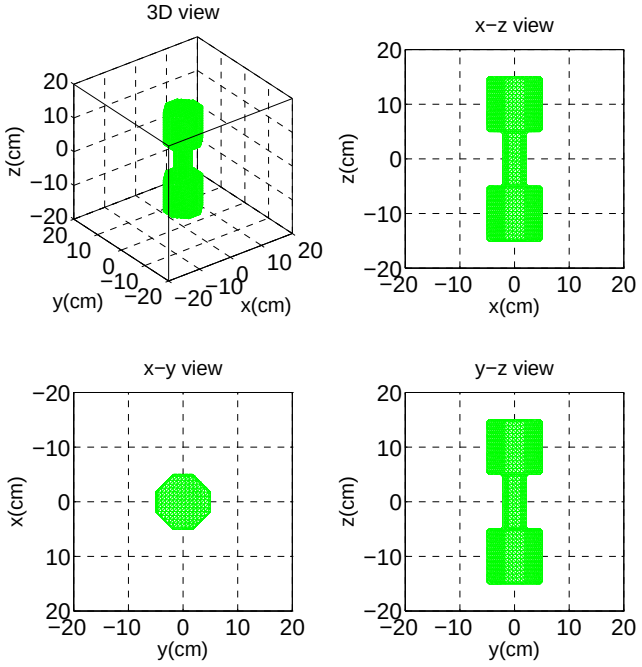

Figure 3.43: The original non-convex object (Fig. 2.14 (a) with a clockwise rotation of $90°$) with $N^3 = 64^3$.

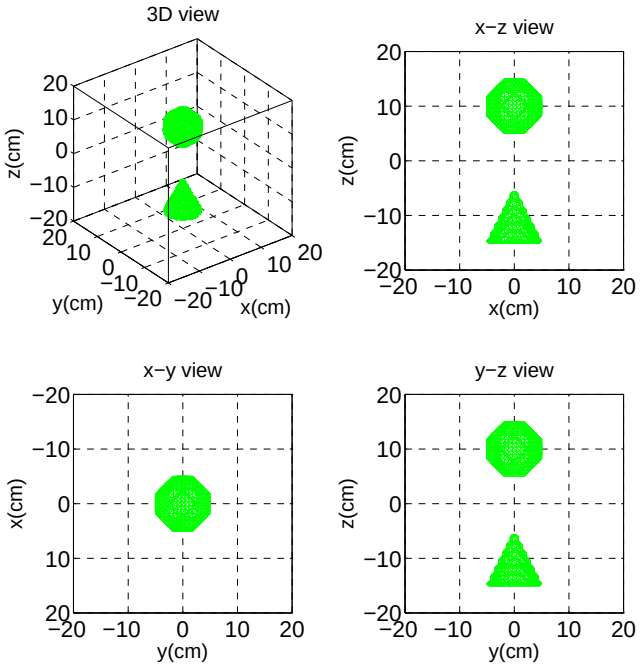

Figure 3.44: The original separated objects (Fig. 2.15 (a) with a clockwise rotation of $90°$) with $N^3 = 64^3$.

Asymmetric object For the asymmetric object (Fig. 3.41), Fig. 3.46 (a) gives its corresponding geometrical profile functions in the 3 mutually orthogonal directions. As shown in Fig. 3.46 (b), although the reconstructed object is a little rough, it is accurate enough with an error in pixels $E_p = 9.2\%$.

Step-cylinder For the step-cylinder (Fig. 3.42), its corresponding geometrical profile functions in the 3 mutually orthogonal directions are presented in Fig. 3.47 (a). Comparing to the original object, the reconstructed object, as shown in Fig. 3.47 (b), is correct with a small error in pixels $E_p = 3.5\%$.

Non-convex object For the non-convex object (Fig. 3.43), its corresponding geometrical profile functions in the 3 mutually orthogonal directions are presented in Fig. 3.48 (a). As shown in Fig. 3.48 (b), the reconstructed object is accurate with a low error in pixels $E_p = 2.7\%$.

Separated objects For the two separated objects (Fig. 3.44), their corresponding geometrical profile functions in the 3 mutually orthogonal directions are presented in Fig. 3.49 (a). As shown in Fig. 3.49 (b), the two objects are correctly reconstructed and are separated as the original objects with a small error in pixels $E_p = 4.4\%$.

The above results confirm that, in the orthogonal case, the narrow band level set method permits to reconstruct accurate three-dimensional images for various object of arbitrary shape.

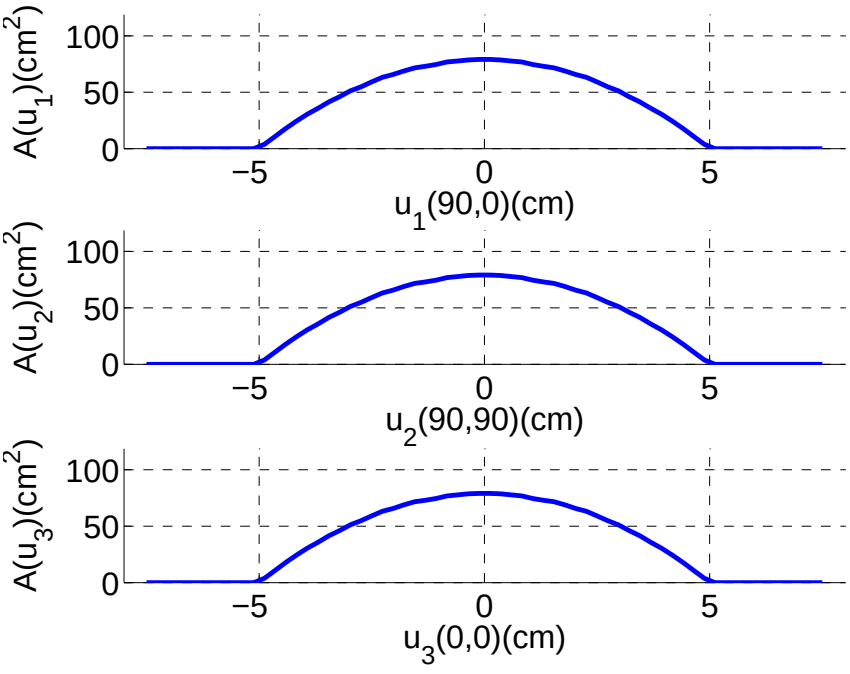

(a)

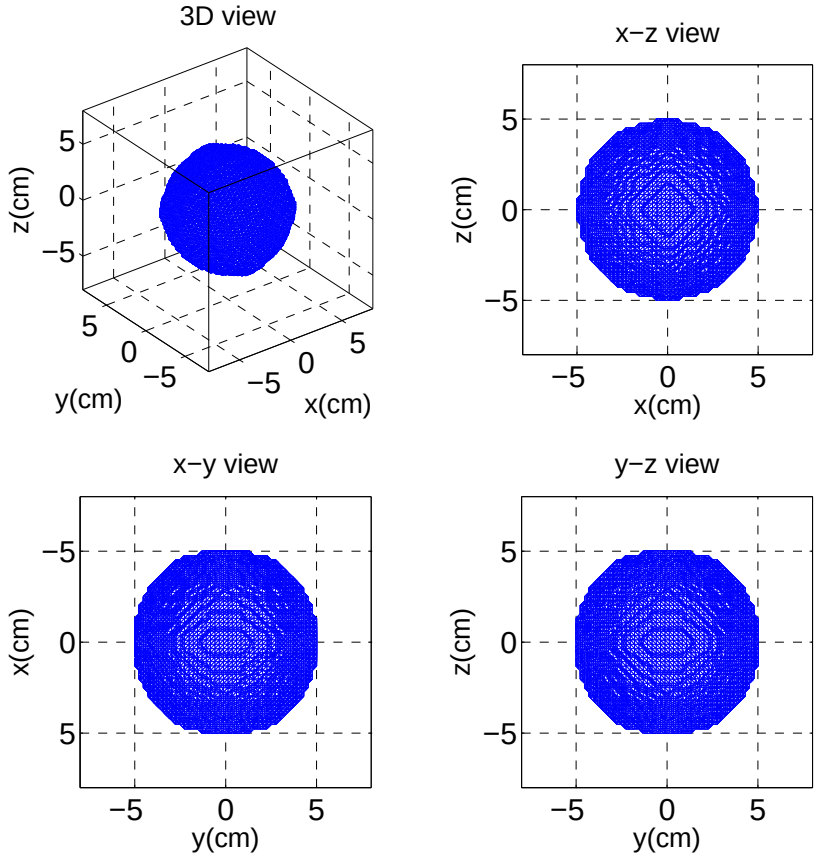

(b)

Figure 3.45: Configuration of study for the sphere (Fig. 3.40) in the '3ortho' case: (a) original geometrical profile functions; (b) reconstructed image obtained using the narrow band method at iteration $k = 80$ with error in pixels $E_p = 3.6\%$.

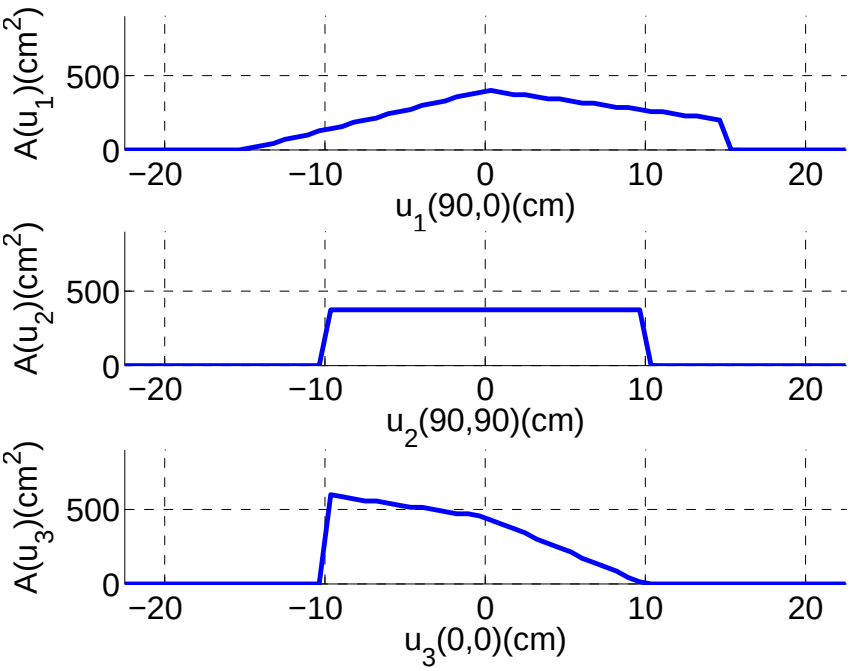

(a)

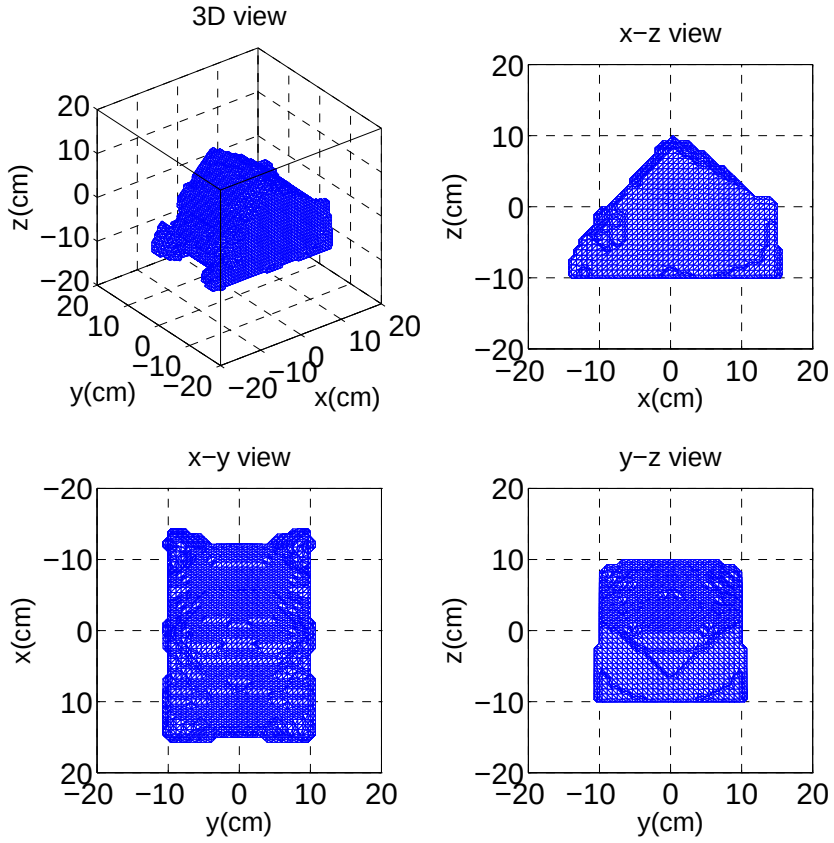

(b)

Figure 3.46: Configuration of study for the asymmetric object (Fig. 3.41) in the '3ortho' case: (a) original geometrical profile functions; (b) reconstructed image obtained using the narrow band method at iteration $k = 80$ with error in pixels $E_p = 9.2\%$.

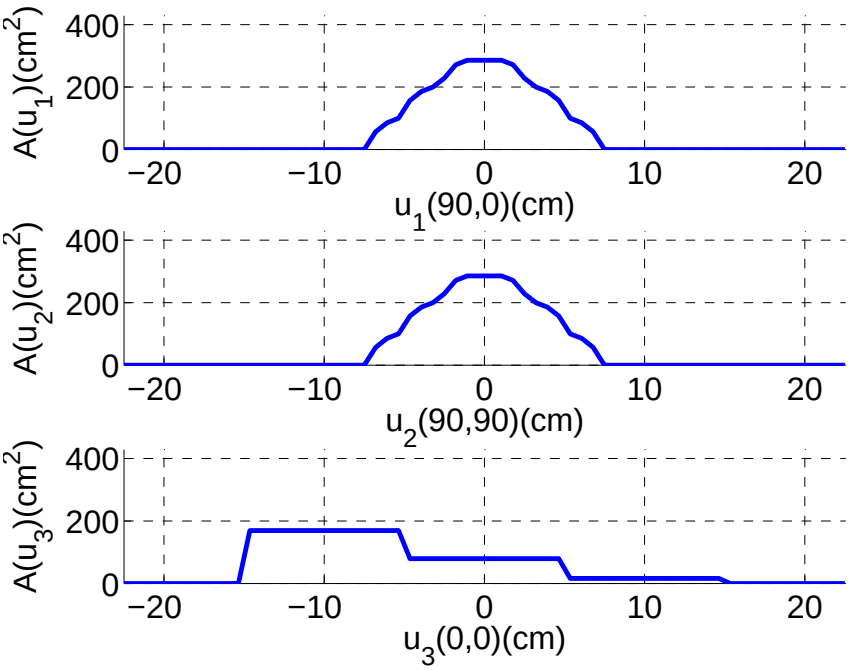

(a)

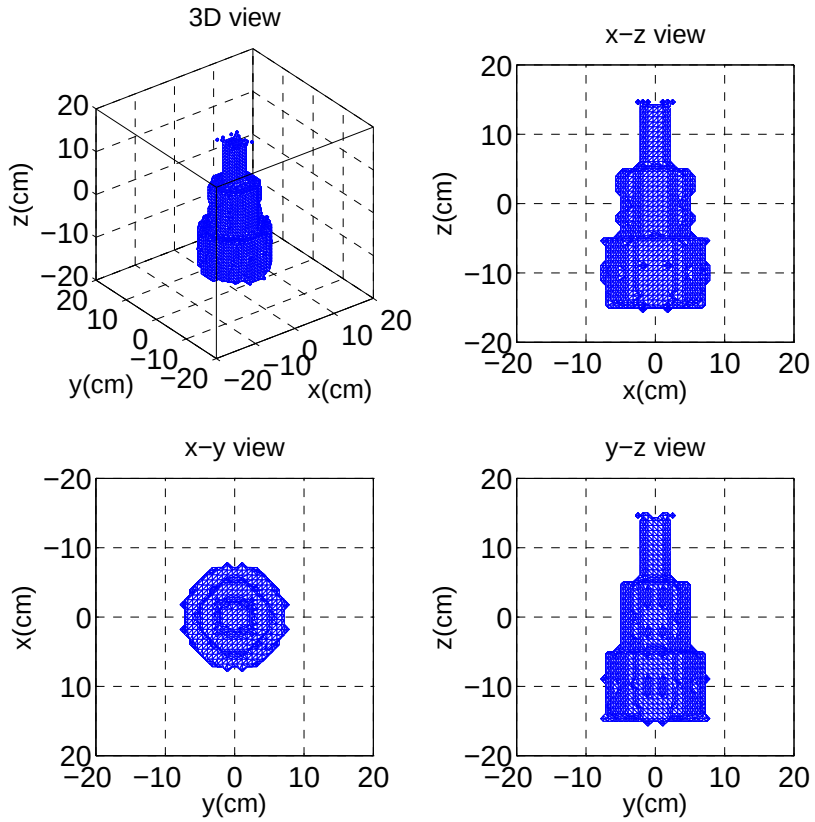

(b)

Figure 3.47: Configuration of study for the step-cylinder (Fig. 3.42) in the '3ortho' case: (a) original geometrical profile functions; (b) reconstructed image obtained using the narrow band method at iteration $k = 80$ with error in pixels $E_p = 3.5\%$.

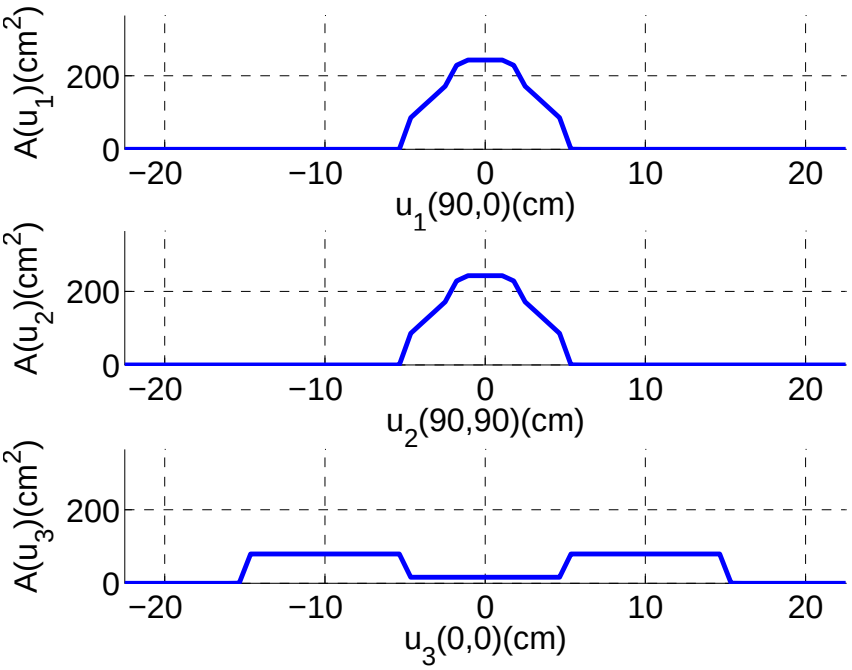

(a)

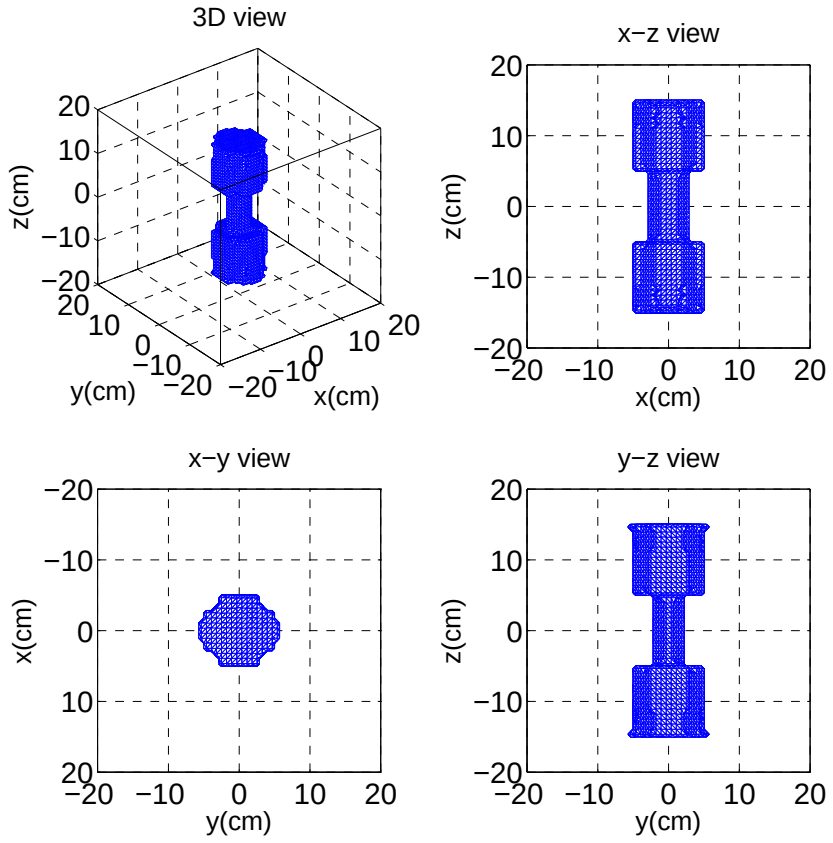

(b)

Figure 3.48: Configuration of study for the non-convex object (Fig. 3.43) in the '3ortho' case: (a) original geometrical profile functions; (b) reconstructed image obtained using the narrow band method at iteration $k = 80$ with error in pixels $E_p = 2.7\%$.

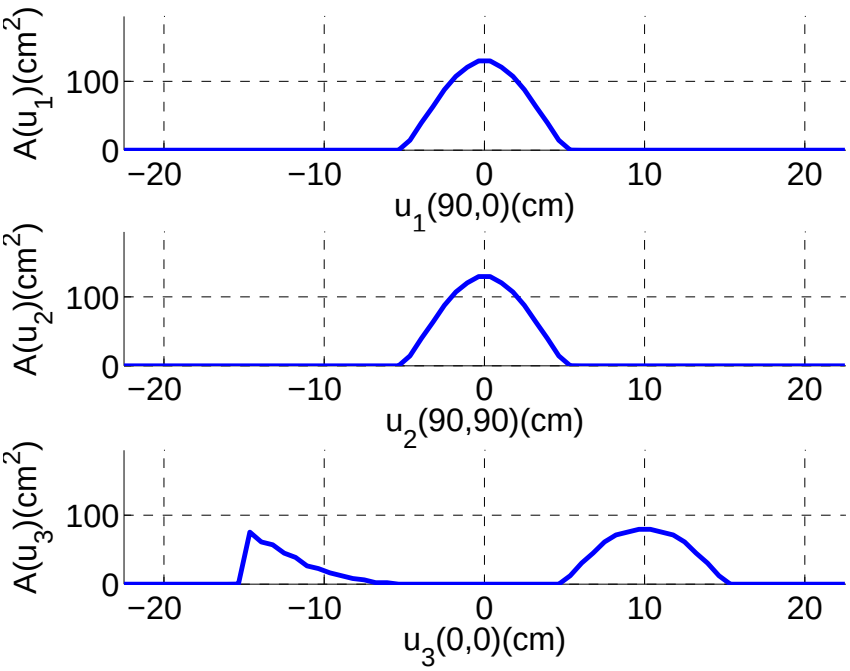

(a)

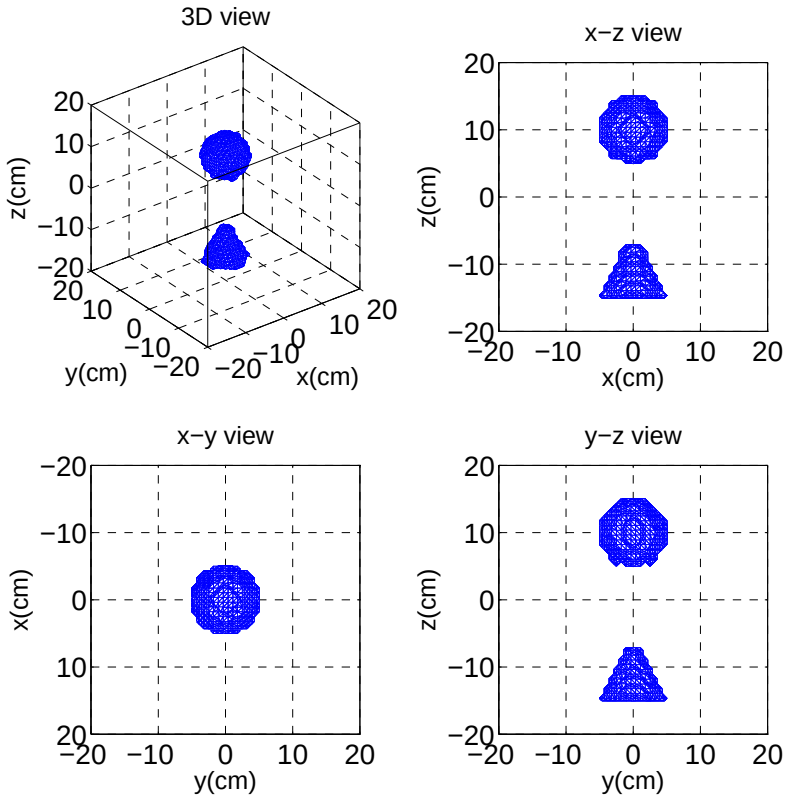

(b)

Figure 3.49: Configuration of study for the separated objects (Fig. 3.44) in the '3ortho' case: (a) original geometrical profile functions; (b) reconstructed image obtained using the narrow band method at iteration $k = 80$ with error in pixels $E_p = 4.4\%$.

3.3.2 Reconstruction with geometrical profile functions in non-orthogonal case

Theoretically, more different the observing directions are, more different characteristic information of the observed object can be exploited. In last section, the level set method has good performance with 3 mutually orthogonal directions. To study the performance of the level set method in ill-conditions, we now consider two sets of 3 observing directions which are much closer than those of the orthogonal case. We firstly choose 2 orthogonal directions plus 1 arbitrary direction $[u_1(90°, 75°), u_2(90°, 90°), u_3(0°, 0°)]$, noted as the '2ortho+1arb' case, and then an even worse case with 3 arbitrary directions $[u_1(90°, 30°), u_2(90°, 90°), u_3(30°, 0°)]$, noted as the '3arb' case. The two cases are presented respectively in Fig. 3.50 (a) and (b).

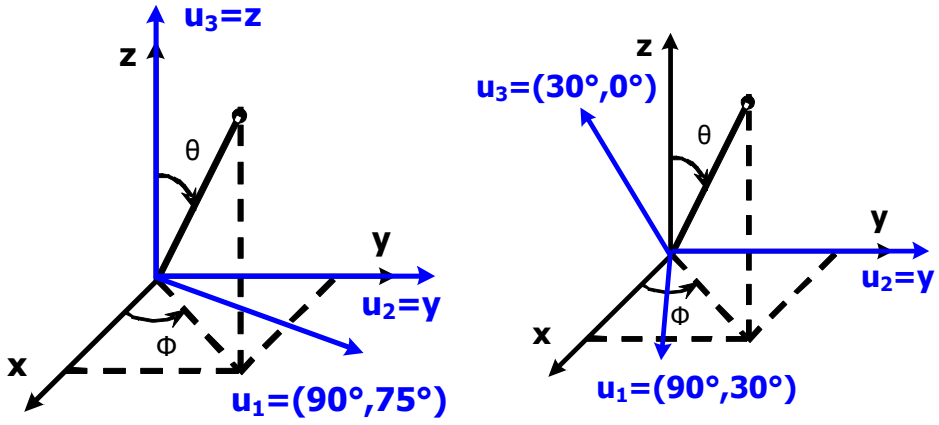

(a) (b)

Figure 3.50: Observing directions: (a) '2ortho+1arb' case with 2 orthogonal directions plus 1 non-orthogonal direction $[u_1(90°, 75°), u_2(90°, 90°), u_3(0°, 0°)]$ and (b) '3arb' case with 3 arbitrary directions $[u_1(90°, 30°), u_2(90°, 90°), u_3(30°, 0°)]$.

Sphere For the sphere (Fig. 3.40), its geometrical profile functions in the '2ortho+1arb' case and the corresponding reconstructed image are shown in Fig. 3.51 (a) and (b), respectively. The reconstructed sphere is correct comparing to the original object with an acceptable error in pixels $E_p = 9.6\%$. Similarly, for the '3arb' case, its geometrical profile functions and the resulting image are shown in Fig. 3.52 (a) and (b), respectively. The reconstructed object image presents a similar error in pixels $Ep = 11.8\%$.

Asymmetric object For the asymmetric object (Fig. 3.41), in the '2ortho+1arb' case, the geometrical profile functions and the reconstructed results are presented in Fig. 3.53 (a) and (b), respectively. From the x-z view, we can see that the reconstructed object is slightly distorted, but it is still accurate enough to meet the needs

of identification with an error in pixels $E_p = 22.0\%$. In the '3arb' case, the geometrical profile functions and reconstructed results are shown in Fig. 3.54 (a) and (b), respectively. Due to the 3 close observing directions, the results are more distorted with a higher error in pixels $E_p = 31.3\%$.

Step-cylinder For the step-cylinder (Fig. 3.42), in the '2ortho+1arb' case, the geometrical profile functions and the reconstructed results are presented in Fig. 3.55 (a) and (b), respectively. It can be seen that comparing to the original object, the second cylinder is larger while the first cylinder has some missing pixels. Therefore, this results in a higher error in pixels $E_p = 20.2\%$. In the '3arb' case, as shown in Fig. 3.56, the reconstructed object is even more distorted with an error in pixels $E_p = 45.3\%$. This is due to the fact that the most characteristic information comes from axis $z(0°, 0°)$, while we use a direction $u_3(30°, 0°)$ deviating from z.

Non-convex object For the non-convex object (Fig. 3.43), in the '2ortho+1arb' case, its corresponding geometrical profile functions and the reconstructed image are presented in Fig. 3.57 (a) and (b), respectively. The results are rough but correct with an error in pixels $E_p = 13.6\%$ comparing to the original object. While in the '3arb' case, the geometrical profile functions and the resulting image are presented in Fig. 3.58 (a) and (b), respectively. The results are strongly distorted and are rotated with a large error in pixels $E_p = 56.7\%$.

Separated objects For two separated objects, the sphere and the cone (Fig. 3.44), in the '2ortho+1arb' case, their corresponding geometrical profile functions and reconstructed image are presented in Fig. 3.59 (a) and (b), respectively. It can be seen that the reconstructed image of the sphere is accurate, while the reconstructed image of the cone has a slight deformation, but is still correct enough to be identified. Therefore, the two reconstructed objects have a total error in pixels $E_p = 6.5\%$. However, as shown in Fig. 3.60, the reconstructed image for the cone is totally distorted and can no to be identified. As a result, the error in pixel $E_p = 24\%$ is much larger.

3.3.3 Reconstruction with physical profile functions

So far, the results reconstructed using the level set method are obtained only from geometrical profile functions. Now we use the sphere as an example to study the performance of this method with physical profile functions. We choose to use the 3 same sets of observing directions, namely the '3ortho' case in Fig. 3.19 (a), the '2ortho+1arb' case in Fig. 3.50 (a) and the '3arb' case in Fig. 3.50 (b). The corre-

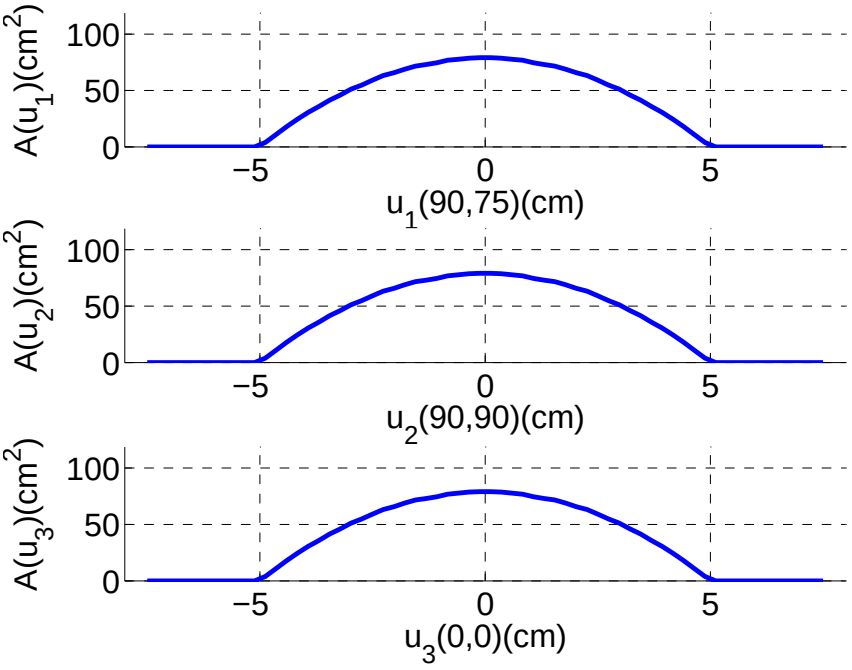

(a)

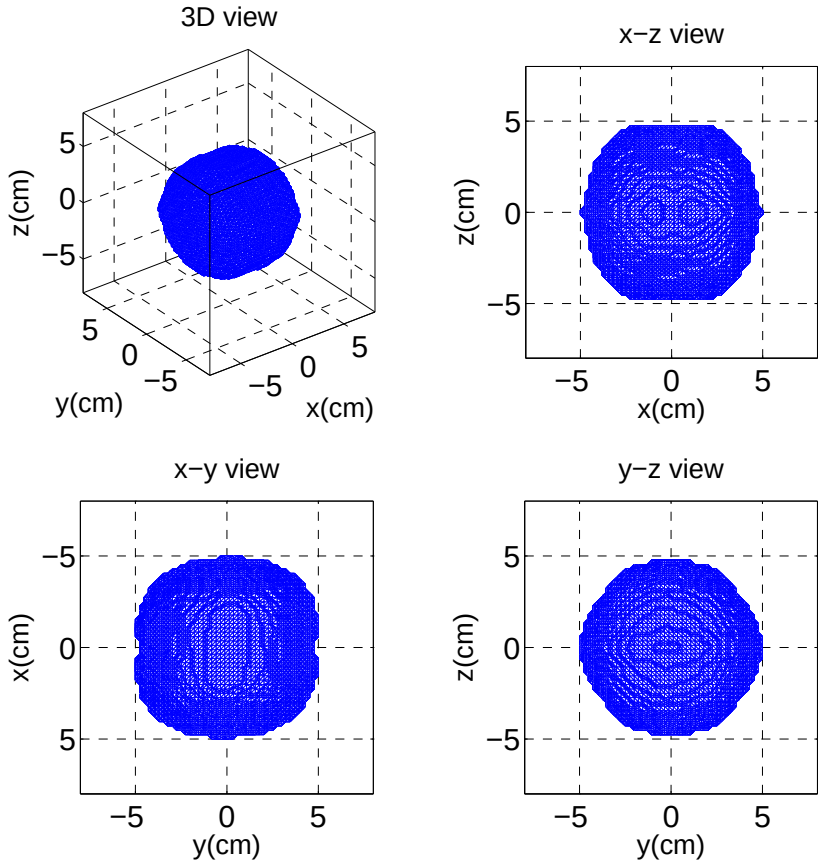

(b)

Figure 3.51: Configuration of study for the sphere (Fig. 3.40) in the '2ortho+1arb' case: (a) original geometrical profile functions; (b) reconstructed image obtained using the narrow band method at iteration $k = 80$ with error in pixels $E_p = 9.6\%$.

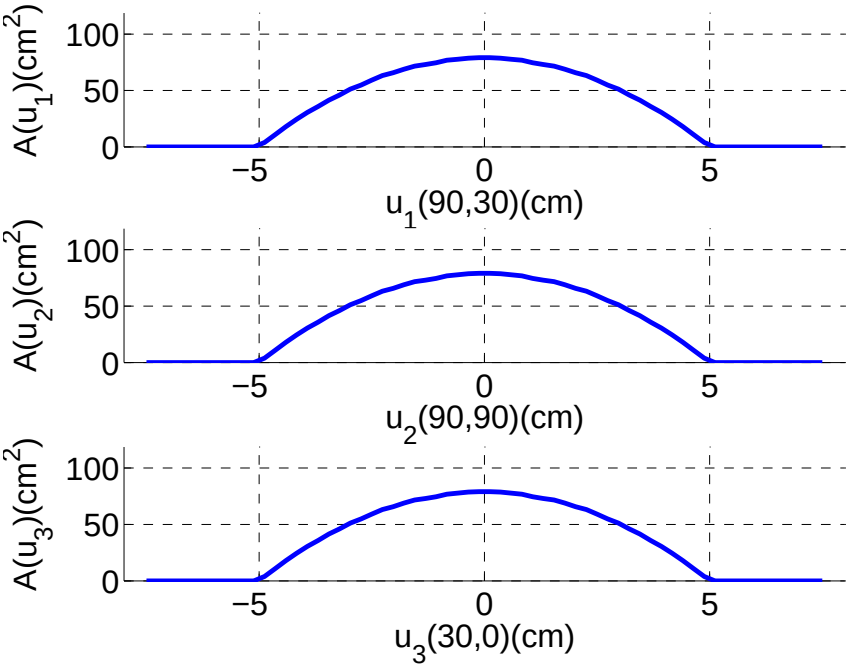

(a)

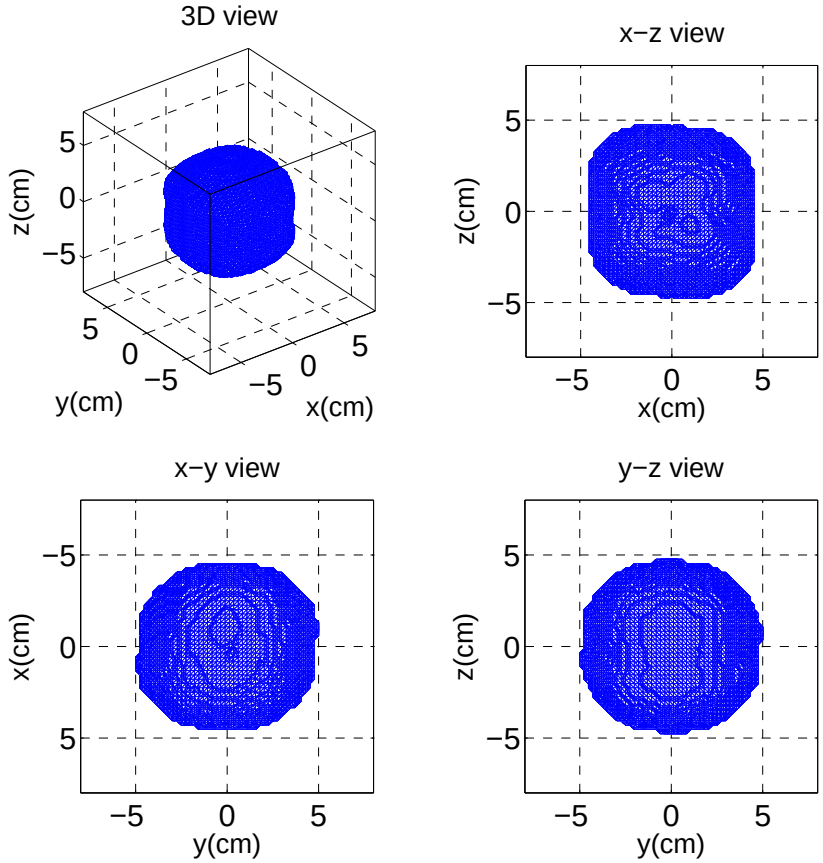

(b)

Figure 3.52: Configuration of study for the sphere (Fig. 3.40) in the '3arb' case: (a) original geometrical profile functions; (b) reconstructed image obtained using the narrow band method at iteration $k = 80$ with error in pixels $E_p = 11.8\%$.

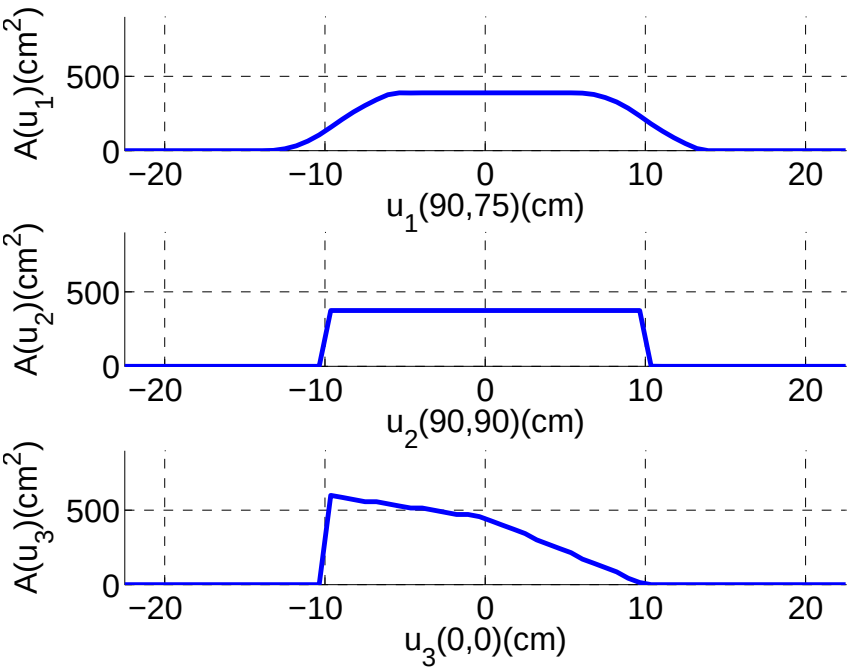

(a)

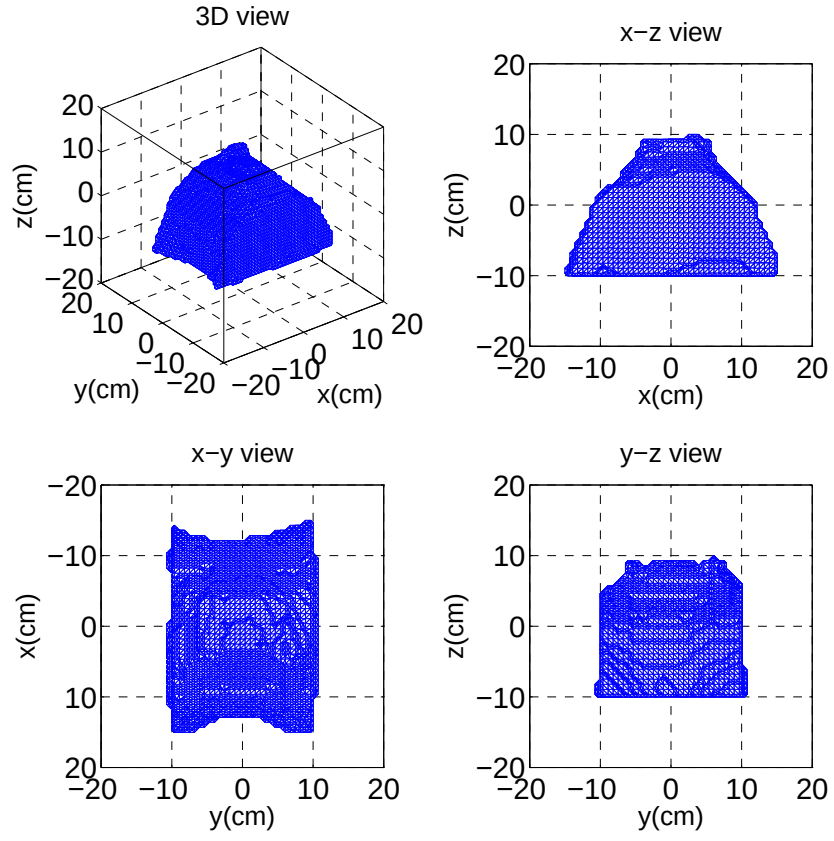

(b)

Figure 3.53: Configuration of study for the asymmetric object (Fig. 3.41) in the '2ortho+1arb' case: (a) original geometrical profile functions; (b) reconstructed image obtained using the narrow band method at iteration $k = 80$ with error in pixels $E_p = 22.0\%$.

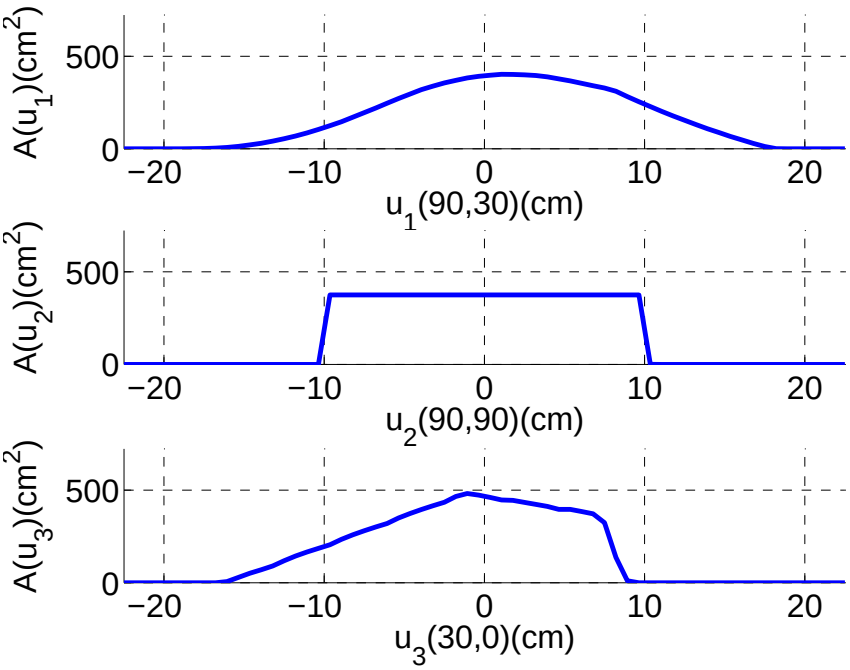

(a)

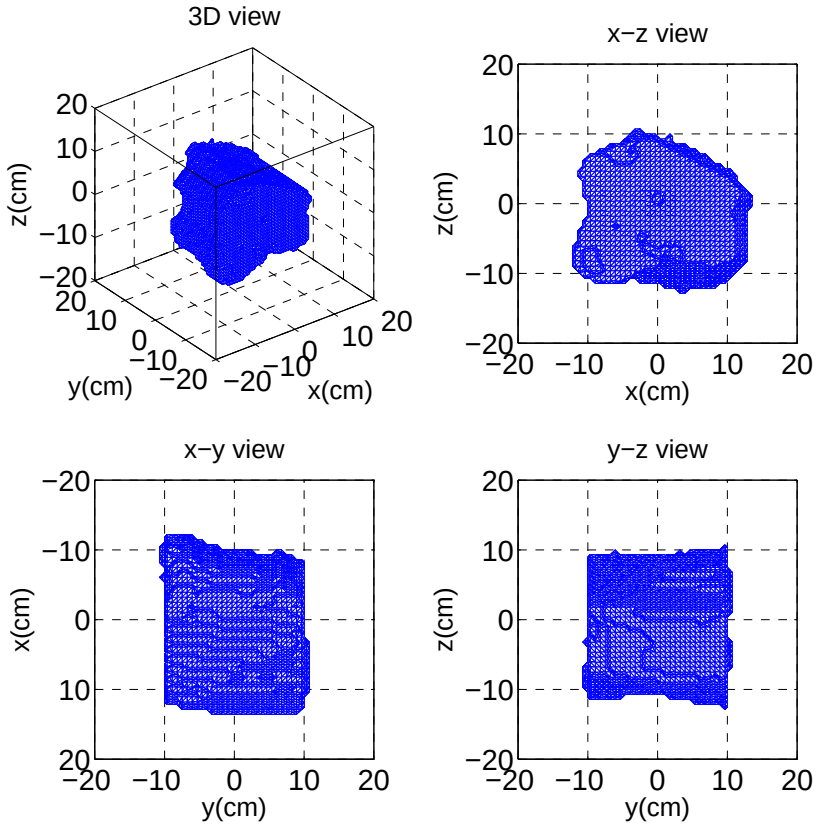

(b)

Figure 3.54: Configuration of study for the asymmetric object (Fig. 3.41) in the '3arb' case: (a) original geometrical profile functions; (b) reconstructed image obtained using the narrow band method at iteration $k = 80$ with error in pixels $E_p = 31.3\%$.

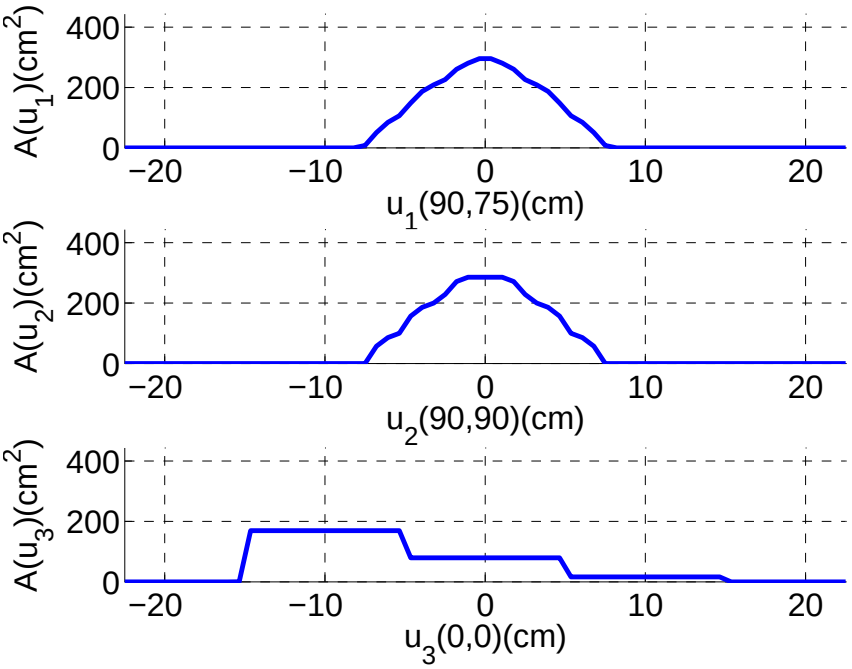

(a)

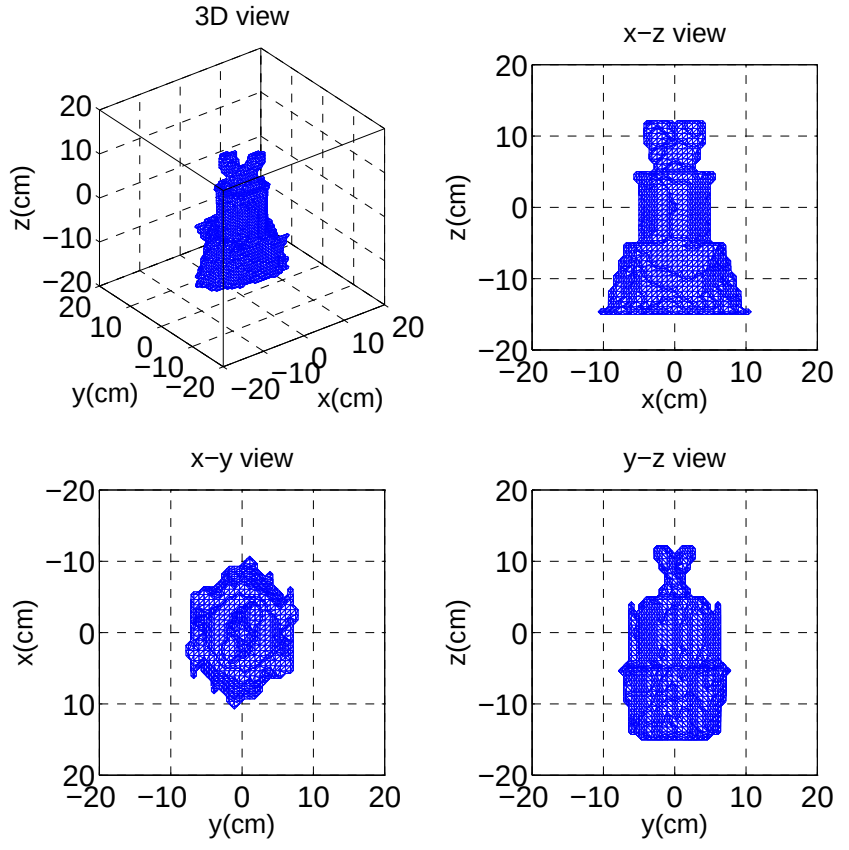

(b)

Figure 3.55: Configuration of study for the step-cylinder (Fig. 3.42) in the '2ortho+1arb' case: (a) original geometrical profile functions; (b) reconstructed image obtained using the narrow band method at iteration $k = 80$ with error in pixels $E_p = 20.2\%$.

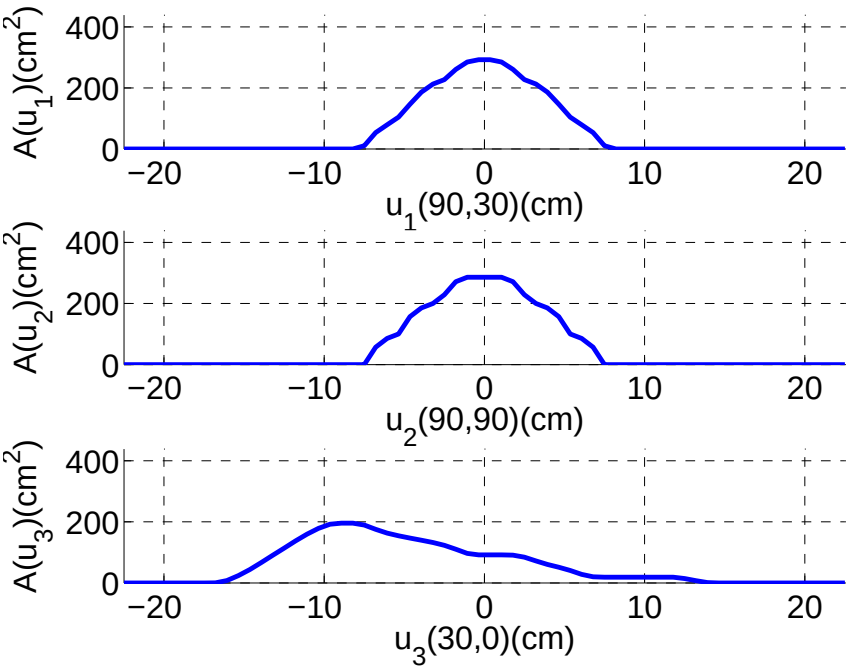

(a)

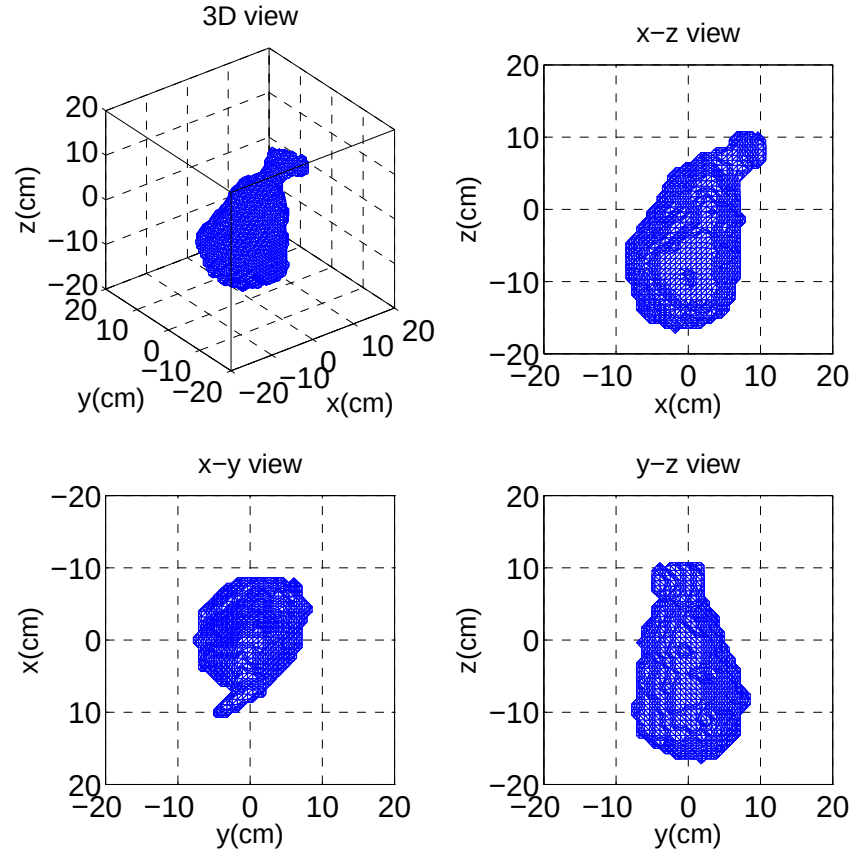

(b)

Figure 3.56: Configuration of study for the step-cylinder (Fig. 3.42) in the '3arb' case: (a) original geometrical profile functions; (b) reconstructed image obtained using the narrow band method at iteration $k = 80$ with error in pixels $E_p = 45.3\%$.

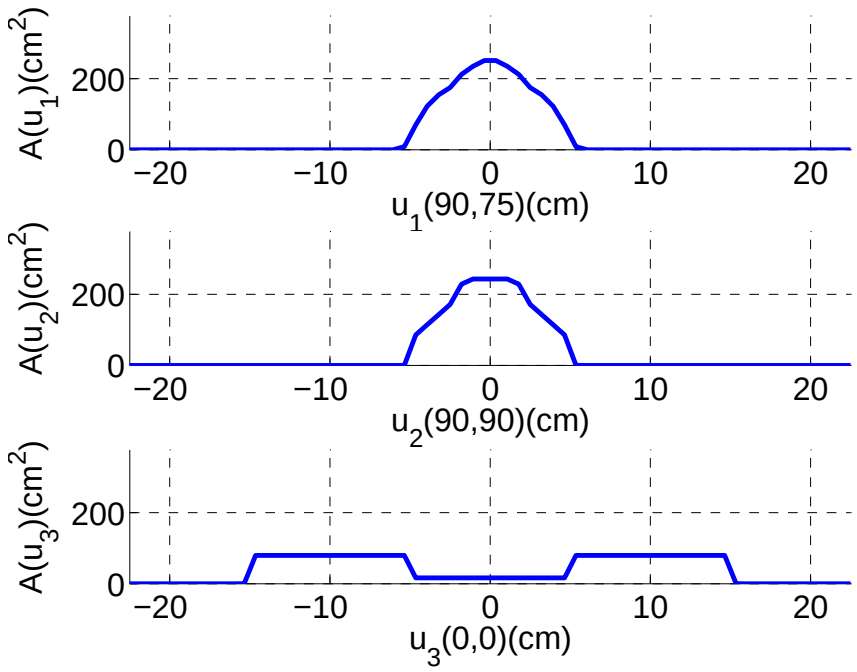

(a)

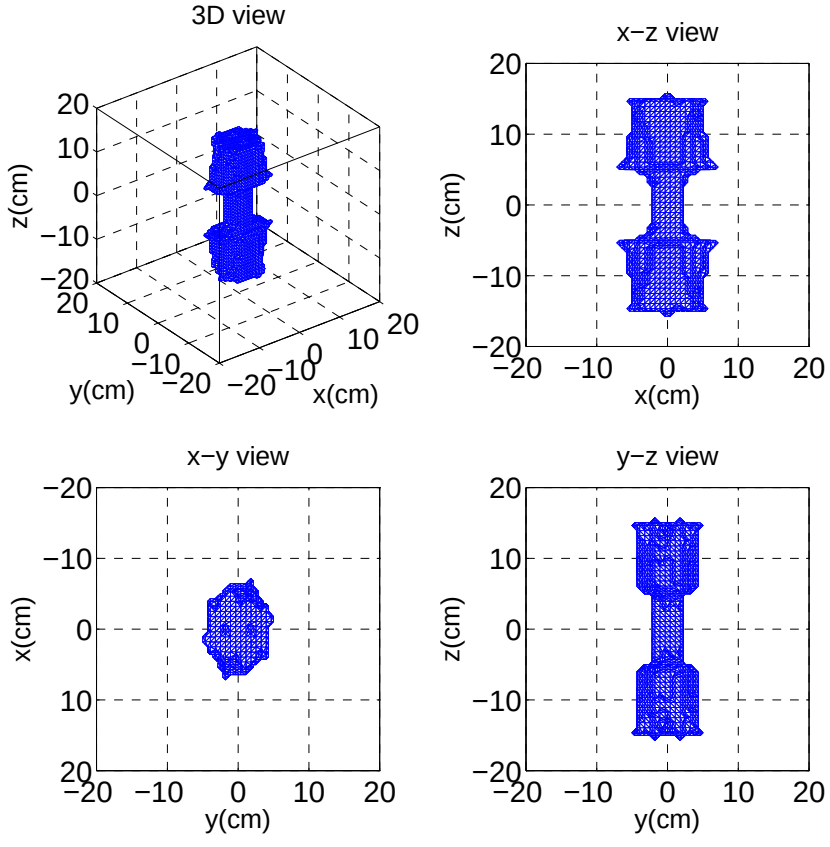

(b)

Figure 3.57: Configuration of study for the non-convex object (Fig. 3.43) in the '2ortho+1arb' case: (a) original geometrical profile functions; (b) reconstructed image obtained using the narrow band method at iteration $k = 80$ with error in pixels $E_p = 13.6\%$.

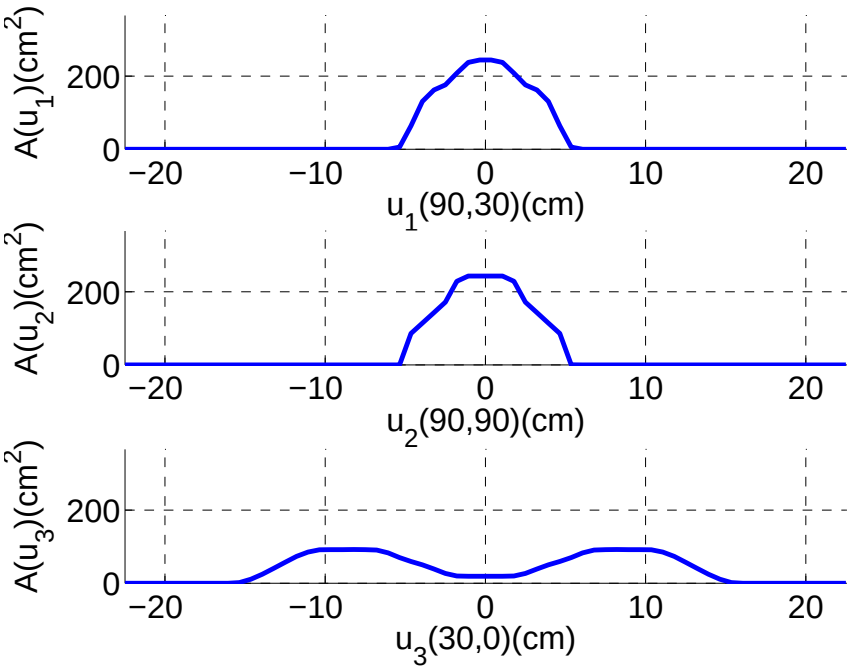

(a)

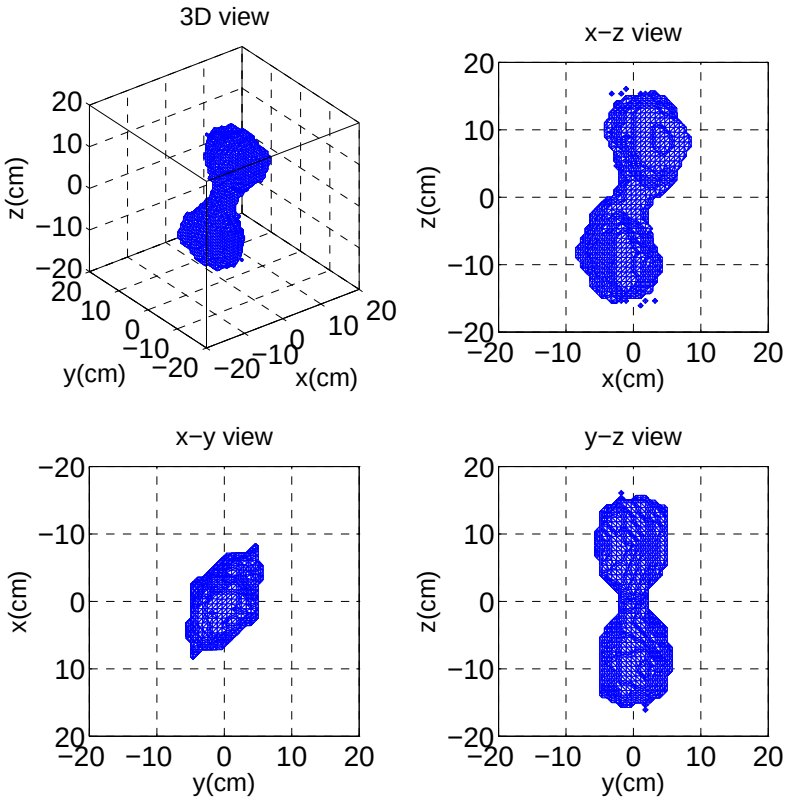

(b)

Figure 3.58: Configuration of study for the non-convex object (Fig. 3.43) in the '3arb' case: (a) original geometrical profile functions; (b) reconstructed image obtained using the narrow band method at iteration $k = 80$ with error in pixels $E_p = 56.7\%$.

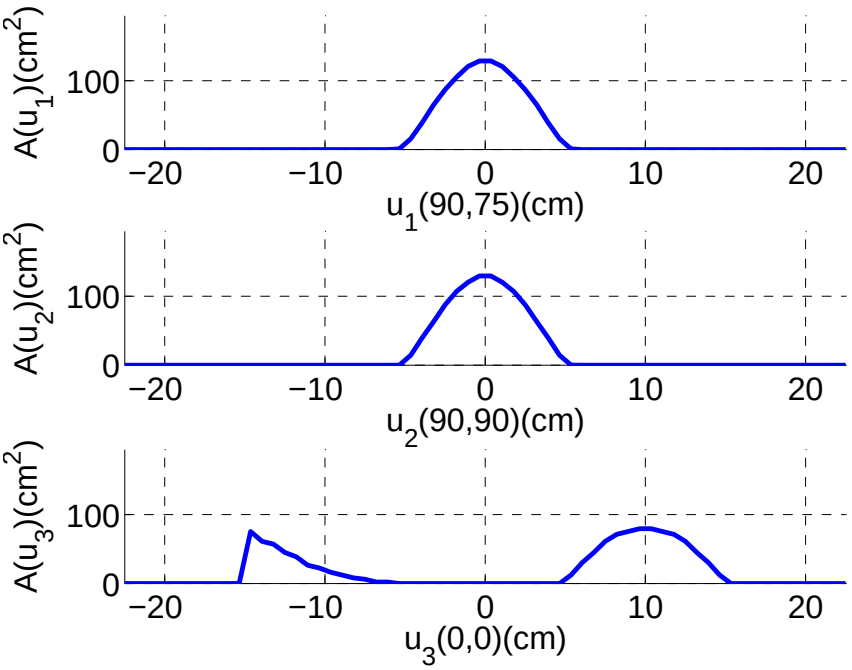

(a)

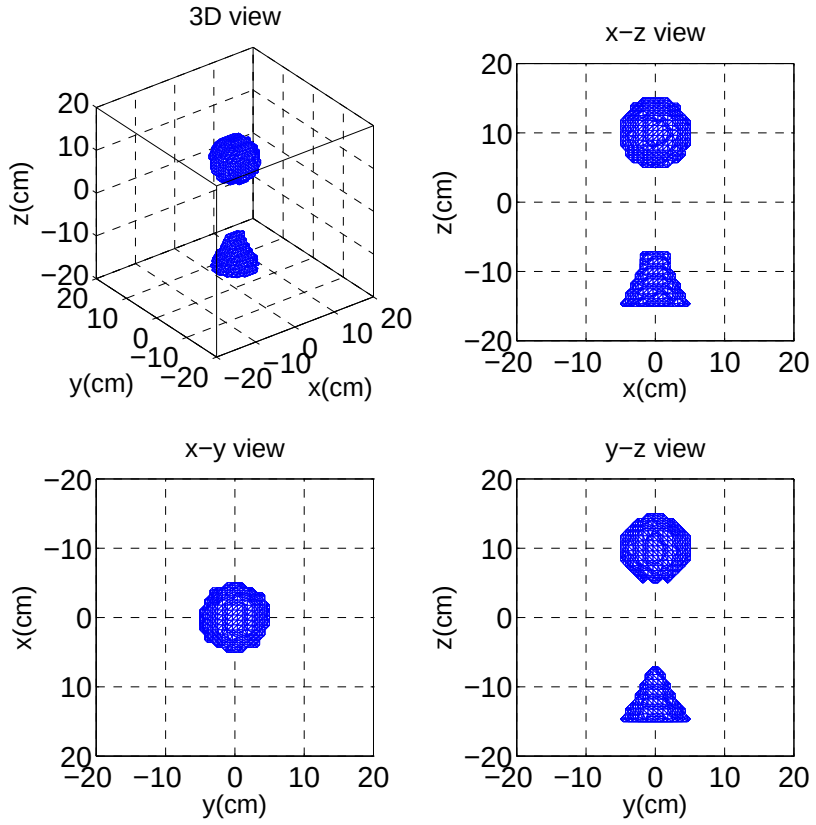

(b)

Figure 3.59: Configuration of study for the separated objects (Fig. 3.44) in the '2ortho+1arb' case: (a) original geometrical profile functions; (b) reconstructed image obtained using the narrow band method at iteration $k = 80$ with error in pixels $E_p = 6.5\%$.

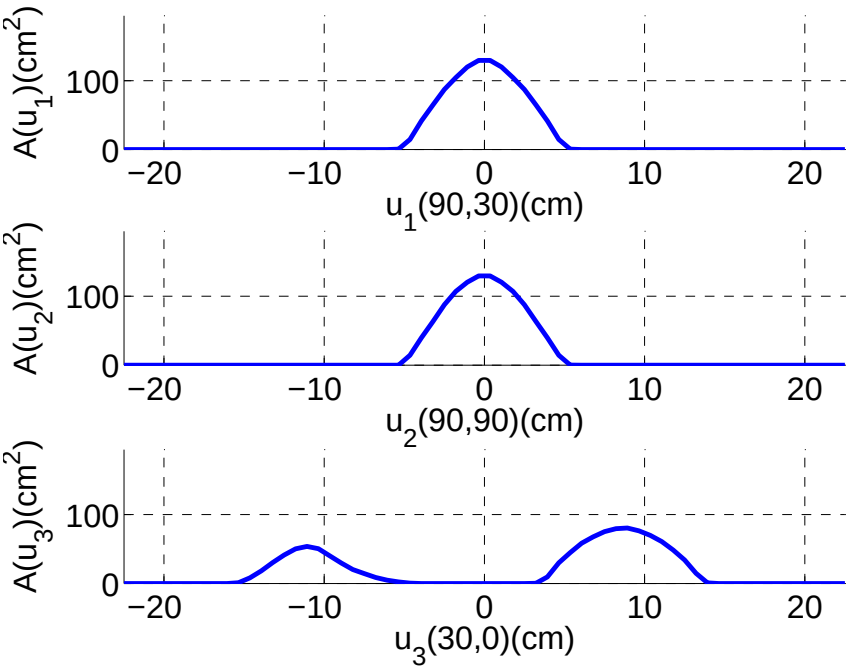

(a)

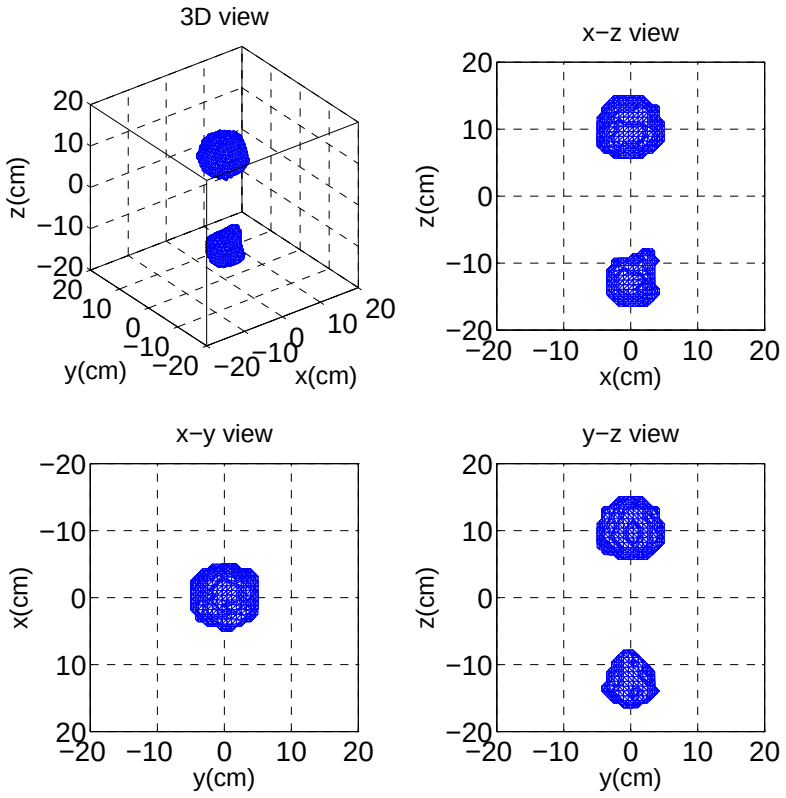

(b)

Figure 3.60: Configuration of study for the separated objects (Fig. 3.44) in the '3arb' case: (a) original geometrical profile functions; (b) reconstructed image obtained using the narrow band method at iteration $k = 62$ with error in pixels $E_p = 24\%$.

sponding reconstructed images are respectively shown in Fig. 3.61 with $E_p = 29.7\%$, in Fig. 3.62 with $E_p = 39.1\%$, and in Fig. 3.63 with $E_p = 35.4\%$. We can see that even with 3 orthogonal directions, the reconstructed object is distorted with a small 'ball' elongating along the direction where the physical profile functions have their extended parts due to the shadow region. The level set method cannot correct this distortion, because the forward mapping matrix G^u is calculated by considering the geometrical profile functions of the object.

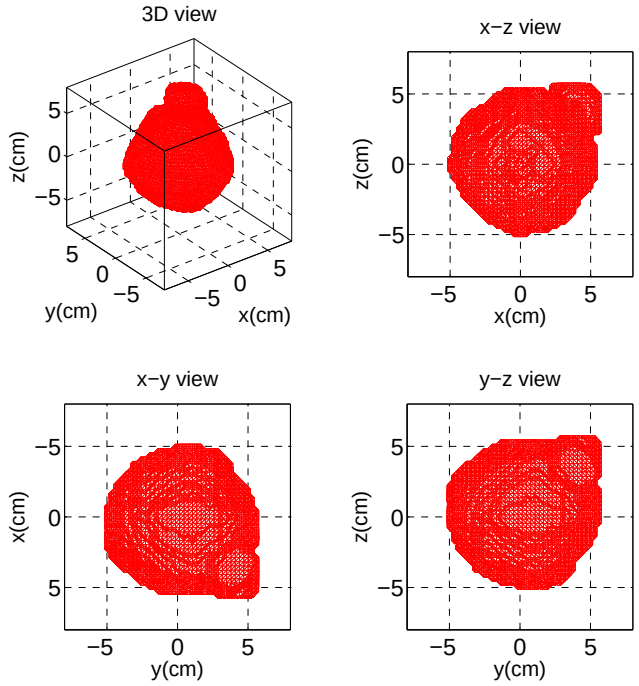

Figure 3.61: 3D reconstructed image of the sphere (Fig. 3.40) from physical profile functions in the '3ortho' case using the narrow band method at iteration $k = 80$ with error in pixels $E_p = 29.7\%$.

3.3.4 Parametric study

Using the narrow band level set method, as we demonstrated above, the quality of the reconstructions from profile functions mainly depends on the accuracy of the observed data (profile functions) and the observing directions. Additionally, during the numerical implementation, the reconstructed results are affected a lot by the choice of some parameters, such as the time step $\triangle t$ and the initial estimate. Therefore, in this section, we study the effect of these parameters on the reconstructed results.

Time step The time step $\triangle t$ plays an important role for the convergence and the stability of the evolution. For a gradient-type velocity, the time step $\triangle t$ should satisfy the CLF condition given by Eq. (3.38). It is calculated by the maximum

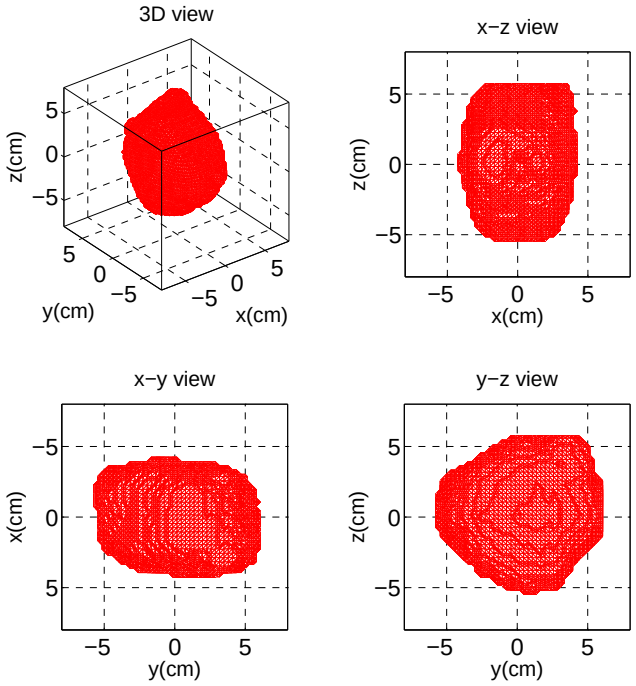

Figure 3.62: 3D reconstructed image of the sphere (Fig. 3.40) from physical profile functions in the '2ortho+1arb' case using the narrow band method at iteration $k = 80$ with error in pixels $E_p = 39.1\%$.

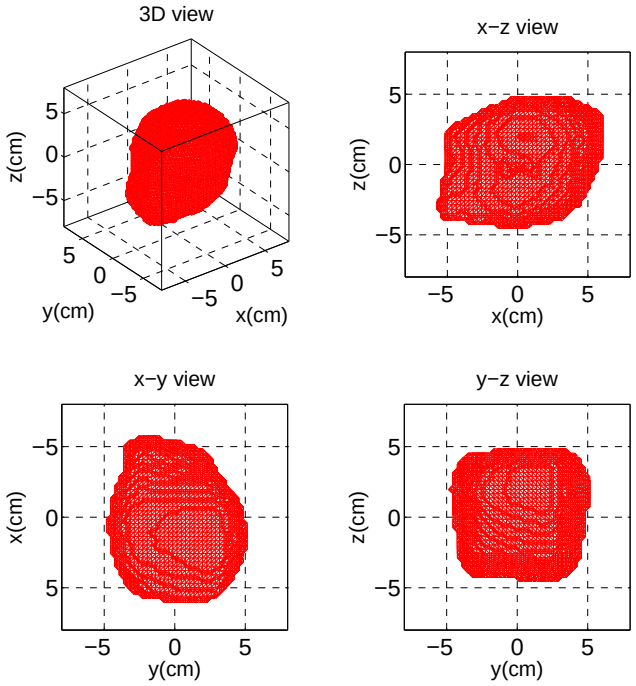

Figure 3.63: 3D reconstructed image of the sphere (Fig. 3.40) from physical profile functions in the '3arb' case using the narrow band method at iteration $k = 80$ with error in pixels $E_p = 35.4\%$.

amplitude of the velocity, the discrete step $\triangle u$ and a coefficient $0 < \alpha < 1$. Because the velocity is determined by the cost function and the discrete step is fixed when a number of points N is chosen, the effect of the time step comes from the choice of α. Here, we consider 3 different values $\alpha = 0.2, 0.5, 0.9$ to study the effect of this parameter on the normalized residual r_k. Taking the reconstruction of the sphere in '3ortho' case as an example, the comparison of r_k, obtained with these 3 values, is presented in Fig. 3.64 (a). It can be seen that, for a small value $\alpha = 0.2$, then a small time step, the resulting residual (red solid curve) decreases very slowly. When the value of α increases, the speed of the convergence increases until a certain tolerance value is achieved. Therefore, the residual with the value $\alpha = 0.9$ converges the fastest. But $\alpha = 0.5$ produces a more stable solution and decrease quickly as well. A similar comparison is given for the step-cylinder in Fig. 3.64 (b). Again, $\alpha = 0.5$ is an optimal choice for the convergence and the stability of the evolution with a gradient-type velocity.

Initial estimate Now, we study the influence of the initial estimate. For the previous numerical results obtained by the narrow band level set method, we used a little cube centered in the computational domain for each single object as the initial estimate. Indeed, we always locate this little cube inside the studied objects. For example, for the separated objects, its reconstructed image in the '3ortho' case (Fig. 3.49) is obtained from two initial little cubes (one for the sphere and another for the cone), each one being located at the center of each single object. But now, in Fig. 3.65 (a), we use only one single cube (black) for both separated objects (green) and put it outside them. As shown in Fig. 3.65 (b), both objects are still accurately reconstructed with a small error in pixels $E_p = 7.6\%$. However, as can be seen in Fig. 3.65 (c), at the beginning, it wastes much more computational time to find the correct position of the original shape and it needs 150 iterations to get such a reconstructed result. Therefore, although the choice of the estimate is somewhat arbitrary, it is better to choose to put it inside the original object for the sake of saving computational cost.

Next, we study the performance of the narrow band level set method for correcting distortions. That is to start the evolution with an initial estimate which is approaching the original shape but is still distorted. Here, we choose to use the inaccurate results reconstructed from geometrical profile functions using Chauveau's method in the non-orthogonal case, $[u_1(90°, 30°),\ u_2 = y,\ u_3 = z]$. As shown in Fig. 3.66 (a), this distorted reconstructed object is elongated along the direction perpendicular to the bisector of the 2 non-orthogonal directions (u_1 and u_2). Using this object as the initial estimate, we present, in Fig. 3.66 (b) and (c), the image reconstructed obtained using the level set method and its corresponding normalized residual r_k. The reconstructed image is still distorted with an error in pixels

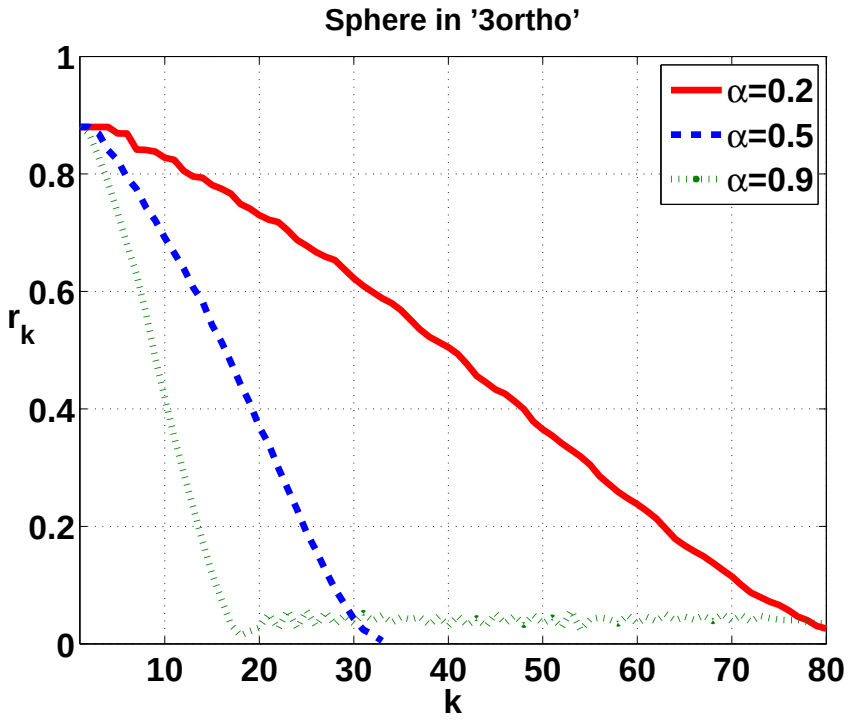

(a)

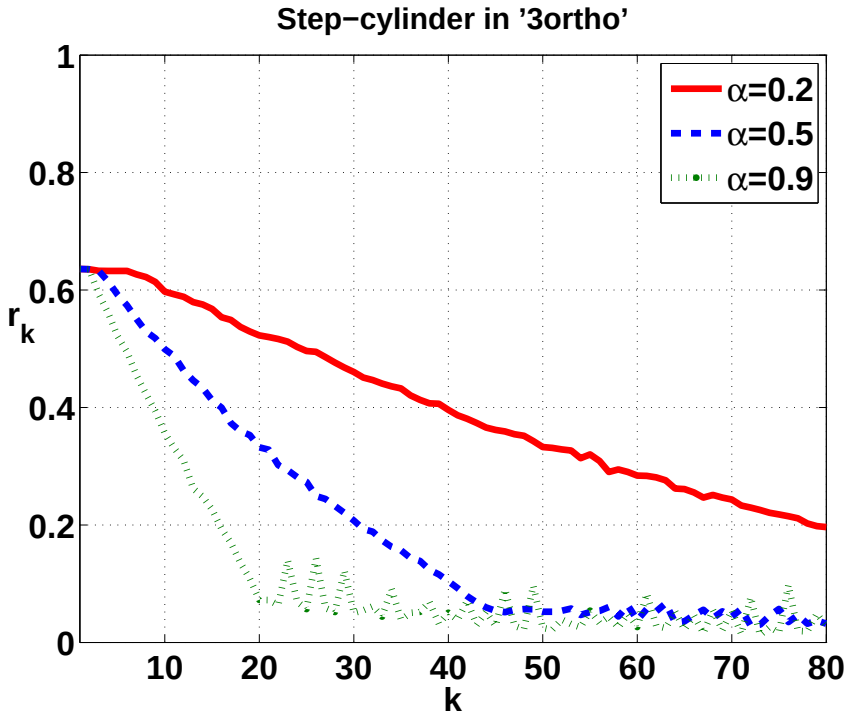

(b)

Figure 3.64: Effect of the time step $\triangle t$ on the normalized residual r_k of the reconstruction with geometrical profile functions using the narrow band level set method for: (a) the sphere, (b) the step-cylinder, in the '3ortho' case.

$E_p = 42.7\%$, this is due to the fact that even though the shape is inaccurate, Chauveau's method can guarantee the agreement between the original profile function and that of the reconstructed object. This results in a small error of the profile functions at the very beginning of the iteration. That is to say, the normalized residual has already achieved a small and stable value so that the evolution velocity becomes a plateau and zero everywhere so that the evolution stops.

3.4 Conclusion

With the algorithm we developed for obtaining geometrical profile functions of a 3D object, the optimization of reconstructions is formalized as an inverse linear problem, which can produce optimal results using an iterative process. At the very beginning, a classical method, the least-square method (LSQR) [14], is tested to solve our problem. However, it fails to extract a correct shape even though it succeeds in minimizing the error between the input and output profile functions. Therefore, an accurate shape representation is needed. The level set method proposed by Osher and Sethian [72] represents the object as the zero level of an implicit higher dimensional function such that shape deformation under a velocity field is completely automatic and implicit during the iteration. Consequently, we studied its principle and different types of velocity depending on the applications. Following the work of Santosa [84] and [85] on the inverse problem involving obstacles, we construct a gradient-type velocity adapted to our problem. We also validate the level set method with the velocity by reconstructing a sphere both in orthogonal and non-orthogonal cases. We use the'Narrow band' method, originally proposed by Chopp [98], to reduce the complexity and computational cost. Numerical results of reconstruction for various objects demonstrate that the 'Narrow band' level set method generates promising results with geometrical profile functions for the '3ortho' and the '2ortho+1arb' cases. However, in the '3arb' case, it produces good results only for a symmetric object as the sphere, and distorted results for other objects. This is because, for the symmetric object, its geometrical characteristic is the same along any direction, but for asymmetric objects or plane-symmetric objects, their geometrical characteristic focus on some specific directions. With physical profile functions, even for a symmetric object in '3ortho' case, the results are distorted.

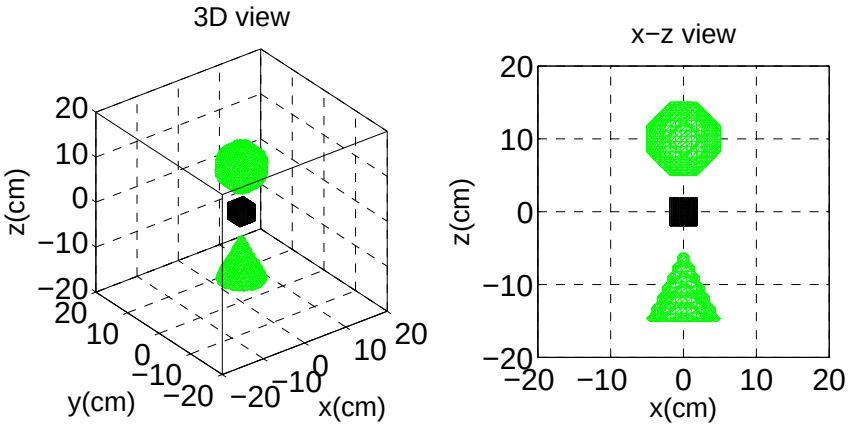

(a)

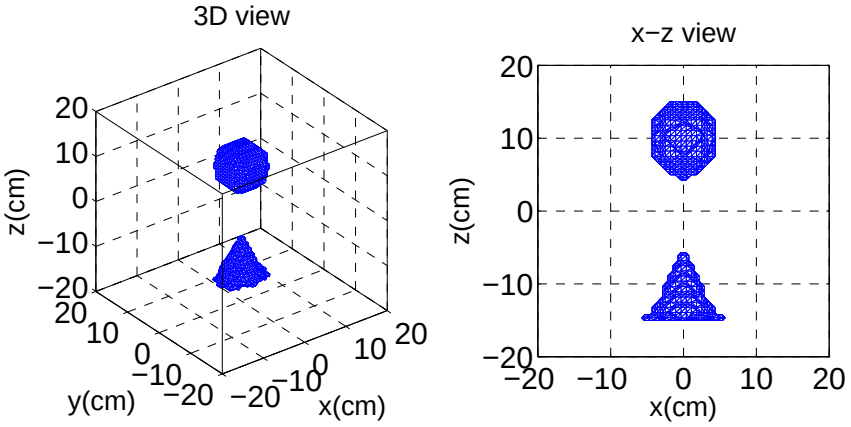

(b)

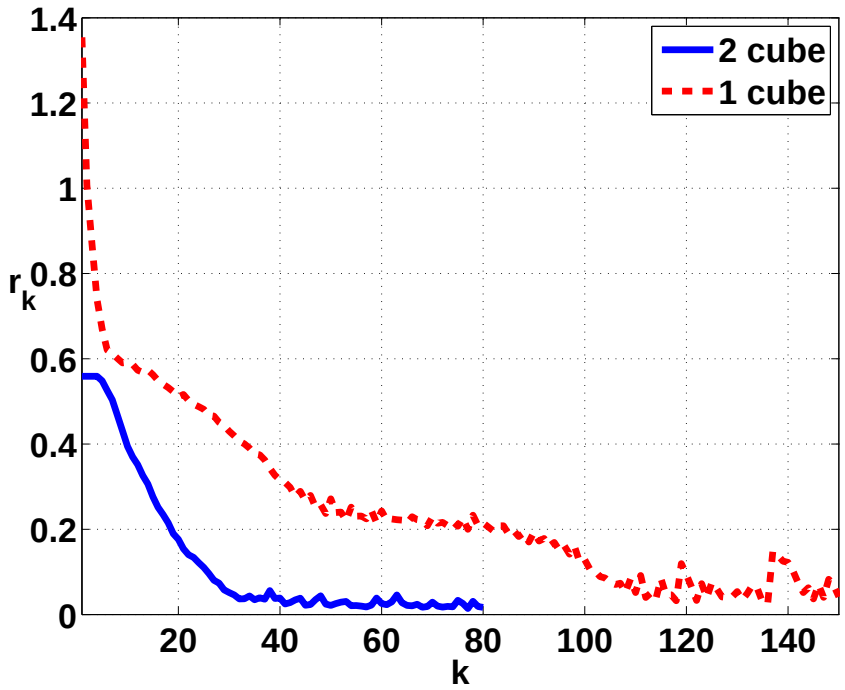

(c)

Figure 3.65: Reconstruction starting with one single initial cube for the two separated objects in the '3ortho' case: (a) the initial single estimate (black) and the original two separated objects (green); (b) reconstructed image; (c) the normalized residual r_k.

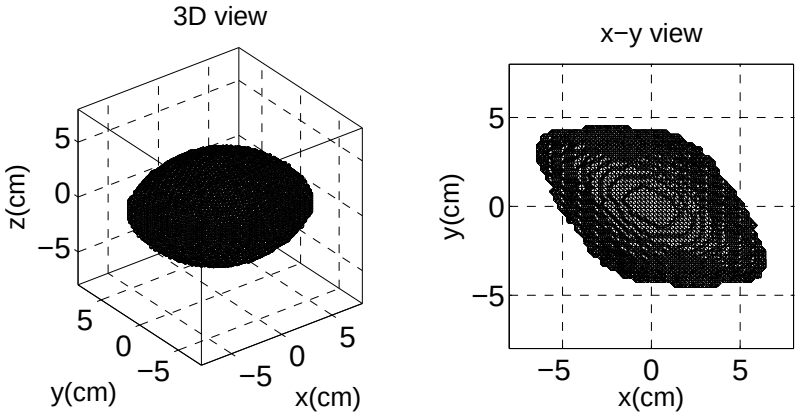

(a)

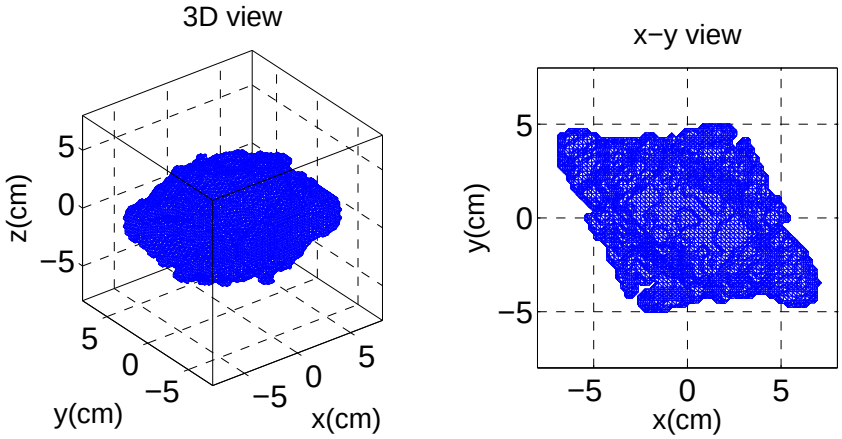

(b)

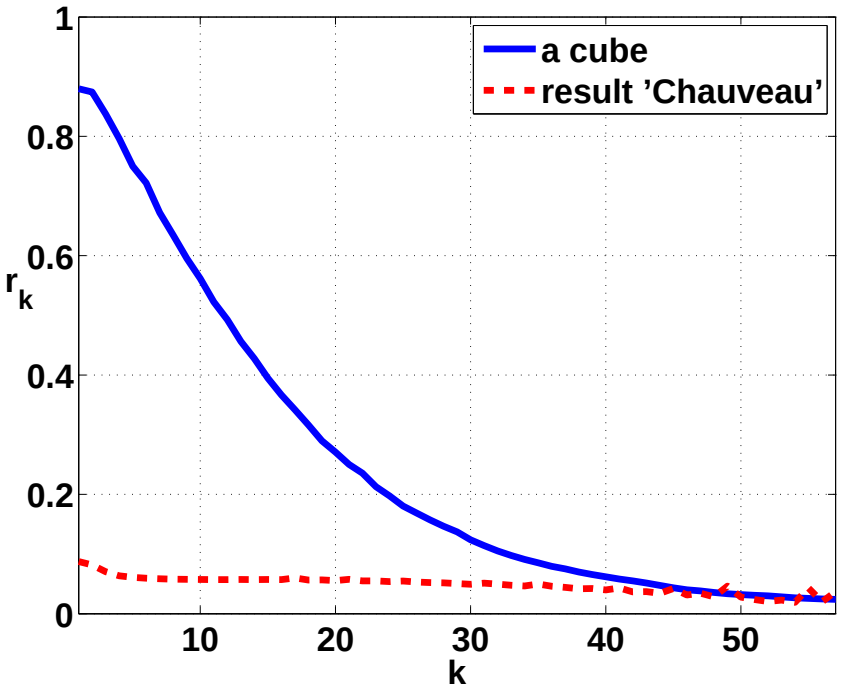

(c)

Figure 3.66: Reconstruction starting with an initial distorted result obtained by Chauveau's method for the sphere: (a) the initial distorted estimate; (b) reconstructed image; (c) the normalized residual r_k.

4

Conclusions and Perspectives

The study presented in this thesis concerns the characterization of radar targets with a low frequency method, the radar imaging form ramp response method. It permits to reconstruct the object with profile functions in only 3 directions. Existing reconstruction algorithms from profile functions give good results with 3 mutually orthogonal directions, but distorted estimates for non-orthogonal case. Therefore, the main work in this thesis is the optimization of target reconstruction from profile functions in arbitrary directions.

In chapter 1, some background knowledges for the characterization of stealthy radar targets were introduced. We firstly recalled some basic notions, such as the radar cross-section (RCS), the radar frequency bands and the transfer function as well as the impulse response. The RCS is an intrinsic information depending on target properties (size, shape and materials), which is widely used in military applications. Then, we reviewed the main stealth and counter-stealth technologies. Low frequency radar corresponds to the Rayleigh and resonance regions for object dimensions respectively small and of the same order compared to wavelengths, so that more RCS is received and the stealth is less effective. Next, we presented some existing inverse scattering methods for exploiting characteristic information from the RCS. The radar imaging from ramp response, adapted to the low frequency band, permits to reconstruct 3D images for the target to be identified with no more than 3 observing directions.

In chapter 2, the method of radar imaging from ramp response was studied. Ramp response is the far-field backscattering response of a radar target from an excitation with a waveform of ramp function, and it was founded to be approximately proportional to the target profile function which is defined as the transverse

cross-sectional area along the incidence direction [3]. With this property, 3D images can be generated by using certain algorithms for reconstruction from profile functions. Therefore, we have considered three existing reconstruction methods: Young's method [5], Chauveau's method [13] and reconstruction from projections [11, 12]. Chauveau's method is the most advanced algorithm that requires only 3 observing directions and overcomes the limitation of object shape in other methods. Consequently, we implemented this method, and applied it to reconstruct various 3D objects of different shapes (symmetric/asymmetric, convex/non-convex and single/separated shapes). Numerical results indicated that, with 3 mutually orthogonal directions, Chauveau's method generates accurate reconstructions from geometrical profile functions for all the studied objects, but it can't correct the distortion caused by the bias in the physical profile functions which is due to the shadow region effect, though the slightly distorted reconstructed object, in most of cases, can still meet the needs of identification. On the contrary, even if we change only one direction and keep the other two directions orthogonal, the reconstructed images from both the geometrical and physical profile functions are inaccurate and can not be identified. Nevertheless, in practice, due to the limited viewing angles of radar equipment for remote sensing or large-scale targets in far distance, it is very difficult, almost impossible, to illuminate the target from 3 mutually orthogonal directions.

In chapter 3, we present our main contribution on the optimization of image reconstructions with profile functions from arbitrary directions. We choose to use an iterative process with a quantitative indicator, i.e. the error between the profile functions observed from the original object and that from the evolving objects. It is important to note that the observed profile functions can be either geometrical profile functions for the ideal case or physical profile functions for the practical case. In order to focus on improving the performance for reconstructions in arbitrary directions, in this thesis, the forward observing matrix is only considered to describe the relationship between the geometrical profile function obtained from the initial object and that from the estimated object. In this chapter, for the optimization of image reconstructions with profile functions from arbitrary directions, different problems were studied:

In section 3.1, we developed an algorithm to solve the direct problem, which is the forward calculation of geometrical profile functions for a 3D object. It has no limitation for any geometries (even irregular shapes) and arbitrary directions. By comparing with the geometrical profile functions analytically calculated with some known formulas, we verified that our algorithm was effective with only a few discretization errors, which can be reduced by increasing the number of samples. Then, we applied it to quantitatively evaluate the quality of reconstructions obtained using Chauveau's method by calculating errors between profile functions from the original object and profile functions from its reconstructed image. Next, with a

database containing possible models, we applied our algorithm to identify a radar target using its reconstructed object obtained from physical profile functions in only 3 directions. Our method permits to compare the reconstructed object and models in a full range of directions so as to avoid that different shapes might have same profile functions in some directions. Taking into account the poor condition of limited resolution encountered in low frequency radar imaging, our identification process succeeded in finding the best possible models for the studied object.

In section 3.2, to solve the inverse problem which aims to find an inverse method adapted to three-dimensional shape reconstruction, we first tested a classical inverse method for linear problems, the least-square method (LSQR) [14]. Examples of the reconstruction for a sphere show that LSQR give an accurate reconstruction with orthogonal directions but a distorted one otherwise. Indeed, the profile function, namely the cross-sectional area along observing directions, is not a direct parameter which can represent the shape of the object. A shape can not be uniquely determined only from its cross-sectional area in 3 (or maybe more) directions. Therefore, even if LSQR, as most of inverse methods, succeeds in minimizing the error of the input and output profile functions, it can not extract a correct shape. The level set method [72] is just adapted to our problem, with an implicit shape representation. It has been proven to be effective for fluid dynamics, image processing and computer vision as well as inverse scattering problems. Therefore, we studied the principle of this method which represents the boundary of an object as the zero-level isocontour of an one-higher dimension function (the level set function) and evolves this function under a velocity field. Then, we reviewed different types of the evolution velocity depending on the domain of applications. For inverse scattering problems, a gradient-type velocity is widely used, because it establishes a relationship between the shape derivate and the cost function [84]. Consequently, we applied the level set method with this gradient-type velocity to optimize the reconstruction in arbitrary directions. Using the sphere as an example, we validate this method for reconstructions from profile functions. Results show that this method produces good results for the sphere, in the case of 3 mutually orthogonal directions as well as in the case of 2 orthogonal directions and 1 arbitrary. Moreover, the 'Narrow band' level set method was used to reduce the computational cost, since this method performs the evolution only in an embedding of the boundary within a finite width.

In section 3.3, numerical results of the reconstruction obtained using the 'Narrow band' level set method are presented for various objects:

- Firstly, with geometrical profile functions from 3 mutually orthogonal directions, namely in the '3ortho' case, accurate results are obtained for each object. The error in pixels is very small ranging from 2.7% to 9.2%.

- Secondly, with geometrical profile functions from 3 non-orthogonal directions, the reconstructed images of the sphere are correct with an error in pixels of the same level as the '3ortho' case. For other objects, in the '2ortho+1arb' case, if we keep the direction where the topology characteristic varies the most, for example $u_3 = z$ for the step-cylinder, even if the other two directions are not orthogonal and very close to each other (with an angle of $15°$), the reconstructed image is accurate enough to be identified. While in the '3arb' case, we use a direction $u_3 = (30°, 0°)$ deviating from the most characteristic direction z. As a result, reconstructed images are completely distorted and can not be identified. The same situation happens to the non-convex object. For two separated objects, the effect of the direction can be separately considered for each sub-object. For the sphere, the directions have low influence on the reconstructions because of its symmetry. While for the cone, distorted images obtained in the '3arb' case are due to the lacking of a direction corresponding to the most characteristic information.

- Thirdly, with physical profile functions, even with 3 mutually orthogonal directions, the reconstructed images of a sphere are distorted. They have an obvious 'extra' part due to the shadow effect on the physical profile functions. Indeed, the forward mapping matrix G is constructed by considering only the geometrical profile functions, so it is not adapted to the physical case and it has to be replaced by a matrix taking into account the physical behavior.

- Finally, the influence of the time step and of the initial estimate is studied. From the CFL conditions, the choice of time step depends on a coefficient α, $0 < \alpha < 1$. Numerical results show that $\alpha = 0.5$ seems to be an optimal choice for the convergence and stability of the evolution. Then, the choice of the initial estimate is proven to be somewhat arbitrary and can be chosen to be inside the object for the sake of saving computational cost. The level set method can not correct the distorted object obtained by Chauveau's method since the residual has already achieved a stable value.

To sum up, the level set method permits to reconstruct quite acceptable 3D images from profile functions in 3 arbitrary directions. It is important to note that, the notion 'arbitrary' here does not mean any observing direction with respect to the studied object, but means that the relationship among the 3 directions is not necessary to be mutually orthogonal. This is meaningful because due to the limit of the limited viewing angles of radar equipment for remote sensing or large-scale targets in far distance, it is very difficult, almost impossible, to illuminate the target from 3 mutually orthogonal directions. The disadvantage of this method for image reconstruction is that at least one direction with as much as possible characteristic shape information is required. Nevertheless, this is the limit for other reconstruction algorithms as well.

In the near future, as any other iterative method, the regularization has to be considered such as the smoothing, the trade off between the resolution depending on the number of points and the computational cost. A possible solution for the contour smoothing is to add into the velocity a regularizing term depending on the object curvature [95]. Moreover, we have to study the effect of the noise in the data for the reconstruction by the level set method.

In a long-term future, concerning the reconstruction with physical profile functions, the forward mapping matrix G for real data must take into account the wave propagation on the object surface. It depends on the shape of the evolving object at each step of the iteration and this is still an open problem.

Part II: Résumé en français

Introduction

Lorsqu'une onde progressive rencontre un obstacle dans un milieu, elle s'écarte de sa direction de propagation initiale. Ce phénomène est appelé diffraction d'ondes. Le problème direct de diffraction correspond au calcul du champ diffracté par un objet connu, alors que le problème inverse de diffraction correspond à la détermination d'informations caractéristiques sur un objet inconnu à partir du champ diffracté, qui est connu [1]. Dans le domaine de l'électromagnétisme, un problème important est la caractérisation et l'identification de cibles radar. Le Radar (RAdio Detection And Ranging) est un système de détection d'objets qui mesure la distance et exploite les informations caractéristiques d'objets par transmission d'ondes électromagnétiques et réception de la réponse de ces objets [2]. Les applications principales du radar appartiennent au domaine militaire. Avec le développement rapide de la technologie radar, les objectifs du radar ne sont pas seulement la détection mais également la caractérisation et d'identification.

Parmi les problèmes d'identification de cibles radar, la caractérisation de cibles furtives est un sujet pertinent. La furtivité est destinée à produire un écho radar très faible et ceci peut être obtenu par le choix de formes spécifiques de la cible ou par l'utilisation de matériaux composites, qui absorbent les ondes électromagnétiques dans les bandes de fréquences radar habituelles. Mais, cela peut être contré en utilisant des fréquences plus basses. En outre, l'utilisation de bandes de fréquences basses est très importante dans le cas des radars à pénétration de sol (en anglais GPR pour Ground Penetrating Radar) pour la caractérisation des cibles enterrées, car l'atténuation des ondes dans la plupart des sols augmente avec la fréquence. Ces bandes de fréquences plus basses correspondent à la région de Rayleigh et à la région de résonance pour des dimensions d'objet respectivement petites et du même ordre de grandeur par rapport aux longueurs d'ondes électromagnétiques. Contrairement à l'imagerie en haute fréquence, les méthodes en basse fréquence ne peuvent pas fournir une haute résolution, mais elles donnent pourtant des informations utiles sur la dimension globale et la forme approximative de la cible.

L'utilisation d'une forme particulière d'onde électromagnétique, dont la dépendance temporelle est celle d'une fonction rampe, a été initialement appliquée à l'identification de cibles radar en basse fréquence par Kennaugh et Moffatt en 1965 [3]. La réponse en rampe est la réponse temporelle rétrodiffusée en champ loin-

tain par une cible éclairée par une telle rampe. Cette réponse en rampe est approximativement proportionnelle à la fonction de profil de la cible radar, qui est définie comme l'aire de la cible dans chaque plan perpendiculaire à la direction d'observation. Cette propriété a été utilisée par Young [4, 5] pour reconstruire la forme de cibles radar à partir d'un nombre limité de directions. Sa méthode, connue sous le nom de technique de la réponse de la rampe, utilise les fonctions de profil dans 3 directions mutuellement orthogonales et consiste à limiter le contour de la cible inconnue par des surfaces approchées, ajustées itérativement pour obtenir des images optimales.

Des efforts considérables ont été réalisés pour améliorer la technique de la réponse en rampe, qui a été appliquée à l'identification de cibles diélectriques [6, 7] ainsi qu'à l'imagerie acoustique d'objets sous-marins [8, 9]. Toutefois, ces applications utilisent la méthode des "surfaces limitantes approchées" proposée par Young, qui est limitée aux objets convexes et isolés [5]. La méthode de reconstruction à partir de projections nécessite un nombre considérable de directions d'observation et des objets à symétrie plane [10, 11, 12]. La méthode de Chauveau [13] permet de générer de bonnes reconstructions non seulement pour des objets de forme arbitraire, mais également pour plusieurs objets séparés, ceci à partir de seulement 3 directions mutuellement orthogonales. Par contre, dans les cas de directions non-orthogonales, les 3 méthodes produisent des images déformées. Cependant, en pratique, les équipements radar ont souvent un angle de vue limité que ce soit en télédétection ou pour de grandes cibles. Par conséquent, il est nécessaire d'optimiser la reconstruction dans des directions arbitraires.

Par conséquent, ma thèse est consacrée à développer un algorithme avec des performances améliorées pour des directions arbitraires. Il est nécessaire d'utiliser un processus d'optimisation pour obtenir des estimées optimales de la cible à partir des données observées. Le processus d'optimisation comprend deux sous-problèmes.

- Un problème direct qui calcule les fonctions de profil à partir d'objets connus, sans aucune restriction sur les formes ou les directions.

- Un problème inverse qui cherche à minimiser les erreurs entre les fonctions de profil calculées à partir de l'objet estimé et les fonctions de profil de l'objet original. Nous choisissons de résoudre ce problème itérativement.

Cette thèse est organisée comme suit :

Dans le chapitre 1, le but est de situer le contexte de cette thèse, en rappelant quelques notions et méthodes pour caractériser la réponse électromagnétique d'une cible radar furtive, comme la Surface Equivalente Radar (SER) et les bandes de fréquence radar. Puis, les technologies principales de furtivité et de contre-furtivité sont abordées, et le choix des radars basse fréquence est expliqué.

Dans le chapitre 2, l'imagerie radar à partir de réponses en rampe est présentée. Après avoir donné les définitions de la réponse en rampe, de la fonction de profil et de la bande de fréquences requise, un état de l'art des algorithmes de reconstruction d'images radar à partir de fonctions de profil est présenté. Des exemples d'objets variés sont reconstruits avec la méthode de Chauveau [13], pour des directions mutuellement orthogonales et non-orthogonales.

Dans le chapitre 3, nous présentons notre contribution à l'optimisation de la reconstruction d'images avec des fonctions de profil dans des directions arbitraires.

Dans la section 3.1, l'objectif est de résoudre le problème direct. Pour cela, nous développons un algorithme pour calculer la fonction de profil géométrique d'un objet 3-dimensionnel (3D) de forme arbitraire. Ensuite, nous l'appliquons pour évaluer quantitativement la qualité des reconstructions d'image et pour identifier des cibles radar avec une base de données de modèles possibles.

Dans la section 3.2, l'objectif est de résoudre le problème inverse. Nous choisissons la méthode level-set, qui est bien adaptée à notre problème : nous introduisons le principe de cette méthode avec les différents types de vitesse d'évolution. Nous présentons la méthode level-set dans notre cas de reconstruction d'image à partir de fonctions de profil dans des directions arbitraires, en prenant l'exemple d'une sphère pour illustrer le processus itératif. Enfin, nous présentons une méthode efficace pour réduire le coût de calcul, la méthode level-set à 'bande étroite'.

Dans la section 3.3, nous présentons des résultats de reconstruction 3D, en utilisant la méthode level-set à 'bande étroite' pour différents objets : d'abord, avec des fonctions de profil géométriques dans des directions orthogonales ; ensuite, avec des fonctions de profil géométriques dans des directions non orthogonales ; enfin, avec des fonctions de profil physiques. L'effet de certains paramètres de reconstruction est étudié.

Finalement, dans le chapitre 4, les conclusions générales sont données pour résumer le travail effectué dans cette thèse, et quelques perspectives sont proposées pour les travaux futurs.

1

Caractérisation et identification de cibles radar

Les systèmes radar utilisent des ondes électromagnétiques pour éclairer des cibles et détecter les signaux renvoyés par ces cibles. L'analyse de ces signaux réfléchis permet d'obtenir des informations caractéristiques (dimension, forme et orientation) pour identifier les cibles, en particulier les cibles furtives. La furtivité consiste à atténuer la surface équivalente radar (SER), ou "radar cross-section" (RCS), qui mesure la capacité de détection d'un objet par un radar. Pour caractériser et identifier des cibles furtives, et donc contrer la furtivité, deux problèmes doivent être considérés :

- le choix de la technologie qui permet d'augmenter la SER.

- le choix de la méthode d'analyse des signaux qui permet d'exploiter efficacement les signaux reçus, en prenant en compte les choix technologiques de contre-furtivité. Dans cette thèse, c'est cette problématique qui nous concerne.

Surface équivalente radar (SER) La SER d'un objet dépend de plusieurs facteurs :

- la relation entre la dimension de l'objet et la longueur d'onde de l'excitation, (donc sa fréquence, $f = c/\lambda$) ;

- la réflectivité de la surface de l'objet (rugosité de la surface et composition du matériau) ;

- la directivité de l'onde réfléchie (forme de la cible) ;

- la polarisation du radar.

La SER est donc une information intrinsèque qui dépend des caractéristiques de la cible (forme, dimension et matériaux) et de l'onde incidente. Cette information est particulièrement importante pour les applications militaires.

La Fig. 1.1 donne la SER d'une sphère parfaitement conductrice électriquement, en fonction du rapport entre la dimension caractéristique de la cible, D, et la longueur d'onde, λ.

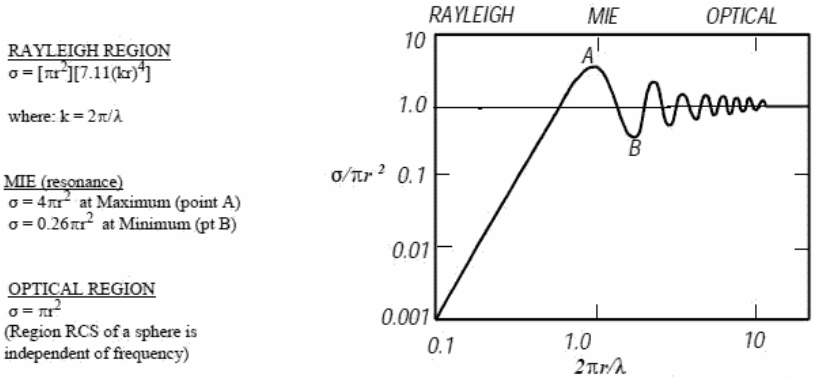

Figure 1.1: SER d'une sphère parfaitement conductrice de diamètre $D = 2r$, en fonction du rapport r/λ.

Le comportement de la SER peut être divisé en 3 zones, selon la valeur de D/λ.

- La zone de Rayleigh ($D \ll \lambda$), quand l'objet est très petit devant la longueur d'onde, correspond aux basses fréquences. La SER varie comme f^4 et donne des informations sur le volume de l'objet.

- La zone de résonance ($D/2 < \lambda < 10D$), appelée zone de Mie dans le cas de la sphère. La SER oscille à cause des interférences entre les ondes directement réfléchies par la surface et les ondes rampantes à la surface de l'objet puis réfléchies. Cette zone donne donc des informations sur la taille de l'objet.

- La zone optique ($D \gg \lambda$), quand l'objet est très grand devant la longueur d'onde, correspond aux hautes fréquences. Cette zone permet d'obtenir plus de détails sur l'objet.

Furtivité et contre-furtivité Les principales techniques de furtivité sont soit d'ordre géométrique, pour renvoyer les ondes radar dans d'autres directions que celles de l'émetteur (facettes ou formes arrondies), soit utilisent des matériaux absorbants les ondes radar. La technique de forme perd son efficacité pour les radars basse fréquence. Ces radars opèrent entre 1 MHz et 3 GHz et correspondent aux zones de Rayleigh et de résonance pour des objets de dimensions petites et du même ordre de grandeur que la longueur d'onde. De plus, en basse fréquence, pour être efficaces, les matériaux absorbants deviennent très épais, donc très lourds et chers. Contrairement aux hautes fréquences, les basses fréquences ne permettent pas d'obtenir une

bonne résolution (détails sur la cible), mais elles fournissent des informations utiles sur l'envergure et la forme globale de la cible.

C'est pourquoi, nous nous intéressons aux méthodes d'identification de cibles radars en basse fréquence. A partir des signaux obtenus en basse fréquence, notre objectif est de caractériser et d'identifier les cibles. Parmi les méthodes de diffraction inverse, l'imagerie radar à partir de réponses en rampe est bien adaptée aux basses fréquences et elle permet de reconstruire des images tri-dimensionnelles (3D) de cibles. Dans cette thèse, cette méthode est donc choisie.

2

Imagerie radar à partir de réponses en rampe

2.1 La réponse en rampe

La réponse en rampe d'une cible est le signal transitoire rétrodiffusé en champ lointain par cette cible, lorsqu'elle est éclairée par une onde électromagnétique plane dont la dépendance temporelle est en forme de rampe. Elle a été utilisée pour l'identification de cibles radar initialement par Kennaugh et Moffatt en 1965 [3, 54], qui ont montré qu'elle est reliée à la fonction de profil.

2.2 La fonction de profil

Tout d'abord, nous définissons la direction incidente sur une cible par le vecteur unitaire $u(\theta, \phi)$, déterminé par son angle d'inclinaison, θ, et son angle d'azimut, ϕ, dans un système de coordonnées sphériques (Fig. 2.1).

La fonction de profil "géométrique" La fonction de profil "géométrique" d'un objet, $A_g(u)$, dans la direction u, est définie comme son aire dans chaque plan de coupe transverse selon u (Fig. 2.2).

$$A_g(u) = \int_{-\infty}^{+\infty} \int_{-\infty}^{+\infty} O(x, y, z) dy dz \tag{2.1}$$

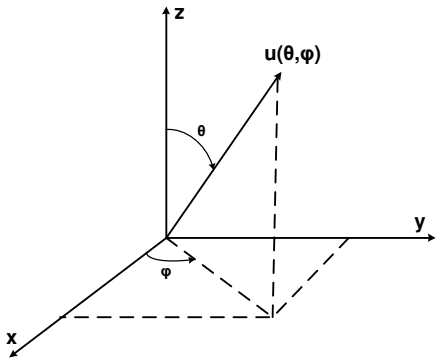

Figure 2.1: Vecteur unitaire $u(\theta, \phi)$ dans un système de coordonnées sphériques.

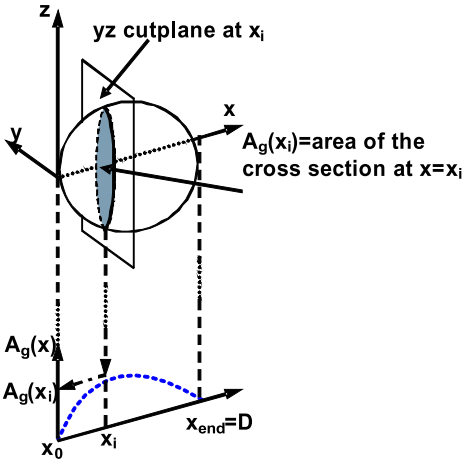

Figure 2.2: Illustration de la fonction de profil géométrique d'un objet, $A_g(x)$, selon la direction x. D est la dimension caractéristique de l'objet dans la direction x.

avec

$$O(x,y,z) = \begin{cases} 1 \text{ si } (x,y,z) \text{ à l'intérieur l'objet} \\ 0 \text{ si } (x,y,z) \text{ à l'extérieur l'objet} \end{cases}$$

où $O(x, y, z)$ est une fonction objet binaire.

En configuration monostatique, Kennaugh et Moffatt ont montré que la fonction de profil géométrique, $A_g(u)$, est approximativement proportionnelle à la réponse en rampe transitoire de la cible, $h_r(t)$, [3, 54] :

$$h_r(t) \approx -\frac{1}{\pi c^2} A_g(u) \quad \text{with} \quad u = \frac{ct}{2} \tag{2.2}$$

où c est la vitesse de la lumière dans l'espace libre, t la variable temporelle et u la variable spatiale.

La fonction de profil "physique" En utilisant la relation Eq. (2.2), nous définissons la fonction de profil "physique", $A_p(u)$, comme exactement proportionnelle à la réponse en rampe :

$$h_r(t) = -\frac{1}{\pi c^2} A_p(u) \tag{2.3}$$

2.3 La bande fréquentielle requise

Pour que la fonction de profil physique, $A_p(u)$, calculée par l'Eq. (2.3) soit une bonne estimée de la fonction de profil géométrique, $A_g(u)$, d'une cible radar, il est nécessaire de choisir une bande fréquentielle d'analyse appropriée à la dimension de la cible. D'après [3, 4, 5, 54], cette bande correspond aux zones de Rayleigh et

de résonance (dimensions d'objets respectivement petites et du même ordre que la longueur d'onde), soit des longueurs d'ondes comprises entre $D/2$ et $200D$, où D est la dimension caractéristique de la cible dans la direction d'incidence. La bande fréquentielle correspondante est donnée par :

$$f = [f_{min}; f_{max}] = \left[\frac{c}{200D}; \frac{2c}{D}\right] \tag{2.4}$$

2.4 Exemple d'une sphère

La Fig. 2.3 considère l'exemple d'une sphère parfaitement conductrice électriquement (PC) de diamètre D = 10 cm dans l'espace libre. Avec cette valeur de D, la bande fréquentielle d'analyse donnée par l'Eq. (2.4) est [15 MHz ; 6 GHz]. La Fig. 2.4, compare la fonction de profil physique, $A_p(x)$, (traits pleins) avec la fonction de profil géométrique, $A_g(x)$, (traits pointillés), calculée analytiquement avec l'Eq. (2.1). Les courbes sont très similaires dans la partie directement éclairée, où la contribution principale au signal rétrodiffusé à l'instant t vient de la réflexion directe sur la surface de la cible à la distance $x = ct/2$. Au contraire, dans la zone d'ombre, les courbes diffèrent, car le signal rétrodiffusé correspond en grande partie aux ondes rampantes sur la surface de la cible, avec un retard additionnel.

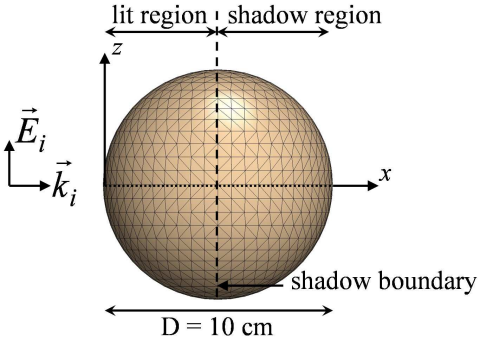

Figure 2.3: Configuration d'étude pour une sphère PC de diamètre $D = 10$ cm.

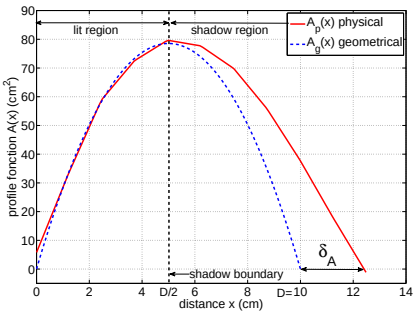

Figure 2.4: Comparaison entres les fonctions de profil physique, $A_p(x)$, et géométrique, $A_g(x)$, d'une sphère PC de diamètre $D = 10$ cm.

2.5 Algorithmes de reconstruction d'image

L'imagerie radar à partir de réponses en rampe consiste à reconstruire une image 3D de la cible avec des fonctions de profil, obtenues à partir de réponses en rampe dans un nombre fini d'angles de vue. A cause de la limitation de résolution due aux basses fréquences, l'objectif est de générer une image approchée du contour de l'objet. L'algorithme initial, proposé par Young [5], nécessite seulement 3

directions d'observation et il utilise des surfaces limitantes approchées englobant la cible. Il a été appliqué à la diffusion électromagnétique [6, 7, 51, 52, 53, 63, 64] et en imagerie acoustique des objets sous-marins [8, 9]. Cet algorithme est limité aux objets convexes et isolés, contrairement à un algorithme plus récent proposé par Chauveau [13], qui calcule une contribution égale au produit des fonctions de profil dans 3 directions d'observation, puis choisit une direction pour balayer les plans de coupe successifs en choisissant les points de plus forte contribution, tels que l'aire résultante soit égale à la valeur de la fonction de profil dans le plan correspondant. Un autre type de méthode consiste à appliquer les algorithmes de reconstruction à partir de projections, qui nécessitent un nombre très élevé d'angles de vue ainsi que des objets à symétrie plane [10, 11, 12].

2.6 Résultats de reconstruction avec la méthode de Chauveau

L'algorithme de Chauveau nécessite seulement 3 directions d'observation et il est capable de reconstruire des objets non convexes et séparés. Nous le choisissons donc pour présenter une exemple de reconstruction à partir de directions arbitraires (orthogonales puis non orthogonales). Nous prenons comme exemple d'objet un "step-cylinder" PC de dimension $D = 30$ cm, Fig. 2.5 (a), dans la bande fréquentielle $[5$ MHz ; 8 GHz$]$. En considérant 3 directions mutuellement orthogonales, $[u_1 = x, u_2 = y, u_3 = z]$, la Fig. 2.5 (b) compare les fonctions de profil géométriques et physiques. L'image est reconstruite avec une bonne précision avec les 3 fonctions de profil géométriques, Fig. 2.5 (c), mais elle est distordue avec les 3 fonctions de profil physiques, Fig. 2.5 (d).

Nous considérons ensuite 3 directions non orthogonales, $[u_1 = (90°, 50°), u_2 = y, u_3 = z]$. L'image reconstruite avec les 3 fonctions de profil géométriques, Fig. 2.6 (a), est allongée perpendiculairement à la bissectrice des 2 directions non orthogonales (u_1 et u_2). De même, l'image reconstruite avec les 3 fonctions de profil physiques, Fig. 2.6 (b), est fortement distordue.

En conclusion, la méthode de Chauveau permet d'obtenir des résultats acceptables avec des directions d'observation mutuellement orthogonales, alors qu'elle donne des résultats très distordus avec des directions non orthogonales. Mais, à cause des contraintes pratiques d'angles de vue limités des équipements radars, il est très difficile, et souvent impossible, d'éclairer une cible à partir de 3 directions orthogonales, il est donc nécessaire d'optimiser la reconstruction à partir de directions arbitraires. Dans le prochain chapitre, nous présentons la contribution principale de cette thèse.

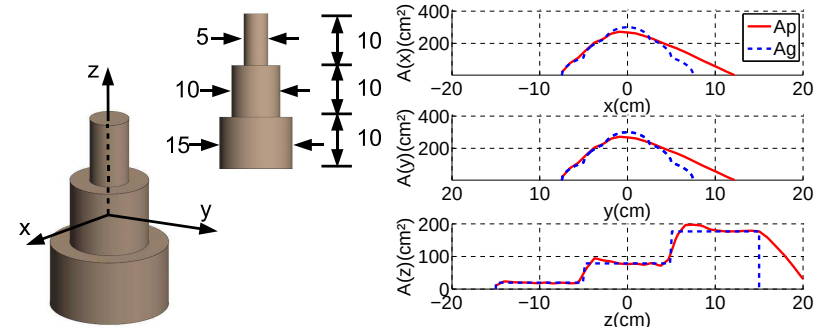

(a) (b)

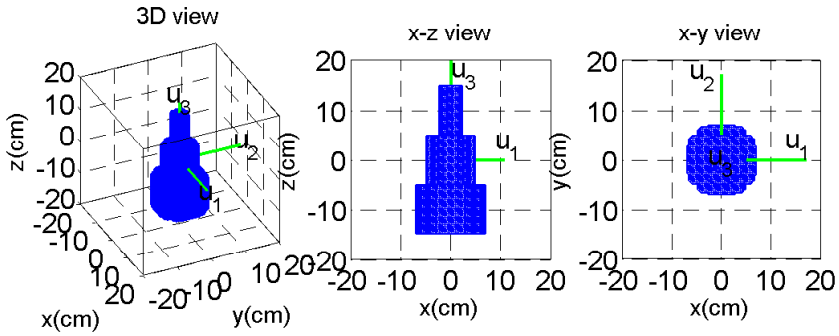

(c)

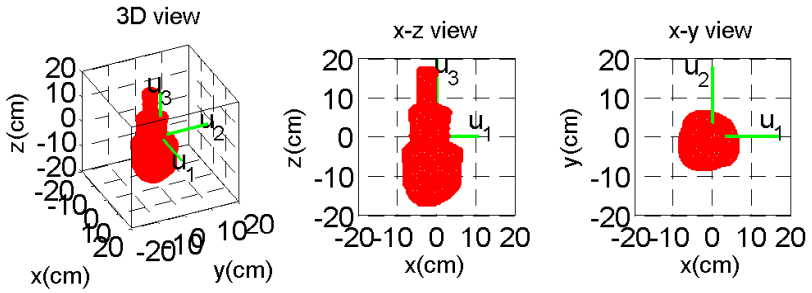

(d)

Figure 2.5: (a) "Stepcylinder" PC ($D = 30$ cm). (b) Comparaison entre les fonctions de profil géométriques et physiques dans les directions x, y et z. Images 3D reconstruites à partir des fonctions de profil géométriques (c) et physiques (d), dans 3 directions orthogonales, avec la direction de balayage z.

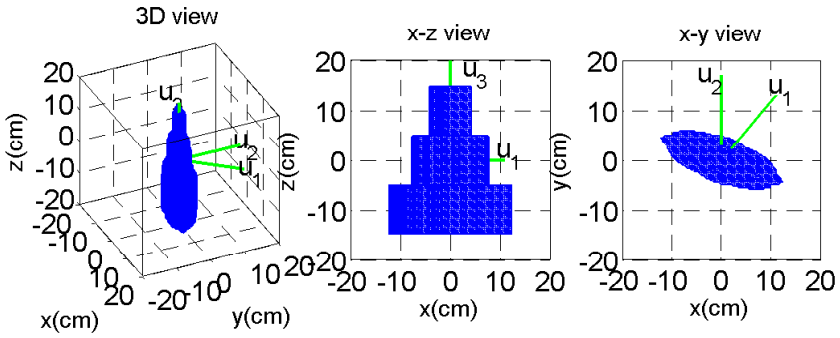

(a)

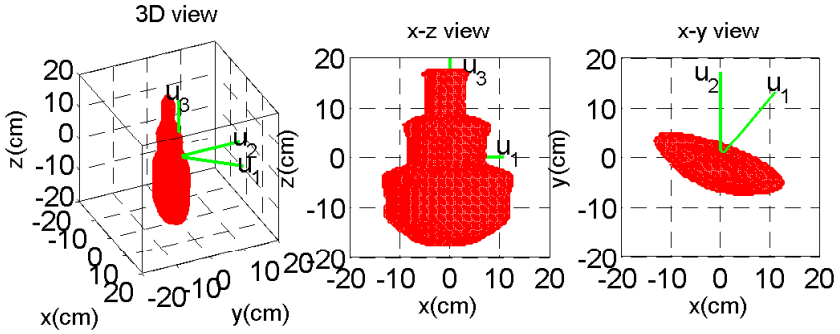

(b)

Figure 2.6: Images 3D du "stepcylinder" (Fig. 2.5) reconstruites à partir des fonctions de profil géométriques (a) et physiques (b), dans 3 directions non orthogonales $[u_1 = 50, u_2 = y, u_3 = z]$, avec la direction de balayage z.

3

Optimisation de la reconstruction dans des directions arbitraires

Pour améliorer les performances dans des directions d'observation arbitraires, il est nécessaire d'utiliser une procédure d'optimisation pour obtenir une estimée correcte de la cible en minimisant l'écart entre les données (les fonctions de profil de l'objet original, qui est inconnu) et les fonctions de profil de l'objet estimé. Notre problème peut se mettre sous la forme, pour chaque direction d'observation :

$$G^u O = A^u \tag{3.1}$$

où $A^u(M, 1)$ sont les données observées, c'est-à-dire la fonction de profil dans la direction d'observation u, en forme de vecteur de dimension M (M étant le nombre de points de la fonction de profil), $O(N^3, 1)$ le vecteur représentant l'objet 3D binaire inconnu (N étant le nombre de points de l'objet dans chaque dimension). $G^u(M, N^3)$ est la matrice d'observation.

Il est important de noter que les fonctions de profil observées peuvent être soit des fonctions de profil géométriques, A_g, pour le cas idéal ou des fonctions de profil physiques, A_p, pour le cas pratique. Afin de se concentrer sur l'amélioration de la performance pour les reconstructions dans des directions arbitraires, dans cette thèse, la matrice d'observation G est seulement considérée comme décrivant la relation entre la fonction de profil géométrique obtenue à partir de l'objet initial et celle de l'objet estimé.

Par conséquent, le processus d'optimisation comprend deux sous-problèmes :

- Problème direct : calculer la fonction de profil géométrique d'un objet 3D quelconque. Ceci peut être utilisé pour obtenir des fonctions de profil géométriques de l'objet estimé au cours du processus itératif, ainsi que leurs erreurs avec les fonctions de profil observées à partir de l'objet original. Cela est nécessaire à chaque itération pour le problème inverse.

- Problème inverse : trouver l'objet inconnu en utilisant une méthode itérative efficace pour diminuer l'erreur entre les fonctions de profil de l'objet estimé et les fonctions de profil observées. Une estimée optimale est obtenue quand une tolérance d'erreur est atteinte.

3.1 Problème direct : calcul de fonctions de profil géométriques

Nous avons développé un algorithme pour calculer les fonctions de profil d'un objet 3D de forme quelconque dans des directions arbitraires [69].

En considérant un objet 3D binaire $O(x, y, z)$ inclus dans un domaine de calcul C_D, l'algorithme de calcul de la fonction de profil géométrique est décrit par les étapes suivantes :

-Étape 1 Couper le domaine de calcul C_D en tranches successives perpendiculaires à la direction d'observation $u(\theta, \phi)$, d'épaisseur δu, où δu est le pas discret dans la direction u. La fonction de profil numérique $A_c(u_i)$ à la position $u = u_i$ peut être calculée par :

$$A_c(u_i) = V_{S_i}/\delta u \tag{3.2}$$

où V_{S_i} est le volume de la tranche S_i à la position $u = u_i$.

-Étape 2 Calculer la contribution, W, que chaque pixel donne à la tranche S_i par :

$$W = \begin{cases} 1 - |d/\delta u|; & d \in [-\delta u, \delta u] \\ 0; & \text{sinon} \end{cases} \tag{3.3}$$

où $d = u_P - u_i$ est la distance signée du centre du pixel P, de coordonnée u_P dans la direction u, au plan à la position u_i.

-Étape 3 Sommer les contributions individuelles de tous les pixels pour obtenir le volume de la tranche S_i :

$$V_{S_i} = \sum_x \sum_y \sum_z W \times \delta u^3 \times O(x, y, z) \tag{3.4}$$

où δu^3 est le volume de chaque pixel et $O(x, y, z)$ est une fonction caractéristique de l'objet binaire, définie par :

$$O(x, y, z) = \begin{cases} 1 \text{ si } P(x, y, z) \text{ intérieur de l'objet} \\ 0 \text{ si } P(x, y, z) \text{ extérieur de l'objet} \end{cases}$$

-Étape 4 Combiner Eq. (3.2) et (3.4) pour calculer la fonction de profil numérique $A_c(u_i)$, à la position u_i :

$$A_c(u_i) = \sum_x \sum_y \sum_z W \times \delta u^2 \times O(x, y, z) \tag{3.5}$$

Pour mesurer quantitativement la différence entre une fonction de profil de référence $A_{ref}(u)$ et une fonction de profil $A_c(u)$ calculée par cet algorithme, selon la direction u, deux types d'erreurs sont considérées :

- L'erreur absolue, qui est une fonction de la position le long de la direction u, est définie comme :

$$E(u) = |A_{ref}(u) - A_c(u)| \tag{3.6}$$

- L'erreur relative globale pour la direction u est définie comme :

$$E_r^{(u)} = \frac{\int E(u)du}{\int A_{ref}(u)du} \times 100\% \tag{3.7}$$

Nous appliquons maintenant cet algorithme pour évaluer quantitativement la qualité de la reconstruction d'image en calculant l'erreur entre la fonction de profil de l'objet original, et la fonction de profil calculée à partir de l'objet reconstruit. La Fig. 3.1 décrit le processus d'évaluation de la qualité pour la reconstruction de l'image 3D à partir de fonctions de profil.

Les notations relatives à ce processus sont données comme suit :

- A_g^O, la fonction de profil géométrique de l'objet original calculée analytiquement par les formules connues pour des géométries régulières

- Rg, l'objet 3D reconstruit à partir de fonctions de profil géométriques A_g^O, par exemple, le step-cylinder reconstruit dans la Fig. 2.5 (c).

En conséquence, les fonctions de profil géométriques sont calculées par l'algorithme que nous avons développé :

- A_c^{Rg}, à partir de l'objet 3D reconstruit Rg.

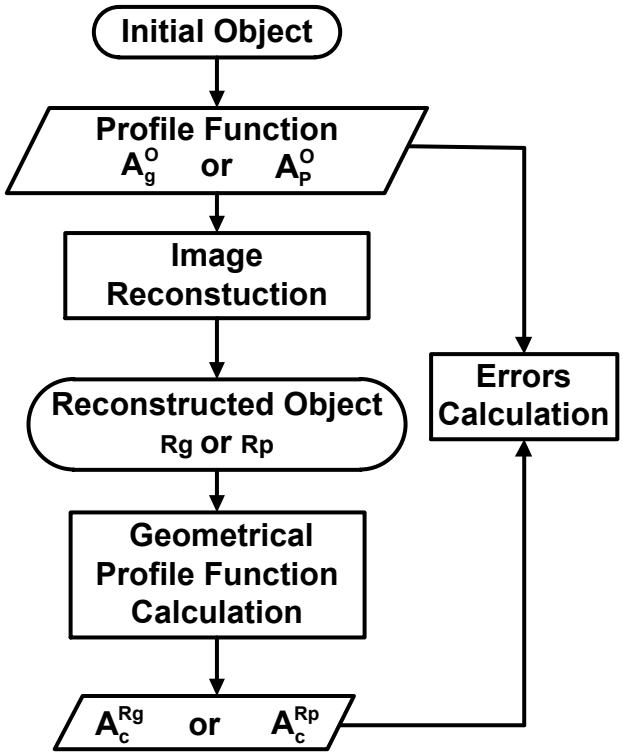

(a)

Figure 3.1: Organigramme décrivant le processus d'évaluation de la qualité pour la reconstruction d'image 3D à partir de fonctions de profil.

L'évaluation de la qualité de l'image reconstruite (Rg) consiste à calculer quantitativement les erreurs entre A_g^O et A_c^{Rg}, avec l'Eq. (3.7).

Nous prenons comme exemple d'objet le step-cylinder reconstruit à partir de fonctions de profil géométriques dans des directions orthogonales (Fig. 2.5 (c)), avec $[u_1 = x, u_2 = y, u_3 = z]$, et non-orthogonales (Fig. 2.6 (b)), avec $[u_1 = 50°, u_2 = y, u_3 = z]$. En raison de la symétrie géométrique de cet objet, sa fonction de profil géométrique est la même dans n'importe quelle direction dans le plan xoy. Par conséquent, les 3 fonctions de profil géométriques initiales, A_g^O, sont présentées sur la Fig. 3.2 (courbe en pointillé bleu) et sont prises comme fonctions de profil de référence. Dans le cas orthogonal, les erreurs globales relatives entre la fonction de profil initiale, A_g^O, et la fonction de profil calculée à partir de l'objet reconstruit, A_c^{Rg} ("ortho"), sont très faibles (6%, 6% , 7% dans les directions x, y, z, respectivement). Au contraire, dans le cas non-orthogonal, les différences entre la fonction de profil initiale, A_g^O, et la fonction de profil calculée, A_c^{Rg} ("non ortho"), sont beaucoup plus importantes (13%, 13%, 7% dans les 3 directions d'observations respectives), ce qui confirme la déformation de l'image.

Ces exemples nous permettent de confirmer que notre algorithme de calcul de fonctions de profil peut être considéré comme un outil efficace pour évaluer quantitativement la qualité des reconstructions d'image.

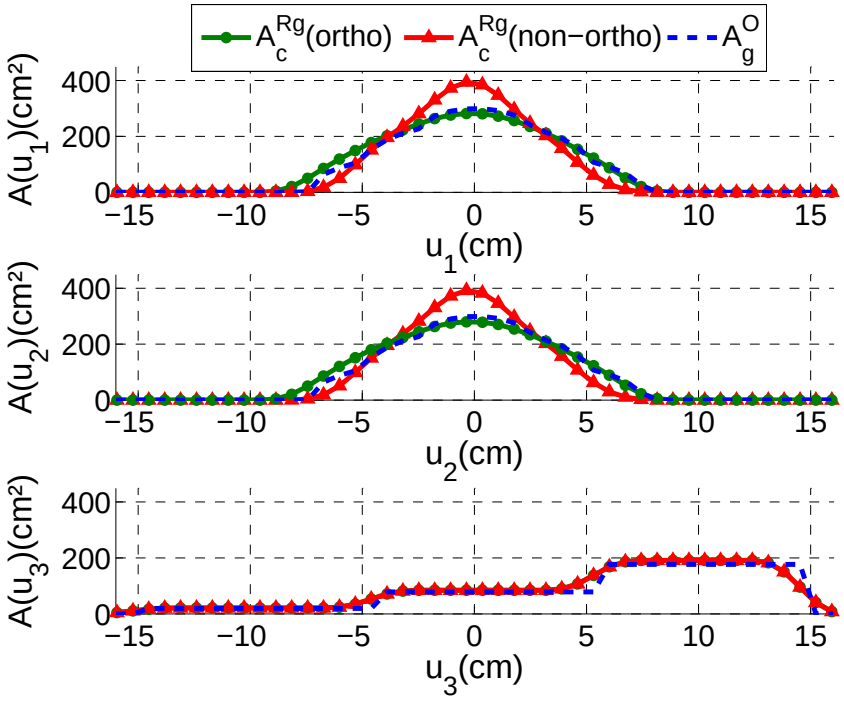

Figure 3.2: Comparaison entre les fonctions de profil géométriques initiales, A_g^O, et les fonctions de profil calculées, A_c^{Rg} (“ortho”), à partir d’ un step-cylinder reconstruit dans le cas orthogonal, $[u_1 = x, u_2 = y, u_3 = z]$, et A_c^{Rg} (“non ortho”) dans le cas non-orthogonal, $[u_1 = 50°, u_2 = y, u_3 = z]$.

De plus, en utilisant une base de données contenant des modèles possibles, nous avons appliqué cet algorithme pour identifier une cible radar à partir de son objet reconstruit obtenu avec des fonctions de profil physiques dans seulement 3 directions [69]. Le procédé permet de comparer l’objet et les modèles reconstruits dans un ensemble complet de directions afin d’éviter que différentes formes puissent avoir les mêmes fonctions de profil dans certaines directions. Compte tenu de la mauvaise condition de la résolution limitée rencontrée dans l’imagerie radar basse fréquence, le processus d’identification réussit à trouver les meilleurs modèles possibles pour l’objet étudié.

L’algorithme développé peut aussi être utilisé, dans la section suivante, pour calculer les fonctions de profil de l’objet en évolution dans le problème inverse.

3.2 Problème inverse : reconstruction d’image avec la méthode level-set

Le problème à résoudre, donné à l’Eq. (3.1), est linéaire. Dans notre cas, nous avons besoin d’une méthode itérative adaptée à un système mal conditionné, avec une matrice creuse de grandes dimensions. Les tests numériques comparant la méthode LSQR (least square method en anglais) avec plusieurs autres algorithmes

de gradient conjugué indiquent que LSQR est la méthode la plus fiable lorsque la matrice d'observation est mal conditionnée [71]. Par conséquent, nous utilisons d'abord la méthode LSQR pour résoudre notre problème. Cependant, comme la plupart de ces méthodes itératives, elle n'est pas adaptée au cas particulier que nous cherchons à résoudre, dans lequel l'objet 3D est binaire. En effet, nous voulons reconstruire la forme globale d'un objet dont chaque pixel est soit vide (état 0) soit occupé (état 1).

La plupart des méthodes itératives font évoluer de façon explicite la forme de l'objet lors de l'itération. Au contraire, la méthode level-set représente la forme comme le niveau zéro d'une fonction de dimension supérieure, ce qui ne nécessite aucune hypothèse a priori sur la géométrie de l'objet ou de la structure. Cet avantage est d'une grande importance pour le problème inverse. La méthode level-set à été introduite à l'origine par Osher et Sethian [72], et a été appliquée dans les domaines de la dynamique des fluides [73, 74, 75, 76, 77], de la segmentation d'image et de la vision par ordinateur [78, 79, 80, 81, 82, 83], ainsi que pour les problèmes de diffraction inverse [84, 85, 86, 87]. En raison de sa représentation implicite de la forme, elle peut gérer les changements topologiques survenant au cours de la déformation de la forme d'une manière complètement automatique et implicite. Par conséquent, nous choisissons cette méthode dans le problème inverse pour obtenir une forme satisfaisante de la cible.

3.2.1 La méthode level-set

Dans un domaine de calcul C_D contenant l'objet Ω, la fonction de niveau $\phi(\vec{x}, t)$, fonction de la variable spatiale $\vec{x}$ et de la variable temporelle t, est définie par :

$$\begin{cases} \phi(\vec{x}, t) > 0 & \text{si} \vec{x} \notin \Omega; \\ \phi(\vec{x}, t) = 0 & \text{si } \vec{x} \in C; \\ \phi(\vec{x}, t) < 0 & \text{si } \vec{x} \in \Omega; \end{cases} \tag{3.8}$$

où Ω est l'objet délimité par sa frontière C (ou Γ). Le paramètre t peuvent être omis pour simplifier puisqu'il s'agit d'un paramètre de temps artificiel. La Fig. 3.3 (a) donne la représentation de la forme en utilisant la fonction de niveau ϕ pour un objet Ω dans le domaine de calcul C_D. Avec cette représentation, l'objet est binaire.

Une fonction de distance signée est communément choisie pour représenter la fonction de niveau :

$$\phi(\vec{x}) = \begin{cases} -min(|\vec{x} - \vec{x_C}|) & \text{si } \vec{x} \in \Omega \\ 0 & \text{si } \vec{x} \in C \\ min(|\vec{x} - \vec{x_C}|) & \text{si } \vec{x} \notin \Omega \end{cases} \tag{3.9}$$

où $\vec{x_C}$ comprend tous les points de la frontière C. Cette fonction satisfait la condition de l'Eq. (3.8). En outre, elle est assez lisse car $min(|\vec{x} - \vec{x_C}|)$ est en fait la distance euclidienne avec gradient $|\bigtriangledown \phi| = 1$.

L'évolution de la fonction de niveau est contrôlée par une vitesse normale V_N par une équation de Hamilton-Jacobi, et elle est connue comme l'équation de level-set [88] :

$$\frac{\partial \phi}{\partial t} + \frac{\partial \vec{x}}{\partial t} \cdot \bigtriangledown \phi = \frac{\partial \phi}{\partial t} + V_N |\bigtriangledown \phi| = 0 \tag{3.10}$$

La Fig. 3.3 (b) montre un exemple de déformation de forme par la méthode level-set, nous pouvons voir que la forme change de topologie en se divisant en deux. Il serait très difficile de décrire cette transformation numériquement par le paramétrage du contour de la forme et en suivant son évolution. On aurait besoin d'un algorithme capable de détecter le moment où la forme se divise en deux parties et, ensuite, de construire des paramétrages pour les deux courbes nouvellement obtenues. Cela prouve qu'il peut être plus facile de travailler avec une forme à travers sa fonction de niveau que directement avec cette forme, car l'utilisation directe de la forme aurait besoin de considérer et de traiter toutes les déformations possibles que la forme pourrait subir.

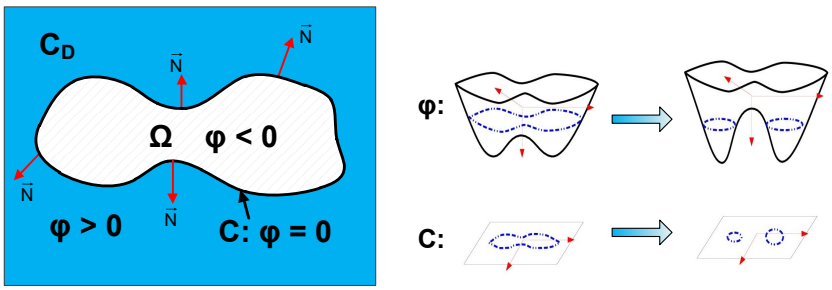

(a) (b)

Figure 3.3: Illustration du principe de la méthode level-set : (a) représentation de la forme; (b) déformation de la forme

3.2.2 La vitesse d'évolution

En général, la vitesse dépend de la position, du temps et de la géométrie de l'interface. Selon l'application, il y a 3 types de vitesse :

-Vitesse externe Une vitesse d'évolution externe est donnée à partir de principes physiques externes, comme l'advection en dynamique des fluides [73, 74, 75, 77].

-Vitesse de type Gradient Ce type de vitesse utilise l'idée de l'algorithme du gradient. Son principe est de construire une vitesse normale comme une fonction du gradient de la forme négative telle qu'une fonction de coût peut être minimisée

avec un pas de temps suffisamment faible. La vitesse est liée à une dérivée continue de la fonction de coût par rapport à une perturbation de la géométrie. Elle a d'abord été introduite par Santosa [84] pour résoudre des problèmes de déconvolution et de diffraction par un écran. Ensuite, elle a été appliquée par Litman et al. [85, 90] et par Ramananjaona et al. [91, 92, 93] à des problèmes de diffraction électromagnétique inverse, et par Dorn et al. [87, 94] et par Ferraye et al. [95] à la tomographie électromagnétique.

-Vitesse dépendant de la courbure moyenne Ce type de vitesse est utilisé dans les modèles de contours actifs (ou modèles "snakes") pour la segmentation d'images et les problèmes de détection de bord [78, 79, 80, 96]. L'idée de base des modèles "snakes" est de faire évoluer une courbe, sous réserve de contraintes à partir d'une image donnée I_0, afin de détecter des objets dans l'image.

L'imagerie tridimensionnelle à partir de fonctions de profil, est en fait un problème de diffraction inverse impliquant la forme de l'objet. Par conséquent, nous choisissons d'utiliser la méthode de level-set avec une vitesse de type Gradient pour résoudre notre problème.

Suivant les travaux de Santosa [84], pour calculer la vitesse de type Gradient, nous définissons une fonction de coût des moindres carrés F selon l'équation formalisée pour notre problème dans Eq. (3.1) :

$$F = \frac{1}{2} \sum_{u} \parallel G^u O - A^u \parallel^2 \tag{3.11}$$

Nous obtenons l'équation de level-set adaptée à notre cas :

$$\phi^{k+1} = \phi^k - \sum_{u} [(G^u)^T (G^u O - A^u)] \triangle t | \bigtriangledown \phi| \tag{3.12}$$

où k est l'indice du pas de l'itération.

Avec la vitesse choisie, l'équation de level-set est une équation de Hamilton hyperbolique. Suivant [85], l'approximation numérique pour le gradient spatial $\bigtriangledown \phi$ dépend du signe de la vitesse.

Si $V_{ijk} \geq 0$, l'approximation de $| \bigtriangledown \phi|$ est donnée par :

$$\begin{aligned} | \bigtriangledown \phi_{ijk}|^2 &= max(D_{ijk}^{-x}, 0)^2 + min(D_{ijk}^{+x}, 0)^2 + max(D_{ijk}^{-y}, 0)^2 + \\ & \quad min(D_{ijk}^{+y}, 0)^2 + max(D_{ijk}^{-z}, 0)^2 + min(D_{ijk}^{+z}, 0)^2 \end{aligned} \tag{3.13}$$

Si $V_{ijk} < 0$, l'approximation de $| \bigtriangledown \phi|$ est donnée par :

$$\begin{aligned} | \bigtriangledown \phi_{ijk}|^2 &= min(D_{ijk}^{-x}, 0)^2 + max(D_{ijk}^{+x}, 0)^2 + min(D_{ijk}^{-y}, 0)^2 + \\ & \quad max(D_{ijk}^{+y}, 0)^2 + min(D_{ijk}^{-z}, 0)^2 + max(D_{ijk}^{+z}, 0)^2 \end{aligned} \tag{3.14}$$

où les opérateurs D^+ et D^- désignent le premier ordre de différence en avant et en arrière, respectivement.

Le premier ordre de différence en avant de ϕ en ce qui concerne la dimension x est défini comme :

$$D_{ijk}^{+x} \approx \frac{\phi_{i+1,j,k} - \phi_{i,j,k}}{\triangle x} \tag{3.15}$$

où $\triangle x$ est le pas spatial discret le long de la dimension x.

Le premier ordre de différence en arrière de ϕ en ce qui concerne x est défini comme :

$$D_{ijk}^{-x} \approx \frac{\phi_{i,j,k} - \phi_{i-1,j,k}}{\triangle x} \tag{3.16}$$

Les premiers ordres de différences en avant et en arrière en ce qui concerne les dimensions y et z sont analogues au cas de x.

Pour assurer la convergence et la stabilité en résolvant numériquement les équations aux dérivées partielles, le choix du pas de temps $\triangle t$ doit satisfaire à la condition CFL [89]. Une formulation possible est largement utilisée :

$$\triangle\, t(\frac{max|\vec{V}|}{min\{\triangle x, \triangle y, \triangle z\}}) = \alpha \tag{3.17}$$

où le coefficient α est tel que $0 < \alpha < 1$.

3.2.3 La méthode level-set dans notre cas

Nous voulons résoudre l'Eq. (3.12). Des critères d'arrêt doivent d'abord être déterminés :

- le nombre maximal d'itérations, k_{max};

- une valeur minimale de la tolérance d'erreur, ε_{tol}.

Pour cela, nous définissons un résidu normalisé r_k pour chaque itération k comme suit :

$$r_k = \frac{1}{3}\sum_{u=1}^{3} \frac{\parallel A^u - G^u O_k \parallel_{L^2}}{\parallel A^u \parallel} \tag{3.18}$$

où $\parallel \bullet \parallel_{L^2}$ est la norme dans l'espace de Hilbert.

A partir d'une fonction de niveau initiale, $\phi^k = \phi^0$, le processus d'itération pour l'imagerie avec des fonctions de profil dans 3 directions d'observation est le suivant :

Tant que $k \leq k_{max}$ et $r_k \geq \varepsilon_{tol}$,

1° Calcul de la vitesse d'évolution par $-\sum_u[(G^u)^T(G^uO - A^u)]$;

2° Calcul du gradient spatial $|\bigtriangledown \phi|$ par Eq. (3.13) ou Eq. (3.14) en fonction du signe de la vitesse obtenue à 1°;

3° Mise à jour de la fonction de niveau ϕ^{k+1} par Eq. (3.12);

4° Détermination de l'objet en sélectionnant les points avec des valeurs non-positives de ϕ;

En fait, à chaque itération, les points proches du niveau zéro de ϕ sont ceux qui sont les plus modifiés. Il est inutile d'effectuer le calcul sur l'ensemble du domaine. Par conséquent, une méthode efficace consiste à n'effectuer l'évolution que sur un ensemble de points voisins de la frontière. Cette méthode est appelée méthode de level-set «bande étroite» («Narrow band» en anglais).

3.2.4 La méthode level-set «bande étroite»

L'idée d'utiliser une bande étroite a été proposée à l'origine par Chopp [98], elle a été appliquée pour retrouver des formes dans les images [78] et largement développée par Adalsteinsson et Sethian [99]. La bande étroite est réalisée sous la forme d'un enrobage de la frontière C en sélectionnant un ensemble de points voisins situés à une distance finie de la courbe ou de la surface de niveau zéro, puis en attribuant des valeurs constantes à la fonction de niveau des autres points situés à l'extérieur de cette bande étroite. L'évolution de la fonction de niveau est effectuée seulement sur cette bande étroite. Au cours de l'évolution, le nouveau contour de niveau zéro (la frontière) est à nouveau déterminé de telle sorte que la bande étroite peut être mise à jour en fonction de cette nouvelle frontière de la même manière, puis le processus d'évolution est répété dans cette nouvelle bande étroite.

La Fig. 3.4 donne l'illustration de la construction de la bande étroite. C étant l'ensemble de niveau zéro, à savoir le contour en évolution, sa bande étroite correspondante est composée par les points se trouvant dans la zone délimitée par les courbes ou les surfaces C^+ et C^-, où C^+ est obtenu en dilatant le contour C vers une courbe située à une distance d_r et C^- en rétrécissant le contour C vers une courbe située à une distance d_r.

Maintenant, pour comparer la méthode de level-set ordinaire et la méthode «bande étroite», nous utilisons les résultats numériques de la sphère de diamètre $D = 10$ cm (Fig. 2.3). Pour montrer la performance dans des directions arbitraires, nous choisissons deux séries de directions d'observation :

- 3 directions orthogonales $[u_1(90°, 0°), u_2(90°, 90°), u_3(0°, 0°)]$, noté cas '3ortho';

- 2 directions orthogonales plus 1 direction non-orthogonale $[u_1(90°, 30°), u_2(90°, 90°), u_3(0°, 0°)]$, noté cas '2ortho+1arb'.

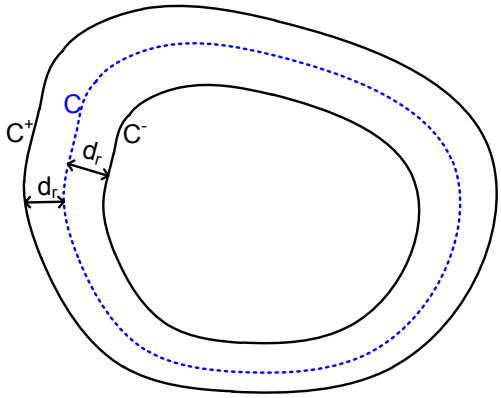

Figure 3.4: Illustration de la «bande étroite».

Ces deux cas sont présentés respectivement dans les Fig. 3.5 (a) et (b).

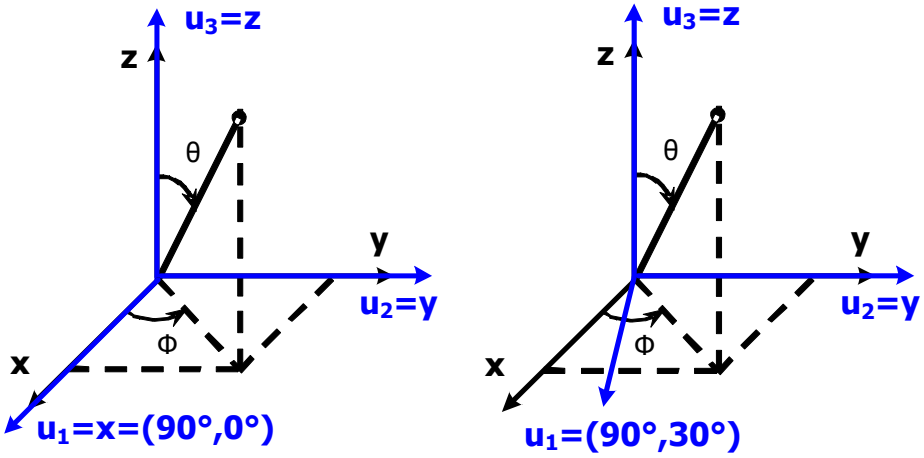

(a) (b)

Figure 3.5: Directions d'observation : (a) cas '3ortho' avec 3 directions orthogonales $[u_1(90°, 0°), u_2 = y, u_3 = z]$; (b) cas '2ortho+1arb' avec 2 directions orthogonales plus 1 direction non-orthogonale $[u_1 = (90°, 30°), u_2 = y, u_3 = z]$.

Pour démarrer le processus d'itération, nous choisissons comme estimée initiale un petit cube de côté = 3,75 cm. Nous fixons une tolérance du résidu $\varepsilon_{tol} = 10^{-2}$, telle que l'itération s'arrête lorsque $r_k \leq \varepsilon_{tol}$ est satisfaite et qu'un nombre maximal d'itérations $k_{max} = 40$. Pour le pas de temps, $\triangle t$, nous choisissons $\alpha = 0,5$ dans l'Eq. (3.17). Le nombre de points choisi est $N = 32$.

La fonction de niveau, $\phi(x, y, z)$, étant difficile à représenter, nous choisissons de suivre l'évolution de la tranche du milieu du domaine de calcul, $S_m = S(z = 0)$, à la position $z = 0$ perpendiculaire à l'axe z.

Nous considérons d'abord la reconstruction de la sphère en utilisant la méthode level-set ordinaire. Tout d'abord, dans le cas '3ortho' avec 3 directions orthogonales, la Fig. 3.6 présente l'évolution de la fonction de niveau $\phi(S_m)$, dans la tranche S_m (gauche) et la vitesse correspondante (droite) aux étapes $k = 5, 10, 15$

et $k_{final} = 19$, respectivement. On peut voir que la partie inférieure de ϕ (valeurs négatives) augmente progressivement vers l'extérieur, ce qui conduit à la déformation de la forme. Ce comportement de déformation, en expansion, est dû à une vitesse normale positive qui diminue les dérivées de la forme. De même, une vitesse négative va provoquer un rétrécissement de la forme. Au cours des itérations, l'amplitude de la vitesse baisse et s'approche finalement partout du niveau zéro, lorsque le résidu à $k_{final} = 19$ devient inférieur à la tolérance $\varepsilon_{tol} = 10^{-2}$. Cela peut être considéré comme un signe de la convergence. Deuxièmement, dans le cas '2ortho +1arb', avec 2 directions orthogonales plus 1 direction non-orthogonale, nous suivons également l'évolution de la tranche du milieu aux étapes $k = 5, 10, 15, 40$: le processus itératif s'arrête à l'étape $k_{final} = k_{max} = 40$ (Fig. 3.7). La vitesse diminue pour atteindre un plateau à une valeur faible après un certain nombre d'étapes ($k = 15$). Donc la fonction de niveau ϕ se déforme vers le contour exact et change très peu entre le résultat de l'itération $k = 15$ et $k = 40$.

Ensuite, la même étude est réalisée en utilisant la méthode «bande étroite». Premièrement, dans le cas '3ortho', l'itération s'arrête à $k_{final} = 17$ quand le résidu devient nul. La Fig. 3.8 montre l'évolution de la de la tranche du milieu à $k = 5, 10, 15$ et $k_{final} = 17$. Contrairement à la méthode level-set ordinaire, ϕ est mise à jour uniquement pour les points situés dans la bande étroite et gardent une valeur constante pour les autres points situés en dehors de la bande étroite, car la vitesse de ces points restants est nulle. Au cours de l'évolution, la vitesse dans la bande étroite diminue et devient presque nulle partout à l'itération $k_{final} = 17$, ce qui indique la convergence. Deuxièmement, dans le cas '2ortho+1arb', l'itération s'arrête à $k_{final} = k_{max} = 40$ avec le résidu $r_k = 0.01$ (Fig. 3.9).

Les Fig. 3.10 (a) et (b) comparent les images 3D finales reconstruites en utilisant la méthode level-set ordinaire dans le cas '3ortho' et '2ortho+1arb', respectivement. De même, les Fig. 3.11 (a) et (b) comparent les images reconstruites en utilisant la méthode «bande étroite» pour les deux cas. Ces résultats montrent que les deux méthodes, level-set ordinaire et level-set «bande étroite» produisent des images correctes pour la sphère étudiée avec 3 directions (orthogonales ou non).

La Fig. 3.13 (a) et la Fig. 3.14 (a) comparent les résidus normalisés r_k dans le cas '3ortho' (courbes solides bleues) et '2ortho+1arb' (courbes tirets rouges) pour les sphères reconstruites en utilisant la méthode level-set ordinaire et la méthode «bande étroite», respectivement. Dans les deux cas, les résidus obtenus par les deux méthodes diminuent très rapidement au cours des 15 premières itérations, puis restent relativement stables quand une certaine valeur faible est atteinte. Avec la méthode level-set ordinaire dans le cas '3ortho', le résidu $r_k = 0.009$ devient à inférieur à la tolérance à l'itération $k_{final} = 19$, alors l'itération s'arrête. Pour le cas '2ortho+1arb', la valeur du résidu oscille un peu entre $[0.01, 0.04]$, ce qui peut également être considéré comme une convergence. Avec la méthode «bande étroite», les

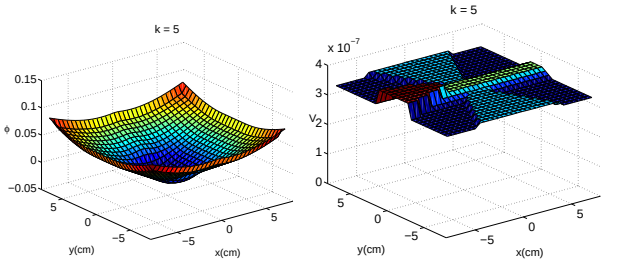

(a)

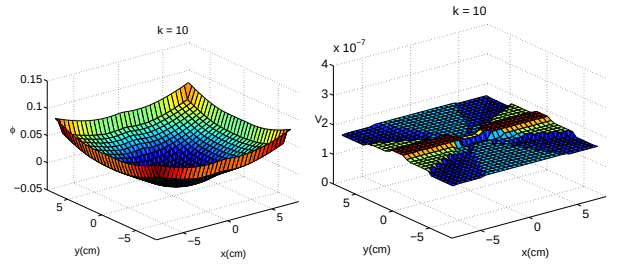

(b)

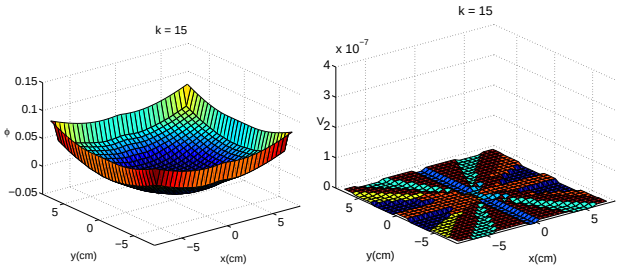

(c)

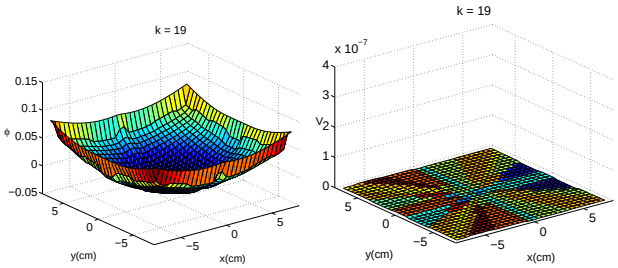

(d)

Figure 3.6: Evolution de la fonction de niveau ϕ (gauche) et de la vitesse V (droite), dans la tranche S_m à $z = 0$, avec la méthode level-set ordinaire dans le cas '3ortho' aux itérations : (a) $k = 5$; (b) $k = 10$; (c) $k = 15$; (d) $k_{final} = 19$.

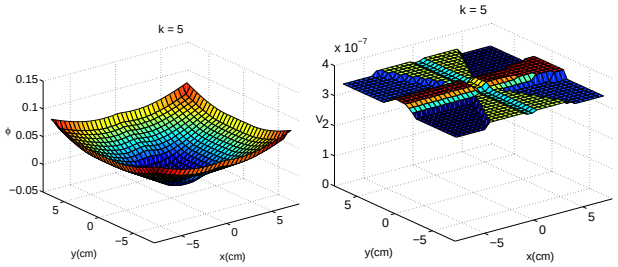

(a)

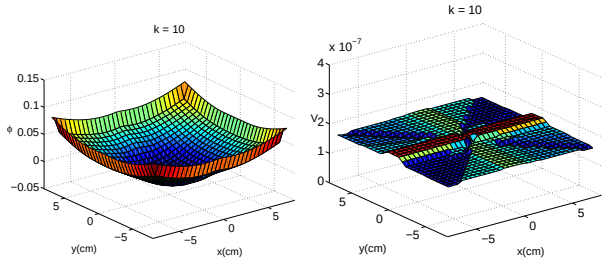

(b)

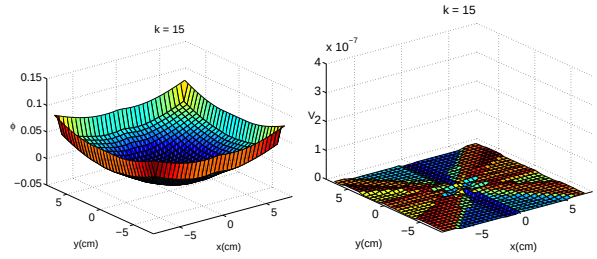

(c)

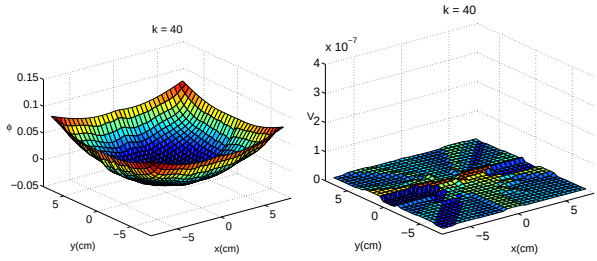

(d)

Figure 3.7: Evolution de la fonction de niveau ϕ (gauche) et de la vitesse V (droite), dans la tranche S_m à $z = 0$, avec la méthode level-set ordinaire dans le cas '2ortho+1arb' aux itérations : (a) $k = 5$; (b) $k = 10$; (c) $k = 15$; (d) $k_{final} = 40$.

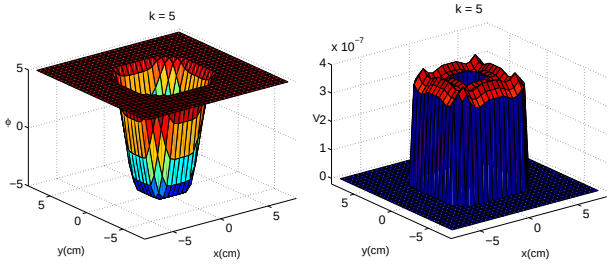

(a)

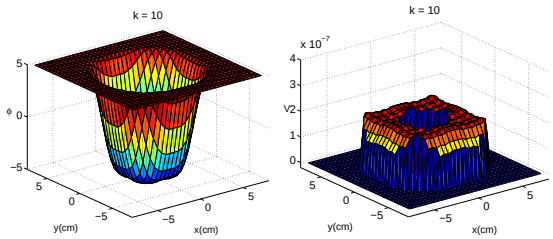

(b)

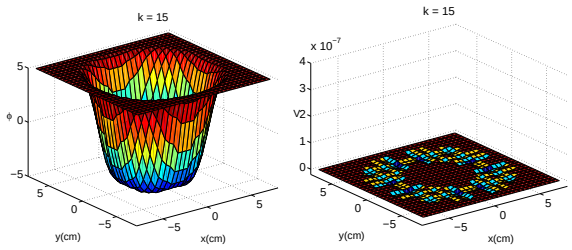

(c)

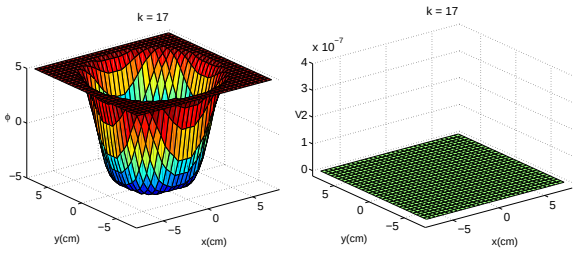

(d)

Figure 3.8: Evolution de la fonction de niveau ϕ et de la vitesse V (droite), dans la tranche S_m à $z = 0$, avec la méthode «bande étroite» dans le cas '3ortho' aux itérations : (a) $k = 5$; (b) $k = 10$; (c) $k = 15$; (d) $k_{final} = 17$.

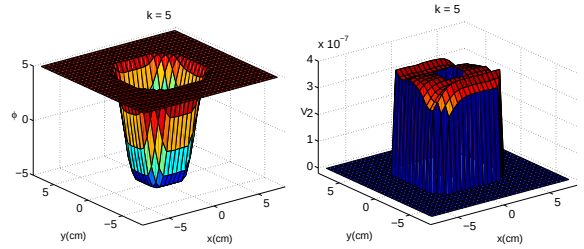

(a)

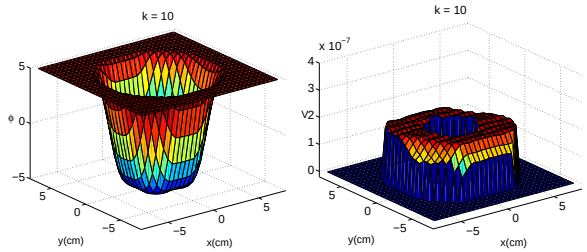

(b)

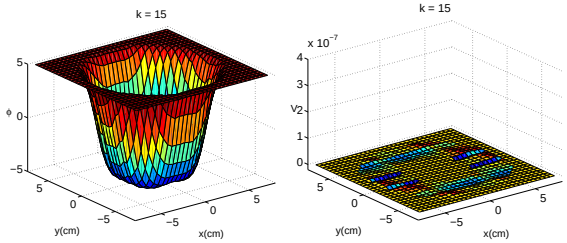

(c)

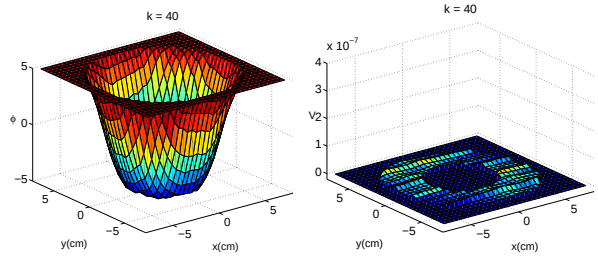

(d)

Figure 3.9: Evolution de la fonction de niveau ϕ (gauche) et de la vitesse V (droite), dans la tranche S_m à $z = 0$, avec la méthode «bande étroite» dans le cas '2ortho+1arb' aux itérations : (a) $k = 5$; (b) $k = 10$; (c) $k = 15$; (d) $k_{final} = 40$.

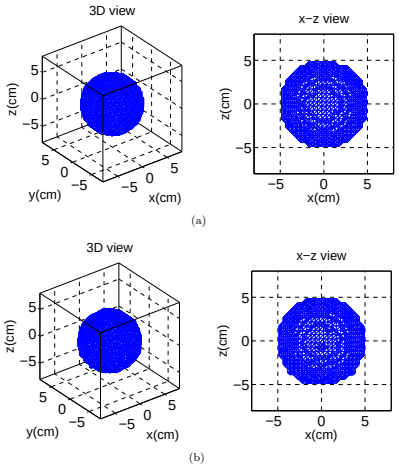

Figure 3.10: Images 3D finales reconstruites en utilisant la méthode level-set ordinaire dans les cas : (a) '3ortho' et (b) '2ortho+1arb'.

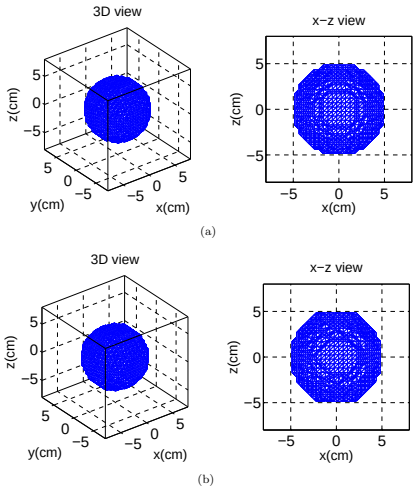

Figure 3.11: Images 3D finales reconstruites en utilisant la méthode «bande étroite» dans les cas : (a) '3ortho' et (b) '2ortho+1arb'.

résidus se comportent de la même manière. Dans le cas '3ortho', le résidu devient nul à l'itération $k_{final} = 17$. Dans le cas '2ortho+1arb',la méthode «bande étroite» permet d'obtenir le même niveau de résidu que la méthode ordinaire.

De plus, afin de d'évaluer quantitativement les deux méthodes, nous mesurons l'erreur en pixels entre l'objet reconstruit et l'objet original. Le schéma de la Fig. 3.12, pour une tranche particulière, montre que certains pixels de l'objet reconstruit appartiennent à l'objet d'origine, les pixels vrais ("true"), P_t, tandis que les autres ne font pas partie de l'objet original, les pixels faux ("false"), P_f. $P_t + P_f$ est exactement le nombre de pixels de l'objet reconstruit. Ensuite, les pixels manquants ("missing"), P_m, sont les pixels appartenant à l'objet original qui ne sont pas sélectionnés dans l'objet reconstruit. $P_t + P_m$ est exactement le nombre de pixels de l'objet original. Enfin, les pixels extérieurs ("outside"), P_o, correspondent aux pixels qui n'appartiennent ni à l'objet original ni à l'objet reconstruit. L'erreur dans chaque tranche S_j est la somme des $P_f(j)$ et $P_m(j)$. L'erreur totale en pixels E_p est ainsi calculée comme étant la somme des erreurs pour chaque tranche, normalisée par le nombre total de pixels appartenant à l'objet original, P_{tot}.

$$E_P(\%) = 100 \times \frac{\sum_j (P_m(j) + P_f(j))}{P_{tot}} = \frac{\sum_j (P_m(j) + P_f(j))}{\sum_j (P_m(j) + P_t(j))} \tag{3.19}$$

La Fig. 3.13 (b) et la Fig. 3.14 (b) comparent l'erreur en pixels E_p dans le cas '3ortho' (courbes solides bleus) et '2ortho+1arb' (courbes tiret rouges) pour les sphères reconstruites en utilisant la méthode level-set ordinaire et la méthode «bande étroite», respectivement. On peut voir que, l'erreur en pixels diminue de la

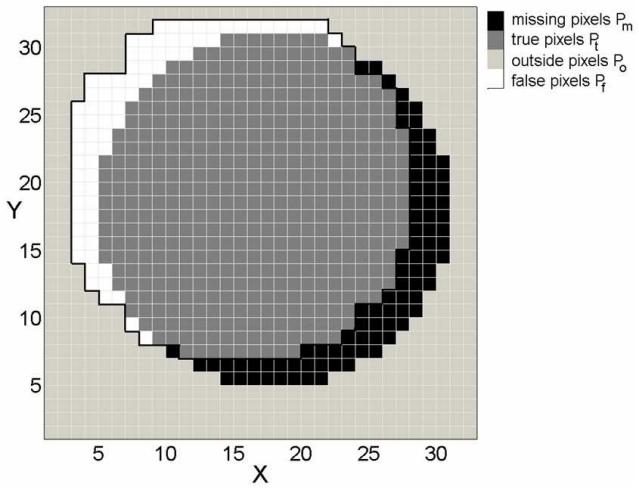

Figure 3.12: Schéma de l'objet original et de l'objet reconstruit dans une tranche.

même façon que le résidu normalisé. Dans le cas '3ortho', les erreurs deviennent négligeables, ce qui montre que les objets reconstruits sont presque identiques à l'objet original. Même si, dans le cas '2ortho+1arb', une oscillation persiste, les erreurs sont très faibles et les objets sont aussi reconstruits avec précision.

Pour étudier le coût de calcul de l'évolution, nous définissons un temps moyen de calcul T_a par chaque itération comme :

$$T_a = T_{tol}/k_{tol} \tag{3.20}$$

où k_{tol} et T_{tol} sont respectivement le nombre d'itérations et le coût de temps total (en secondes) lorsque l'évolution s'arrête.

La table 3.1 compare, pour la reconstruction de la sphère, la durée moyenne T_a (Environnement d'exécution : Hp Intel Core2 Duo CPU 3.16GHZ, win7 32bits 4G, Matlab) requise par la méthode level-set ordinaire avec celle requise par la méthode «bande étroite», dans les cas '3ortho' et '2 ortho+1arb ' avec un nombre différent de points ($N = 32$ ou 64). Lorsque N est petit, la différence de temps de calcul est faible pour les deux méthodes. Cependant, quand N augmente, la méthode «bande étroite» est beaucoup plus rapide (environ 10 fois) que la méthode level-set ordinaire. Par conséquent, pour réduire le coût de calcul, dans les configurations suivantes, nous choisissons la méthode «bande étroite» pour la reconstruction d'image à partir de fonctions de profil.

3.3 Résultats reconstruits avec la méthode «bande étroite»

Dans cette section, pour présenter les performances de la méthode «bande étroite» dans des cas plus complexes que la sphère, nous considérons deux exemples : le step-cylinder (Fig. 3.15) et deux objets séparés (une sphère et un cône, Fig. 3.16),

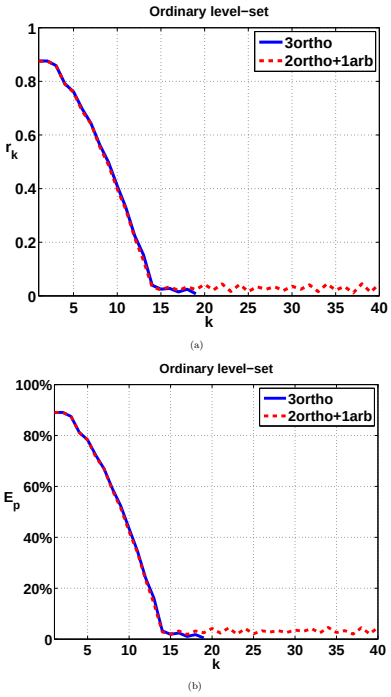

Figure 3.13: Comparaison des résultats entre les cas ’3ortho’ (courbes solides bleues) et ’2ortho+1arb’ (courbes tirets rouges) en utilisant la méthode level-set ordinaire : (a) le résidu normalisé r_k; (b) l’erreur en pixels E_p.

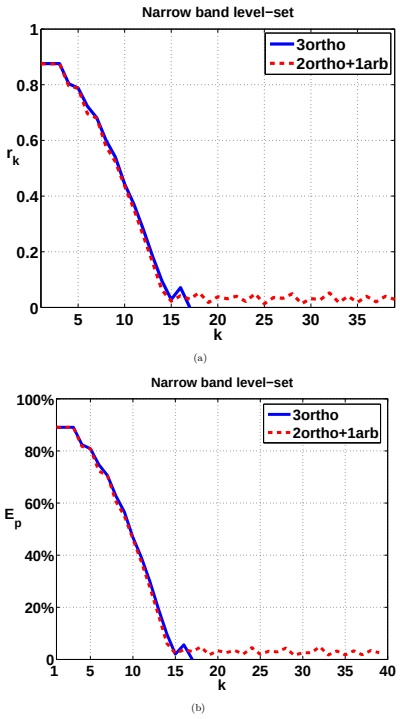

Figure 3.14: Comparaison des résultats entre les cas ’3ortho’ (courbes solides bleues) et ’2ortho+1arb’ (courbes tirets rouges) en utilisant la méthode «bande étroite» : (a) le résidu normalisé r_k; (b) l’erreur en pixels E_p.

Table 3.1: Comparaison de la durée moyenne entre les méthodes level-set ordinaire et «bande étroite» (Environnement d'exécution : Hp Intel Core2 Duo CPU 3.16GHZ, win7 32bits 4G, Matlab).

Nombre de points N	Direction	$T_a(s)$ Ordinaire	$T_a(s)$ «bande étroite»
$N = 32$	'3ortho'	8.7	6.6
	'2ortho+1arb'	8.9	6.8
$N = 64$	'3ortho'	222	23
	'2ortho+1arb'	225	23

avec un grand nombre de points $N^3 = 64^3$. Comme estimée initiale, nous choisissons un petit cube (centré dans le domaine de calcul pour un seul objet ou un petit cube pour chaque sous-objet pour les objets séparés). Pour arrêter l'itération quand un résidu acceptable est atteint, nous avons mis la tolérance du résidu normalisé $r_k \leq \varepsilon_{tol} = 0.01$ et un nombre maximal d'itérations $k_{max} = 80$. Pour étudier les performances dans des directions arbitraires, nous construisons tous les objets avec 3 directions orthogonales ou non.

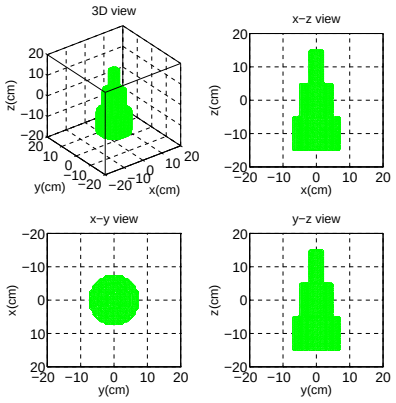

Figure 3.15: Le step-cylinder original avec $N^3 = 64^3$.

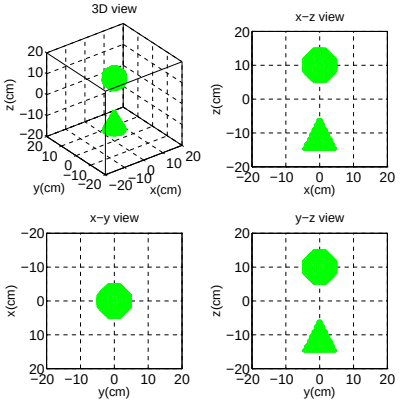

Figure 3.16: Deux objets séparés (une sphère et un cône,) avec $N^3 = 64^3$.

3.3.1 Reconstruction avec des fonctions de profil géométriques dans le cas orthogonal

Tout d'abord, nous considérons la reconstruction dans le cas '3ortho' (Fig. 3.5 (a)). Pour le step-cylinder (Fig. 3.15), l'objet reconstruit, Fig. 3.17 (a), est correct avec une erreur en pixels $E_p = 3.5\%$. Pour les objets séparés, les deux objets sont également correctement reconstruits, Fig. 3.17 (b), avec une petite erreur en pixels $E_p = 4.4\%$.

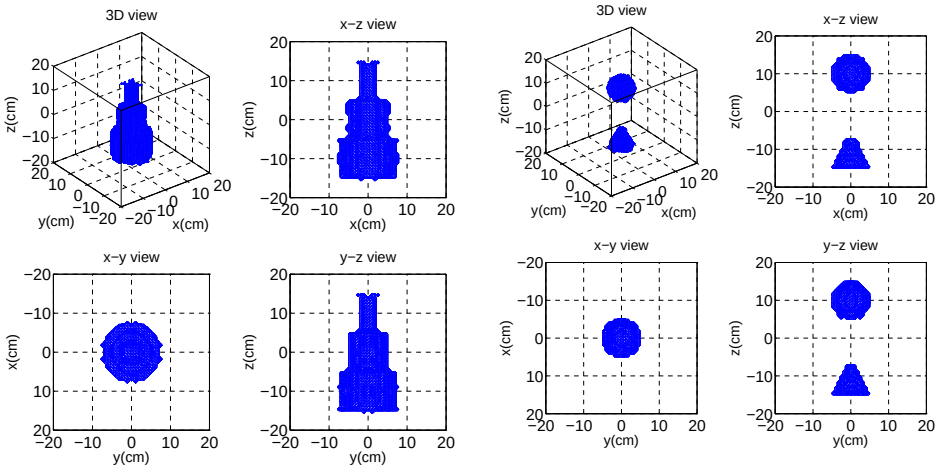

(a) (b)

Figure 3.17: Images 3D reconstruites à partir des fonctions de profil géométriques dans le cas '3ortho' pour : (a) le step-cylinder (Fig. 3.15) avec $E_p = 3.5\%$ et (b) les objets séparés (Fig. 3.16) avec $E_p = 4.4\%$.

3.3.2 Reconstruction avec des fonctions de profil géométriques dans le cas non-orthogonal

Nous venons de voir que la méthode «bande étroite» a de bonnes performances avec 3 directions orthogonales. Pour étudier ses performances dans de mauvaises conditions, nous considérons maintenant deux séries de 3 directions d'observation qui sont plus proches les unes des autres que celles du cas orthogonal. Nous choisissons deux séries de directions d'observation non-orthogonales :

- 2 directions orthogonales plus 1 direction non-orthogonale $[u_1(90°, 75°), u_2(90°, 90°), u_3(0°, 0°)]$, noté cas '2ortho+1arb'.

- 3 directions arbitraires $[u_1(90°, 30°), u_2(90°, 90°), u_3(30°, 0°)]$, noté cas '3arb'.

Ces deux cas sont présentés respectivement dans dans la Fig. 3.18.

Step-cylinder Pour le step-cylinder (Fig. 3.15), dans le cas '2ortho+1arb', les résultats reconstruits sont présentés sur la Fig. 3.19 (a). En comparant à l'objet original, le cylindre du milieu est plus grand tandis que le cylindre du haut possède un grand nombre de pixels manquants. Par conséquent, il en résulte une grande erreur en pixels $E_p = 20.2\%$. Mais il peut encore être identifié. Dans le cas '3arb', comme indiqué dans la Fig. 3.19 (b), l'objet reconstruit est encore plus déformé avec une grande erreur en pixels $E_p = 45.3\%$. Cela est dû au fait que l'information la plus caractéristique est selon l'axe $z(0°, 0°)$, alors que nous utilisons une direction $u_3(30°, 0°)$ qui s'en écarte.

Objets séparés : Pour les deux objets séparés (Fig. 3.16), dans le cas '2ortho+1arb', les images reconstruites sont présentées dans la Fig. 3.20 (a). On voit que

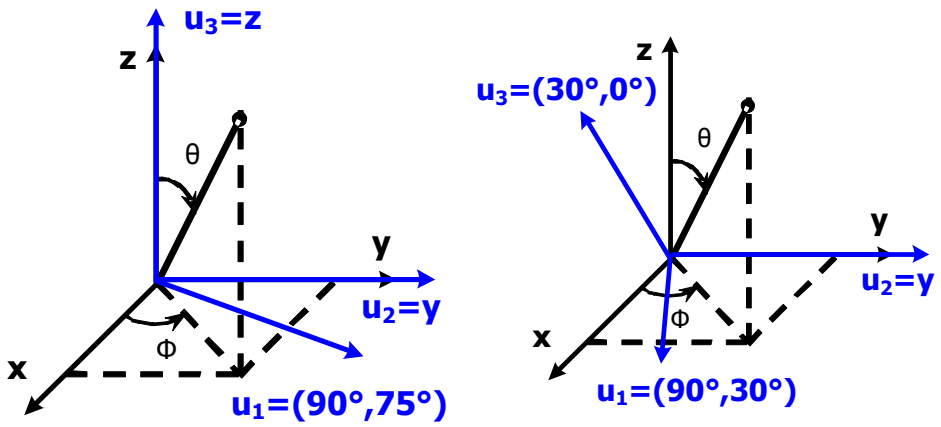

(a) (b)

Figure 3.18: Directions d'observation : (a) le cas '2ortho+1arb' avec 2 directions orthogonales plus 1 direction arbitraire $[u_1(90°, 75°), u_2(90°, 90°), u_3(0°, 0°)]$ et (b) le cas '3arb' avec 3 directions arbitraires $[u_1(90°, 30°), u_2(90°, 90°), u_3(30°, 0°)]$.

les images reconstruites de la sphère sont correctes, alors que les images reconstruites du cône présentent une légère déformation, mais sont encore identifiables. Par conséquent, les deux objets reconstruits ont une erreur totale en pixels $E_p = 6.5\%$. Cependant, dans le cas '3arb', comme indiqué dans la Fig. 3.20 (b), l'image reconstruite pour le cône est totalement faussée et ne peut être identifiée. En conséquence, l'erreur en pixels $E_p = 24\%$ est beaucoup plus grande.

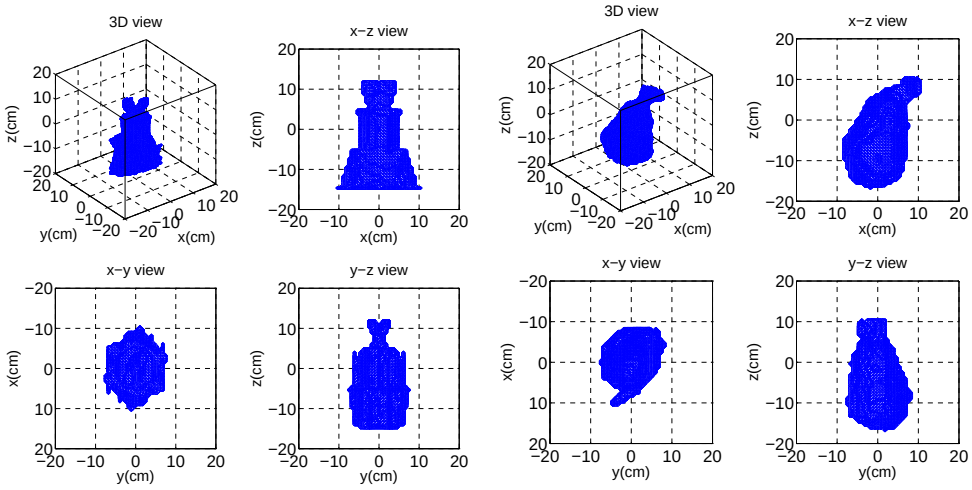

(a) (b)

Figure 3.19: Les images 3D du step-cylinder (Fig. 3.15) reconstruites à partir des fonctions de profil géométriques dans le cas : (a) '2ortho+1arb' avec $E_p = 20.2\%$; (b) '3arb' avec $E_p = 45.3\%$.

Les résultats ci-dessus démontrent que la méthode «bande étroite» permet de générer des résultats acceptables avec la fonction de profil géométrique dans des directions arbitraires. Ici, il est important de noter que la notion "arbitraire" ne signifie pas que l'on peut prendre des directions d'observation quelconques par rapport

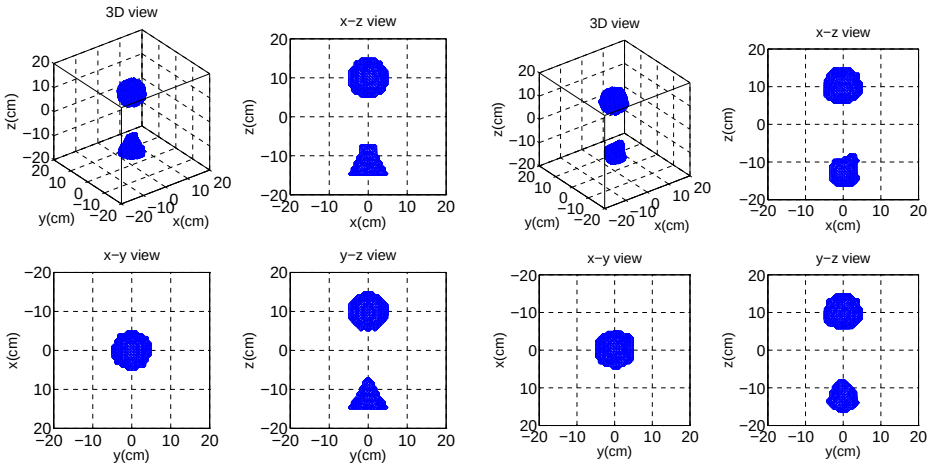

(a) (b)

Figure 3.20: Images 3D des objets séparés (Fig. 3.16) reconstruites à partir des fonctions de profil géométriques dans le cas : (a) '2ortho+1arb' avec $E_p = 6.5\%$; (b) '3arb' avec $E_p = 24\%$.

à l'objet étudié, mais cela signifie que les 3 directions ne sont pas nécessairement mutuellement orthogonales. Ceci est significatif car en raison de la limite des angles de vision des équipements radar, il est très difficile, voire impossible, d'illuminer la cible dans 3 directions orthogonales. L'inconvénient de cette méthode pour la reconstruction d'image est qu'il est nécessaire d'avoir au moins une direction avec autant que possible des informations de forme caractéristique. Néanmoins, cette limite est valable également pour d'autres algorithmes de reconstruction.

3.3.3 Reconstruction avec des fonctions de profil physiques

Jusqu'à présent, les résultats reconstruits en utilisant la méthode level-set sont obtenus uniquement à partir des fonctions de profil géométriques. Maintenant, nous utilisons la sphère comme exemple pour étudier la performance de cette méthode avec des fonctions de profil physiques. La Fig. 3.21 présente les objets reconstruits dans le cas '3ortho'. Nous pouvons voir que même avec 3 directions orthogonales, l'objet reconstruit est déformé avec une petite "boule" s'allongeant le long de la direction dans laquelle les fonctions de profil physiques sont distordues en raison de la zone d'ombre (Fig. 2.4). La méthode level-set ne peut pas corriger cette distorsion, parce que la matrice d'observation G^u est calculée en tenant compte des fonctions de profil géométriques de l'objet.

3.3.4 Etude paramétrique

En utilisant la méthode «bande étroite», comme nous l'avons démontré ci-dessus, la qualité des reconstructions à partir de fonctions de profil dépend en grande

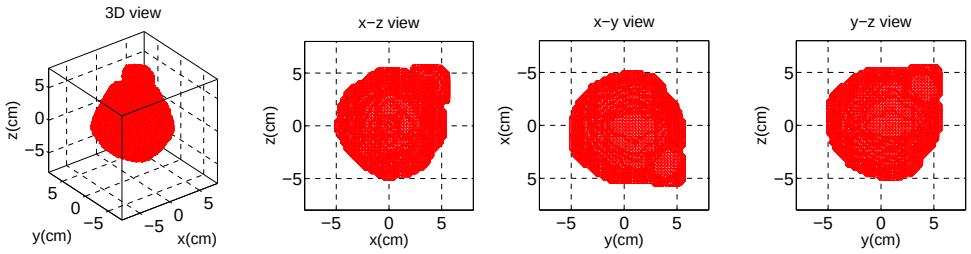

Figure 3.21: Images 3D de la sphère reconstruites à partir des fonctions de profil physiques dans le cas '3ortho ' avec $E_p = 29.7\%$

partie de l'exactitude des données observées (fonctions de profil) et des directions d'observation (orthogonales ou non). De plus, les résultats reconstruits sont affectés par le choix de certains paramètres, tels que le pas de temps $\triangle t$ et l'estimée initiale. Par conséquent, dans cette section, nous étudions l'effet de ces deux paramètres sur les reconstructions.

Pas de temps Pour une vitesse de type gradient, le pas de temps $\triangle t$ doit satisfaire la condition donnée par l'Eq. (3.17). Son effet vient du choix de α qui est tel que $0 < \alpha < 1$. Ici, nous considérons 3 valeurs différentes $\alpha = 0.2; 0.5; 0.9$ pour étudier l'effet de ce paramètre sur le résidu normalisé r_k. En prenant comme exemple la reconstruction de la sphère dans le cas '3ortho', la comparaison des r_k, obtenus avec ces 3 valeurs de α, est présentée sur la Fig. 3.22 (a). On peut constater que, pour une petite valeur $\alpha = 0,2$, donc un faible $\triangle t$, le résidu résultant (courbe solide rouge) diminue très lentement. Lorsque la valeur de α est plus grande, la vitesse de convergence augmente jusqu'à ce qu'une certaine valeur de tolérance soit atteinte. Par conséquent, le résidu converge le plus rapidement avec $\alpha = 0,9$. Mais $\alpha = 0,5$ produit une solution plus stable. Une comparaison similaire est effectuée pour le step-cylinder sur la Fig. 3.22 (b). Encore une fois, $\alpha = 0,5$ est le choix optimal pour la convergence et la stabilité de l'évolution avec une vitesse de type gradient.

Estimée initiale Maintenant, nous étudions l'influence de l'estimée initiale. Pour les objets séparés, la sphère et le cone, les images reconstruites précédemment dans le cas '3ortho' (Fig. 3.17) étaient obtenues à partir de deux petits cubes initiaux (un pour la sphère et un autre pour le cône), chacun étant positionné au centre de chaque sous-objet. Maintenant, dans la Fig. 3.23 (a), on n'utilise qu'un seul cube initial pour les deux objets séparés, positionné dans l'espace entre ces deux objets. Comme le montre la Fig. 3.23 (b), les deux objets sont encore reconstruits exactement avec une faible erreur en pixels $E_p = 7.6\%$. La Fig. 3.23 (c) compare l'évolution des résidus r_k selon le choix d'estimée initiale : deux cubes (courbe solide) et un seul cube (courbe tiret). On peut voir que, avec un seul cube, au début, l'évolution gaspille beaucoup plus de temps de calcul pour trouver la position

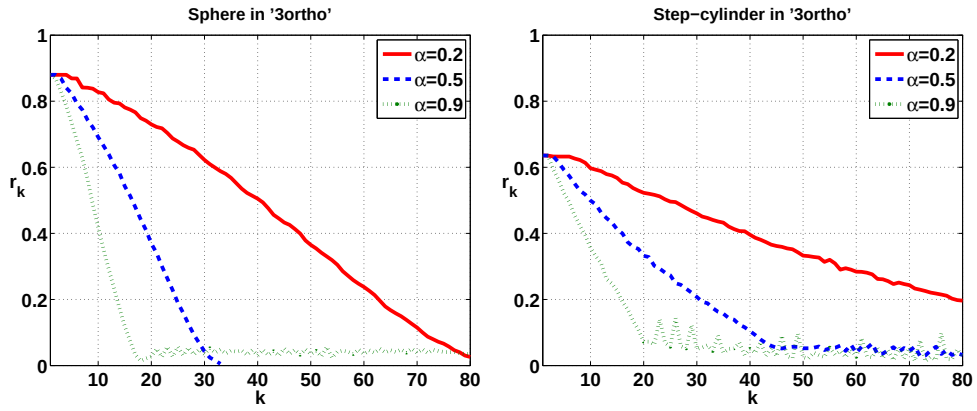

(a) (b)

Figure 3.22: Effet du pas de temps $\triangle t$ sur les résidus normalisés r_k de la reconstruction avec des fonctions de profil géométriques en utilisant la méthode «bande étroite» pour : (a) la sphère et (b) le step-cylinder, dans le cas '3ortho'.

exacte de l'objet original et il y a besoin de 150 itérations pour obtenir un résultat correctement reconstruit. Par conséquent, même si le choix de l'estimée initiale est quelque peu arbitraire, il est préférable de choisir de la mettre à l'intérieur de l'objet original dans l'intérêt de réduction du coût de calcul.

Ensuite, nous choisissons d'utiliser, comme estimée initiale, les résultats déformés reconstruits à partir des fonctions de profil géométriques en utilisant la méthode de Chauveau dans le cas non-orthogonal, $[u_1(90°, 30°), u_2 = y, u_3 = z]$. Comme le montre la Fig. 3.24 (a), cet objet déformé est allongé dans la direction perpendiculaire à la bissectrice des 2 directions non orthogonales (u_1 et u_2). Avec cette estimée initiale, la Fig. 3.24 (b) présente l'image reconstruite, qui est toujours déformée, avec une erreur en pixels $E_p = 42.7\%$. La Fig. 3.24 (c) compare le résidu r_k selon le choix d'estimée initiale : un cube (courbe solide) ou l'objet déformé obtenu par la méthode de Chauveau (courbe tiret). En effet, même si la forme initiale est incorrecte, la méthode de Chauveau peut garantir l'accord entre la fonction de profil originale et celle de l'objet reconstruit. Il en résulte une faible erreur des fonctions de profil, au tout début de l'itération. C'est-à-dire que le résidu normalisé a déjà atteint une valeur petite et stable, et la vitesse d'évolution devient quasiment nulle partout de sorte que l'évolution s'arrête.

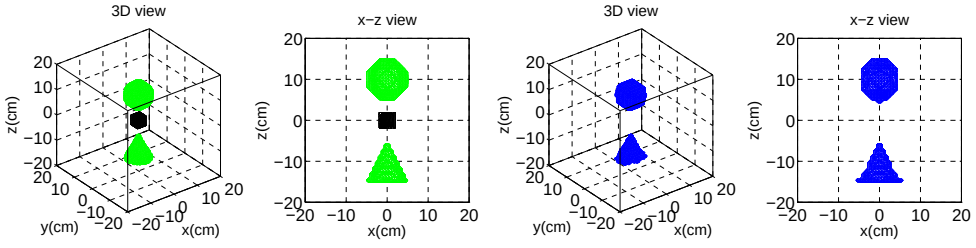

(a) (b)

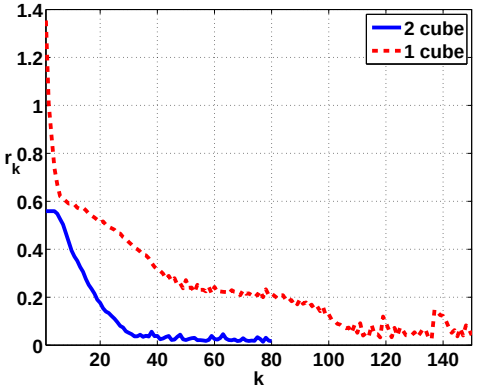

(c)

Figure 3.23: Influence de l'estimée initiale : (a) l'estimée initiale unique (noir) et les deux objets séparés originaux (vert), (b) image 3D reconstruite à partir des fonctions de profil géométriques dans le cas '3ortho', (c) le résidu normalisé r_k.

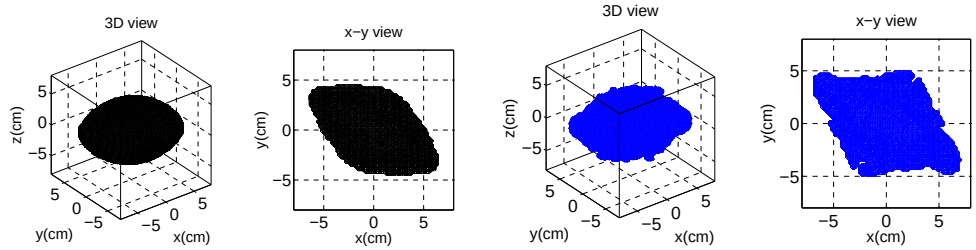

(a) (b)

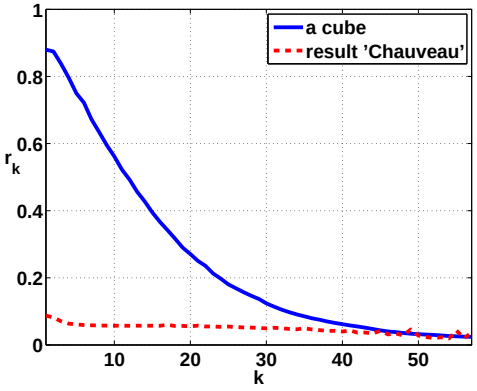

(c)

Figure 3.24: Influence de l'estimée initiale : (a) l'estimée initiale déformée obtenue par la méthode de Chauveau pour la sphère; (b) image reconstruite; (c) le résidu normalisé r_k.

4

Conclusions et Perspectives

L'étude présentée dans cette thèse concerne la caractérisation des cibles radar avec une méthode de basse fréquence, l'imagerie radar à partir de la réponse en rampe. Elle permet de reconstituer un objet avec des fonctions de profil uniquement dans 3 directions. Les algorithmes de reconstruction existants donnent de bons résultats avec 3 directions orthogonales, mais des estimations distordues dans le cas non-orthogonal. Par conséquent, le travail principal effectué dans cette thèse est l'optimisation des reconstructions à partir de fonctions de profil dans des directions arbitraires.

Dans le chapitre 1, les différentes notions utiles pour la caractérisation des cibles radar furtives ont été introduites. Tout d'abord, nous avons rappelé ce qu'est la Surface Equivalente Radar (SER). Ensuite, nous avons abordé les techniques principales de la furtivité et de la contre-furtivité ce qui a motivé le choix de travailler en basses fréquences. Parmi les méthodes de diffraction inverse, l'imagerie radar à partir de réponses en rampe est bien adaptée aux basses fréquences et elle permet de reconstruire des images tri-dimensionnelles (3D) de cibles.

Dans le chapitre 2, la méthode d'imagerie radar à partir de réponses en rampe a été étudiée. Cette méthode utilise la réponse en rampe, qui est reliée à la fonction de profil, définie comme l'aire de la cible dans chaque plan perpendiculaire à la direction d'observation. Parmi les algorithmes de reconstruction à partir de fonctions de profil, la méthode de Chauveau est la plus avancée. Elle nécessite seulement 3 directions d'observation et s'affranchit des limites de la forme de l'objet liées à d'autres méthodes. Par conséquent, nous avons implémenté cette méthode et nous l'avons appliquée pour reconstituer des objets 3D de formes variées. Les résultats numériques indiquent que, avec 3 directions orthogonales, la méthode de

Chauveau génère des images 3D exactes reconstruites à partir de fonctions de profil géométriques, mais cette méthode ne peut pas corriger la distorsion causée par le biais des fonctions de profil physiques qui est dû à l'effet de la zone d'ombre. Par contre, même si nous changeons une seule direction et que nous gardons les deux autres directions orthogonales, les images reconstruites à partir des fonctions de profil géométriques et physiques sont inexactes et ne peuvent pas être identifiées. Cependant, les équipements radar ont souvent un angle de vue limité que ce soit en télédétection ou pour de grandes cibles. Par conséquent, il est nécessaire d'optimiser la reconstruction dans des directions arbitraires.

Dans le chapitre 3, nous avons présenté notre contribution principale, c'est-à-dire l'optimisation de la reconstruction d'image à partir des fonctions de profil dans des directions arbitraires. Nous utilisons une procédure itérative pour obtenir une estimée correcte de la cible en minimisant l'écart entre les données (les fonctions de profil de l'objet inconnu) et les fonctions de profil de l'objet en évolution. Afin de se concentrer sur l'amélioration des performances dans des directions arbitraires, la matrice d'observation est seulement considérée comme décrivant la relation entre la fonction de profil géométrique obtenue à partir de l'objet original et celle de l'objet estimée. dans ce chapitre, pour optimiser la reconstruction d'image à partir de fonctions de profil dans des directions arbitraires, différents problèmes ont été étudiés.

Dans la section 3.1, nous avons développé un algorithme pour résoudre le problème direct, qui est le calcul des fonctions de profil géométriques d'un objet 3D. Ensuite, nous l'avons appliqué pour évaluer quantitativement la qualité des reconstructions obtenues en utilisant la méthode de Chauveau, par le calcul de l'erreur entre les fonctions de profil à partir de l'objet d'origine et des fonctions de profil calculées à partir de son image reconstruite. Ensuite, avec une base de données contenant des modèles possibles, nous avons appliqué notre algorithme pour identifier une cible radar en utilisant son objet reconstruit obtenu à partir de fonctions de profil physiques dans seulement 3 directions.

Dans la section section 3.2, pour résoudre le problème inverse, dont le but est de trouver une méthode adaptée à la reconstruction de formes d'objets 3D, nous avons d'abord testé une méthode inverse classique, la méthode des moindres carrés (LSQR) [14]. Cependant, comme la plupart des méthodes inverses, elle remplit l'objet inconnu avec des valeurs arbitraires de sorte qu'elle n'est pas adaptée pour représenter un objet binaire. Au contraire, la méthode level-set représente la forme comme le niveau zéro d'une fonction de dimension supérieure, la fonction de niveau, qui est négative à l'intérieur de l'objet et positive à l'extérieur de l'objet, de telle sorte qu'une représentation de forme binaire est obtenue. Son principe est de faire évoluer la fonction de niveau dans un champ de vitesse. Donc, cette méthode peut gérer le changement topologique survenant au cours de la déformation

de la forme d'une manière complètement automatique et implicite. Pour les problèmes de diffusion inverse, une vitesse de type gradient est largement utilisée, car elle établit une relation entre la dérivée de la forme et de la fonction de coût [84]. Après avoir construit une vitesse adaptée, nous avons validé la méthode level-set pour les reconstructions à partir des fonctions de profil en prenant l'exemple d'une sphère. Les résultats montrent que cette méthode donne de bons résultats pour la sphère dans le cas des 3 directions orthogonales ainsi que le cas avec 2 directions orthogonales et 1 arbitraire. De plus, la méthode «bande étroite» a été utilisée pour réduire le coût de calcul, puisque cette méthode effectue l'évolution seulement pour les points voisins du contour à une distance finie.

Dans la section 3.3, des résultats numériques de la reconstruction obtenus en utilisant la méthode "bande étroite" sont présentés pour des objets variés et plusieurs directions :

- Tout d'abord, avec des fonctions de profil géométriques dans 3 directions orthogonales, cas '3 ortho', nous obtenons de bons résultats. L'erreur en pixels est faible variant entre $2,7\%$ et 9.2%.

- D'autre part, avec des fonctions de profil géométriques dans 3 directions non-orthogonales, les images reconstruites de la sphère sont correctes avec une erreur en pixels de même niveau que dans le cas '3ortho'. Dans le cas '2ortho+1arb', si nous gardons la direction où la caractéristique topologique varie le plus, par exemple $u_3 = z$ pour le step-cylinder, même si les deux autres directions ne sont pas orthogonales et sont très proches les unes des autres (avec un angle de $15°$), l'image reconstruite est suffisamment précise pour être identifiée. Dans le cas '3arb', nous utilisons une direction $u_3 = (30°, 0°)$ s'écartant de la direction la plus caractéristique z. En conséquence, les images reconstruites sont complètement déformées et ne peuvent pas être identifiées. Pour les deux objets séparés, l'effet de la direction peut être considéré séparément pour chaque sous-objet. Pour la sphère, les directions ont peu d'influence sur les reconstructions en raison de sa symétrie. Alors que pour le cône, la déformation des images obtenues dans le cas '3arb' est due à l'absence d'une direction correspondant à la plupart des informations caractéristiques.

- Ensuite, avec des fonctions de profil physiques, même dans 3 directions orthogonales, les images reconstruites de la sphère sont déformées. Elles ont une partie surajoutée due à l'effet d'ombre dans les fonctions de profil physiques. En effet, la matrice d' observation est construite en prenant en compte seulement les fonctions de profils géométriques, de sorte qu'elle n'est pas adaptée au cas physique. Cette matrice doit être remplacée par une matrice qui tienne compte des phénomènes physiques.

- Enfin, l'influence du pas de temps et de l'estimé initiale a été étudiée. A partir des conditions CFL, le choix du pas de temps dépend d'un coefficient $0 < \alpha < 1$.

Les résultats numériques montrent que $\alpha = 0,5$ semble être un choix optimal pour la convergence et la stabilité de l'évolution. Ensuite, le choix de l'estimée initiale est quelque peu arbitraire, mais peut être choisie à l'intérieur de l'objet pour des raisons de réduction des coûts de calcul. La méthode level-set ne peut pas corriger l'objet déformé obtenu par la méthode de Chauveau puisque le résidu a déjà atteint une valeur stable.

Dans un avenir proche, comme toute méthode itérative, la régularisation doit être considérée comme le lissage de contour, le compromis entre la résolution en fonction du nombre de points et le coût de calcul. Une solution possible pour le lissage de contour est d'ajouter à la vitesse un terme de régularisation dépendant de la courbure de l'objet [95]. De plus, nous devons étudier l'effet du bruit dans les données sur la reconstruction par la méthode level-set.

Dans un avenir à long terme, concernant la reconstruction avec des fonctions de profil physiques, la matrice d'observation pour des données réelles doit tenir compte de la propagation des ondes à la surface de l'objet. Cela dépend de la forme de l'objet évoluant à chaque étape de l'itération et c'est encore un problème ouvert.

Bibliography

[1] L. V. Blake. *Radar range performance analysis*. Artech House, Norwood, USA, 1986. 3, 10, 145

[2] M.I Skolnick. *Introduction to Radar Systems*. McGraw-Hill, 1980. 3, 145

[3] E.M. Kennaugh and D.L. Moffatt. Transient and impulse response approximations. *Proceedings of the IEEE*, 53:893–901, 1965. 3, 18, 19, 23, 25, 27, 138, 145, 153, 154

[4] J. D. Young. *Target imaging from multiple frequency radar returns*. PhD thesis, The Ohio State University, Columbus, 1971. 4, 19, 27, 146, 154

[5] J. D.Young. Radar imaging from ramp response signatures. *Antennas and Propagation, IEEE Transactions on*, 24:276–282, 1976. 4, 17, 18, 19, 26, 27, 31, 32, 43, 138, 146, 154, 155, 197

[6] S. Nag. *Ramp Response Signatures of Dielectric Scatterers*. PhD thesis, The Ohio State University, Columbus, 1971. 4, 31, 146, 156

[7] S. Nag and L. Peters. Radar images of penetrable targets generated from ramp profile functions. *Antennas and Propagation, IEEE Transactions on*, 49:32–40, 2001. 4, 20, 31, 146, 156

[8] X. M. Zhang, W. Lib, and G. R. Liu. A new technique in ramp response for acoustic imaging of underwater objects. *Applied Acoustics*, 63:453–465, 2002. 4, 31, 146, 156

[9] W. Li, G. R. Liu, and V. K. Varadan. Acoustical imaging of underwater objects using the bistatic ramp response signals. *IOP, Smart Mater. Struct.*, 13:169–174, 2004. 4, 20, 31, 146, 156

[10] L. Anton and S. Pican. Reconstruction and recognition of the radar target image. In *Telecommunications in Modern Satellite, Cable and Broadcasting Service, 2001. TELSIKS 2001. 5th International Conference on*, volume 1, pages 61–64 vol.1, 2001. 4, 31, 33, 62, 146, 156

[11] Y. Das and W. Boerner. On radar target shape estimation using algorithms for reconstruction from projections. *Antennas and Propagation, IEEE Transactions on*, 26(2):274–279, 1978. 4, 31, 33, 35, 43, 138, 146, 156

[12] N.G. Nebabin. *Methods and Techniques of Radar Recognition*. Methods and Techniques of Radar Recognition, 1994. 4, 31, 33, 35, 43, 138, 146, 156, 197

[13] J.Chauveau and N. de Beaucoudrey. A new algorithm of 3D image reconstruction of radar targets from ramp responses in low frequency. *Progress In Electromagnetic Research M.*, 16:1–18, 2011. 4, 5, 31, 32, 33, 43, 138, 146, 147, 156

[14] O. Bretscher. *Linear Algebra with Applications*. Prentice Hall College Div, 1995. 5, 69, 134, 139, 186

[15] G. T. Ruck, D. E. Barrick, W. T. Stuart, and W. T. Krichbaum. *Radar Cross Section Handbook*. Plenum Press, 1970. 8

[16] A.K. Bhattacaryya and D.L Sengupta. *Radar cross section analysis and control*. Artech House, Norwood, USA, 1991. 8

[17] E. Knott, Shaeffer J.K, and Tuley M. T. *Radar Cross Section, its prediction, measurement and reduction*. Artech House, Inc., 1993. 10

[18] D. L. Moffat. *Radar Cross Section, Measurements Processing and Analysis of Radar Target Signatures*. The Ohio state University Electroscience Laboratory, Juin 1984. 12

[19] http://www.northropgrumman.com. 14, 15, 197

[20] http://www.lockheedmartin.com/. 15, 197

[21] D. Richardson. *Stealth Warplanes: Deception, Evasion, and Concealment in the Air*. MBI Publishing Company, New York, 2001. 14

[22] D. V. Dranidis. Airborne stealth in a nutshell. *Magazine of the Computer Harpoon Community*, 2009. 14

[23] C-L. Teo. Bistatic radar system analysis and software development. Master's thesis, Naval Postgraduate School, Monterey CA, 2003. 16

[24] D. Moffatt, J. Young, A.A.Ksienski, H-C Lin, and C. Rhoads. Transient response characteristics in identification and imaging. *Antennas and Propagation, IEEE Transactions on*, 29:192–205, 1981. 16

[25] H. Kuschel. VHF/UHF radar. 1. characteristics. *Electronics & Communication Engineering Journal*, 14(2):61–72, 2002. 16

[26] H. Kuschel, J. Heckenbach, S. Müller, and R. Appel. Countering stealth with passive, multi-static, low frequency radars. *Aerospace and Electronic Systems Magazine, IEEE*, 25(9):11–17, 2010. 16

[27] I. M. Gelfand, M. I. Graev, and N. Ya. Vilenkim. Generalized functions. *Academic Press, Newyork*, 5:1–74, 1964. 17, 33

[28] A. Mohammad Djafari et G. Demoment. Tomographie de diffraction et synthèse de fourier à maximum d'entropie. *Revue Phys. Appl.*, 22:153–167, 1987. 17

[29] G. Chavent and P.C. Sabatier. Inverse problems of wave propagation and diffraction. In *Lecture Notes in Physics*, volume 486, Aix-les-Bains, France, September 1997. 17

[30] A.J. Devaney. A filtered backpropagation algorithm for diffraction tomography. *Ultrason. Imag.*, 4:336–350, 1982. 17

[31] N.N. Bojarski. Three-dimensional electromagnetic short pulse inverse scattering. Technical report, Syracuse University, Res. Corp., Syracuse, NY, 1967. 17, 18

[32] J.H. Rose and J.A. Krumhansl. Determination of flaw characteristics from ultrasonic scattering data. *Journal of Applied Physics*, 50(4):2951–2952, 1979. 17

[33] D.J. Vezzetti and S.O. Aks. Reconstructions from scattering data: analysis and improvements of the inverse born approximation. *Ultrasonic Imaging*, 1:333, 1979. 17

[34] A. Roger. Newton-Kantorovitch algorithm applied to an electromagnetic inverse problem. *Antennas and Propagation, IEEE Transactions on*, 29:232–238, 1981. 17

[35] W.C. Chew and Y.M. Wang. Reconstruction of two-dimensional permittivity distribution using the distorted born iterative method. *Medical Imaging, IEEE Transactions on*, 9(2):218–225, 1990. 17

[36] N. Joachimowicz, C. Pichot, and Hugonin J.P. Inverse scattering: an iterative numerical method for electromagnetic imaging. *Antennas and Propagation, IEEE Transactions on*, 39(12):1742–1753, 1991. 17

[37] C-C. Chiu and Y-W. Kiang. Electromagnetic imaging for an imperfectly conducting cylinder. *Microwave Theory and Techniques, IEEE Transactions on*, 39(9):1632–1639, 1991. 17

[38] D. Colton and A. Kirsch. A simple method for solving inverse scattering problems in the resonance region. *Inverse Problems*, 12(4):383, 1996. 17, 20

[39] M. Brandfass, A. Lanterman, and K. F. Warnick. A comparison of the Colton-Kirsch inverse scattering method with linearized tomographic inverse scattering. *Inverse Problems*, 17:1797–1816, 2001. 17

[40] E. Wolf. Three-dimensional structure determination of semi-transparent objects from holographic data. *Opt. Commun.*, 1:153–156, 1969. 17

[41] N.N. Bojarski. Inverse scattering inverse source theory. *J. Math. Phys.*, 22:1647–1650, 1981. 17

[42] J. Richmond. Scattering by a dielectric cylinder of arbitrary cross section shape. *Antennas and Propagation, IEEE Transactions on*, 13(3):334–341, 1965. 17

[43] W. Tabbara. On an inverse scattering method. *Antennas and Propagation, IEEE Transactions on*, 21(2):245–247, 1973. 18

[44] W. Tabbara. On the feasibility of an inverse scattering method. *Antennas and Propagation, IEEE Transactions on*, 23(3):446–448, 1975. 18

[45] E.M. Kennaugh and R.L. Cosgriff. The use of impulse response in electromagnetic scattering problem. *IRE National Convention Records*, 1:72–77, 1958. 18, 19

[46] N. Bleistein. Physical optics farfield inverse scattering in the time domain. *J. Acoust. Soc. Amer.*, 60(6):1249–1255, 1976. 18

[47] W. Perry. On the bojarski-lewis inverse scattering method. *Antennas and Propagation, IEEE Transactions on*, 22(6):826–829, 1974. 18

[48] S. Rosenbaum-Raz. On scatterer reconstruction from far-field data. *Antennas and Propagation, IEEE Transactions on*, 24(1):66–70, 1976. 18

[49] W-M. Boerner and C-M. Ho. Development of physical optics far field inverse scattering (poffis) and its limitations. In *Antennas and Propagation Society International Symposium, 1979*, volume 17, pages 240–243, 1979. 18

[50] I. M. Gelfand, M. I. Graev, and N. Ya. Vilenkim. Generalized functions. *Academic Press, New York*, 5:1–74, 1966. 18, 20

[51] K. Shubert, J. Young, and D.L. Moffatt. Synthetic radar imagery. *Antennas and Propagation, IEEE Transactions on*, 25(4):477–483, 1977. 20, 31, 156

[52] S-J. J. Tsao. *Image reconstruction using ramp response signatures*. PhD thesis, The Pennsylvania State University, 1985. 20, 31, 156

[53] Chi-Chih Chen and L. Peters. Radar scattering and target imaging obtained using ramp-response techniques. *Antennas and Propagation Magazine, IEEE*, 49(3):13–27, 2007. 20, 31, 156

[54] D.L. Moffat and E.M. Kennaugh. The axial echo area of a perfectly conducting prolate spheroid. *Antennas and Propagation, IEEE Transactions on*, 13:401–409, 1965. 20, 23, 25, 27, 153, 154

[55] C.E. Baum. The singularity expansion method. *Transient Electromagnetic Field, L.B. Felsen Ed. New York*, pages 129 –179, 1976. 21

[56] R. Toribio, P. Pouliguen, and J. Saillard. Identification of radar targets in resonance zone: E-pulse techniques. *Progress In Electromagnetics Research, PIER*, 43:39–58, 2003. 21

[57] S. Rouquette and N. Mohamed. Estimation of frequencies and damping factors by two-dimensional esprit type methods. *Signal Processing, IEEE Transactions on*, 49:237–245, 2001. 21

[58] M.L. Burrows. Two-dimensional esprit with tracking for radar imaging and feature extraction. *Antennas and Propagation, IEEE Transactions on*, 52(2):524–532, 2004. 21

[59] D. Moffatt, J. Young, A.A. Ksienski, H-C Lin, and C. Rhoads. Transient response characteristics in identification and imaging. *Antennas and Propagation, IEEE Transactions on*, 29(2):192–205, 1981. 26

[60] J. Chauveau, N. de Beaucoudrey, and J. Saillard. Radar target imaging from ramp responses using low frequency extrapolation. In *Progress In Electromagnetics Research Symposium Abstracts*, Moscow, Russia, August 2009. 27

[61] J. Chauveau and N. de Beaucoudrey. Ramp response radar imaging: Analysis of frequency parameters. In *EuMW/EuMC 2010*, page EuMW/EuMC 2010, Paris, France, October 2010. 27

[62] Software of electromagnetic simulations. http://www.feko.info/, FEKO. 28, 52

[63] S. Nag and L. Peters Jr. Ramp response signatures of dielectric targets, especially land mines. In *Geoscience and Remote Sensing Symposium Proceedings, 1998. IGARSS '98. 1998 IEEE International*, volume 1, pages 213–215 vol.1, 1998. 31, 156

[64] Chi-Chih Chen and L. Peters. Ramp response signatures for uxos. In *Geoscience and Remote Sensing Symposium, 2000. Proceedings. IGARSS 2000. IEEE 2000 International*, volume 4, pages 1436–1438 vol.4, 2000. 31, 156

[65] J. Chauveau and N. de Beaucoudrey. Low frequency imaging of separated objects using the ramp response technique. In *APS/URSI july 2010, Toronto, Ontario, Canada*, pages 1–4, 2010. 32

[66] J. Chauveau, Y. Wen, and N. de Beaucoudrey. Low frequency radar target imaging using ramp response signatures in arbitrary directions. In *PIERS Proceedings*, 2011. 33

[67] D. Ludwig. The radon transform on euclidean space. *Comm. Pure. Appl. Math.*, 19:49–81, 1966. 33

[68] SR. Deans. *The Radon Transform and Some of Its Applications*. New York: John Wiley and Sons, 1992. 33

[69] Y. Wen, N. de Beaucoudrey, J. Chauveau, and P. Pouliguen. Algorithm for profile function calculation of 3D objects: Application for radar target identification in low frequency. *Progress In Electromagnetics Research B*, 50:273–193, 2013. 48, 160, 163

[70] Y. Saad. *Iterative methods for sparse linear system*. Society for Industrial and Applied Mathematics, 2001. 68, 69

[71] C. C. Paige and M. A. Saunders. An algorithm for sparse linear equations and sparse least squares. *ACM Trans. Math. Soft.*, 8:43–71, 1982. 69, 70, 164

[72] S. Osher and J.A. Sethian. Fronts propagating with curvature dependent speed: Algorithms based on Hamilton-Jacobi formulations. *J.omput. Phys*, 79:12–49, 1988. 74, 134, 139, 164

[73] M. Sussman, P. Smereka, and S. Osher. A level set approach for computing solutions to incompressible two-phase flow. *Journal of Computational Physics*, 114(1):146 – 159, 1994. 74, 77, 164, 165

[74] A-K. Tornberg and B. Engquist. A finite element based level-set method for multiphase flow applications. *Computing and Visualization in Science*, 3(1-2):93–101, 2000. 74, 77, 164, 165

[75] I. Ginzburg and G. Wittum. Two-phase flows on interface refined grids modeled with vof, staggered finite volumes, and spline interpolants. *Journal of Computational Physics*, 166(2):302 –335, 2001. 74, 77, 164, 165

[76] J. A. Sethian and P. Smereka. Level set methods for fluid interfaces. *Annual Review of Fluid Mechanics*, 35:341–372, 2003. 74, 164

[77] S. Gross, V. Reichelt, and A. Reusken. A finite element based level set method for two-phase incompressible flows. *Computing and Visualization in Science*, 9(4):239–257, 2006. 74, 77, 164, 165

[78] R. Malladi, J. A. Sethian, and B.C. Vemuri. Shape modeling with front propagation: A level set approach. *IEEE Trans. Pattern Anal. Mach. Intell.*, 17(2):158–175, February 1995. 74, 82, 96, 164, 166, 168

[79] H-K. Zhao, T. Chan, B. Merriman, and S. Osher. A variational level set approach to multiphase motion. *J. Comput. Phys.*, 127:179–195, 1996. 74, 82, 164, 166

[80] V. Caselles, R. Kimmel, and G. Sapiro. Geodesic active contours. *Int. J. Comput.Vision*, 22:61–79, 1997. 74, 82, 83, 164, 166

[81] T.F. Chan and L.A. Vese. Active contours without edges. *Image Processing, IEEE Transactions on*, 10(2):266–277, 2001. 74, 164

[82] D.E. Breen and M. Kirby. Level set and pde methods for visualization. Technical report, Proceedings of IEEE Visualization, 2005. 74, 164

[83] C-M. Li, C-Y. Xu, C-F. Gui, and M.D. Fox. Distance regularized level set evolution and its application to image segmentation. *Image Processing, IEEE Transactions on*, 19(12):3243–3254, 2010. 74, 93, 164

[84] F. Santosa. A level-set approach inverse problems involving obstacles. Technical report, Ithaca, NY, USA, 1995. 74, 79, 80, 134, 139, 164, 166, 187

[85] A. Litman, D. Lesselier, and F. Santosa. Reconstruction of a two-dimensional binary obstacle by controlled evolution of a level-set. *Inverse Problems*, 14:685–706, 1997. 74, 79, 82, 134, 164, 166

[86] A.G. Tijhuis, K. Belkebir, A. Litman, J.M. Geffrin, and J.C. Bolomey. Two-dimensional inverse profiling: Nonlinear optimization and embedding. *RTO Lecture Series*, 214:6.1–6.3, 1998. 74, 164

[87] O. Dorn, E. L. Miller, and C. M. Rappaport. A shape reconstruction method for electromagnetic tomography using adjoint fields and level sets. *Inverse Problems*, 16(5):1119–1156, 2000. 74, 80, 164, 166

[88] S. J. Osher and R. P. Fedkiw. Level set methods and dynamic implicit surfaces. *Applied Mechanics Reviews*, 57(3), 2004. 75, 165

[89] R. Courant, K. Friedrichs, and H. Lewy. On the partial difference equations of mathematical physics. *IBM Journal of Research and Development*, 11(2):215–234, 1967. 79, 167

[90] A. Litman. Reconstruction by level sets of n-ary scattering obstacles. *Inverse Problems*, 21:S131–S152, 2005. 79, 166

[91] C. Ramananjaona, M. Lambert, D. Lesselier, and J-P. Zolésio. Shape reconstruction of buried obstacles by controlled evolution of a level set: from a min-max formulation to numerical experimentation. *Inverse Problems*, 17(4):1087, 2001. 79, 166

[92] C. Ramananjaona, M. Lambert, and D. Lesselier. Shape inversion from TM and TE real data by controlled evolution of level sets. *Inverse Problems*, 17(6):1585, 2001. 79, 166

[93] C. Ramananjaona, M.Lambert, D.Lesselier, and J.P.Zolesio. On novel developments of controlled evolution of level sets in the field of inverse shape problems. *Radio Science*, 38:242–254, 2002. 79, 166

[94] E.L.Miller O.Dorn and C.M.Rappaport. Shape reconstruction in 2D from limited-view multifrequency electromagnetic data, in: Radon transform and tomography. *AMS series Contemporary Mathematics*, 278:97–122, 2001. 80, 166

[95] R. Ferraye, J. Dauvignac, and C. Pichot. An inverse scattering method based on contour deformations by means of a level set method using frequency hopping technique. *Antennas and Propagation, IEEE Transactions on*, 51:1100–1113, 2003. 80, 141, 166, 188

[96] V. Caselles, F. Catte, T. Coll, and F. Dibos. A geometric model for active contours in image processing. *Numerische Mathematik*, 66:1–31, 1993. 82, 83, 166

[97] M. Kass, A. Witkin, and D. Terzopoulos. Snakes: Active contour models. *INTERNATIONAL JOURNAL OF COMPUTER VISION*, 1(4):321–331, 1988. 83

[98] D.L. Chopp. Computing minimal surfaces via level set curvature flow. *J. Comput. Phys.*, 106(1):77–91, May 1993. 96, 134, 168

[99] D. Adalsteinsson and J.A. Sethian. A fast level set method for propagating interfaces. *J.Comp.Phys.*, 118(2):269–277, 1995. 96, 168

List of Figures

List of Tables

l'université nantes angers le mans
PÔLE DE RECHERCHE ET D'ENSEIGNEMENT SUPÉRIEUR

UNIVERSITÉ DE NANTES

Thèse de Doctorat

Yanhua WEN

Imagerie radar basse fréquence à partir de réponses en rampe dans des directions arbitraires

Low frequency radar imaging from ramp responses in arbitrary directions

Résumé

L'imagerie basse fréquence peut être utilisée pour caractériser des cibles, furtives aux fréquences radar usuelles, ou des objets enfouis. Les méthodes basses fréquences ne permettent pas d'obtenir des images haute résolution, mais elles fournissent des informations sur l'envergure et la forme globale de la cible. Les méthodes inverses de diffraction telles que la tomographie nécessitent un nombre élevé de directions d'observation pour reconstruire une image tridimensionnelle (3D). Au contraire, la technique de la réponse en rampe permet de générer une image 3D de l'enveloppe d'une cible à partir de seulement 3 directions d'observation. Cette possibilité est apportée par la forme de la réponse temporelle rétrodiffusée par la cible, appelée réponse en rampe , qui est reliée à la fonction de profil, définie comme l'aire de la cible dans chaque plan perpendiculaire à la direction d'observation. Les méthodes de reconstruction existantes donnent de bons résultats pour des directions d'observation mutuellement orthogonales, mais leurs performances se dégradent pour des directions arbitraires. Pour cela, nous utilisons un processus itératif. Dans le problème direct, nous avons développé un algorithme pour calculer la fonction de profil d'un objet 3D, qui peut être utilisé pour calculer les erreurs de la fonction de profil entre l'objet d'origine et l'objet estimé. Dans le le problème inverse, nous utilisons la méthode level-set, qui peut traiter le changement de topologie d'une manière complètement implicite et automatique lors de l'itération. Avec une vitesse adaptée, cette méthode donne des résultats corrects avec 3 directions arbitraires pour des objets variés.

Mots clés

Imagerie radar, basse fréquence, réponse en rampe, méthode level-set.

Abstract

Radar imaging in low frequency can be used to characterize targets, stealthy in common radar frequencies, or buried objects. The low frequency methods cannot provide high-resolution images, but they provide information on the size and global shape of the target. Inverse methods such as diffraction tomography require a great number of observing directions to reconstruct a three-dimensional (3D) image. On contrary, the ramp response technique permits to generate a 3D image of the global shape of a target from only 3 directions. This possibility is realized by the back-scattered ramp response, which is related to the profile function, defined as the area of the target in each cut-plane perpendicular to the incident direction. Existing reconstruction methods give good results for mutually orthogonal directions, but their performance degrades for arbitrary directions. For this, we use an iterative process. In the direct problem, we developed an algorithm to calculate the profile function of a 3D object, which can be used to calculate the error function profile between the original object and the estimated object. In the inverse problem, we use the level set method, which can fully handle the topology change implicitly and automatically during the iteration. With an adapted velocity, this method gives correct results with three arbitrary directions.

Key Words

Radar imaging, low frequency, ramp response, level-set method.